

Abstract

Wave Chaos in Dielectric Resonators: Asymptotic and Numerical Approaches

Hakan E. Türeci
2004

Dielectric optical micro-resonators and micro-lasers represent a realization of a wave-chaotic system, where the lack of symmetry in the resonator shape leads to non-integrable ray dynamics in the short-wavelength limit. Understanding and controlling the emission properties of such resonators requires the investigation of the correspondence between classical phase space structures of the ray motion inside the resonator and wave-functions. Semi-classical approaches to the resonances of deformed cylindrical resonators are analyzed first within the closed limit, which corresponds to the quantum billiard problem from the field of quantum chaos. The results are then generalized to the dielectric case. We develop an efficient numerical algorithm to calculate the quasi-bound modes of dielectric resonators, which play a crucial role in determining the emission properties of micro-lasers based on dielectric resonators. Resonances based on stable periodic ray orbits of dielectric cavities are constructed in the short-wavelength limit using the parabolic equation method, and an associated wavevector quantization rule for the complex wavenumbers is derived. The effect of discrete symmetries of the resonator is analyzed and shown to give rise to quasi-degenerate multiplets. A recent experiment on lasing emission from deformed GaN micro-cavities is analyzed, leading to the appearance of scarred modes and non-specular effects in the farfield emission pattern. A framework is presented for treating the non-linear laser equations in a form suitable for treating the dielectric micro-lasers.

Wave Chaos in Dielectric Resonators: Asymptotic and Numerical Approaches

A Dissertation
Presented to the Faculty of the Graduate School
of
Yale University
in Candidacy for the Degree of
Doctor of Philosophy

by
Hakan E. Türeci

Dissertation Director: A. Douglas Stone

May 2003

Copyright © 2004 by Hakan E. Türeci
All rights reserved.

Hayatıma yön veren ve teşekkür
etmeye fırsat bulamadığım iki insana:

Yurdanur Türeci
ve
Tahir Zozan Balkaş'a

Contents

Acknowledgments	xiv
1 Introduction	1
1.1 Overview	1
1.2 Brief Overview of this Thesis	12
2 Asymptotic Physics: Where rays and waves meet	18
2.1 Introduction	18
2.2 Semi-classical limit of the Helmholtz equation	20
2.3 Eikonal Equation as an initial value problem	22
2.4 A paradigm for integrable systems: The circle billiard	29
2.5 Generic Billiards and appearance of Chaos	38
2.6 Hamiltonian description of Ray Motion	40
2.7 Poincaré Surface of Section and Discrete Maps	44
2.8 The monodromy matrix and periodic orbits	48
2.9 KAM Transition – from integrability to Chaos	52
2.10 Semiclassics in a mixed phase space	60
2.11 Quantum Poincaré-SOS	63
2.12 Breakdown of local expansions	66
2.13 PUSC and Quantum Scars	67
2.14 Refractive Billiards	69
3 Scattering quantization method for optical billiards	77
3.1 Introduction	77
3.2 Reduction of Maxwell’s equations	78
3.3 Scattering Quantization-Philosophy and Methodology	81
3.4 Numerical Implementation	86
3.5 Root-search strategy	88
3.6 Scattering eigenstates and classical phase space structures	98
3.7 Role of discrete symmetries	100
3.8 Conclusion and Outlook	102

4	Gaussian Optics for Microcavities	104
4.1	Introduction	104
4.2	Gaussian Optical approach to the Dirichlet cavity	108
4.3	Boundary Conditions	111
4.4	Ray dynamics in phase space	113
4.5	Single-valuedness and quantization	114
4.6	Transverse excited modes	117
4.7	Perturbation Theory	119
4.8	Opening the cavity - The dielectric resonator	121
4.9	Symmetry Analysis and Quasi-Degeneracy	125
4.10	Symmetrized modes for the quadrupole	126
4.11	Simple Rule for Quasi-Degeneracy	128
4.12	Conclusions and Relation to Experiment	132
5	Non-classical phenomena in Dielectric Resonators	136
5.1	Introduction	136
5.2	Blue Lasers: Experimental Setup and Results	137
5.3	Configuration Space theory of Scars	143
5.4	Non-specular effects in emission in refractive billiards	151
6	Towards a Non-Linear Theory of Dielectric Resonators	159
6.1	Introduction	159
6.2	Single-mode Lasing	161
6.3	Adiabatic Elimination	164
6.4	Multi-mode Lasing	165
6.4.1	Diagonal Inversion: Non-degenerate lasing	167
6.4.2	Non-Diagonal Inversion: Degenerate lasing	169
7	Conclusion and Open Questions	171
A	Uniform expressions valid on the caustic	173
B	Tunneling in the dielectric cylindrical cavity	175
C	Coordinate Systems on the PO	179
D	Linear Ray Reflection & Refraction transformations	181
E	Perturbation Theory for Gaussian Modes	183
F	The Lens Transform for a Cavity	188
	Bibliography	191

List of Figures

1.1	A comparison of scattering and emission perspectives. Variation of the intensity scattered off a dielectric circular cylinder with the wavenumber k of an incoming plane-wave is plotted on the back panel ($I - \text{Re}[kR]$ plane). The intensity is observed at 170° with respect to the incoming wave direction. The complex quasi-bound mode frequencies are plotted on the $\text{Re}[kR] - \text{Im}[kR]$ plane. Notice that the most prominent peaks in scattering intensity are found at the values of k where a quasi-bound mode frequency is closest to the real-axis. These are the long-lived resonances of the cavity. Also visible is the contribution of resonances with shorter lifetimes (higher values of $\text{Im}[kR]$) to broader peaks and the scattering background.	3
1.2	A schematics of the Fabry-Perot type laser cavity is shown on the left. An actual Fabry-Perot mode. The right mirror is assumed to be formed by a dielectric interface.	4
1.3	(a) A scanning electron micrograph picture of a VCSEL device [1]. The horizontal scale of the device is $4\mu m$. (b) Schematics of the structure of such a device (courtesy of Jung Han, Yale University)	4
1.4	(a) Fresnel reflection and refraction in a planar dielectric cavity. (b) The high-reflectivity mirror action is provided by total internal reflection.	5
1.5	(a) A scanning electron micrograph of a microdisk laser on a pedestal [2]. The horizontal scale of the device is about $5\mu m$. (b) Top panel: real space false color plot of the modulus of the electric field for a calculated quasi-bound state of a planar microdisk cavity. Lower panel: Ray trajectories associated with the mode on the top panel.	6
1.6	The construction of the surface of section plot. Each bounce from the boundary is represented by a point in the SOS by recording the angular position of the bounce on the boundary (ϕ) and the angle of incidence with respect to the local outward pointing normal ($\sin \chi$). For $\sin \chi > \sin \chi_c > 1/n$, total internal reflection takes place. Refractive escape results when a bounce point (bounce #4 in the figure) falls below the “critical line” $\sin \chi > \sin \chi_c$. Note that $\sin \chi < 0$ correspond to clockwise sense of circulation. We do not plot the $\sin \chi < 0$ region-the SOS has reflection symmetry.	8

1.7	The Poincaré surface of section at an intermediate quadrupolar deformation of $\epsilon = 0.08$. Regular motion takes place along invariant curves in the SOS, i.e. any trajectory started on such a curve will remain on the same curve throughout its motion. Note that a curve is obtained by discrete points in the large bounce limit. The regions containing scatter of points represent chaotic motion. A generic initial condition within a given connected area will come arbitrarily close to any point within that component. Note that the invariant curves act as barriers to the chaotic motion. This feature is limited to two-dimensional systems.	9
1.8	(a) A real space false color plot of the electric field intensity for a chaotic whispering gallery resonance at $n = 2$, illustrating the generic emission pattern from points of highest curvature on the boundary in the tangent direction. (b) Emission of a dynamically eclipsed state at $n = 1.54$ (after [3, 4])	10
1.9	(a) Scanning electron micrographs of the top and side-view of one of the deformed cylindrical quantum cascade micro-lasers. (b) Numerically calculated resonance corresponding to the bowtie-mode observed for the deformation $\epsilon = 0.16$. (c) Angular dependence of the emission intensity for deformations $\epsilon = 0$ (triangles), $\epsilon = 0.14$ (open circles), $\epsilon = 0.16$ (filled circles). Dashed line represents the calculated farfield pattern corresponding to the resonance in (b). The right inset shows the coordinate system used and the left inset shows the logarithmic plot of the measured power spectrum. The free-spectral range of the peaks is found to agree with the calculated bowtie free spectral range (after [5]).	11
2.1	Schematics showing the level-curves of the Eikonal $S(q)$, $S(q) = S_0$ and $S(q) = S_1$. The normals of $S(q) = S_0$, form a normal congruence of rays and yield the next level-curve $S(q) = S_1$. Depicted is a situation where the index of refraction $n(q)$ is monotonically increasing from the top of the figure to the bottom.	21
2.2	Schematics showing the ray coordinates (s, τ) . The dashed lines are equi-coordinate curves $s = constant$ and $\tau = constant$, which are the wavefronts and rays.	23
2.3	Different boundary conditions Σ resulting in different geometry of wavefronts.	25
2.4	Schematics showing the mapping of an initial line element ∂D_{τ_0} on an initial wavefront at $\tau = 0$ by ray flow to its value at $\tau > 0$, ∂D_{τ} . Note that the “tube of rays” shrinks or expands depending on the curvature of the initial wavefront.	26
2.5	Schematics showing the evolute-involute and wavefront-caustic relationship. There are two possible ray directions at each point N in the vicinity of the caustic.	28

2.6	Involutes S_{\pm} of a circular curve. The two sheets are colored in blue (S_-) and red (S_+). The solid black lines are the rays corresponding to S_{\pm} . Note that (S_-) rays ingoing to the caustic are everywhere normal to the blue curves and outgoing (S_+) rays are everywhere normal to the red curves.	29
2.7	Reflection condition at the boundary and the choice of wavefront orientation.	31
2.8	(a) A quasi-periodic ray motion and (b) a periodic 5-bounce orbit. . .	32
2.9	The two vector field $\mathcal{M}^{\pm}(\chi)$ on the covering spaces Ω^{\pm} can be glued together to obtain a continuous vector-field on a covering-space topologically equivalent to a 2-torus.	33
2.10	The deformability of a contour of integration within the vector field $\mathcal{M}^{\pm}(\chi)$, derived locally from a potential multi-valued potential $S(q)$	34
2.11	Basis curves on the two-torus and a particular realization of these in the circular domain. The solid curves denote the (+) sheet, and dashed curves the (-) sheet.	35
2.12	Paths for the calculation of the Eikonals at a point (r, ϕ) . We take $S_{\pm}(a, 0) = 0$. Both $\Gamma_{1,2}$ start tangent to the caustic at $(a, 0)$. Γ_1 is composed of an arc of length $\tau = a(\phi - \cos^{-1}(a/r))$ and a straight line segment of length $\tau = \sqrt{r^2 - a^2}$. Γ_2 contains an arc of length $\tau = a(\phi + \cos^{-1}(a/r) - 2 \cos^{-1}(a/R))$, two straight line segments of total length $2\sqrt{R^2 - r^2} - \sqrt{r^2 - a^2}$. Because of the reflection, π/k has to be subtracted.	37
2.13	A schematics showing the simulation of a ray \mathbf{p}_0 started at a point q_0 in the stadium. The observation at a second point q (within a finite cell Δq around q) would result in approximately isotropic distribution of ray directions in a long run. For the results of an actual simulation see Fig. 2.14.	39
2.14	(a) A real-space trajectory and (b) the SOS plot of a stadium at a fractional deformation of $\epsilon = 0.43$	46
2.15	(a) The bouncing-ball (BB) periodic orbit (corresponding to fixed point $\xi^{(0)} = (-\pi/2, 0)$) is the solid black line. The red trajectory drawn in red is a typical trajectory in the vicinity of the BB orbit. (b) The action of the exact section map \mathbf{M} and the monodromy operator M . A point $\xi^{(1)} = \xi_0 + \delta\tilde{\xi}$ is mapped to $\xi^{(2)} = \mathbf{M}(\xi^{(1)})$, and $\xi^{(3)} = \mathbf{M}^2(\xi^{(1)})$. Here, $\xi^{(3)}$ is back to the neighborhood of the original fixed point $\xi^{(0)}$. The action of the monodromy matrix M for the two-bounce orbit is hence $\delta\tilde{\xi} = M\delta\tilde{\xi}$	49
2.16	An actual segment of the SOS of an elliptic billiard of fractional deformation $\epsilon = 0.12$, around the stable bouncing ball orbit fixed points.	50
2.17	An actual segment of the SOS of an elliptic billiard of fractional deformation $\epsilon = 0.12$, around the unstable bouncing ball orbit fixed point at $\phi = 0, \sin \chi = 0$	51

2.18	The bifurcation of the two-bounce orbit of the circle. (a) The original two-bounce orbit comes in an infinite family, some of which are shown in the trajectory plot below the section plot. The associated invariant curve is the thick black line in the SOS. (b) At a deformation of $\epsilon = 0.02$, one sees the two isolated two-bounce orbits. Drawn in blue is the stable fixed points and in red, the unstable partner.	53
2.19	The SOS of ellipse at $\epsilon = 0.07$ deformation. Two representative orbits belonging to a rotational, whispering-gallery-like motion, and of librational, bouncing-ball-like motion.	54
2.20	The separatrices of the ellipse at a deformation of $\epsilon = 0.07$. The blue axes represent the <i>linearized</i> stable manifolds H_- and the unstable manifolds H_+ , which is placed on the actual, non-linear manifolds of the fixed points Q_1 . The points P_n are obtained from the iterations of the two-bounce map M^2 on an initial point P_0 on the unstable manifold.	55
2.21	A zoom in to the separatrix region of the quadrupole 2-bounce orbit at a deformation $\epsilon = 0.03$. Note that the chaotic layer is delimited by KAM curves on both sides.	56
2.22	(a) A 50-bounce simulation of an initial condition P_0^- close to the fixed point $Q_1 : (0, 0)$. The subsequent intersections of motion with the SOS fail to fall on a continuous curve, which is a signature of chaotic motion (b) An initial ensemble of starting conditions (6000 points, gaussian distributed around $(0, 0)$) are propagated forward and backward to generate the homoclinic tangle. The red curve forms the unstable manifold of the fixed point $Q_1 : (0, 0)$ (and the stable manifold of $Q_2 : (\pi, 0)$), and the blue curve forms the stable manifold (unstable manifold of Q_2). Note that the area within the loops are conserved (hatched region) because of the property of Hamiltonian flow; thus when the intersections lie closer together the loops undergo wider excursions.	57
2.23	The SOS of a quadrupole at fractional deformations $\epsilon = 0, 0.05, 0.11, 0.18$. The closed curves and curves crossing the SOS represent types of regular motion, the regions of scattered points represent chaotic portions of phase space. A single trajectory in this “chaotic component” will explore the entire chaotic region. With increasing deformation the chaotic component of the SOS (scattered points) grows with respect to regular components. Note in (b) the separatrix region where the transition to chaotic motion sets in first	59
2.24	Local coordinate system for the bouncing-ball periodic orbit.	62

2.25	(a) Effective surface of section with linear elliptic manifolds, as calculated with Eq. (2.121) at a deformation of $\epsilon = 0.13$. Note that it's topologically not possible to cover the whole SOS with these approximate manifolds. (b) Exact SOS for the quadrupole at $\epsilon = 0.13$ deformation. Note the secondary island (which is associated with a bowtie-like orbit), and the finite extent of the primary island.	67
2.26	A schematics of the refractive billiard system and the variables used in the text.	70
2.27	(a) Initial coordinates for ray simulation are chosen on the emitting invariant curve, which touches the critical line (red curve) $\sin \chi_c = 1/N$ at the points of highest curvature $\phi = 0, \pi$ leading to tangent emission, shown schematically on the right. (b) Observed farfield emission pattern is represented by the blue curve; the green curve is the result of simulation with initial conditions in (a).	75
2.28	(a) Initial coordinates for ray simulation are chosen above the critical line (red curve) $\sin \chi_c = 1/N$. The stable diamond island leads to a large deviation from adiabatic motion close to the points of highest curvature $\phi = 0, \pi$, eclipsing the emission. As a result, rays escape through a flow around the island, leading to displaced emission points, shown schematically on the right. (b) Observed farfield emission pattern is represented by the blue curve; the green curve is the result of simulation with initial conditions in (a).	76
3.1	Illustration of the reduction of the Maxwell equation for an infinite dielectric cylinder to the 2D Helmholtz equation for the TM case (E field parallel to axis) and $k_{\parallel} = 0$	78
3.2	Schematics describing the quantum Poincaré mapping induced by the internal scattering operator.	84
3.3	A gray-scale representation of the scattering matrix Eq. (3.37), calculated for a quadrupolar resonator at $\epsilon = 0.1$ deformation, $n = 2.5$ and $nkR = 40$. The number of evanescent channels used in the calculation is $\Lambda_{ev} = 15$. Note the strong diagonal form for $ m > nkR$. The spread around the diagonal is proportional to the deformation. Here, the internal scattering couples approximately 20 angular momentum modes.	85
3.4	The logarithm of the condition number λ as a function of the size Λ of H_2^+ , calculated for quadrupolar resonator with deformation $\epsilon = 0.16$, $n = 3.2$ and $nkR = 128$. The dashed line represents the machine precision, where we cutoff the matrix in a typical calculation. In this example, this corresponds adding $\Gamma_{ev} \approx 8$ evanescent channels. This would be the singularity limit for a calculation with inversion. Owing to the diagonalization technique we are using, we can add many more channels without a numerical degradation.	87

3.5	Distribution of scattering eigenphases (red circles) in the complex plane for $nkR = 106$, $\epsilon = 0.12$, $n = 2.65$. Blue dashed line is the unit circle $ z = 1$	88
3.6	The tracing of the overlap calculated for a set of states in the interval $nkR = 106 - 107.5$, for $\epsilon = 0.12$ and $n = 2.65$. The associated classical structures are found by the Husimi projections of the respective states. The encoding is: sBB= n th transverse excitation of the stable bouncing ball mode, uBB=unstable bouncing ball mode.	93
3.7	Two eigenvectors are traced by the criterion that the overlap is largest in two <i>consecutive</i> iterations. The figure shows the overlap of the two sets of states resulting with respect to one of the <i>initial</i> states, $ \alpha_0\rangle$	94
3.8	Several representative eigenphases traced in the complex plane through real and imaginary values of k . At first, real $\text{Re}[k]$ is varied, resulting in the circular arcs; subsequently $\text{Im}[k]$ is varied resulting in a radial motion. The simulations are performed at $\epsilon = 0.12$ quadrupolar deformation, $n = 2.65$	95
3.9	For the eigenstates of Fig. 3.8, variation of (a) $e^{\eta(k)}$ with change in $\text{Re}[k]$, (b) $e^{i\theta(k)}$ with change in $\text{Im}[k]$, normalized to initial values. Note that the variation is negligible. The larger variation of the second fish-eigenstate in (b) is due to an avoided crossing encountered during the imaginary k scan.	97
3.10	For the eigenstates of Fig. 3.8, variation of (a) $\theta(k)$ with a scan in $\text{Re}[k]$, (b) $\eta(k)$ with scan in $\text{Im}[k]$. Note that the variation in both cases display approximately constant slopes.	97
3.11	Real-space false color plot of a solution at (a) $\epsilon = 0$, and (c) $\epsilon = 0.03$. (b,d) Husimi projections of states (a,c). The solutions are obtained at $nkR = 82$ and $n = 2$	99
3.12	Real-space false color plots and Husimi projections of transverse excited bouncing ball modes. The solutions are obtained at $nkR = 106$ and $n = 2$	100
3.13	Real-space plots and Husimi distributions of scattering eigenvectors scarred by the unstable bouncing ball orbit. Superimposed on the SOS are the stable and unstable manifolds. (a),(b) fundamental mode; (c),(d) eigenvector scarred by (c),(d) the primary intersection and (e),(f) the secondary intersection. These solutions are found at $nkR = 106$, $\epsilon = 0.12$ and $n = 2.65$	101

- 4.1 Surface of section illustrating the different regions of phase space for a closed quadrupole billiard with boundary given by $r(\phi) = R(1 + \epsilon \cos 2\phi)$ for $\epsilon = 0.072$. Real-space ray trajectories corresponding to each region are indicated at right: a) A quasi-periodic, marginally stable orbit. b) A stable four-bounce “diamond” periodic orbit (surrounded by stability “islands” in the SOS) c) A chaotic ray trajectory. Orbits of type (b) have associated with them regular gaussian solutions as we will show below. 105
- 4.2 Black background gives the surface of section for the quadrupole at $\epsilon = 0.17$ for which the four small islands correspond to a stable bow-tie shaped orbit (inset). A numerical solution of the Helmholtz equation for this resonator can be projected onto this surface of section via the Husimi projection (cf. Section 2.11) and is found to have high intensity (in false color scale) precisely on these islands, indicating that this is a mode associated with the bow-tie orbit. 106
- 4.3 (a) Vertical lines indicate wavevectors of bound states of the closed quadrupole resonator for $\epsilon = 0.17$; no regular spacings are visible. (b) Spectrum weighted by overlap of the Husimi function of the solution with the bow-tie island as in Fig. 4.2. Note the emergence of regularly spaced levels with two main spacings Δk_{long} and Δk_{trans} . These spacings, indicated by the arrows, are calculated from the length of the bow-tie orbit and the associated Floquet phase (see Section 4.5 below). The color coding corresponds to the four possible symmetry types of the solutions (see Section 4.9 below). In the inset is a magnified view showing the splitting of quasi-degenerate doublets as discussed in 4.11. Note the pairing of the $(+, +)$ and $(+, -)$ symmetry types as predicted in Section 4.11. The different symmetry pairs alternate every free spectral range (Δk_{long}). 107
- 4.4 Coordinate systems used in the calculations. Only one of the bounces, the m^{th} bounce, is illustrated. 108
- 4.5 The bouncing ball mode transverse width is of the order of $1/\sqrt{k}$. The periodic orbit axis is also indicated. 110
- 4.6 The path of $e^{i\pi m}q(z)$, ($z_{m-1} < z < z_m$, $m = 0 \dots N$) in the complex plane as z varies within a complete period for the solution in Fig. 4.7. The chosen branch-cut is shown with the rippled line extending from the origin to the negative real axis. The arrow indicates the motion of $q(z)$ as z starts out from $z = 0$ and completes a period. 115
- 4.7 Intensity of the TM solution for a bow-tie mode plotted in a false color scale, (a) calculated numerically and (b) from the gaussian optical theory with parameters $m = 100$, $\varphi = 2.11391$, $N_\mu = 1$ and $N = 4$. Note the excellent agreement of the quantized values for kR (R is the average radius of the quadrupole). 117

4.8	Schematic indicating a direct tunneling process (black arrow) and a chaos-assisted tunneling process (yellow arrow) which would contribute to splitting of bow-tie doublets.	131
4.9	A numerically calculated transverse series of modes based on the bowtie periodic orbit. The calculations are performed at $nkR \approx 128$, $n = 3.3$, $\epsilon = 0.16$. With these parameters the bowtie periodic orbit hits the boundary exactly at the critical angle. (a) the fundamental mode, (b) the 1st excited mode (c) the second excited mode. Note the strong “near-field” fluctuations of especially the second order mode in (c).	134
4.10	The farfield emission patterns of the transverse excitations of the bowtie modes of Fig. 4.9 compared to the experimentally measured farfield pattern. The arrow denotes the direction of tangent emission.	135
5.1	(a) A scanning electron micrograph of the GaN resonators used in the experiments. The device in the figure has a diameter of $200\mu m$. (b) Experimental setup for measuring simultaneously far-field intensity patterns and images of the sidewall emission.	138
5.2	(a) Experimental data showing in color scale the CCD images (converted to sidewall angle ϕ) as a function of camera angle θ . Three bright spots are observed on the boundary for camera angles in the 1st quadrant, at $\phi \approx 17^\circ, 162^\circ, -5^\circ$. (b) Calculated image field corresponding to the scarred mode shown in Fig. 5.5. (c) Calculated and experimental far-field patterns obtained by integrating over ϕ for each θ	139
5.3	The SOS of the quadrupolar billiard at a deformation of $\epsilon = 0.12$. The red vertical lines indicate the values of ϕ at which the bright spots in the imagefield are observed. On the right is a schematic of the bright spots in the real space.	140
5.4	The variation of trace of the monodromy matrix with respect to the quadrupolar deformation ϵ . The black circle indicates the experimental value $\epsilon = 0.12$, at which $\text{Tr}(M) = -5.27$. The two dashed lines delimit the regime $-2 < \text{Tr}(M) < 2$ at which the triangular orbit is stable. In the inset is shown real space simulation of a ray orbit started with initial conditions which are away from the triangle fixed point at least by $\delta\phi = 10^{-3}$, $\delta \sin \chi = 10^{-4}$, followed for 20 bounces.	141

- 5.5 (a) Real-space false color plot of the modulus of the electric field for a calculated quasi-bound state of $nk_r o \approx 129$ (n is the index of refraction, k is the real part of the resonant wavevector) and $\epsilon = 0.12$ which is scarred by the triangular periodic orbits shown in the inset (M. V. Berry has termed this the “Scar of David”). The four points of low incidence angle which should emit strongly are indicated. (b) Husimi (phase-space distribution) for the same mode projected onto the surface of section of the resonator. The x-axis is ϕ_w and the y-axis is $\sin \chi$, the angle of incidence at the boundary. The surface of section for the corresponding ray dynamics is shown in black, indicating that there are no stable islands (orbits) near the high intensity points for this mode. Instead the high intensity points coincide well with the bounce points of the unstable triangular orbits (triangles). The black line denotes $\sin \chi_c = 1/n$ for GaN; the triangle orbits are just above this line and would be strongly confined whereas the stable bow-tie orbits (bow-tie symbols) are well below and would not be favored under uniform pumping conditions. 142
- 5.6 The periodic orbit coordinates used in the text, for the particular case of a triangular periodic orbit. The trajectory in black is a closed trajectory in the vicinity. 146
- 5.7 The function $F_j(k)$ calculated for the parameters of the unstable triangle at $\epsilon = 0.12$. The length of the orbit is $L = 5.3$ and $u = 1.62$. Note that the spectral peaks are well-resolved. 149
- 5.8 Schematics showing the three emitted “beams” detected in the experiment (solid lines) and illustrates their strong deviation from Snell’s law (dashed tangent lines). 151
- 5.9 Angular farfield intensity distributions $I(\phi) = |E_e(\phi)|^2$ for: (dotted line): critical incidence on a planar interface with $n = 1.56, \Delta = 8.82, z_0 = 5$ using the gaussian model (Eq. (5.52)). (solid line): Exact quasi-normal mode with diamond geometry at $nk_o r_o \approx 90$, for a quadrupolar ARC with $\epsilon = 0.1, n = 1.56$. (dot-dashed line): Chiral version of diamond resonance (see text) which eliminates interference effects. Inset: Coordinates and variables for the GM calculation. . . . 153
- 5.10 (a) Field intensity plot (gray-scale) for a diamond resonance of the quadrupole at critical incidence for the points at $\phi_w = 0, \pi$, calculated numerically at $nk_o r_o \approx 90, n = 1.56, \epsilon = 0.1$. Note that there is negligible emission from the upper and lower bounce points at $\phi_w = \pm 90^\circ$ because they are above the critical angle (b) Chiral counterpart of this exact resonance, simulating a gaussian beam (see text). . . . 156
- 5.11 Comparison of peak angular farfield values ϕ_{max} for varying critical angle $\theta_c = \sin^{-1}(1/n)$. (Diamonds): exact resonances at $nk_o r_o \approx 90$. (Solid line): GM calculation with $\Delta \approx 8.82$. (Dashed line): Snell’s law prediction: $\sin \phi_{max} = n \sin \theta_i$ where $\theta_i \approx 39^\circ$. $\Delta \theta_{FF}^c$ designates the deviation from Snell’s law at $\theta_c = \theta_i$ 157

5.12	Solid line: Central beam emission angle χ_e^o vs. central incidence angle χ_i^o for a beam of angular spread equivalent to the scarred mode of Fig. 5.5 incident on a plane interface. Dashed line is Snell's law, the discrepancy is the Fresnel Filtering angle $\Delta\theta_{FF}$. Inset schematic shows the three emitted "beams" detected in the experiment and illustrates their strong deviation from Snell's law (dashed tangent lines).	158
B.1	The reflectivity calculated using Eq. (B.5) with exact quantized wavevectors calculated using Eq. (B.3) at different regimes of NkR . Note that as $k \rightarrow \infty$ the calculated reflectivities approach those obtained from Fresnel law Eq. (2.172). The dashed vertical line represents the critical value $\sin \chi_c = 1/N$. The calculations are performed for an index of refraction $N = 2$	176
B.2	The effective potential $V_{eff}(r)$ for $m = 70$, $kR = 100$, $n = 2$	177
D.1	Coordinates of a single ray bounce event for the derivation of the ray reflection and refraction transformations	182

List of Tables

3.1	A typical run at $kR_0 = 40$, $\epsilon = 0.12$ and $n = 2.65$. The first column represents the predicted value by constant speed requirement determined from two successive diagonalizations separated by $\Delta kR = 10^{-4} + i10^{-4}$. The second column is the error of this prediction, obtained by a full root search, measured by the distance in the complex plane between the eigenphase and the quantization point. The last two columns are the overlaps of the original eigenvectors (internal and external) with the actual quantized ones.	96
4.1	Table comparing the gaussian optical prediction for the complex k values of bow-tie resonances of the quadrupole ($\epsilon = 0.17$) to numerically obtained values for three different indices of refraction corresponding to incidence below, at and above the critical angle for total internal reflection. The schematic at right depicts the bow-tie island in comparison to the critical line for total internal reflection for the three cases (horizontal lines).	125
4.2	Table illustrating the application of the two symmetry rules to five short POs. The second column is the total number of orbits of this shape related by spatial symmetry; the third column is the total number of orbits of this shape generated by time-reversal symmetry. By Rule 1 the quasi-degeneracy is the product of these two numbers. Column 4 gives the symmetry-reduced orbit which leads via Rule 2 to the symmetry pairing indicated in column 5.	129

Acknowledgments

There are so many friends and colleagues who deserve thanks for having contributed to my life and education during my years at Yale. Needless to say, the greatest credit for this dissertation goes to my advisor Douglas Stone, who with his continuous guidance and support has turned the bumpy roads of research experience into a pleasant hike. I have learnt a lot from his wide range of experience, his uncanny ability of simplifying difficult problems, and even a few moves in soccer. Fortunately I will be able to enjoy another year of collaboration and a long-lasting friendship with him.

I would like to especially thank Richard Chang, who has been a great mentor and collaborator. He served and will serve as an ideal model of a great scientist and a great man for me.

Some of the work reported in this thesis, especially that of Chapter 3, was done in collaboration with Harald Schwefel, who sits right now next to me going over the last draft (excluding this section), having spent the last night up going over and over; being there just when I needed his help most, as always. Looking back, I feel extremely lucky to have shared office with him.

I was fortunate enough to have had great teachers during my PhD period. I owe a lot to their patience and hard work at grinding down mountains to hills for students to pass through: David Sattinger, Steven Orszag, Gregory Moore and R. Shankar. I feel privileged to have known Martin Gutzwiller. It was great to have known the man who was behind it all, and I will always cherish the memory of his visits and the stimulating discussions we had.

I have enjoyed and benefitted greatly from my interactions, both professionally and personally, with Philippe Jacquod. I hope we will keep in touch.

There are several former members of Professor Stone's group, whose past (and present) work has shaped my current knowledge: Jens Nöckel, Evgenii Narimanov, and Gregor Hakenbroich. I would like to use this opportunity to thank them.

I would also like to acknowledge the valuable help I received from Stanley Eisenstat, which led to the improvement of the numerical method of Chapter 3.

There are good friends, real good friends who have shared the good and the frustrating times: George, Sotiria, Al, Swati, Chiranjeeb, Stacey, Grace, Seema. I owe them many of the memorable moments of this period of my life.

Suha Hanim: She is such a youthful, charming Lady who has been always there whenever I needed a good advice or for just a nice evening chat. But she means to

me much more than that: The noble lifestyle she and Feza Bey represent is one of the few reasons I still think highly and as more than just a profession of the life as a scientist.

Dide Su, Damla and Metin were the sweetest people around. I just wish I had met them earlier. Well, the future is ahead at least.

My family, despite the physical distance, has always been close to me. I want to thank them for being always there, from the bottom of my heart!

Finally, the sweet taste of my life, Esin. Not only has she patiently endured my endless writing, she also participated actively at almost all the stages, be it logistics for a night shift, proofreading or printing. Most importantly, she turned our home into the most comforting refuge, which provided me with the strength I needed for the coming day. Biricik muntuim benim...bak bir chapter daha bitirdik.

Chapter 1

Introduction

1.1 Overview

The work underlying this thesis is an attempt to understand certain properties of *dielectric resonators* operating in the optical regime with emphasis on properties which scale in a simple manner with the wavelength (and persist over a wide range of wavelengths). This becomes possible when the wavelength of operation is much shorter than the geometric features of the resonator, namely in the *semi-classical limit*. To do this, the present work draws from tools widely used in the disciplines of quantum chaos and asymptotic analysis of differential operators.

Devices utilizing the interaction between matter and an electromagnetic field typically require the radiation to be confined to a small region of space. A common component of such devices is the *resonator* or the *cavity*. There are a host of such devices operating over a wide range of frequencies, and we are in particular interested in lasers, which operate in the optical regime of the electromagnetic spectrum, broadly defined to be ranging from near infrared ($\sim 1\mu m$) to the ultraviolet ($\sim 200-300nm$). The dielectric resonators we will be interested in range from $10\mu m - 500\mu m$, and are often referred to as *micro-resonators*. In all cases we will study they are significantly larger than the wavelength of the light they confine and so appropriate for treatment in the semi-classical limit.

Resonators are characterized by a discrete set of *quasi-bound modes* [6, 7], or *resonances*. In contrast to ideal cavities which possess discrete normal modes at real frequencies, a mathematical abstraction representing a structure which contains energy perfectly, resonators are inherently open systems due to their coupling to the external world. As a result, the quasi-bound modes of a resonator are characterized by a frequency $\omega = ck$ and a lifetime τ , where c is the speed of light and $k = 2\pi/\lambda$ is the wavevector in vacuum. Experiments on resonators fall into two broad categories, and the presence of quasi-bound modes are manifested differently in these two situations. In scattering experiments, an incoming field produced by a source in the *farfield* (spatial infinity) gives rise to an outgoing field which represents the response of the resonator, as measured by an ideal detector in the farfield. In the

ideal case, where absorption is absent, this corresponds to a situation where energy is conserved and hence this situation the EM field has a real frequency ω , which is arbitrary and set by the source. In emission experiments, on the other hand, there is no incoming field, but only an outgoing field. As a result, energy is depleted from the system, and this process is characterized by decay. The simplest mathematical description of these two experiments correspond to the solution of the wave-equation (which is derived from the Maxwell's equations as described in Section 3.2)

$$\left(\nabla^2 - \frac{n^2(\mathbf{x})}{c^2} \frac{\partial^2}{\partial t^2} \right) \Psi(\mathbf{x}, t) = 0 \quad (1.1)$$

where the solutions have the separable, time-harmonic dependence

$$\Psi(\mathbf{x}, t) = \psi(\mathbf{x})e^{i\omega t} \quad (1.2)$$

so that $\psi(\mathbf{x})$ obeys the *Helmholtz equation*

$$(\nabla^2 + n^2(\mathbf{x})k^2) \psi(\mathbf{x}) = 0 \quad (1.3)$$

Here, $n(\mathbf{x})$ represents the index of refraction. In general, one can define a complete set of incoming $\{\psi_\mu^{(-)}(k; \mathbf{x})\}$ and outgoing modes $\{\psi_\mu^{(+)}(k; \mathbf{x})\}$ at a given k , in the absence of the resonator. The exact form of these sets is dictated by convenience, and depends on the dimensionality and symmetry of the problem.

The two experimental situations at this point are distinguished by two different boundary conditions in the farfield. The scattering experiment corresponds to the boundary condition

$$\psi(\mathbf{x}) \sim \psi_\mu^{(-)}(k; \mathbf{x}) + \sum_\nu S_{\mu\nu}(k) \psi_\nu^{(+)}(k; \mathbf{x}), \quad |\mathbf{x}| \rightarrow \infty \quad (1.4)$$

and experimentally, it is the scattering matrix $S_{\mu\nu}(k)$, which contains the information measured by the farfield detector. In the typical case $S_{\mu\nu}(k)$ will display sharp peaks at a discrete set of real wavevectors k_i , where the width of these peaks are given by Γ_i (in case of isolated resonances; see the back panel (Re $[kR]$ - I plane) on Fig. 1.1). This is the signature of *long-lived* quasi-bound modes with frequency $\omega = ck_i$; their lifetimes τ are encoded in the functional form of the peaks, which in general is of Fano shape, with direction-dependent parameters. This makes scattering boundary conditions less convenient for the extraction of the quasi-bound mode structure.

The emission experiments are modeled by the outgoing wave (radiation) boundary conditions at infinity

$$\psi^{(i)}(\mathbf{x}) \sim \sum_\nu \gamma_\nu(k_i) \psi_\nu^{(+)}(k_i; \mathbf{x}), \quad |\mathbf{x}| \rightarrow \infty \quad (1.5)$$

This form at infinity does not permit solution for any real k as it manifestly violates current conservation. Instead the solutions of Eq. (1.3), indexed by i , exist only at

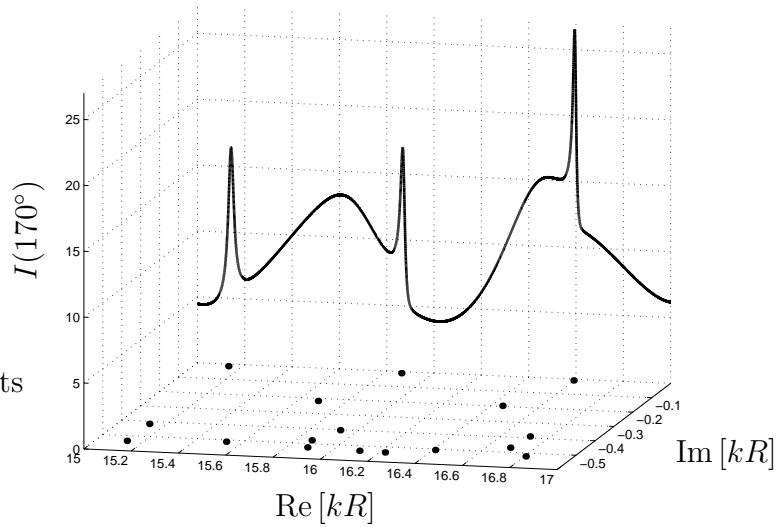


Figure 1.1: A comparison of scattering and emission perspectives. Variation of the intensity scattered off a dielectric circular cylinder with the wavenumber k of an incoming plane-wave is plotted on the back panel ($I - \text{Re}[kR]$ plane). The intensity is observed at 170° with respect to the incoming wave direction. The complex quasi-bound mode frequencies are plotted on the $\text{Re}[kR] - \text{Im}[kR]$ plane. Notice that the most prominent peaks in scattering intensity are found at the values of k where a quasi-bound mode frequency is closest to the real-axis. These are the long-lived resonances of the cavity. Also visible is the contribution of resonances with shorter lifetimes (higher values of $\text{Im}[kR]$) to broader peaks and the scattering background.

discrete complex wavevectors $k_i = \kappa_i + i\gamma_i$. The connection to quasi-bound modes is then direct; the real part gives the quasi-bound mode frequency $\omega_i = c\kappa_i$ and the imaginary part represents the lifetime of the mode, $\tau_i = 1/c\gamma_i$. In this thesis, we will use the radiation boundary conditions exclusively, and quote the dimensionless complex variable kR instead, where R is the mean radius of the resonator. In standard resonator theory these quasi-bound modes of the linear wave equation are routinely used to describe the oscillating modes of a laser, and we will do so in this thesis; however as the laser is a fundamentally non-linear device described by an intensity dependent dielectric function this simple correspondence must be used with caution.

The relation between the linear emission and scattering picture is easily visualized in the extended complex wavevector space of the scattering matrix $S_{\mu\nu}(k)$, depicted in Fig. 1.1. The discrete quasi-bound wavevectors k_i are the *poles* of $S_{\mu\nu}(k)$. As can be seen from the figure, in general there are multiple quasi-bound modes contributing to a given resonance peak, but the quasi-bound modes which are closest to the real-axis lead to the sharpest peaks (some of which might not even be resolved in the scattering profile). Note that via Eq. (1.2), the quasi-bound mode solutions damp in time. An important experimental value often quoted is the Q-value of a resonator, which is defined by the number of cycles of the optical field at frequency ω to decay to half of its value, and thus can be related to quasi-bound mode parameters by the relation

$Q = \omega\tau$. This quantity, being device-specific, is dependent on the transmissivity of the mirrors in the ideal case, but in experimentally relevant situations includes other optical damping mechanisms.

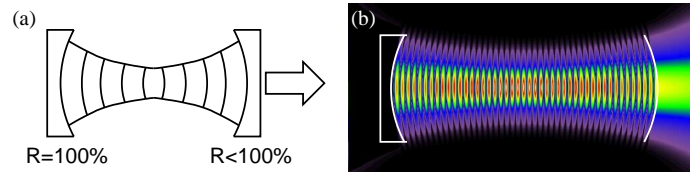


Figure 1.2: A schematics of the Fabry-Perot type laser cavity is shown on the left. An actual Fabry-Perot mode. The right mirror is assumed to be formed by a dielectric interface.

The archetypal design for laser resonators is based on the Fabry-Perot configuration. In its simplest realization, the electromagnetic field is confined between two parallel, highly reflective mirrors. It is a well known and well-utilized fact that the long-lived modes of such a resonator are formed by constructive interference of approximate plane-waves with wavevectors along the axis of the resonator. The Q-values of such modes are device-specific but in general depend on the reflectivities of the end-mirrors, or in some cases their shape, size or other physical properties.

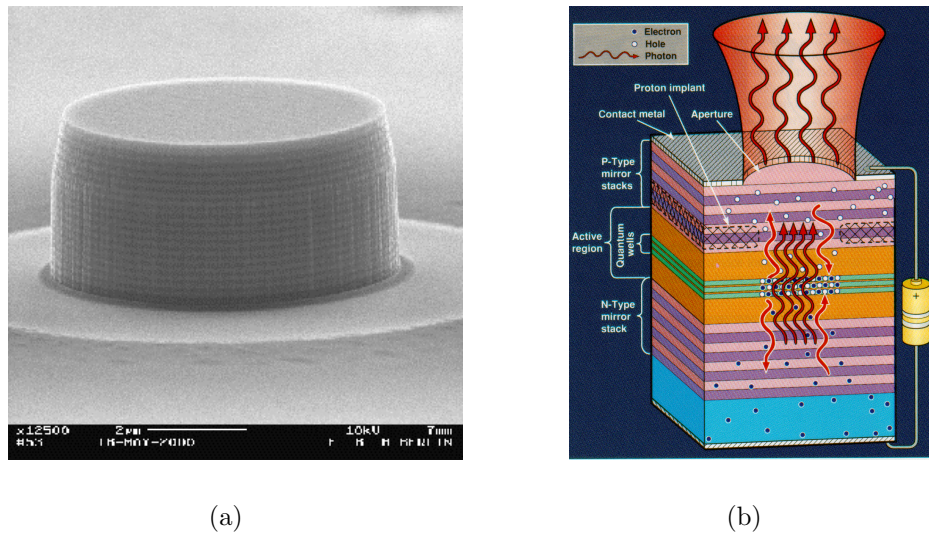


Figure 1.3: (a) A scanning electron micrograph picture of a VCSEL device [1]. The horizontal scale of the device is $4\mu m$. (b) Schematics of the structure of such a device (courtesy of Jung Han, Yale University)

Modern day opto-electronic applications requires the miniaturization of this whole process and material fabrication techniques have matured to a degree that this challenge can be met. In fact, optical resonators with dimension of the order of wave-

length can presently be fabricated in a wide variety of solid state systems, including semiconductors, organic materials and glasses [8]. An important requirement for opto-electronic and photonic applications of such micro-resonators is low power-consumption. One of the roadblocks in this effort is the production of high-quality reflective mirrors in small dimensions because the laser threshold, the input power at which coherent emission is achieved, is ultimately linked to gain balancing the resonator losses. For instance, a modern incarnation of the Fabry-Perot type configuration is the VCSEL (*Vertical Cavity Surface Emitting Laser*). Here, the high internal reflectivity is achieved by employing an old idea from X-ray diffraction physics: stacking layers of alternating semiconducting material of two different dielectric constants, so as to utilize Bragg reflection at normal incidence. With the typical size of the active region of a VCSEL of the order of a few wavelengths, the quality of the mirrors becomes an important issue for attaining a small threshold energy.

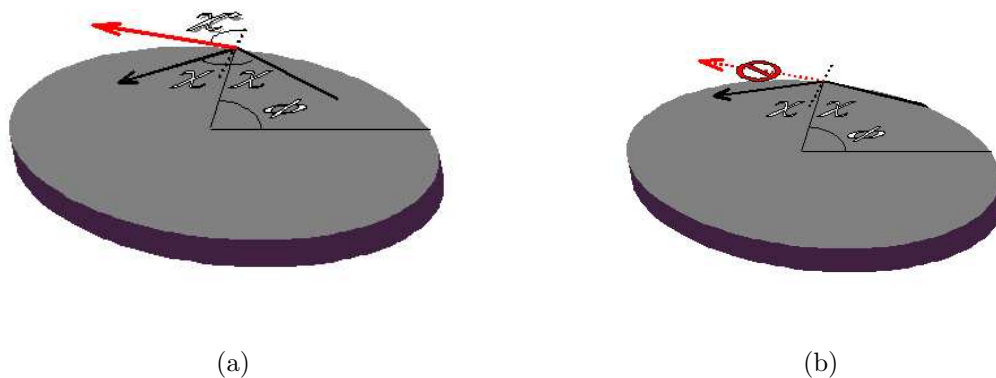


Figure 1.4: (a) Fresnel reflection and refraction in a planar dielectric cavity. (b) The high-reflectivity mirror action is provided by total internal reflection.

A relatively simple and effective mirror that nature provides us is formed at a dielectric interface when *total internal reflection* condition is satisfied. In the mid-1980's several groups began exploiting this mechanism to trap light in the dielectric micro-resonators which form the central theme of this thesis. The original devices employed the *whispering-gallery modes* of symmetric geometries such as nearly spherical liquid droplets [9, 10] or semiconductor microcavities formed into disc and cylindrical shapes [11, 12, 13]. These modes are solutions of the wave-equation which are strongly localized near the dielectric interface, in analogy to similar phenomenon in acoustics first discussed by Lord Rayleigh a century ago [14, 15]. For rotationally symmetric shapes, whispering gallery modes correspond to rays that strike the interface at a conserved incidence angle $\sin \chi$, and satisfy the total internal reflection condition $\sin \chi > 1/n$, where n is the relative index of refraction of the resonator. Despite the satisfaction of total internal reflection condition, exact solutions of the wave-equation for a dielectric disk [16] or sphere [17] show that the trapping is not perfect. The totality of internal reflection is only possible in the ideal limit of an infinite plane interface and incident plane waves. Here, the curvature of the bound-

ary gives rise to an exponentially small leakage via evanescent coupling which is very similar to the process of tunneling in quantum mechanics (see Appendix B). As a result, it is possible to attain relatively high Q -values ($Q \approx 500 - 5000$) for semiconductor microdisks, which are limited mainly by optical imperfections resulting from the fabrication process (roughness of the boundary). Spectacularly high Q -values ($Q \approx 10^9$) were measured in glass micro-spheres [18], where it is possible to fabricate extremely uniform surfaces. The possibilities that such high Q -values offer are not limited to device applications. Dielectric micro-resonators can serve as a “unique micro-laboratory” [8] for the study of cavity quantum electrodynamic (CQED) effects, because of the small modal volume combined with low losses. Furthermore, extreme field intensities reached within the resonator can reveal information about non-linear properties of materials which would be otherwise out of reach [19].

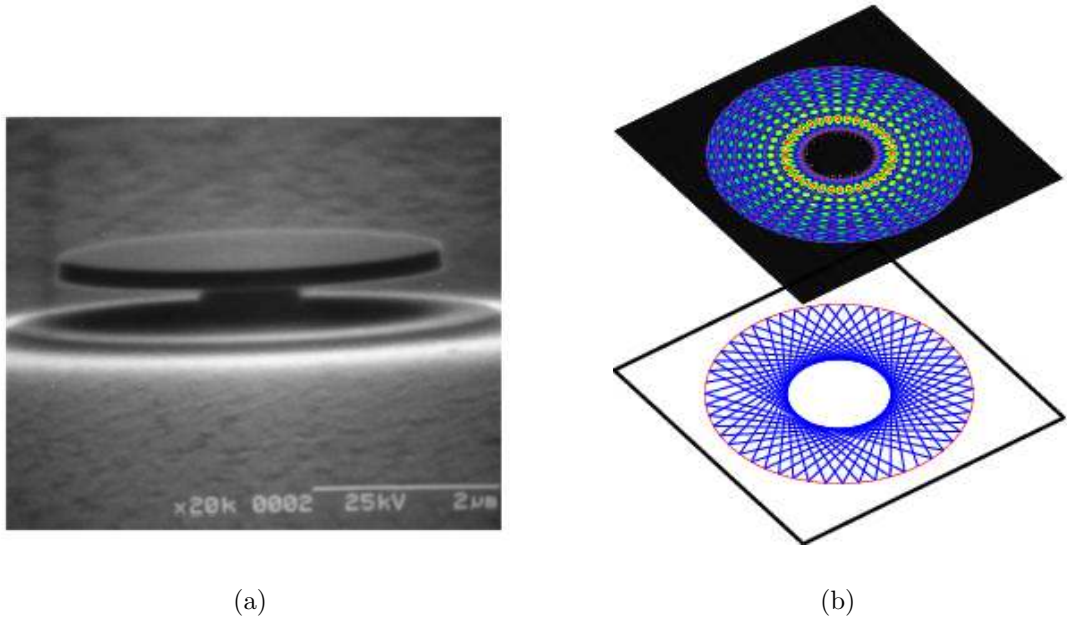


Figure 1.5: (a) A scanning electron micrograph of a microdisk laser on a pedestal [2]. The horizontal scale of the device is about $5\mu\text{m}$. (b) Top panel: real space false color plot of the modulus of the electric field for a calculated quasi-bound state of a planar microdisk cavity. Lower panel: Ray trajectories associated with the mode on the top panel.

One drawback of symmetric structures like microdisks is their poor directionality and low output power. The former is a very important problem, because proper integration of planar resonators in opto-electronics applications requires output generated by these devices to be coupled to optical fibers or other photonic circuit elements. The latter is the flip-side of the coin for high Q -values and low-thresholds. There are two general approaches to the coupling problem: the symmetry is either broken by an external coupling element (*extrinsic approach*), and the coupling

achieved via the tunneling process or the resonator itself is deformed (*intrinsic approach*). The current industrial standard is the extrinsic approach. However, this approach is very sensitive to the placement of the elements and ambient conditions (such as cavity-fiber distance). The intrinsic approach was taken originally with microdisk resonators by building various symmetry-breaking structures, like gratings, tabs and notches [20, 21] on the device. However, it is not easy to control the deteriorating effect of these extra structures on the resonator Q-values and vertical focusing of emission, especially in the case of small resonators. While the space of deformations is infinitely large, a fruitful approach has been to consider smooth deformations, leading to the concept of asymmetric resonant cavities (ARCs) [22, 23, 24, 3, 25]. ARCs offer the promise of a more robust method of coupling control.

In contrast to the Fabry-Perot resonator or rotationally symmetric dielectric resonators where the wave-equation is separable and reduces to a solution of ordinary differential equations, ARCs don't allow such a treatment, because of the non-separability of Maxwell boundary conditions. Determination of the modes of asymmetric resonators is a challenging task on its own. Although "brute force" methods exist for their numerical calculation (one of which is developed in Chapter 3), a deeper problem is the classification of these modes. There is not a complete set of quantum/mode numbers, such as those of the separable problem, that one can use to characterize the ARC modes. Furthermore, a boundary perturbation theory [26, 27] in the deformation parameter is destined to break down, because even at low deformations, it is known that there exist modes which are not analytic in the deformation parameter.

At this juncture ray models have proven to be a particularly powerful guide. This is justified in the limit where the geometric features of the resonator are small in comparison to the wavelength, in what we call here the semi-classical limit (other variants in literature are short-wavelength approximation, quasi-classical limit, WKB, Eikonal theory). The rotational symmetry which gives rise to isotropic emission in the case of microdisk resonators is also responsible for the integrability of the internal ray dynamics, manifested by the constancy of $\sin \chi$ (χ is the angle of incidence with respect to the normal). Here, what we mean by integrability is integrability of classical dynamics, which can be obtained by mapping the ray motion into a motion of an ideal point particle with total *conserved* momentum $p = p_x^2 + p_y^2 = 1$ (i.e. energy of the particle is conserved). The analogy is completed by requiring that the particle undergo specular reflection at the boundary of the resonator, i.e. hard-wall boundary conditions which reverse the normal component of the momentum $\hat{\mathbf{n}} \cdot \mathbf{p}$ at each bounce from the wall. This is the well-studied problem of *classical billiards* [28]. To take into account the leakage of radiation in true resonators, ray models additionally have to be augmented with an escape condition. In our context, we account for this by the Fresnel laws for angles of incidence $\sin \chi > \sin \chi_c = 1/n$.

The hope is then to extract information about emission characteristics and lifetimes from the internal ray dynamics. However, an important attribute of ray motion inside a deformed resonator which makes it unsuitable for standard ray tracing methods commonly used in optics, is that the motion is in general chaotic. At the

simplest level, this means that the long-time result of the simulation of a given ray trajectory is exponentially sensitive to initial conditions chosen at the start of the simulation. It is at this point that contact is made with the field of quantum chaos. The aforementioned analogy between internal ray motion and the motion of a point particle specularly reflecting at the boundary makes available an enormous body of literature on classical and quantum billiard problem, and results from the study of non-integrable Hamiltonian systems, which are central to this field.

To this end, if we consider *smooth* perturbations starting from an integrable Hamiltonian system a result known as the Kolmogorov-Arnold-Moser (KAM) theorem [29] establishes rigorously that the transition to chaos is a gradual one. This result was extended by Lazutkin [30] to include the case of billiard systems with smooth boundaries. Initial work [22, 3] on the theory of dielectric resonators has centered on smooth deformations away from symmetric (integrable) shapes, and the signature of KAM-Lazutkin transition to chaos on the universal emission properties of these resonators.

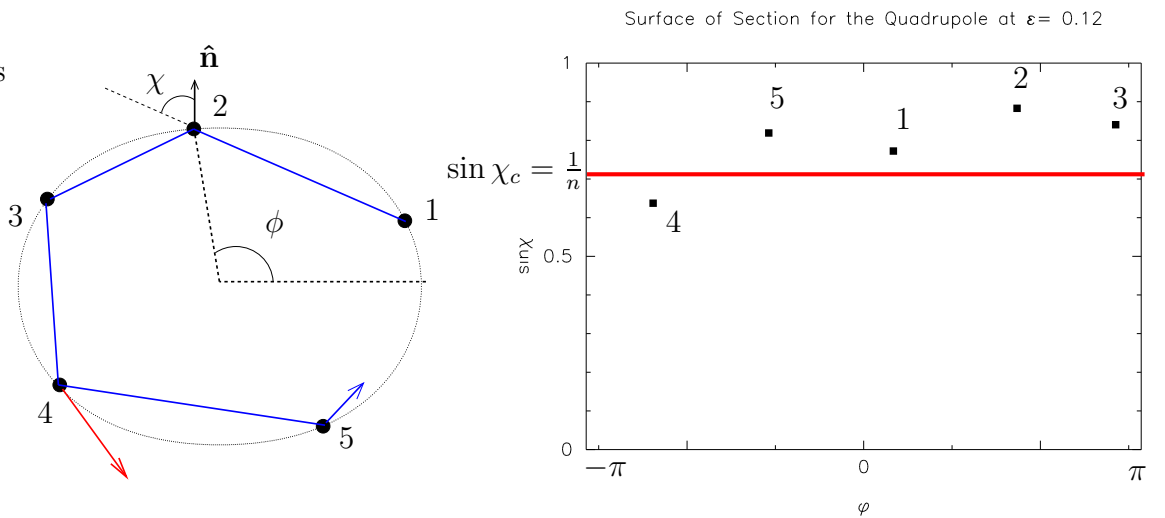


Figure 1.6: The construction of the surface of section plot. Each bounce from the boundary is represented by a point in the SOS by recording the angular position of the bounce on the boundary (ϕ) and the angle of incidence with respect to the local outward pointing normal ($\sin \chi$). For $\sin \chi > \sin \chi_c > 1/n$, total internal reflection takes place. Refractive escape results when a bounce point (bounce #4 in the figure) falls below the “critical line” $\sin \chi > \sin \chi_c$. Note that $\sin \chi < 0$ correspond to clockwise sense of circulation. We do not plot the $\sin \chi < 0$ region-the SOS has reflection symmetry.

The deformed shapes considered in most of these works are based on smooth deformations of a cylinder, specifically quadrupolar deformations of the cross-section characterized by a *deformation parameter* ϵ ,

$$R(\phi) = 1 + \epsilon \cos 2\phi \quad (1.6)$$

which in the zero deformation limit $\epsilon = 0$ reduce to a circular cross-section. When the shape is gradually deformed, it quickly becomes unfeasible to capture the types of ensuing ray motion by standard ray tracing methods in real space. A standard tool of non-linear dynamics, which proves to be very useful in disentangling the dynamical information, is the *Poincaré surface of section* (SOS) [31, 32], to be explored in depth in Chapter 2. In this two-dimensional phase-space representation, the internal ray motion is conveniently parametrized by recording the pair of numbers $(\phi_i, \sin \chi_i)$ at each reflection i , where ϕ_i is the polar angle denoting the position of the i th reflection on the boundary and $\sin \chi_i$ is the corresponding angle of incidence of the ray at that position (see Fig. 1.6). Each initial point is then evolved in time through the iteration of the SOS map $i \rightarrow i + 1$, resulting in basically two general classes of distributions. If the iteration results in a one-dimensional distribution (an *invariant curve*), the motion represented is *regular*. On the other hand exploration of a two-dimensional region is the signature of *chaotic* motion.

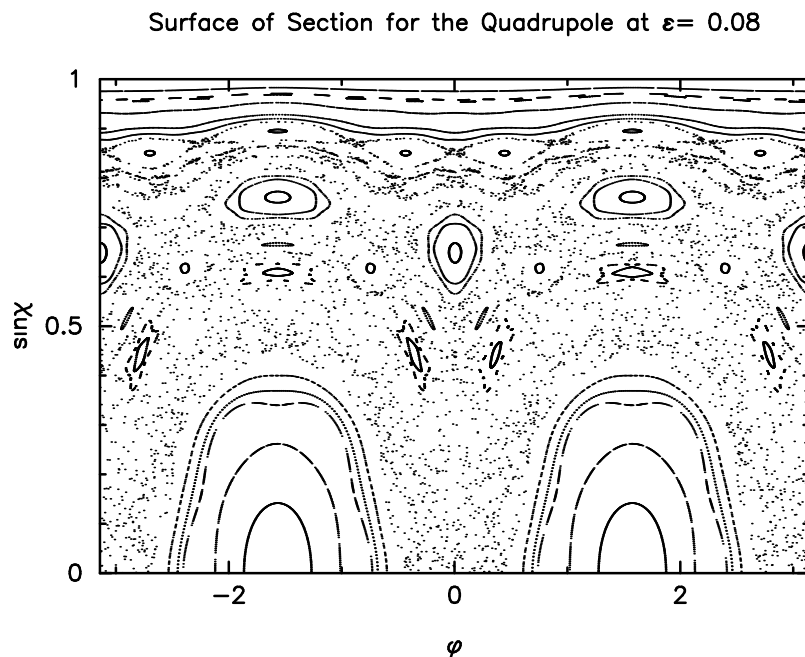


Figure 1.7: The Poincaré surface of section at an intermediate quadrupolar deformation of $\epsilon = 0.08$. Regular motion takes place along invariant curves in the SOS, i.e. any trajectory started on such a curve will remain on the same curve throughout its motion. Note that a curve is obtained by discrete points in the large bounce limit. The regions containing scatter of points represent chaotic motion. A generic initial condition within a given connected area will come arbitrarily close to any point within that component. Note that the invariant curves act as barriers to the chaotic motion. This feature is limited to two-dimensional systems.

The KAM-Lazutkin transition to chaos for the quadrupole billiard is discussed in detail in Chapter 2. At zero deformation the conservation of $\sin \chi$ results in straight lines trajectories throughout the SOS and we have globally regular motion. As the

deformation is increased (see Fig. 1.7) chaotic motion appears and a given initial condition explores a larger range of values of $\sin \chi$. Note that the classical escape condition (Fig. 1.6) is demarcated by the line $\sin \chi = \sin \chi_c$: any ray falling below this line refracts out with probability given by the Fresnel law of refraction (assuming a TM mode):

$$T(\sin \chi) = \frac{2\sqrt{1 - \sin^2 \chi}}{\sqrt{1 - \sin^2 \chi} + \sqrt{\sin^2 \chi_c - \sin^2 \chi}} \quad (1.7)$$

providing a classical loss-mechanism.

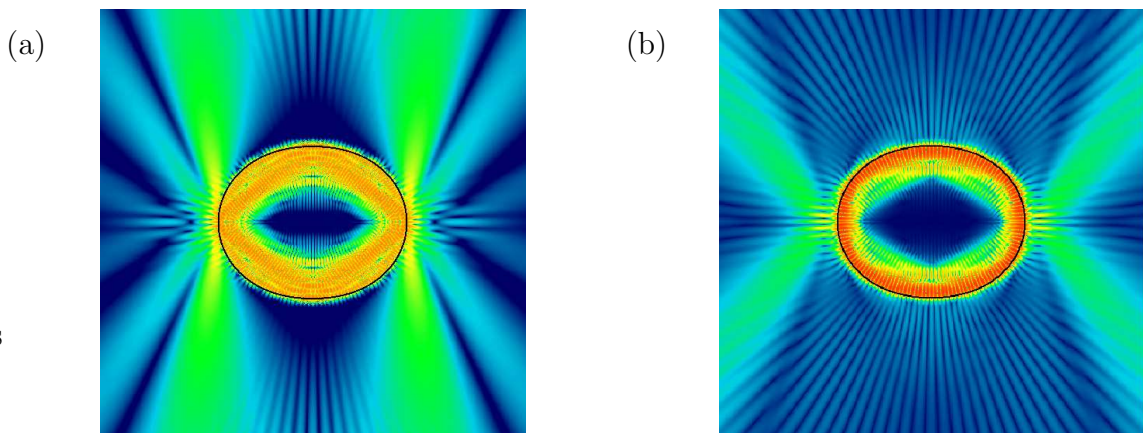


Figure 1.8: (a) A real space false color plot of the electric field intensity for a chaotic whispering gallery resonance at $n = 2$, illustrating the generic emission pattern from points of highest curvature on the boundary in the tangent direction. (b) Emission of a dynamically eclipsed state at $n = 1.54$ (after [3, 4])

The early pioneering works on ARCs by Nöckel and Stone [22, 24, 3, 16] analyzed this chaotic phase space flow in order to model the lifetime and emission patterns of these “chaotic whispering gallery modes”. This work focused on the emission properties of dielectric resonators which are relatively transparent. Resonators fabricated from a broad range of materials, polymers ($n \sim 1.5 - 2$) [33, 34, 35], fused silica [18, 36] ($n \sim 1.5$), and liquid droplets [37, 38, 10, 39, 40, 41] ($n \sim 2$) fall under this category. For these materials escape from the resonator occurs at rather large values of $\sin \chi$. Although one might have expected the chaotic ray motion to lead to short lifetimes and highly fluctuating emission patterns this was not the case. It was found [16, 24, 3] that although individual ray trajectories are chaotic at long time scales, there is a dominant phase space flow pattern along *adiabatic invariant curves* [3, 42] in the SOS at shorter time scales, resulting in a phase space motion which is highly anisotropic and of whispering gallery type. These considerations lead to the existence of chaotic whispering gallery modes which emit in a highly directional manner from the points of highest curvature (see Fig. 1.8(a)), which was justified by direct numerical solutions [3], and tested experimentally in lasing micro-droplets in Ref. [23, 24]. A crucial aspect of the ray-model is that it predicts a k -independent

lifetime and a universal emission directionality above a critical deformation, dependent only on the index of refraction of the resonator. Ref. [24] also pointed out a breakdown in the adiabatic model leading to an effect called “dynamical eclipsing” which is manifested by a dramatic change in the emission directionality from the tangent direction as the index is changed (see Fig. 1.8(b)). This effect is discussed in detail in Chapter 2. Very recent experimental work by Rex on polymer micro-lasers and analysis by Schwefel et al. [43] finds a very strong change in emission directionality as predicted but indicates that the original adiabatic model interpretation cannot fully explain the data. Success and limitations of the ray-model for chaotic whispering gallery modes have been discussed in [3, 44, 45].

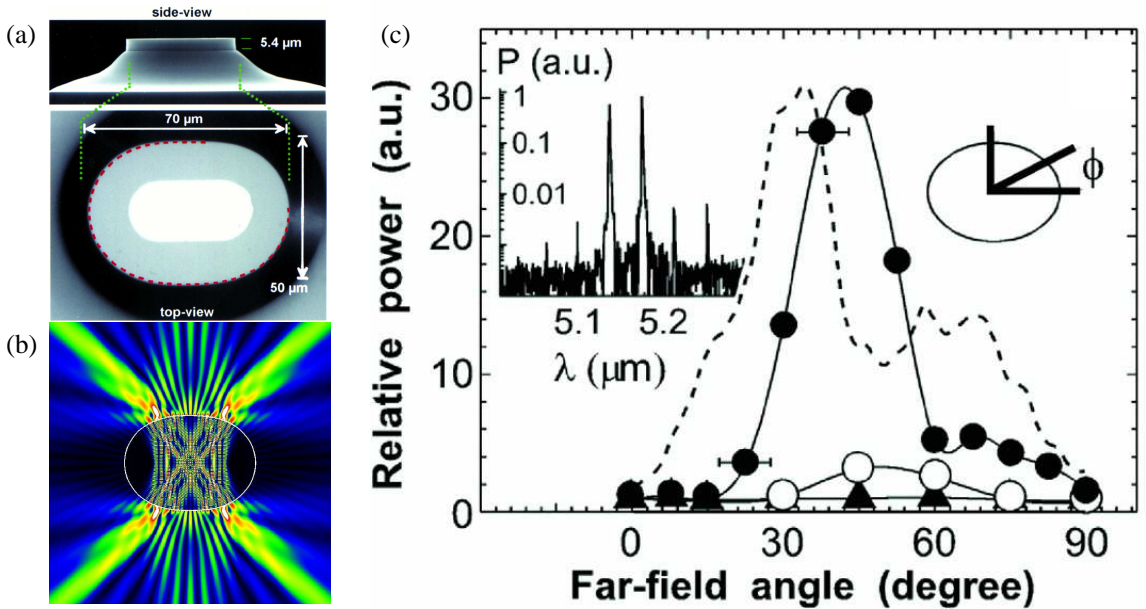


Figure 1.9: (a) Scanning electron micrographs of the top and side-view of one of the deformed cylindrical quantum cascade micro-lasers. (b) Numerically calculated resonance corresponding to the bowtie-mode observed for the deformation $\epsilon = 0.16$. (c) Angular dependence of the emission intensity for deformations $\epsilon = 0$ (triangles), $\epsilon = 0.14$ (open circles), $\epsilon = 0.16$ (filled circles). Dashed line represents the calculated farfield pattern corresponding to the resonance in (b). The right inset shows the coordinate system used and the left inset shows the the logarithmic plot of the measured power spectrum. The free-spectral range of the peaks is found to agree with the calculated bowtie free spectral range (after [5]).

An important milestone in the study of dielectric resonators is the 1997 Bell Labs experiment [5] on quantum cascade lasers [46]. In contrast to bipolar semi-conductor lasers (diode lasers) [11, 47] which rely on electron-hole recombination mechanism between the conduction and valence bands, the active region of a quantum cascade laser is fabricated into a multiple-quantum well structure, in which the lasing transition is between broadened electronic mini-bands. To test the effect of deformation on the

lasing properties, these experiments employed a series of cylindrical resonators with the cross-section of a flattened quadrupole of varying deformation. It was found that beyond a threshold deformation of about 10%, the collected output power displayed a quasi-exponential increase in the deformation. Furthermore, beyond a deformation of about 16%, the farfield pattern developed a strong directionality which could not be explained by chaotic whispering gallery modes. The lasing mode was identified as a “bowtie”-resonance, related to stable ray motion in the vicinity of a bowtie-like periodic orbit. A crucial point is that this kind of stable motion does not exist below a deformation of 11%, and is “born” through a period doubling bifurcation from the stable bouncing-ball orbit at $\phi = \pm\pi/2$. Below a deformation of about 14%, the corresponding bowtie resonances are too leaky to provide efficient laser feedback. However, further deformation slowly moves the stable island up in $\sin \chi$ and at about 16% it becomes the favored lasing mode. The observed spectrum and the strong directionality was found to be consistent with numerically determined bowtie modes. The fabrication process and material system used (non-existence of non-radiative recombination processes, reduced roughness scattering in the mid-IR, existence of a polarization selection rule [5] etc.) have an important contribution to the efficiency of these lasers. However, something which exceeded the expectations was the effect of the resonator geometry on the optical power extraction: the total output power collected in the four lobes of the bowtie lasers was about 1000 times larger than that of the omni-directional whispering gallery output of the undeformed devices residing on the same chip.

From the technological point of view, an important implication of the results discussed so far is the introduction of a new parameter for laser design, namely the resonator shape [48, 49]. Traditionally, it has been the length of the resonator, a one-dimensional variable which determined the output power. The two-dimensional freedom embodied in the SOS, combined with the choice of the index of refraction, offers a new dimension in laser design: phase-space engineering of cavity modes. A recent catalogue of resonator shapes includes: disks and cylinders [11, 12, 13], spheres [36, 18], quadrupoles [5, 50, 51, 52, 53], deformed spheres [54], squares [55], hexagons [56], and spirals [35]. Many different mode geometries, e.g. whispering gallery modes, bowtie modes, triangular and square modes have been observed in such resonators.

Given the rich structure of a typical mixed phase space at large deformations, one can expect an equally rich structure in modal patterns. It is one of the primary tasks of this thesis to investigate the structure of the quasi-bound modes of a passive dielectric resonator both numerically and analytically based on classical phase space structure of the equivalent refractive billiard system in the semi-classical limit. Below is a short overview.

1.2 Brief Overview of this Thesis

- Chapter 2 Overview

The main problem in the semi-classical description of resonators is not the complexity of ray motion *per se*, but the correspondence between rays and modes which are solutions of wave-equation with prescribed boundary conditions. In principle we could determine the propagation of an individual ray within a finite time interval with given initial conditions numerically. The issue of establishment of the ray-wave connection forms the core of *semi-classical quantization* methods [57, 58]. In Chapter 2 we give an introductory discussion drawing from results of asymptotic theories of wave propagation, quantum chaos and non-integrable Hamiltonian systems. We will develop some of the concepts and tools that will be used throughout the thesis, while at the same time clarifying the common themes of the aforementioned fields, each of which has its own characteristic language.

We will set up the connection between rays and waves in the context of the Helmholtz equation Eq. (1.3), through the introduction of the universal *semi-classical ansatz*

$$\psi(\mathbf{x}) = A(\mathbf{x})e^{ikS(\mathbf{x})} \quad (1.8)$$

in the limit $k \rightarrow \infty$. In optics, this type of asymptotics is known as the Eikonal theory, or short-wavelength asymptotics. A recurring theme is the multi-valuedness of the solutions $S(\mathbf{x})$, so that the solution is expressed as a sum over multiple wavelets

$$\psi(\mathbf{x}) = \sum_n A_n(\mathbf{x})e^{ikS_n(\mathbf{x})} \quad (1.9)$$

where $S_n(\mathbf{x})$ represent the sheets of the $S(x)$.

The key question is: Under what circumstances is it possible to write down an ansatz Eq. (1.9) representing the asymptotic solution of the Helmholtz equation with given resonator boundary conditions? We review the answer to this question first in the case of the modes of a “closed” resonator, which is mathematically modelled by Dirichlet boundary condition on the solutions $\psi(\mathbf{x})|_{\partial D} = 0$, where ∂D is the cavity boundary. Then the problem becomes identical to the *quantum billiard* problem: the stationary solutions of the Schrödinger equation for Dirichlet boundary conditions on ∂D . The semi-classical limit is then formally obtained by letting the Planck’s constant $\hbar \rightarrow 0$, and maps to the problem of a point particle in a classical billiard with specularly reflecting boundary. The phase function $S(\mathbf{x})$ in this framework obeys the classical Hamilton-Jacobi equation. When the Schrödinger equation is *integrable* (excluding a few known exceptions, this is equivalent to *separability*) for a given shape of the boundary, the semi-classical quantization is possible and a coordinate-independent recipe is provided by EBK quantization method [59, 60, 61, 62], which is a geometric extension of the old quantum theory [63, 64] including certain corrections. We review the EBK theory in the setting of this thesis for the case of a circular cavity. This theory relies on the integrability of the classical dynamics, i.e. the existence of conserved quantities equal in number to the dimension of the system. A major point, anticipated by Einstein himself [59], is that in the regime where the motion is non-integrable, there turns out to be no semi-classical quantization method for individual eigensolutions which works globally (i.e. for all states in the spectrum). The reason

for this is that a finite set of functions $S_n(x)$ needed for the ansatz Eq. (1.9) does not exist when Hamilton-Jacobi equation is not integrable (this will be explained in detail in Chapter 2).

It is the central theme of the field of *quantum chaos* to understand the properties of the solutions of the Schrödinger equation when the semi-classical limit leads to non-integrable dynamics. As pointed out before, the behavior of non-integrable ray systems is most effectively described in the phase space, or on a section in the phase space (SOS). The generic behavior is a mixed phase space comprising regions of regular and chaotic motion. Semi-classical quantization of individual states can typically be done locally on the regular components of phase space. In the classification and determination of these phase space sets, a key role is played by the *periodic ray orbits*, and the dynamics in their vicinity, which might either be stable, unstable or neutral. In Section 2.8, we describe methods which allows us to classify classical motion based on local behavior in the phase space close to the periodic and quasi-periodic orbits. This is the scaffolding on which we will be building throughout the remainder of this thesis. The resulting linearized, local dynamics is then used to develop asymptotic expansions for associated classes of modes; in the words of Berry, we will “sew the wave flesh on classical bones” [57]. When such a consistent construction is possible, the quantized eigenvalues k_n obtained approximate well the exact ones [30, 65, 66]. The Husimi projection of a mode is defined as a method for determining its connection to a particular region of the mixed phase space.

Finally it is shown how the EBK quantization procedure can be generalized to calculate analytically the quasi-bound states of dielectric resonators of integrable shape. Although straightforward, this generalization of EBK theory does not seem to have been given before in either the optics or quantum chaos literature. The generalization provides a deeper justification of the ray model introduced by Nöckel and Stone for the description of dielectric resonators.

The various SOS plots in this and later chapters have been generated by a program written by Harald Schwefel.

• Chapter 3 Overview

In this chapter we develop a novel numerical method for solving the Helmholtz equation for deformed dielectric resonators. The numerical results we obtain from this method not only give a benchmark against which semiclassical results are checked, but can also spawn new results by pointing out deviations and corrections. They also provide a first insight into any experimental result, and the result will acquire a meaning in light of the semi-classical descriptions we developed.

But beyond this pragmatic function, considered as a mathematical and numerical problem in its own right, it has its own challenges. The numerical quantum billiard problem, the “closed” counterpart of the dielectric resonator, has a long history [67], which mainly centers on the choice of a convenient basis, best adapted to the situation at hand. The openness of a dielectric resonator contributes an additional aspect to the problem. Thus, what we are seeking is an efficient numerical algorithm

which provides us with the quasi-bound modes of a dielectric resonator, as defined by Eq. (1.5).

The method we are proposing is a hybrid between a point-matching technique [68] and scattering approach to quantization [69, 70]. In contrast to existing methods [68, 16, 71] which employ the external scattering matrix to extract the quasi-bound modes of a dielectric resonator, we consider the *internal scattering operator*.

In this approach one employs radiation boundary conditions and calculates the quasi-bound modes individually by solving a *homogeneous* equation, which possesses solutions only at discrete, complex k values, determined by a singularity condition on a determinant

$$\det M(k) = 0. \quad (1.10)$$

The internal scattering approach is closely related to the external scattering problem for quantum billiards, in fact for a hard-wall billiard there is an exact mathematical relation based on the concept of inside-outside duality [69, 72, 73]. In this case $M(k) = 1 - S(k)$ where $S(k)$ the on-shell scattering matrix of the external problem. For a dielectric resonator there is no exact duality of this type but formally the development is very similar and we often refer to our method as the ‘‘S-matrix’’ method. An important conceptual difference with respect to wave-function matching methods is that the internal scattering approach permits the identification of a *discrete set* of internal scattering states at each value of k . This is realized by writing the matching conditions in the form of an off-shell eigenvalue problem instead of a linear inhomogeneous equation. In this way we can ‘‘follow’’ individual quasi-bound states to quantization, whereas in the external scattering problem a single resonance peak might contain several quasi-degenerate quasi-bound modes. In this chapter we show that due to regularities in the k -dependence of the eigenvalues of our internal scattering operator we can find its complex roots very efficiently using a simple interpolation scheme. Moreover we are able to show that the off-shell eigenstates have the same semiclassical properties as the quantized quasi-bound modes; hence we can find many interesting properties (emission patterns, phase-space support and angular momentum content) for all the quasi-bound states with a single diagonalization.

The work of this chapter has been done in collaboration with Harald Schwefel and Philippe Jacquod and remains to be published.

• Chapter 4 Overview

Motivated by the experiments on bowtie-lasers, we develop in this chapter an analytic description of the resonances of a dielectric resonator, which are based on stable periodic ray orbits in the semi-classical limit. For a generic boundary shape, these modes coexist with ‘‘chaotic’’ and whispering gallery modes.

The long-lived modes of Fabry-Perot-like resonators with curved end-mirrors (and no sidewalls for the sake of argument) are known to have approximately a Gauss-Hermite profile transverse to the resonator-axis. The theory of such modes has been developed early on after the invention of the laser (for an extensive list of references

see Ref. [74, 75]), and the standard approach [76] is based on paraxial ray propagation. This theory makes use of the fact that Gauss-Hermite beams are approximate free-space solutions of the Helmholtz equation with complex valued parameters which can be obtained by standard theory of ABCD matrices [76]. Such Fabry-Perot-like modes exist in dielectric resonators too, and corresponds to ray motion which is of bouncing-ball type. However, because such rays strike the boundary at approximately normal incidence, the resulting modes are not long-lived and hence in practice don't show up as lasing modes. There are however other multiple-bounce periodic ray orbits, like the bowtie-orbit, in the vicinity of which the ray motion can be stable. If such periodic orbits strike the boundary above the critical incidence, they can lead to long-lived modes [5]. Because of the stability of ray motion around the periodic orbits, only the local properties of the pieces of boundaries are expected to contribute to the description of the corresponding modes. In this respect, the problem can be thought of as a multiple-mirror resonator problem.

We base our description on a rigorous mathematical construction, the *parabolic equation approximation* [77], which was used to formulate a theory of natural oscillations of multiple-mirror resonators [66], and generalize it to dielectric resonators. We find a wave-vector quantization rule which yields complex resonance wave-vectors, and give a simple physical interpretation of the results in terms of Fresnel reflection/refraction.

The modes constructed by this method do not in general respect the symmetry properties of the resonator; we rectify this problem by using the symmetry projection operators of the discrete symmetry group of the resonator to obtain modes which are very close to those we obtain numerically.

The parabolic equation method we develop here provides a controlled asymptotic expansion for solutions and we illustrate this by calculating the first correction to the standard quantization conditions for such resonators.

The material of this chapter is based on the article [78].

• Chapter 5 Overview

In this chapter, we consider the theoretical analysis of a recent experiment on GaN-based lasers [52, 79, 43], which illustrates the relevance of wave-phenomena which are out of reach of the standard geometric ray-optics descriptions.

The experimental results are very well described by assuming that the lasing mode is based on a three-bounce periodic orbit, which however is unstable. It is one of the interesting and well-studied results of quantum chaos theory that modes can localize in the vicinity of unstable periodic orbits, the phenomenon known as “scarring”. We demonstrate the existence of such scarred quasi-bound modes numerically, and show that they account rather well for the experimental results.

One crucial point of the analysis is that although the numerical calculations are performed at rather low wavenumbers with respect to the experiments, we are able to reproduce the experimental results. We argue that scarring is a robust phenomenon when considered in a statistical sense, in other words if we are interested in the average emission of a group of states which are close to a short periodic orbit. Even if

we could numerically find the exact solutions of individual states at extremely high wavenumbers (as high as those used in the experiments), they would be sensitive to small changes in system parameters, such as those introduced by weak non-linear effects in the gain medium or the boundary imperfections, and might not provide much intuition about the overall behavior of the laser. On the other hand, statistical predictions of the scar theory depend only on a few classical parameters and are known to be robust [80]. There are a few approaches within the realm of quantum chaos theory to illustrate these statements, and we choose to do it within the framework of the configuration space theory of scars developed by Bogomolny [81].

While the numerically determined scarred states agree well with experiment, their far-field emission pattern deviates substantially from that expected from simple ray considerations. We explain this observation as an effect of Fresnel Filtering [82], which arises when a beam of finite extent is incident on a dielectric boundary.

This chapter is based on the articles [52] and [82].

- **Chapter 6 Overview**

In this chapter we formulate the laser equations in a form suitable for treating the dielectric micro-lasers. We provide some speculations about new phenomena which can occur in such lasers and we point out directions for future work.

Chapter 2

Asymptotic Physics: Where rays and waves meet

2.1 Introduction

In this chapter, we will discuss the *semiclassical limit* $k \rightarrow \infty$ of the *Helmholtz equation*

$$(\nabla^2 + n^2(\mathbf{x})k^2) \psi(\mathbf{x}) = 0 \quad (2.1)$$

to provide a unified framework for concepts and techniques throughout this thesis. A major theme will be the investigation of the feasibility of various asymptotic approaches to the Helmholtz equation based on the underlying ray dynamics.

The Helmholtz equation describes a variety of stationary wave-phenomena studied in electro-magnetism, acoustics, seismology and quantum mechanics. Here, we have in mind its application to the classical electro-magnetic wave-fields of dielectric resonators which obey Maxwell's equations. Under suitable conditions on the geometry of the resonator and the type of fields of interest, Maxwell's equations can be reduced to the two-dimensional wave-equation

$$\left(\nabla^2 - \frac{n^2(\mathbf{x})}{c^2} \frac{\partial^2}{\partial t^2} \right) \Psi(\mathbf{x}, t) = 0 \quad (2.2)$$

for a complex scalar wave-function $\Psi(\mathbf{x}, t)$, where the function $n(\mathbf{x})$ represents the *index of refraction* variation of the medium. This reduction will be examined in Chapter 3 and its details are not relevant to the discussion here. The Helmholtz equation Eq. (2.1) is obtained for the spatial variation $\psi(\mathbf{x})$ of time-harmonic (stationary) solutions

$$\Psi(\mathbf{x}, t) = \psi(\mathbf{x})e^{-i\omega t} \quad (2.3)$$

where $\omega = ck$ is the oscillation frequency of the fields, c is the speed of light in vacuum and k is the wave-vector in vacuum. This is the class of solutions we are interested in this thesis. Note that in the most general case, ω is a complex variable.

Another time-dependent equation which results in the Helmholtz equation for its time-harmonic solutions is the *Schrödinger equation* describing the quantum mechanical wavefunction $\Psi(\mathbf{x}, t)$ of a point particle of mass m with energy E moving under the influence of a potential $V(\mathbf{x})$

$$\left(i\hbar \frac{\partial}{\partial t} + \frac{\hbar^2}{2m} \nabla^2 - V(\mathbf{x}) \right) \Psi(\mathbf{x}, t) = 0 \quad (2.4)$$

which becomes

$$\left(-\frac{\hbar^2}{2m} \nabla^2 + V(\mathbf{x}) \right) \psi(\mathbf{x}) = E\psi(\mathbf{x}) \quad (2.5)$$

where $E = \hbar\omega$. Substituting $\frac{E}{\hbar^2/2m} \rightarrow k^2$, $\frac{V}{\hbar^2/2m} \rightarrow k^2(1 - n^2)$, we obtain Eq. (2.1). Thus, the stationary phenomena predicted by Fig. 2.4 and Eq. (2.2) can be described mathematically by the same equation (2.1). However, as we will see in the last section on dielectric resonators, this formal analogy is not complete, and there is an important class of phenomena in electromagnetism as $k \rightarrow \infty$ not found in quantum mechanics as $\hbar \rightarrow 0$.

In the limit $k \rightarrow \infty$ the solutions of the Helmholtz equation display oscillations on increasingly finer spatial scales, denoted by the wavelength $\lambda = 2\pi/k$, simultaneously becoming more sensitive to the spatial details of the function $n(\mathbf{x})$. Thus, a numerical treatment of the problem becomes highly costly. That's where asymptotic theories prove to be very valuable and effective. Notice that the above described oscillatory behavior is nicely captured in the approximate form

$$\psi(\mathbf{x}) \sim A(\mathbf{x})e^{\frac{i}{\lambda}S(\mathbf{x})} \quad (2.6)$$

for the solution $\psi(q)$. In fact as $\lambda \rightarrow 0$, such a functional form would display the fast oscillations required without the need for a violent behavior in the functions $A(\mathbf{x})$ and $S(\mathbf{x})$ themselves. This approach can be developed into a full-blown asymptotic theory for the Helmholtz equation, and the resulting collection of methods are known as *WKB* or *semi-classical* methods in quantum mechanics, and *short-wavelength* or *high-frequency* approximations in electro-magnetism.

In any case, application of these asymptotic methods result in a Hamiltonian description involving families of trajectories. In the case of quantum mechanics, these are paths of classical particles, whereas in the case of electromagnetism they are the rays of geometrical optics. A wavefield $\psi(\mathbf{x})$ then corresponds to a *family* of trajectories rather than a single trajectory and the family is defined by the (action) function $S(\mathbf{x})$, the phase function in Eq. (2.6). For resonators and other structures which can “confine” electro-magnetic radiation, the ray motion proceeds in bounded regions. Depending on the geometry of this region and the form of $n(\mathbf{x})$, the ray dynamics can be fairly complicated, and in general is chaotic.

Geometric ray optics and associated ray tracing methods have a long history in the context of wave-propagation and scattering problems [83, 77, 84, 66, 85]. The plethora of methods developed however are not very suitable for the description of

ray motion in bounded regions of space. Real-space ray-tracing methods fall short of giving useful results.

Our interest in the quantum mechanical viewpoint stems from the fact that the semi-classical limit of the Schrödinger equation is a well-studied and mature subject. The body of modern research known as "Quantum Chaos" has provided a great deal of insight into this problem in the past two decades, and it has been recognized for some time now that the above-mentioned analogy can be used to carry over methods and concepts to the treatment general wave phenomena. The strength of these methods rests mainly on the Hamiltonian description of the underlying classical dynamics, which takes a higher dimensional phase space view of the motion. The Hamiltonian description of non-integrable motion is an essential ingredient of the semiclassical description of wave-phenomena in resonators.

We shall begin with the derivation of the standard geometric ray theory and subsequently introduce the necessary concepts from the theory of Hamiltonian flows. Then, we will proceed to introduce the paradigm system of quantum chaos theory: the quantum billiard, which in electro-magnetism corresponds to a perfect metallic cavity. Finally, in the last section we will generalize the semi-classical tools developed to dielectric resonators, which exhibits an extra layer of complication because of its openness. We will also show that this system is unique to electro-magnetism and an exact quantum mechanical analogue of this system does not exist.

2.2 Semi-classical limit of the Helmholtz equation

We will concentrate on a 2D system with coordinate variables $q = \{q_i\}$. Higher dimensional systems, although they intrinsically offer more complexity, involve no essentially new ideas.

In the formal limit $k \rightarrow \infty$ of the Helmholtz equation Eq. (2.1), the standard procedure [86] is to seek an approximate solution for the complex scalar wave-function $\psi(q)$ of the form

$$\psi(q) \sim e^{\frac{i}{\delta} S(q)} \sum_n \delta^n A_n(q) \quad (2.7)$$

where δ is a small parameter, in general a function of the small parameter $1/k$; in practice one writes $\delta = O(k^{-\nu})$. We will assume here that $A_n(q)$ and $S(q)$ are *real* functions, which will lead to a description in terms of real rays. Substituting Eq. (2.7) into Eq. (2.1) and separating the real and imaginary parts, we get

$$\text{Im}[] : \frac{2}{k^2 \delta} \nabla S \cdot \nabla A_0 + \frac{1}{k^2 \delta} A_0 \nabla^2 S + \dots = 0 \quad (2.8)$$

$$\text{Re}[] : \frac{1}{k^2 \delta^2} (\nabla S)^2 - n^2(\mathbf{x}) - \frac{1}{k^2 A_0} \nabla^2 A_0 \dots = 0 \quad (2.9)$$

The size of δ is decided by an argument based on *method of dominant balance*. I will not go into the discussion of this method, except saying that in asymptotic formulas like the one above, it's usually the case that the asymptotic limit involves a balance

between a small number of terms, and refer to Ref. [86] for a general discussion. As one can easily infer from Eq. (2.8) and Eq. (2.9), such a balance can be achieved by choosing $\delta = k^{-1}$. Then, one can rewrite Eq. (2.8) and Eq. (2.9) to lowest order $O(k^0)$ as

$$(\nabla S)^2 = n^2(q) \quad (2.10)$$

$$2\nabla S \cdot \nabla A + A\nabla^2 S = 0 \quad (2.11)$$

where we have replaced A_0 by A . The first equation Eq. (2.10) is known as the *Eikonal equation* in optics. Note that, given the optical properties of the medium in $n(q)$, the *Eikonal* $S(q)$ can in principle be solved using Eq. (2.10), and subsequently the amplitude $A(q)$ can be determined using the *transport equations* Eq. (2.11). The lowest order approximation to the wave-function can then be written as

$$\psi(q) \sim A(q)e^{ikS(q)} \quad (2.12)$$

Rays of geometric optics are obtained from the vector field

$$\mathbf{p}(q) = \nabla S(q) \quad (2.13)$$

Eq. (2.10) tells us that the length of this vector at point q in space is equal to the index of refraction $n(q)$ at that point. From Eq. (2.13) and Eq. (2.10), the rays are orthogonal to the level curves $S(q) = \text{constant}$ of the Eikonal $S(q)$. These level curves are nothing but the *wavefronts* of geometrical optics. It's important to notice that a given wave-function $\psi(q)$ viz. Eq. (2.7) corresponds to a *family* of rays, called a *normal congruence* [87, 83, 66], rather than a single ray (see Fig. 2.1).

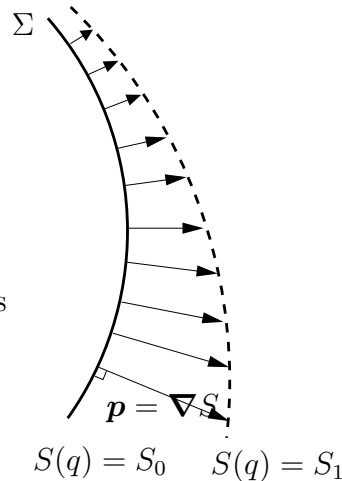


Figure 2.1: Schematics showing the level-curves of the Eikonal $S(q)$, $S(q) = S_0$ and $S(q) = S_1$. The normals of $S(q) = S_0$, form a normal congruence of rays and yield the next level-curve $S(q) = S_1$. Depicted is a situation where the index of refraction $n(q)$ is monotonically increasing from the top of the figure to the bottom.

2.3 Eikonal Equation as an initial value problem

Eq. (2.10) is a first order non-linear partial differential equation for $S(q)$, and for its solution appropriate boundary conditions have to be introduced. A general and often implemented boundary condition is to specify $S(q)$ on a curve Σ :

$$S(q(s)) = S_0(s) \quad (2.14)$$

where s is a coordinate which parametrizes the points on Σ . The general theory of solving first order non-linear PDEs with boundary conditions of the form Eq. (2.14) employs the *method of characteristic curves* [88], which has a fairly elementary geometrical interpretation in our case.

For simplicity, and without loss of any physical content, we will assume the initial curve Σ is a wave-front, i.e. $S_0(s) = S_0 = \text{constant}$. A family of rays can then be constructed which are orthogonal to this curve, their lengths proportional to the local index of refraction $n(q)$. The tips of this vector field (interpreted as a differential operator $d = \sum_i p_i \partial / \partial q_i$) can then be joined to obtain the next wave-front. Iterating this process ad infinitum we can construct the whole functional variation of $S(q)$ beginning with the initial surface (see Fig. 2.1). Generically, this optimistic scenario is obstructed by the singularities of $S(q)$.

The above geometrical construction of the solution can be formalized by regarding the ray field $\mathbf{p}(q)$ as a family of curves $\mathbf{q}(\tau) = (q_1(s, \tau), q_2(s, \tau))$, where s , as introduced before runs along the level curves and parametrizes each individual ray of $S(q)$ and τ represents the arclength along the rays (see Fig. 2.2). Then the condition of orthogonality can be written as

$$\frac{d\mathbf{q}}{d\tau} = \frac{1}{n(q)} \nabla S(q) \quad (2.15)$$

the prefactor $1/n(q)$ ensures that τ is the arclength along the trajectory, i.e. that $|d\mathbf{q}/d\tau| = 1$. This equation has to be supplemented by the variation of the ray vectors $\mathbf{p} = \nabla S$ with τ via Eq. (2.10):

$$\frac{d\mathbf{p}}{d\tau} = \nabla n(q) \quad (2.16)$$

We have managed to reduce the solution of a non-linear partial differential equation Eq. (2.10) to a set of ordinary differential equations Eq. (2.15-2.16). The basic optical processes such as reflection and refraction following Snell's law are contained in these equations.

Note that by rewriting equations Eq. (2.15-2.16) using the scaled variable $\sigma = n(q)\tau$ and using $\mathbf{p} = \nabla S$ in Eq. (2.15) we obtain the set of equations

$$\frac{dq}{d\sigma} = \mathbf{p} \quad (2.17)$$

$$\frac{dp}{d\sigma} = \frac{1}{2} \nabla n^2(q) \quad (2.18)$$

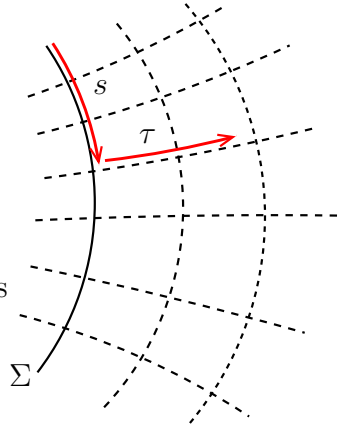


Figure 2.2: Schematics showing the ray coordinates (s, τ) . The dashed lines are equi-coordinate curves $s = \text{constant}$ and $\tau = \text{constant}$, which are the wavefronts and rays.

Note that these are equations of motion of the Hamiltonian form, for the canonical conjugate pair (\mathbf{q}, \mathbf{p}) , in the hypothetical time-variable σ . Thus, they are derivable via the Hamilton's equations of motion

$$\frac{dq_i}{d\sigma} = \frac{\partial H(q, p)}{\partial p_i} \quad (2.19)$$

$$\frac{dp_i}{d\sigma} = -\frac{\partial H(q, p)}{\partial q_i} \quad (2.20)$$

from a *conserved* Hamiltonian ($dH/d\sigma = 0$), given by

$$H(\mathbf{p}, \mathbf{q}) = \frac{1}{2}p^2 - \frac{1}{2}n^2(q) = \text{constant} \quad (2.21)$$

which is essentially a restatement of the Eikonal equation Eq. (2.10), with the constant equal to zero¹. Note that, the Eikonal equation itself, in terms of the function $S(q)$, can be identified to be the time-independent *Hamilton-Jacobi* equation

$$H(q, \nabla S) = 0 \quad (2.22)$$

of mechanics, where $S(q)$ is identified as the *action* (more precisely, Hamilton's characteristic function). This point of view takes the action $S(q)$ (i.e. the wavefronts) as the fundamental object; we will come back to this point later.

Hence the ray dynamics can be mapped onto the motion of a point particle of mass $m = 1$ and energy $E = 0$ moving in a potential of the form $V(q) = -\frac{1}{2}n^2(q)$. This simple analogy would explain for example the tendency of rays to turn away

¹Another alternative to reach a Hamiltonian form is to keep the variable τ , which would result in the Hamiltonian $H = \frac{p^2}{2n(q)}$, representing a motion where the mass of the particle changes depending on the position, and where the canonical momentum is no longer $p = \nabla S$.

from regions of smaller index of refraction and move towards regions of greater index, which is the fundamental idea used in the design of configurations that confine and guide light, such as dielectric resonators and waveguides.

To get a more detailed understanding of the basic ramifications of this method, let us obtain the explicit solutions for the simpler case of an isotropic and homogeneous medium described by $n(q) = 1$. Then the Eikonal equation is

$$(\nabla S)^2 = 1 \quad (2.23)$$

i.e. $H = p^2 = 1$, the ray field is equivalent to a Hamiltonian “flow” with conserved momentum $|\mathbf{p}| = 1$. The equations of motion are

$$\frac{d\mathbf{q}}{d\tau} = \mathbf{p} \quad (2.24)$$

$$\frac{d\mathbf{p}}{d\tau} = 0 \quad (2.25)$$

Thus giving the straight-line trajectories

$$\mathbf{q}(\tau) = \mathbf{p}_0\tau + \mathbf{q}_0 \quad (2.26)$$

$$\mathbf{p}(\tau) = \mathbf{p}_0 \quad (2.27)$$

The initial conditions are nothing but the pairs $(\mathbf{q}_0(s), \mathbf{p}_0(s) = \nabla S(\mathbf{q}_0(s)))$ on the initial wave-front Σ . Thus, the solution of Eq. (2.23) can be obtained from the two-parameter family of solutions

$$\mathbf{q}(s; \tau) = \mathbf{p}_0(s)\tau + \mathbf{q}_0(s) \quad (2.28)$$

$$\mathbf{p}(s; \tau) = \mathbf{p}_0(s) \quad (2.29)$$

by integrating $\mathbf{p} = \nabla S(\mathbf{q})$ along these trajectories using Eq. (2.29)

$$S(\mathbf{q}(s; \tau)) = S_0 + \int_0^\tau d\mathbf{q} \cdot \nabla S(\mathbf{q}(s; \tau)) = S_0 + \int_0^\tau d\tau \quad (2.30)$$

The quantity $\int_0^\tau d\tau$ is called the *optical path length*. For $n = n(q)$, the optical path length is generalized to $\int d\tau n(\tau)$. Since this path length is the same on every ray (unlike the case of inhomogeneous index case, for instance), the resulting wavefronts form a family of *parallel* curves, consistent with what we know for example about plane waves which are the simplest known solution of the free-space ($n = 1$) Helmholtz equation in the absence of the boundaries. The freedom of choice of the initial curve Σ however can lead to solutions with an infinitely many possible forms of the wavefronts, generated by families of rays which always move on straight line trajectories (see Fig. 2.3). This is why we obtain different form of wavefronts when we solve the free Helmholtz equation in different separable coordinates; cartesian coordinates yield regular plane-waves, polar coordinates result in circular waves represented by Bessel functions (cylindrical harmonics).

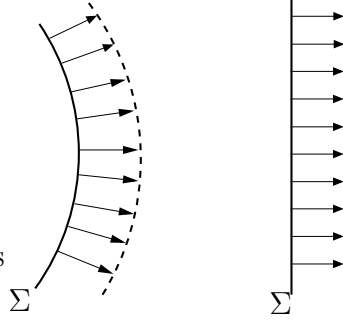


Figure 2.3: Different boundary conditions Σ resulting in different geometry of wave-fronts.

To solve Eq. (2.11), we rewrite it in the form

$$\nabla \cdot (\rho \nabla S) = 0 \quad (2.31)$$

where $\rho(q) = A^2(q)$. Consider now a narrow tube D of trajectories around $q(s; \tau)$ with infinitesimal caps ∂D_{τ_0} and ∂D_{τ} and apply Gauss theorem to the vector field $\rho \nabla S$

$$\int_D dA \nabla \cdot (\rho \nabla S) = 0 = \left(\int_{\partial D_{\tau_0}} - \int_{\partial D_{\tau}} \right) ds \rho |\nabla S| \quad (2.32)$$

just because the boundaries of the tube are defined along the rays and wavefronts. Here ds is a line element on the wave-front. This can be written in the differential form

$$\rho(s; \tau_0) ds(s; \tau_0) = \rho(s; \tau) ds(s; \tau) \quad (2.33)$$

Thus, the amplitude behaves like a density transported along the flow generated by the rays. The quantity

$$\xi_s(\tau, \tau_0) = \frac{ds(s; \tau)}{ds(s; \tau_0)} \quad (2.34)$$

is called the *expansion ratio* [83], and measures the divergence of a tube of rays along a given ray, denoted by s . Hence, the amplitude at a point q is given as

$$A(q) = \xi_s(\tau, \tau_0) A(q_0) \quad (2.35)$$

where q_0 is a point on Σ which is connected by the ray s to the observation point q .

The lowest order asymptotic formula for $\psi(q)$ for the free-space Helmholtz equation is therefore

$$\psi[q(s, \tau)] = A[q(s, \tau_0)] \sqrt{\frac{ds(s, \tau_0)}{ds(s, \tau)}} e^{ikS[q(s, \tau)]} \quad (2.36)$$

A considerably more useful expression can be found if we adopt the view that (s, τ) forms an orthogonal coordinate system as depicted in Fig. 2.2, and consider the

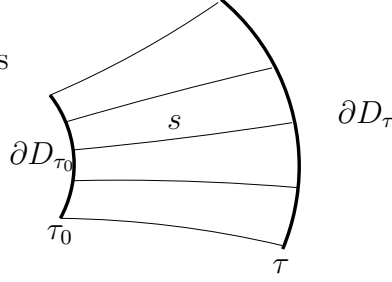


Figure 2.4: Schematics showing the mapping of an initial line element ∂D_{τ_0} on an initial wavefront at $\tau = 0$ by ray flow to its value at $\tau > 0$, ∂D_{τ} . Note that the “tube of rays” shrinks or expands depending on the curvature of the initial wavefront.

coordinate transformation $q_i = q_i(s, \tau)$. From elementary differential geometric arguments [89], it can be shown that

$$\frac{ds(s; \tau_0)}{ds(s; \tau)} = \frac{J(s; \tau_0)}{J(s; \tau)} \quad (2.37)$$

where $J(s; \tau)$ is the Jacobian of the transformation $(s, \tau) \rightarrow (q_1, q_2)$:

$$J(s; \tau) = \frac{\partial(q_1, q_2)}{\partial(s, \tau)} \Big|_{\tau} = \begin{vmatrix} \frac{\partial q_1}{\partial s} & \frac{\partial q_1}{\partial \tau} \\ \frac{\partial q_2}{\partial s} & \frac{\partial q_2}{\partial \tau} \end{vmatrix} \quad (2.38)$$

Thus, we can write

$$\psi[q(s; \tau)] = A[q(s; \tau_0)] \sqrt{\frac{J(s; \tau_0)}{J(s; \tau)}} e^{ikS[q(s; \tau)]} \quad (2.39)$$

The Jacobian can be calculated for the case of a uniform index [66] in terms of the radius of curvature $\varrho(s)$ of the initial wave-front

$$J(s; \tau) = \frac{dp_{01}/ds}{p_{02}} (\tau + \varrho(s)) \quad (2.40)$$

Here, the sign of the radius of curvature ϱ of an initial wave-front is defined with respect to the normal chosen in the direction of the rays. We can rewrite Eq. (2.36) as

$$\psi[q(s, \tau)] = A[q(s, \tau_0)] \left(\frac{\varrho(s)}{\tau + \varrho(s)} \right)^{1/2} e^{ikS[q(s, \tau)]} \quad (2.41)$$

We observe that when $\tau = -\varrho(s)$ the Jacobian Eq. (2.40) becomes singular, i.e. the map $(s, \tau) \rightarrow (q_1, q_2)$ cannot be inverted, and the amplitude of the wave-function blows up. The locus of these points forms a curve called the *caustic*; in the case in which it degenerates to a point, it's called a *focus*.

The non-invertibility of the coordinate transformation can be easily understood: there are points in space (such as N in Fig. 2.5) which are reached by two or more

different rays emanating from the original wave-front Σ . In case of a focus such points are on the caustic itself, in the generic case they are in the vicinity and only on one side of the caustic. This is an indication that the solution to the Eikonal equation, $S(q)$, is multi-valued. In this case the superposition principle is invoked, and $\psi(q)$ is represented as a sum of interfering terms of the form Eq. (2.36), one for each ray through q

$$\psi(q) = \sum_{\nu} A_{\nu}(q) e^{ikS_{\nu}(q) - m_{\nu}(q)\frac{\pi}{2}} \quad (2.42)$$

Here, $A_{\nu}(q)$ is the amplitude of the ν th ray, constructed according to Eq. (2.35), and $m_{\nu}(q)$ is the number of times the ν th ray encounters a caustic from Σ to q ; for a focus, $m_{\nu}(q)$ is increased by two. The origin of the caustic phase shift $m_{\nu}(q)$ will be explained later.

Eq. (2.42) applies away from the caustic, but exactly on the caustic, both the amplitude and the Eikonal $S(q)$ have problems: the former becomes singular and the latter becomes undefined. That such *catastrophes* [90, 84, 91], are an artifact of our asymptotic expansion can clearly be seen from the fact that the original equation Eq. (2.1), being an elliptic equation, has regular solutions [88] as long as the boundary conditions are well-behaved. Clearly, the breakdown of the asymptotic expansion occurs because one (or several) of the terms in the asymptotic expansion Eqs. (2.8-2.9) is not as small as it was assumed to be. In fact, the term $\nabla^2 A_0/k^2 A_0$ is found to diverge on the caustics. The problem cannot be fixed by including more terms of the expansion Eq. (2.7), and solving to higher order in the algebraic powers k^{-1} . The remedy has been devised by various techniques, like redefining the asymptotic expansion locally (boundary layer analysis) [66], uniform approximations [84, 92, 93] or complexifying the rays [85], among others. A simple and familiar example in which this problem is solved is Gaussian optics of resonators near a focus; this falls under the first of these categories and is discussed for dielectric resonators in Chapter 4.

Despite the failure of the simple Eikonal theory on a caustic curve (or point), the presence of the caustic does not prevent one from constructing a consistent solution everywhere in space “above” the caustic. The geometric construction involved is straightforward for the case of uniform index we are considering. Let Σ in Fig. 2.5 be the initial wavefront. For the uniform index case, the rays are simply straight lines normal to Σ . The envelope of this family of normals define in the generic situation a curve Γ , which is the caustic. In mathematics, a curve Γ whose tangents are normal to another curve Σ , is called the *evolute* of Σ ; and Σ in turn is called the *involute* of Γ [94]. Thus, there are an infinite number of involutes of Γ , all of which are the wave-fronts of the solution of Helmholtz equation.

If the parametric equations describing Γ are written as $x = f(\alpha)$, $y = g(\alpha)$, then one can work “backwards” and write the following parametric form of all its involutes $(\bar{x}(\tau, \alpha), \bar{y}(\tau, \alpha))$ [94, 66]

$$\bar{x} = f(\alpha) + (\tau - s(\alpha))\gamma_1 \quad (2.43)$$

$$\bar{y} = g(\alpha) + (\tau - s(\alpha))\gamma_2 \quad (2.44)$$

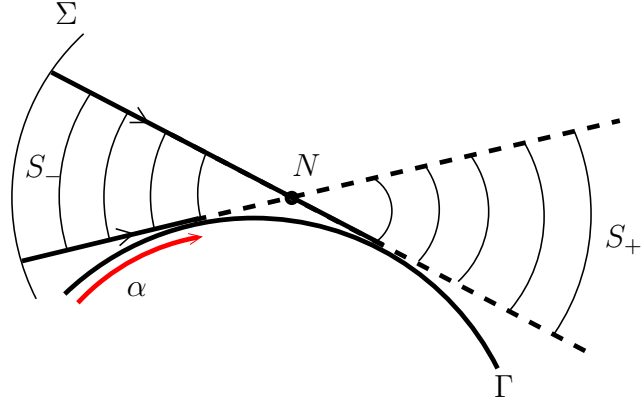


Figure 2.5: Schematics showing the evolute-involute and wavefront-caustic relationship. There are two possible ray directions at each point N in the vicinity of the caustic.

where

$$\gamma_1(\alpha) = \frac{f'}{\sqrt{f'^2 + g'^2}}, \quad \gamma_2(\alpha) = \frac{g'}{\sqrt{f'^2 + g'^2}} \quad (2.45)$$

are the unit vectors tangent to Γ , and $s(\alpha)$ is the arclength measured along Γ from a fixed point. Each individual involute is obtained by $\tau = \text{constant}$, which is the optical path length defined in Eq. (2.30). Note τ is equal to the value of the Eikonal $S(q)$. From Eqs. (2.43-2.44), τ can be determined as a function of x and y . Note however that this function will be double-valued because two rays pass through each point N on the upper side of the caustic and in this case there will be two terms in Eq. (2.42). When the caustic is of circular shape, an explicit expression for the involutes, and hence the Eikonal can be found [66, 84]

$$S_{\pm}(r, \phi) = \pm \left(\sqrt{r^2 - a^2} - a \cos^{-1} \frac{a}{r} \right) + a\phi \quad (2.46)$$

where r, ϕ are the polar coordinates at which the Eikonal is calculated, and a is the radius of Γ . Note in Fig. 2.6 that the two “branches” of wavefronts belonging to S_{\pm} are joined exactly on the caustic, because as $r \rightarrow a$ and $\phi \rightarrow \phi_0$, $S_+(r, \phi) \rightarrow S_-(r, \phi)$. It’s not only instructive but also mathematically appropriate to regard the rays of S_+ converging onto the caustic from one “sheet”, and reappearing after briefly touching the caustic on another sheet (and being normal to S_-), simply because the functions $S_{\pm}(r, \phi)$ have a branch point singularity at $r = a$.

As we will see, the ansatz Eq. (2.42) breaks down only locally, in a layer of the order of $O(k^{-2/3})$ surrounding the caustic. According to the interpretation outlined in the previous paragraph, the solution

$$\psi(q) = A_- e^{ikS_-} + A_+ e^{ikS_+ + i\frac{\pi}{2}} \quad (2.47)$$

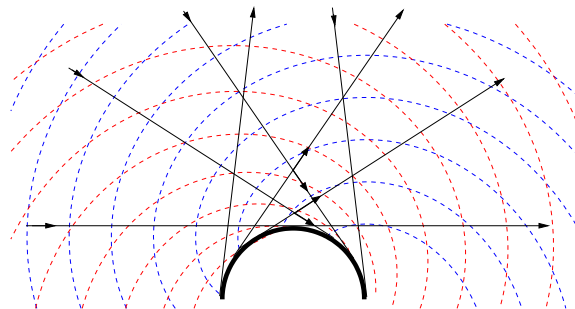


Figure 2.6: Involutes S_{\pm} of a circular curve. The two sheets are colored in blue (S_-) and red (S_+). The solid black lines are the rays corresponding to S_{\pm} . Note that (S_-) rays ingoing to the caustic are everywhere normal to the blue curves and outgoing (S_+) rays are everywhere normal to the red curves.

can be interpreted as a converging wave ($-$) “scattering” off the caustic into the wave denoted by ($+$), and thereby picking up a phase-shift $\pi/2$. Thus we can formally write that on the caustic

$$kS_+ = kS_- - \frac{\pi}{2} \quad (2.48)$$

to take into account the phase loss suffered at a caustic crossing. This is the same kind of phase loss a gaussian beam suffers when going through a focus, which in physical optics is called the *Guoy effect* [76]. Only in the latter case because the caustic is a point, the phase loss is π^2 .

Last, note that according to the above description, since no rays penetrate below the caustic, that region can be thought of the shadow region, under the illumination provided on Σ .

2.4 A paradigm for integrable systems: The circle billiard

In this thesis, we will deal almost exclusively with billiard systems and a simple variant we call refractive (dielectric) billiards. A billiard is simply defined by the *Dirichlet problem*

$$(\nabla^2 + k^2)\psi(q) = 0, \quad \psi|_{\partial D} = 0 \quad (2.49)$$

where the boundary ∂D encloses a simply-connected, finite domain D . We will be mainly concerned with 2 dimensional domains D in this thesis. We attempt to write the usual semiclassical form Eq. (2.42) for the wave-function $\psi(q)$

$$\psi(q) = \sum_{\nu=1}^N A_{\nu}(q)e^{ikS_{\nu}} \quad (2.50)$$

²A second difference is that the gaussian beams cannot be represented with real Eikonals, and result in complex rays.

The crucial difference from our previous discussion is that we are now discussing a boundary-value problem, not an initial value problem. The boundary condition on the wave-function in Eq. (2.49) cannot be reduced to an “initial wavefront” problem; nonetheless it is possible to find consistent solutions based on Eikonal theory.

Note that the solution to the *interior problem* Eq. (2.49) exists only at certain discrete values of the wave-vector k , the eigenvalues of the Laplacian $\mathcal{L} = -\nabla^2$ with Dirichlet boundary conditions. We will call the procedure of the determination of these eigenvalues in the limit $k \rightarrow \infty$ using the semiclassical ansatz Eq. (2.50), *semi-classical quantization*. We will begin our treatment with the well-known example of a billiard of circular shape. The quantization procedure outlined below, but restated in a slightly different form, is the well-known *EBK quantization* method [59, 61, 62].

Let us begin by assuming that an expansion of the form Eq. (2.50) exists with a finite number N terms for the solution of Eq. (2.49), with ∂D given by

$$r(\phi) = R = \text{constant} \quad (2.51)$$

It's not known a priori what the value of N is, but it's clear that one cannot satisfy the boundary condition on ∂D by a single term asymptotic expansion Eq. (2.50), for $\psi(q \in \partial D) = 0$ would then mean $A(q \in \partial D) = 0$ and then the transport equations Eq. (2.11) would imply that $\psi(q)$ has to vanish identically within the billiard. Let's take $N > 1$; then the Dirichlet boundary conditions

$$\sum_{\nu=1}^N A_{\nu}(q) e^{ikS_{\nu}(q)} = 0, \quad q \in \partial D \quad (2.52)$$

can then be implemented by the pairwise annihilation of terms at each point of the boundary

$$A_{\nu}(q) e^{ikS_{\nu}(q)} + A_{\nu'}(q) e^{ikS_{\nu'}(q)} = 0 \quad (2.53)$$

for $\nu \neq \nu'$. Such a situation conforms with the physical picture of wave reflection at a metallic boundary, when one of the terms is regarded as the incoming wave and the other term as the reflected wave. This leads to the relations

$$S_{\nu} = S_{\nu'} \quad (2.54)$$

$$A_{\nu}(q) = -A_{\nu'} \quad (2.55)$$

Note that the latter condition can be incorporated into the phase as a phase shift of π at each reflection:

$$kS_{+} = kS_{-} - \pi \quad (2.56)$$

Furthermore using Eq. (2.49) and Eq. (2.55) we find that $\hat{\mathbf{n}} \cdot \nabla S_{\nu} = \pm \hat{\mathbf{n}} \cdot \nabla S_{\nu'}$, where $\hat{\mathbf{n}}$ is the outward pointing unit normal to the boundary. Again one can argue that the positive sign would generate the trivial solution $\psi(q) = 0$, so that the solution we are seeking has to satisfy the reflection condition

$$\hat{\mathbf{n}} \cdot \nabla S_{\nu} = -\hat{\mathbf{n}} \cdot \nabla S_{\nu'} \quad (2.57)$$

which, since $\mathbf{p} = \nabla S$, can be interpreted to be the reversal of the normal component of the momentum (see Fig. 2.7), or simply specular ray reflection. Let us denote the angle a particular ray (corresponding to any of the branches S_ν) makes with the boundary by $\chi = \cos^{-1} |\hat{\mathbf{n}} \cdot \nabla S|$.

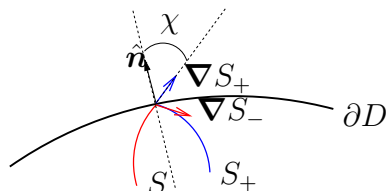


Figure 2.7: Reflection condition at the boundary and the choice of wavefront orientation.

Consider an initial curve Σ , which we take to be the level-curve of one of the functions $S_\nu(q)$ in the expansion Eq. (2.50), the form of which is undetermined at this point. We will consider the propagation of this wavefront via its associated normal congruence, as described in detail in the previous section. This wavefront, after several reflections from the boundary has either to reproduce itself or another term in the sum Eq. (2.50) for this expansion to be well-defined in D (or a subregion of it) and contain a finite number of terms N .

To assess this we look at what kind of trajectories typical rays in this billiard \mathbf{p} follow. As we have established above, the motion is simply described by straight line motion and specular reflection, when the trajectories intercept the boundary. This is the well known problem of a *classical billiard*.

First we consider the case of a circular boundary ∂D for which the Eikonal solutions are well known [95]. The global properties of the trajectories in this case can be found from elementary geometry:

- The ray motion conserves χ
- The trajectory can be either periodic (closes on itself) or quasi-periodic (closes on itself in the infinite time limit; the terminology will be clarified in the next section)
- In either case, the trajectories form a circular envelope of radius $a(\chi) = R \sin \chi$

These observations are summarized in Fig. 2.8. Thus classes of trajectories can simply be parametrized by giving χ . It follows from the third statement that when we start out a ray with a given χ , it can only pass through a point q between the caustic $a(\chi)$ and R in two different directions $\mathbf{p}_\nu(\chi)$, $\nu = +, -$; $\mathbf{p}_+(\chi)$ is directed from the caustic towards the boundary, and $\mathbf{p}_-(\chi)$, from the boundary to the caustic. From the relation $\mathbf{p}_\nu(\chi) = \nabla S_\nu(\chi)$, for the case of a circle, there can only be two terms in the expansion Eq. (2.50), $N = 2$.

Assume we start out with a level-curve of $S_+(\chi)$, denoted by Σ . Note that this can already be constructed by drawing a family of rays making an angle χ with

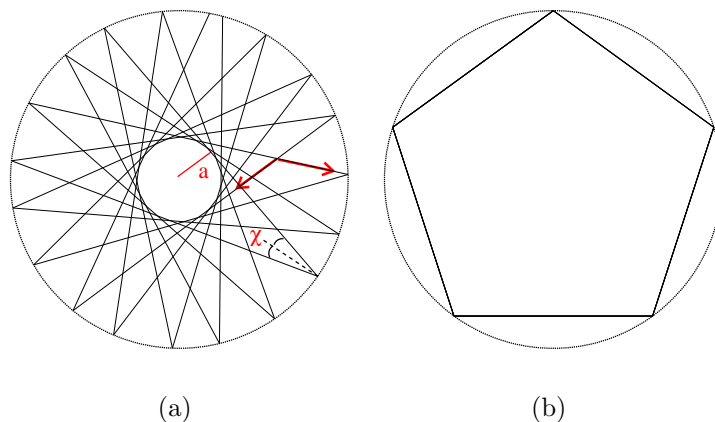


Figure 2.8: (a) A quasi-periodic ray motion and (b) a periodic 5-bounce orbit.

the boundary and finding the curves orthogonal to them. After reflection the ray family is represented by $S_-(\chi)$ which are obtained by reflection viz. Eq. (2.53) and Eq. (2.57). At each point q on the boundary ∂D , we have

$$S_-(\chi; q) = S_+(\chi; q) - \frac{\pi}{k} \quad (2.58)$$

The reflected family of rays $S_-(\chi)$ subsequently pass through a circular caustic at $r = a(\chi)$ and are in turn scattered into $S_+(\chi)$, which is exactly the scenario we have encountered at the end of the previous section. The result is a phase loss of $\pi/2$.

The following visualization [59] is very helpful: Consider two vector fields $\mathcal{M}^\pm(\chi)$, representing the family of rays of $S_\pm(\chi)$ defined on two sheets Ω^\pm , which form two copies of the annular region Ω delimited by $r = R$ and $r = a(\chi)$. This construction is no different than the construction of Riemann for multiple-valued complex functions. The situation is depicted in Fig. 2.9. The arguments given in the previous paragraphs can be restated as follows: A ray through an arbitrary point q on one of the sheets, say Ω^+ , will find itself in sheet Ω^- upon reaching the boundary. And this ray in turn will find itself on sheet Ω^+ , upon reaching the caustic boundary. The inner and outer circles hence can be glued together and the resulting structure is a covering space $S^2 = \Omega^+ \cap \Omega^-$ which has a topology of a torus.

Now note that, although we were able to define a single-valued vector-field on the torus, the Eikonal $S(\chi) \equiv S_\pm(\chi)$ itself, from which this field is derived is in general not uniquely defined. For consider a ray starting out on the wavefront $\Sigma = S_+(\chi)$, and after being reflected $\mu_b(\chi)$ times, and crossing the caustic $\mu_c(\chi)$ times, this ray returns to the original wavefront it started with. From Eqs. (2.30),(2.48) and (2.56), we know that the value of $S_+(\chi)$ must have advanced by the path length covered by this ray minus the phase shifts:

$$\Delta S_+(\chi) = \int d\mathbf{q} \cdot \nabla \mathbf{S} - \frac{1}{k} \mu_c(\chi) \frac{\pi}{2} - \frac{1}{k} \mu_b(\chi) \pi \quad (2.59)$$

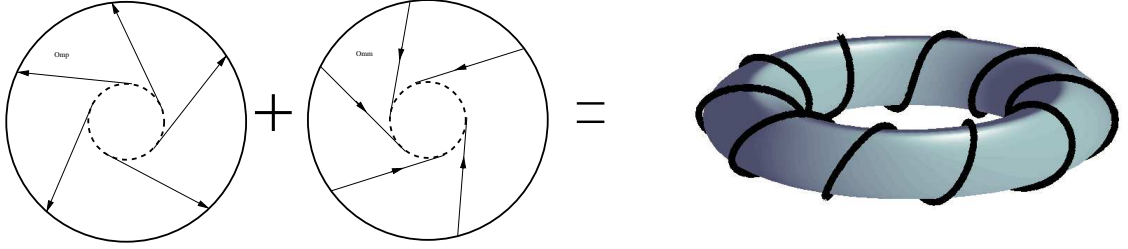


Figure 2.9: The two vector field $\mathcal{M}^\pm(\chi)$ on the covering spaces Ω^\pm can be glued together to obtain a continuous vector-field on a covering-space topologically equivalent to a 2-torus.

∇S here implies using the appropriate sheet of $S(\chi) \equiv S_\pm(\chi)$ on each segment of the path. Note that since the path integral only involves the vector-fields, it's uniquely defined, in contrast to the Eikonals themselves. Also, although the point of departure may be any q in the real-space, the indices $\mu_b(\chi)$ and $\mu_c(\chi)$ are unique, and can be related to the topological invariant, the winding number $w(\chi)$ of the glued vector field $\mathcal{M}(\chi) = \mathcal{M}^+(\chi) \cap \mathcal{M}^-(\chi)$ over the torus.

Hence, the resulting Eikonal $S(\chi) = S_\pm(\chi)$ is actually infinite-valued, if we consider multiple passages. But this itself is not a problem for the existence of the asymptotic expansion Eq. (2.50). The crucial requirement is the single-valuedness of the wavefunction. Consider a ray of the wavefront of $S(\chi)$ departing from $Q \in \Sigma$ and after a roundtrip arriving at $q \in \Sigma$. Then the necessary conditions are:

$$|A(\chi; Q)e^{ikS(\chi; Q)}| = |A(\chi; q)e^{ikS(\chi; q)}|, \quad \arg(A(\chi; Q)e^{ikS(\chi; Q)}) = \arg(A(\chi; q)e^{ikS(\chi; q)}) \quad (2.60)$$

The point Q mapped into q by the particular ray may or may not be the same point, depending whether $\mathcal{M}(\chi)$ represents a periodic or quasi-periodic ray motion. Using Eq. (2.39), the first condition can be fulfilled only if

$$A(\chi; Q) = \frac{c}{\sqrt{J(\chi; Q)}} \quad (2.61)$$

where c is a constant. The second condition can be satisfied if

$$kS(\chi; q) = kS(\chi; Q) + 2\pi n \quad (2.62)$$

This imposes a restriction on the possible values (χ, k) can take (recall that q and Q are on the same level-curve of $S(\chi)$). Note that Eq. (2.62) actually represents an infinity of conditions, as it has to be satisfied at all points $q \in \Omega$. We will now replace these conditions with *two* conditions (in general this number is equal to the number of spatial degrees of freedom of the integrable system).

The crucial observation enabling us to do this is the observation that the ray path *on the torus*, which makes a roundtrip in order to end up on the wavefront it started

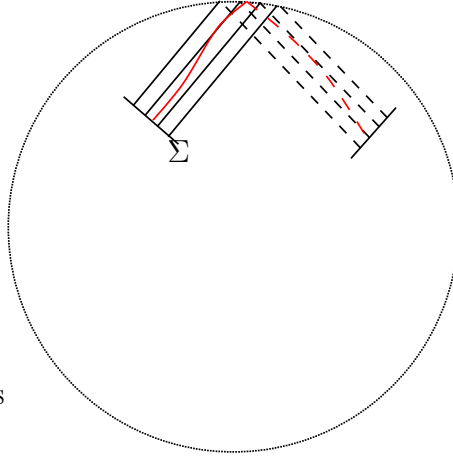


Figure 2.10: The deformability of a contour of integration within the vector field $\mathcal{M}^\pm(\chi)$, derived locally from a potential multi-valued potential $S(q)$.

with, can be replaced with an *arbitrary* path which is continuously deformable to the original ray path, with respect to the satisfaction of the condition Eq. (2.62). This property is due to the fact that the ray (vector) field $\mathcal{M}(\chi)$ is derivable from a local potential, $S(\chi)$, albeit multi-valued. This ensures that the optical path length

$$\tau(\chi) = \int d\mathbf{q} \cdot \nabla S \quad (2.63)$$

is invariant with respect to deformations. This situation is depicted in Fig. 2.10. The original ray path integral can be written as infinitesimal zig-zag paths which extend along wavefronts and rays. The contribution to integration along the wavefronts are zero because $d\mathbf{q} \perp \nabla S$, and the integrations on rays is equal to the original ray integral, because all the rays constitute a ray family with identical actions. We can proceed further and replace the original path by any *closed* one, say Γ_χ , starting and ending on the same wavefront. Finally, the continuous deformability condition (on the torus) additionally guarantees that the indices $\mu_b(\chi)$ and $\mu_c(\chi)$ are identical to those of the original path. Hence, we replace the condition Eq. (2.62) by

$$k \oint_{\Gamma} d\mathbf{q} \cdot \nabla S - \mu_c(\chi) \frac{\pi}{2} - \mu_b(\chi) \pi = 2\pi n \quad (2.64)$$

It's worth reiterating that an arbitrary vector field would not satisfy this deformability condition; it is true only for fields derivable from a potential via $\mathbf{p}(q) = \nabla S(q)$.

Now, we make use of a theorem in topology which states that for any such covering space, there is a basis of n_b independent curves $\Gamma_i, i = 1 \dots n_b$, no one of which can be deformed into another, nor into a linear combination of the other with integer coefficients. However any other curve can be expressed as a linear combination of basis curves (quite like the concept of an complete and independent set of basis

vectors for a vector space).

$$\Gamma = \sum_{i=1}^{n_b} c_i \Gamma_i \quad (2.65)$$

This is to be understood in the following sense: the contour Γ can be obtained by continuous deformation from the composite contour made up of Γ_1 repeated c_1 times, etc. If $c_i < 0$, then we must reverse the direction of traversal on Γ_i . Therefore, Eq. (2.64) will hold for every curve on the covering space S^2 if it holds for each of the basis curves, with a suitable integer c_i for each. The number of such fundamental curves (called the first Betti number in topology) depends on the topology of the covering space and in our case, for a 2-torus, it's $n_b = 2$. Note that we have effectively reduced the infinity of conditions Eq. (2.64) to two conditions. The concept is a topologic equivalent of continuous versus discrete Fourier decomposition, where the ‘‘harmonics’’ will be the set of asymptotic eigenfunctions we set out to find. This comparison gains a literal meaning in the particular instance when the shape ∂D is a rectangle.

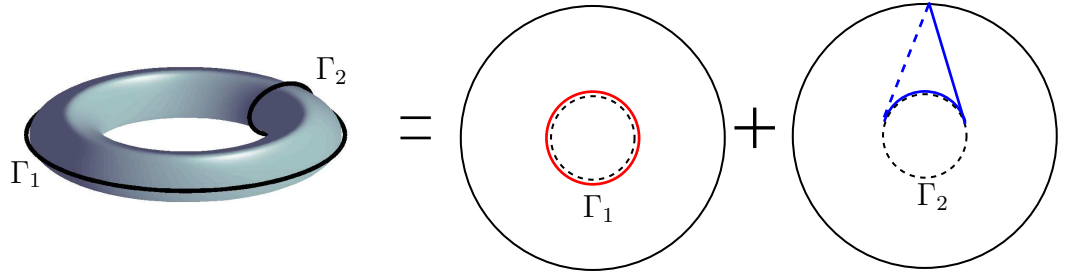


Figure 2.11: Basis curves on the two-torus and a particular realization of these in the circular domain. The solid curves denote the (+) sheet, and dashed curves the (-) sheet.

A possible choice for the two basis curves of the torus are shown in Fig. 2.11. Thus the quantization condition is

$$k \oint_{\Gamma_i} d\mathbf{q} \cdot \nabla S - \mu_c^i \frac{\pi}{2} - \mu_b^i \pi = 2\pi n_i, \quad i = 1, 2 \quad (2.66)$$

The first loop integral is along caustic itself, and since $\nabla S \parallel \Gamma_1$, the integral is just the perimeter of the circle, $\oint_{\Gamma_1} d\mathbf{q} \cdot \nabla S = 2\pi R \sin \chi$, and if we require the curve to remain on the same covering space, $\mu_c = \mu_b = 0$, we get our first condition to be

$$k \cdot 2\pi \sin \chi = 2\pi n_1 \quad (2.67)$$

The convention is to call this quantum number m and we will do so. We obtain the following condition, which we will use again and again in this thesis:

$$\sin \chi = \frac{m}{kR} \quad (2.68)$$

The second curve Γ_2 consists of a ray tangent to the caustic, its subsequent reflection from the boundary ∂D , each of length $R\sqrt{1 - \sin^2 \chi}$ and the segment of caustic closing the curve, of length $2R(\frac{\pi}{2} - \chi) \sin \chi$, and since we cross the caustic and the boundary once, $\mu_c = \mu_b = 1$, in this case

$$2kR[\sqrt{1 - \sin^2 \chi} - (\frac{\pi}{2} - \chi) \sin \chi] = 2\pi n + \frac{\pi}{2} + \pi \quad (2.69)$$

eliminating $\sin \chi$ using Eq. (2.68), we obtain the final form of our quantization condition as a transcendental equation for k

$$\sqrt{(kR)^2 - m^2} - m \cos^{-1} \left(\frac{m}{kR} \right) = \pi \left(n + \frac{3}{4} \right) \quad (2.70)$$

Note the appearance of k always in the dimensionless form kR . An analytic expression can easily be found for $m \approx kR$, by setting $m/kR = 1 - \epsilon$ and solving for ϵ , we obtain the quantization condition

$$kR \sim m + \frac{1}{2} m^{1/3} [3\pi(n + \frac{3}{4})]^{2/3} \quad (2.71)$$

The corresponding solutions, as we shall see, are confined to the narrow layer between the boundary and the caustic, which is at $R \sin \chi \approx (1 - \epsilon)R$. Such solutions were first noted by Lord Rayleigh in connection with acoustic wave propagation in closed domains, and are called “whispering gallery modes”.

The wave-functions can be constructed, too [95]. Since, through the above conditions on k and $\sin \chi$ we are assured that a unique wave-field can consistently be constructed, we can use the basis curves Γ_i , or their continuous deformations to calculate the value of the Eikonals at a chosen point (r, ϕ) in the domain $R \sin \chi < r < R$, starting from any reference point. We choose $S_{\pm}(r = a(\chi), \phi = 0) = 0$ and calculate the path length for the two rays going through (r, ϕ) shown in Fig. 2.12:

$$S_+(r, \phi) = \left(\sqrt{r^2 - a^2} - a \cos^{-1} \frac{a}{r} \right) + a\phi \quad (2.72)$$

$$S_-(r, \phi) = - \left(\sqrt{r^2 - a^2} - a \cos^{-1} \frac{a}{r} \right) + a\phi + \frac{2\pi}{k} \left(n + \frac{3}{4} \right) - \frac{\pi}{k} \quad (2.73)$$

where we have used Eq. (2.69) in Eq. (2.73). Note that these expressions are equivalent to the involutes of a circle of radius a found in Eq. (2.46).

The amplitude can be determined using the formula Eq. (2.41) with $\varrho(s)$ calculated from the level curves of the expressions given in Eq. (2.72) and Eq. (2.73):

$$A_{\pm}(r, \phi) = \frac{A_0}{(r^2 - a^2)^{1/4}} \quad (2.74)$$

where the constants in Eq. (2.61) are fixed by the application of Dirichlet boundary conditions. The branch in the above expression is chosen so that $(r^2 - a^2)^{1/4} > 0$ in both amplitudes.

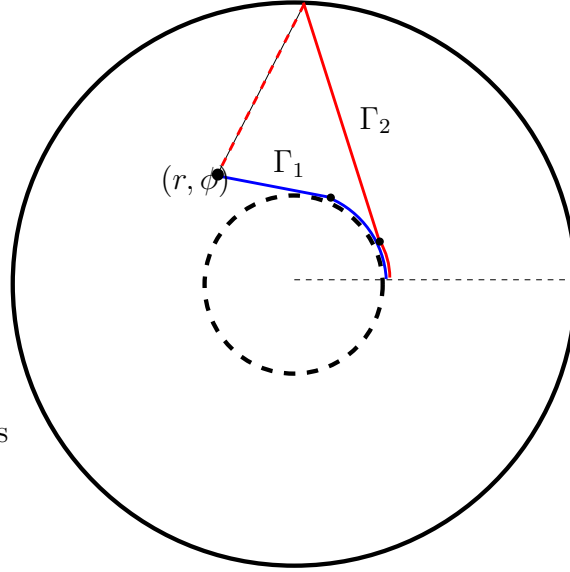


Figure 2.12: Paths for the calculation of the Eikonals at a point (r, ϕ) . We take $S_{\pm}(a, 0) = 0$. Both $\Gamma_{1,2}$ start tangent to the caustic at $(a, 0)$. Γ_1 is composed of an arc of length $\tau = a(\phi - \cos^{-1}(a/r))$ and a straight line segment of length $\tau = \sqrt{r^2 - a^2}$. Γ_2 contains an arc of length $\tau = a(\phi + \cos^{-1}(a/r) - 2\cos^{-1}(a/R))$, two straight line segments of total length $2\sqrt{R^2 - r^2} - \sqrt{r^2 - a^2}$. Because of the reflection, π/k has to be subtracted.

Finally, the asymptotic expression for the wavefunctions of a circular billiard can be written as

$$\psi(r, \phi) = \frac{1}{[(kr)^2 - m^2]^{1/4}} \cos \left[\sqrt{(kr)^2 - m^2} - m \cos^{-1} \left(\frac{m}{kr} \right) - \frac{\pi}{4} \right] e^{im\phi} \quad (2.75)$$

As we stated earlier, the singularity of this solution on the caustic $r = a = m/k$ is of course an artifact of our asymptotic expansion and corresponds to the classical turning point problem well known from WKB of one-dimensional systems. Here, the turning point is generated by the angular momentum barrier for radial motion. From physical optics point of view, the interior of the caustic $r < a$ is the shadow zone, an area where the rays cannot penetrate, and the optical wavefield decays very fast. However, light can be shed into what's happening in the shadow region using a beautiful generalization of the ray theory. Keller's geometric theory of diffraction accounts for this by allowing the ray coordinates to be complex. The discussion can best be followed by consulting to the original reference [62] and lies beyond the mainstream of this thesis. For our purposes here, it's sufficient to point out that the ray through a point (r, ϕ) , $r < a$, is a complex line initially spawned from a real point on the caustic. The phases are found to be double-valued again, given by

$$S_{\pm}(r, \phi) = \pm i \left(\sqrt{a^2 - r^2} - a \cosh^{-1} \frac{a}{r} \right) + a\phi \quad (2.76)$$

and the amplitudes are

$$A_{\pm}(r, \phi) = \pm \frac{A_0 e^{i\pi/4}}{(a^2 - r^2)^{1/4}} \quad (2.77)$$

However, in contrast to the “allowed region”, one of the solutions have to be discarded here, and it’s the one which increases exponentially as as we move away from the caustic. Hence our solution becomes

$$\psi(r, \phi) = \frac{1}{2[m^2 - (kr)^2]^{1/4}} \exp \left[\sqrt{m^2 - (kr)^2} - m \cos^{-1} \frac{m}{kr} \right] e^{im\phi}, \quad r < a \quad (2.78)$$

which decreases exponentially as we move away from the caustic, on a length scale $\propto k^{-2/3}$. Solutions *on the caustic* may be found by a uniform approximation yielding Airy functions (see Appendix A).

Last, note that the asymptotic expansions Eq. (2.78), Eq. (2.75) and Eq. (A.10) are the asymptotic expansions of one and the same function, namely the Bessel function of the first kind, $J_m(kr)$, supplemented by the simple factor $e^{im\phi}$. The exact solution for the Helmholtz equation with Dirichlet boundary conditions can simply be obtained by separation of variables in polar coordinates:

$$\psi(r, \phi) = J_m(kr) e^{im\phi} \quad (2.79)$$

where the boundary condition provides the quantization

$$J_m(k_{nm}R) = 0 \quad (2.80)$$

and m is the angular momentum quantum number and n is the radial quantum number. The three expansions are usually listed as the asymptotic expansions for *large* index m , with different regimes of validity, depending on whether $m < kr$, $m \sim kr$ or $m > kr$ [96].

2.5 Generic Billiards and appearance of Chaos

What happens for a quantum billiard with a generic boundary ∂D turns out to be a formidable problem and forms the core of this thesis. The detailed treatment we have given in the previous section for the circular billiard is important to an understanding of the generic case.

At the heart of a consistent construction of the asymptotic expansion given in Eq. (2.50) is the existence of a well-defined vector field $\mathbf{p}(q)$ defined possibly on a multi-sheeted covering space, derivable from a locally well-defined scalar function $S(q)$ via $\mathbf{p}(q) = \nabla S(q)$ which obeys the Eikonal equation

$$(\nabla S)^2 = 1 \quad (2.81)$$

supplemented with the boundary conditions on ∂D , which determines the global properties of the solutions.

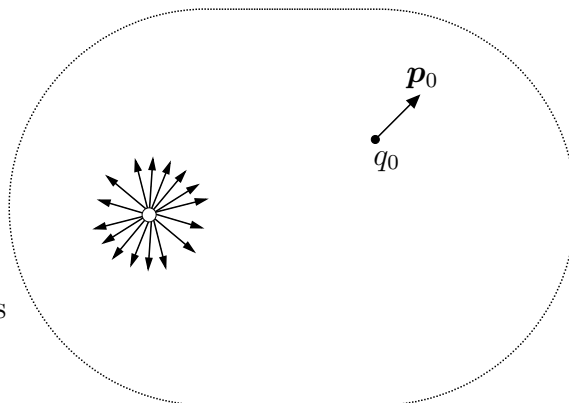


Figure 2.13: A schematics showing the simulation of a ray \mathbf{p}_0 started at a point q_0 in the stadium. The observation at a second point q (within a finite cell Δq around q) would result in approximately isotropic distribution of ray directions in a long run. For the results of an actual simulation see Fig. 2.14.

For the case of a circle, for any given initial condition (q_0, p_0) , we were able to define always two vectors $\mathbf{p}_{\pm}(q)$ at each point q within the covering space. It's a simple matter to check whether property holds for a given boundary ∂D . For example, for the stadium shape given in Fig. 2.13, we start a ray in the direction \mathbf{p}_0 at point q_0 and record the directions of rays at each passage at a second point q . The result for a finite time simulation would show that the directions we obtain are much more than 2 and are approximately uniformly distributed. Of course, such a simple simulation would have a finite precision and one might attribute this behavior to this limited precision. However, it turns out even if tighten the cell of observation around q and increase the precision of root-finding routine, at a longer run of simulation we again would obtain a similar result. We can repeat this experiment with any pair of initial and final conditions, and the same result will obtain for this particular boundary. This is simply a manifestation of globally chaotic motion.

The implication of this result for our quantization procedure is that a vector field $\mathbf{p}(q)$ in this case *cannot* be defined. Einstein was the first to point this out in a 1917 paper [59] whose seminal importance was not realized until very recently; he concluded that for such systems quantization by means of the “old quantum theory” cannot be carried out. The asymptotic expansion Eq. (2.50) can accommodate a finite number of ray directions N in a given covering space, which are then derivable from a multi-valued function $S(q)$ satisfying the Eikonal equation, but not an infinity of them. In addition to the circle, asymptotic solutions of the form Eq. (2.50) can be found for the ellipse with $N = 2$, rectangle ($N = 4$) and equi-lateral triangle ($N = 6$). How many more such shapes can we find? Was the stadium shape a pathology?

The answer to this is that all the cases where N is finite are highly non-generic. A general boundary ∂D exhibits ray motion which is of mixed character. Depending on the initial conditions q_0, p_0 chosen, the motion can either be chaotic or regular. In the latter case, regular motion covers a finite region in the real-space and it's possible

to assign a finite number of ray directions at each point of this covering space.

While this realization may sound disheartening, a lot of distance has been covered in the past two decades within the field of Quantum Chaos for the semi-classical quantization of generic systems. There are in general two major approaches to address the quantization problem in mixed systems:

- **Local asymptotics:** The integrable portion of the motion can be described locally (i.e. by locally working in the covering space laid out by initial conditions which leads to regular motion). In this way, it's possible to account for a *subset* of the spectrum $\{k_n\}$ and associated modes. There exist in general a one-to-one correspondence between modes and ray-congruences, just like in EBK quantization.
- **Statistical descriptions:** It has been found that it is not possible semi-classically to calculate the individual modes associated with the chaotic component of the ray-motion. It is however possible to calculate statistical properties, like density of states, energy spacing distributions, correlation functions. In fully chaotic systems explicit analytic calculations can be done using Random Matrix Theory for example, and leads to statistical quantities which are universal. Another important technique in this category is Gutzwiller's trace formula for calculating density of states (and related approaches), which complements the random matrix theory approaches in the sense that it yields non-universal properties of a specific chaotic system.

A brief review of the techniques in the first category will be given in Section 2.10. Furthermore, the quantization method of Chapter 4 is also in this category. The treatment of scarred modes in Chapter 5 briefly touches on both approaches, and describes the shift in focus required when dealing with chaotic motion.

Results from the theory of Hamiltonian systems has been crucial in paving the path in Quantum chaos. Thus, at this point, it's worthwhile to discuss some generalities of the theory of Hamiltonian systems in the context of our discussion so far.

2.6 Hamiltonian description of Ray Motion

We already made contact with the Hamiltonian description in Section 2.2. The strength of Hamiltonian formalism is the formulation of the problem as a flow in a $2d$ -dimensional phase-space $(q, p) = (q_i, p_i)$, $i = 1, \dots, d$, where both coordinates and momenta are treated on an equal footing. The equations of motion for rays obey the equations of motion of a special form given by Hamilton's equations of motion

$$\frac{dq_i}{d\tau} = \frac{\partial H(q, p)}{\partial p_i} \quad (2.82)$$

$$\frac{dp_i}{d\tau} = -\frac{\partial H(q, p)}{\partial q_i} \quad (2.83)$$

derivable from a unique, conserved Hamiltonian

$$H = H(q, p) \quad (2.84)$$

Within established theory, the shapes circle, ellipse, rectangle and equilateral triangle fall under the class of *integrable systems*. Note that this terminology refers to the ray motion, not to the wider notion of the integrability of the Helmholtz equation. A completely integrable d -dimensional system possesses d independent functions $F_i(q, p)$ which are conserved along each trajectory

$$F_i(q(\tau), p(\tau)) = f_i \quad (2.85)$$

In the case of the circle, these were the magnitude of the momentum vector $p^2 = 1$, which follows from the Eikonal equation Eq. (2.23), and the value of $\sin \chi$. This can formally be expressed in the above form in polar coordinates (r, ϕ) , instead of the cartesian coordinates, where the Eikonal equation can be written as $(\nabla S)^2 = p_r^2 + p_\phi^2/r^2 = p^2 = 1$. Here, $p_\phi = R \sin \chi$ is the angular momentum with respect to the origin, or the ray impact parameter, which is conserved. The coordinates $q_i = (r, \phi)$ and $p_i = (p_r, p_\phi)$ then preserve the Hamiltonian structure of equations of motion, Eq. (2.82-2.83). The integrals of motion are written as

$$F_1 = E = p^2 = 1 \quad (2.86)$$

$$F_2 = p_\phi^2 = R \sin \chi \quad (2.87)$$

In the mechanical equivalent of the billiard, $E = p^2$, which is the energy of the particle of mass $1/2$, can take any value. Due to the *scalability* of the billiard system, all the dynamical information about the motion is however contained in one value of the energy. This is a general property of Hamiltonian systems which have homogeneous Hamiltonians, $H(\gamma p, \gamma q) = \gamma^\nu H(p, q)$. For such *scalable* Hamiltonians the dynamical variables obey simple scaling transformations when energy is scaled. We will confine our discussion to billiard systems and take $E = 1$.

Eqs. (2.85) can in principle be solved for p in terms of q and $f = \{f_i\}$

$$p_i = p_i(q, f) \quad (2.88)$$

We can view the integrals of motion F_i as new momenta, $P_i = F_i(p, q)$, of a new set of conjugate variables (Q, P) . From Eq. (2.83), the new Hamiltonian K cannot depend on Q , so $K = K(P)$, and Eq. (2.82 would then give

$$Q_i(t) = \frac{\partial K(P)}{\partial P_i} \tau + Q_0 \quad (2.89)$$

Thus, we found a solution to Eqs. (2.82-2.83) if we can solve obtain a relation between Q and the old coordinates q . This is achieved by demanding that the transformation $(q, p) \rightarrow (Q, P)$ is *canonical*, and this in turn can be accomplished by a *generating function*

$$S(q, P = f) = \int_{q_0}^q p_i(q, P = f) \cdot dq_i \quad (2.90)$$

where a quantity we have already found, Eq. (2.88), is used. From here, Q is obtained from

$$Q_i = \frac{\partial S(q, P)}{\partial P_i} \quad (2.91)$$

which is an algebraic equation for q in terms of Q and P . This is what is meant by integrability. It also follows from Eq. (2.90) that

$$p_i = \frac{\partial S(q, P)}{\partial q_i} \quad (2.92)$$

Now note that Eq. (2.90) is nothing but the Eikonal $S(q)$ in Eq. (2.30). For a Hamiltonian

$$H(q, p) = p^2 \quad (2.93)$$

we obtain the Eikonal equation using Eq. (2.92) in Eq. (2.93), which is the time-independent Hamilton-Jacobi equation.

The existence of d integrals of motion Eq. (2.85) for an integrable system restricts the flow in the phase space to a d -dimensional hyper-surface. This hypersurface is called a *Lagrangian manifold* \mathcal{M} . It's possible to show that this manifold is (with some known exceptions) always a d -torus. This is because one can define the following "smooth" $2d$ -dimensional vector fields in phase space

$$V_i(q, p) = \left(\frac{\partial F_i}{\partial p}, -\frac{\partial F_i}{\partial q} \right) \quad (2.94)$$

Note that these vector fields are nothing but the tangent vectors to the manifold \mathcal{M} defined by $F_i(q, p) = f_i$. A theorem from topology then states that a compact manifold (because the motion is bounded) parallelizable with d smooth and independent vector fields must be a d -torus. This represents an enormous limitation on the motion, for an orbit starting on one torus will always remain on that torus. We have encountered the two-dimensional version of the invariant tori in the case of the circular billiard.

The invariant tori in the previous section were parametrized with the conserved quantity $F_2 = R \sin \chi$. There are many ways of doing this parametrization given the conserved quantities Eq. (2.86) and (2.87). However, there is one standard and useful way, which leads to the most natural canonical representation of motion on a torus: the *action-angle variables* (I, θ) . These have the property that, the integrals of motion $F_i(q, p)$, when expressed in terms of (I, θ) only depend on the momenta I , and that θ_i represent angle coordinates on the torus, such that in one circuit along one of the i th irreducible direction (curves $\Gamma_{1,2}$ of the previous section), θ_i returns to its original value. There is a recipe for the construction of the action-angle coordinates: Determine d irreducible circuits Γ_i , and calculate the following d generating functions using Eq. (2.90). Then

$$I_i = \frac{1}{2\pi} S_{\Gamma_i}(f) \quad (2.95)$$

where

$$S_{\Gamma_i}(f) = \oint_{\Gamma_i} p_i(q, f) \cdot dq_i \quad (2.96)$$

Note that to calculate this, we again have to use the integrals of motion Eq. (2.85) to determine Eq. (2.88). This algebraic equation can be used to find $f = f(I)$, so that the angles are calculated from

$$\theta_i = \frac{\partial S_{\Gamma_i}(f(I))}{\partial I_i} \quad (2.97)$$

In one particular circuit Γ_i only θ_i changes by 2π , and $\theta_{i \neq j}$ remain constant. This indicates that in the canonical transformation $(q, p) \rightarrow (\theta, I)$, q and p are periodic functions of θ with period 2π :

$$q(t) = \sum_{\mathbf{m}} q_{\mathbf{m}}(I) e^{i\mathbf{m} \cdot \boldsymbol{\theta}(\tau)} \quad (2.98)$$

$$p(t) = \sum_{\mathbf{m}} p_{\mathbf{m}}(I) e^{i\mathbf{m} \cdot \boldsymbol{\theta}(\tau)} \quad (2.99)$$

where $\mathbf{m} \cdot \boldsymbol{\theta} = \sum_i m_i \theta_i$ and $\mathbf{m} = \{m_i\}$ is a d -dimensional vector with integer components. The time-dependence of $\theta(\tau)$ is simple, since $f_1 = f_1(I)$ represents the conserved energy and so we can determine $H = H(I)$. Then, Eq. (2.82) yields

$$\theta_i(\tau) = \omega_i(I)\tau + \delta_i \quad (2.100)$$

The frequencies $\omega_i(I) = \frac{\partial H(I)}{\partial I_i}$ are the characteristic frequencies of a multiply periodic motion

$$q(t) = \sum_{\mathbf{m}} q_{\mathbf{m}}(I) e^{i(\mathbf{m} \cdot \boldsymbol{\omega} \tau + \mathbf{m} \cdot \boldsymbol{\delta})} \quad (2.101)$$

$$p(t) = \sum_{\mathbf{m}} p_{\mathbf{m}}(I) e^{i(\mathbf{m} \cdot \boldsymbol{\omega} \tau + \mathbf{m} \cdot \boldsymbol{\delta})} \quad (2.102)$$

This kind of multiply periodic motion is actually what is meant by the existence of a torus in phase space. In the circular billiard, we found that the ray motion $\mathbf{p}(q)$ could be periodic or quasi-periodic. The meaning of quasi-periodicity can be put on a rigorous basis within this framework. Namely, it corresponds to an *irrational* frequency ratio

$$w = \frac{\omega_\phi}{\omega_r} \quad (2.103)$$

between the radial and angular rotation frequencies³. The quantity w is called the *winding number*.

Finally, we recognize the quantities Eq. (2.95) to be very similar to those appearing in our quantization conditions Eq. (2.66). In fact, if we for a moment ignore the

³Because circle is a separable system, the irreducible circuits take place in the decoupled phase space coordinates (r, p_r) and (ϕ, p_ϕ) .

(boundary and caustic) phase shifts, the quantization conditions can be rewritten as:

$$kI_i = 2\pi n_i \quad (2.104)$$

These conditions are the Bohr-Sommerfeld-Wilson quantization rules of the “old quantum theory” ([63, 64]. The correct form of the quantization conditions with caustic corrections could only be found after the introduction of the Schrödinger equation. The modern semi-classical quantization rules along the lines described in the previous section were written down by Keller [62], based on previous but incomplete works of Brillouin [61], Kramers [97], and most notably Einstein [59]. The one-dimensional version came to be known as WKB(J) quantization, and the multi-dimensional version as EBK quantization.

Integrability is however the exception rather than the rule. Generic billiards are non-integrable, and they have in general only one of the two required integrals of motion, the energy E , which constrains the motion onto a three-dimensional energy hypersurface. Thus, there are not enough constraints to confine the motion *a priori* to a two-dimensional torus-surface in the phase space. The important implication of this for a semi-classical quantization procedure is that the solutions to the Eikonal equation $(\nabla S)^2 = 1$ ceases to exist globally! As we shall see, results from canonical perturbation theory show however that there are remnants of integrability, namely invariant tori, embedded in the otherwise chaotic phase space.

2.7 Poincaré Surface of Section and Discrete Maps

An important technique, originally suggested by Poincaré, for the assessment of the extent of chaos in non-integrable billiards, is the *surface of section* (SOS). To construct a surface of section, one chooses a two-dimensional surface Σ in the four-dimensional phase space and plots the successive intersections of a single trajectory with this surface. The intersections are only to be recorded when the trajectory pierces Σ in a particular sense.

The phase space of the two-dimensional billiard is the four dimensional space spanned by (q_1, q_2, p_1, p_2) . One observable we know for sure is conserved is the energy E , thus we can write

$$E = E(q_1, q_2, p_1, p_2) \quad (2.105)$$

which defines then a three-dimensional constant-energy surface Σ_E on which the motion proceeds. Using this equation, we can in principle solve for one of the variables, say p_2 .

$$p_2 = p_2(q_1, q_2, p_1; E) \quad (2.106)$$

and project the trajectory onto a three-dimensional volume (q_1, q_2, p_1) . If we now define our surface of section Σ by $q_2 = Q_2 = \text{const.}$, which defines a plane with coordinates (q_1, p_1) in this volume, then the (oriented) intersections of the trajectory

with the SOS would generate a two-dimensional scatter of points. On the other hand, if we were to be able to determine a second conserved quantity, say

$$f = F_2(q_1, q_2, p_1, p_2) = F_2(q_1, q_2 = Q_2, p_1, p_2(q_1, q_2 = Q_2, p_1; E); E) = \tilde{F}_2(q_1, p_1; Q_1, E) \quad (2.107)$$

in addition to E , then Eq. (2.107) would describe a *curve* $\sigma_{(f,E)}$ on the surface Σ_E , parametrized by the two constants (f, E) (and implicitly by our choice of Q_2). On the other hand, if such a constant of motion didn't exist, we would have at most a two-dimensional scatter of points defined by the projection of Σ_E on $q_2 = Q_2$. Thus, the SOS is an effective indicator of integrability and one which is easy to visualize as it is a two-dimensional plot.

To generate the SOS for our billiard, we will choose the section Σ to be the intersection of the constant energy hyper-surface $\Sigma_E : p^2 = E = 1$ and $\partial D : r = R(\phi)$, where $R(\phi)$ describes the boundary of our billiard. This surface $\Sigma = \Sigma_E \cap \partial D$ is parametrized simply by a coordinate on the boundary ∂D and its conjugate momentum. Note the important qualitative shift in the description of the motion, from continuous flow on phase space to discrete mapping on SOS. In general discrete maps don't need to have any structure of flow, and when compared to continuous flow of the same dimensionality can possess much higher degree of complexity. But because of the reduction of the map on the SOS from a Hamiltonian flow in a higher dimensional space, certain structures are inherited. One such important constraint is that because the mapping can be described by a canonical transformation generated by Hamilton's equations, it is *area preserving*. One possible choice for our SOS would be the arclength s measured from $\phi = 0$ and the tangential momentum $p_t = \sin \chi$, which are known as the Birkhoff coordinates [98]. But we will use instead of s , the polar angle ϕ and $\sin \chi$ for the momentum coordinate⁴.

The SOS for the circle billiard is shown in Fig. 2.23(a), and we observe that it's composed of straight horizontal lines, the *invariant curves*, indicating clearly the conservation of $p_\phi = R \sin \chi$, the angular momentum besides the energy, and hence integrability. The invariant curves are the intersections of the invariant tori with the section. For the circle, the associated mapping can be written down explicitly

$$\sin \chi_{n+1} = \sin \chi_n \quad (2.108)$$

$$\phi_{n+1} = \phi_n + 2 \cos^{-1}(\sin \chi_n) \quad (2.109)$$

At each bounce ϕ_n , the particle receives the same amount of "kick" from the boundary, determined by the conserved angle of incidence χ .

How do things look for an arbitrary shape ∂D ? Let's take another simple shape, formed by taking the circle apart along a diameter and pasting in straight sections, hence forming a *Bunimovich stadium*, which we used as a toy model in the previous section. It can be thought as a deformation of the circle, with deformation parameter $\epsilon = l/R$, where l is the length of the straight sections. For any ϵ , it is found

⁴With this choice we give up the area preservation but instead have a certain other *measure* conserved.

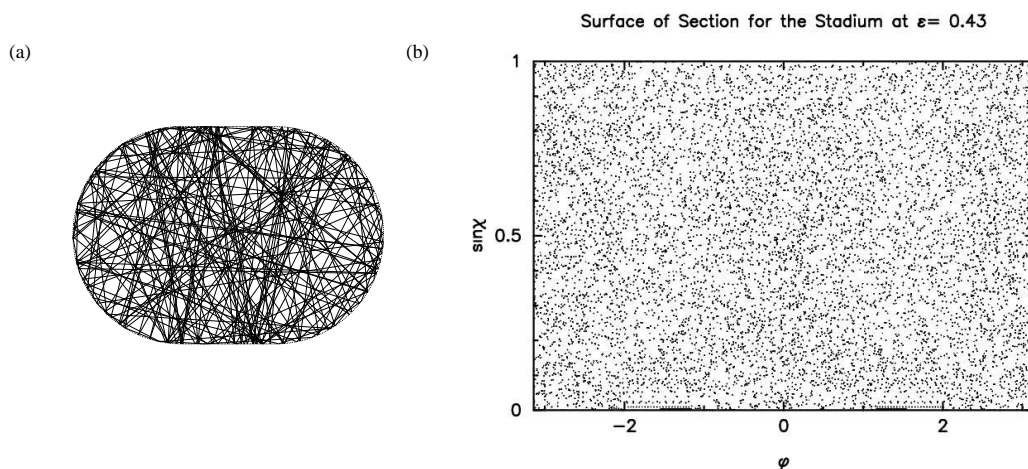


Figure 2.14: (a) A real-space trajectory and (b) the SOS plot of a stadium at a fractional deformation of $\epsilon = 0.43$.

that the SOS is composed of a two dimensional scatter of points. The stadium billiard is chaotic. One instance is shown in Fig. 2.14(b) and in Fig. 2.14(a) is shown the real-space motion for a trajectory started with arbitrary initial conditions. It can be shown that any initial condition, iterated enough number of times, visits all the available SOS area *uniformly*⁵. Let us now consider the Dirichlet problem Eq. (2.49) in the semi-classical limit. Our semi-classical ansatz assumes that there are N possible ray directions at each point of the covering space. But, from the SOS of the stadium billiard we find that each point in the phase space is uniformly covered, so that at each position q we have an isotropic distribution of ray directions ∇S , i.e. $N \rightarrow \infty$, as opposed to the circle where $N = 2$! This observation has lead Berry [99] to conjecture that the semi-classical eigenstates of chaotic systems would locally look like random superpositions of plane waves. In the case of quantum billiards, because of the condition Eq. (2.23), each plane wave component would have a random phase and direction, but the same wavevector k , hence we can write

$$\psi(\mathbf{r}) = \sum_n a_n \cos(\mathbf{k}_n \cdot \mathbf{r} + \xi_n) \quad (2.110)$$

The amplitudes a_n , phases ξ_n , and the directions are chosen to be random variables. Normalization requirement in the asymptotic limit $k \rightarrow \infty$ for a billiard of area A would yield

$$\lim_{N \rightarrow \infty} \frac{A}{2} \sum_{n=1}^N a_n^2 = 1 \quad (2.111)$$

which using central limit theorem would imply a Gaussian random distribution for the amplitudes a_n . Equivalently, because the Fourier transform of a Gaussian random variable is also Gaussian, a simple calculation would imply the Gaussian amplitude

⁵Such a system is called *strongly mixing*

distribution for the wavefunctions

$$P(|\psi|) = \sqrt{\frac{A}{2\pi}} \exp(-A|\psi|^2/2) \quad (2.112)$$

It turns out that a big proportion of all the eigenstates of the stadium in the semi-classical limit behaves this way. This argument finds its more precise expression in the theorems of Shnirelman [100], Zelditch [101] and Colin de Verdiere [102](SZCdV), which state that this is true for all semi-classical eigenstates *except a set of measure zero*. The italicized part of this statement might have remained an academic curiosity, were it not for Heller [103] who, motivated by unpublished work of McDonald [104] on a numerical study of stadium eigenstates, uncovered certain states displaying anomalous enhancement of intensity on apparently non-random patterns and devised an explanation. It turns out that the non-randomness is caused by certain invariant structures of the billiard map, which are a *set of measure zero* in the SOS generated by the particular boundary shape ∂D . This induces extra correlations between the “wavelets” $A_j \exp(ikS_j)$ on a random backdrop. These invariant structures are the *fixed points* or *periodic orbits* of the billiard map, and the associated enhancement in certain eigenstates is dubbed as “scarring”. We will come back to this phenomenon in Chapter 5. We should note in passing that even random wavefunctions based on random superposition of plane-waves display certain ridge patterns, and this is associated with the correlation between the “random wavelets” induced by merely the fact that each of them satisfies the Helmholtz equation by itself (but not the boundary condition). In other words, such ridge patterns would be the most random pattern one can get among the solutions of the Helmholtz equation.

The last two picks from the random pool of boundary shapes ∂D , are representatives of two extreme cases. But what then is the generic behavior? This is studied most suitably by starting with an integrable shape and deforming it smoothly. So far, the only integrable shape we know is the circular billiard. Are there others? It turns out that integrability is really not a common behavior. All the integrable shapes we know are actually separable systems, i.e. the boundary shapes coincide with constant coordinate curves of separable coordinate systems. However, integrability is a more general concept than separability⁶. Remembering that we used caustics of the circle to construct the complete solutions of Hamilton-Jacobi equation, and hence the asymptotic eigenstates, we might choose to ask which shapes have a caustic. This question has been answered partially by Poritski [105], who proved that if a *convex and smooth* billiard contains a smooth family of closed caustics then it is an ellipse. However, it’s still an open question whether *any integrable, smooth billiard is an ellipse*⁷. And furthermore, there is a large class of polygonal billiards, which are not smooth, some of which are known to be integrable and some are pseudo-integrable⁸.

⁶For instance, equilateral triangle billiard is not separable but integrable

⁷The related statement has come to be known as Birkhoff-Poritski conjecture.

⁸“Pseudo” refers merely to the fact that the topology of the covering space is no more a 2-torus, as it was in the case of circle and other integrable shapes in two dimensions, but has a more complicated topology.

We will begin our investigation of smoothly deformed shapes with the circle billiard, and consider a certain family of shapes called quadrupoles. Their boundary ∂D is described in polar coordinates

$$R(\phi) = R_0(1 + \epsilon \cos 2\phi) \quad (2.113)$$

which is symmetric with respect to reflections around X and Z axes. The surface of sections at four successive deformations starting from the circle, $\epsilon = 0$, are shown in Fig. 2.23. The gradual transition to chaos which unfolds as we deform from complete integrable limit is referred to as the KAM transition, named after Kolmogorov, Arnold and Moser, who investigated this scenario in a more general context of Hamiltonian systems. Note the coexistence of regular and chaotic regions in the SOS. Such a symbiosis in phase space is termed “mixed”, which covers the vast behavior from integrability to complete chaos.

2.8 The monodromy matrix and periodic orbits

As the transition to chaos ensues, a crucial role is played by the *periodic orbits*. In this section, we will introduce the concept of periodic orbits, and the linearized dynamics in their vicinity embodied by the monodromy matrix. We will also study the general properties of the monodromy matrix, which will be used at various stages of this thesis.

Periodic orbits are simply fixed points of the billiard map. Let us denote the SOS variables collectively by the vector $\boldsymbol{\xi} = \begin{pmatrix} q \\ p \end{pmatrix}$, where p is conjugate to q . The mapping can in general be described by

$$\boldsymbol{\xi}^{(n+1)} = \mathbf{M}(\boldsymbol{\xi}^{(n)}) \quad (2.114)$$

where \mathbf{M} is a non-linear (vector-)function. N^{th} iteration of the map will be denoted by \mathbf{M}^N , i.e. $\mathbf{M}^N(\boldsymbol{\xi}) \equiv \mathbf{M}(\mathbf{M}(\cdots \mathbf{M}(\boldsymbol{\xi}) \cdots))$. Then, if

$$\mathbf{M}^N(\boldsymbol{\xi}) = \boldsymbol{\xi} \quad (2.115)$$

then $\boldsymbol{\xi}$ is a fixed point of the map, and the orbit traced out in the configuration space is an N -bounce periodic orbit. Periodic orbits can be characterized further by their stability, which refers to the character of motion in its neighborhood. Let $\boldsymbol{\xi}_0 = \begin{pmatrix} q_0 \\ p_0 \end{pmatrix}$ be a fixed point, then one can Taylor expand the function \mathbf{M}^N to see how a nearby point $\boldsymbol{\xi}_0 + \delta\boldsymbol{\xi}$ moves in one period (of N bounces). Let this point be mapped to $\boldsymbol{\xi}_0 + \delta\tilde{\boldsymbol{\xi}}$ under \mathbf{M}^N

$$\mathbf{M}^N(\boldsymbol{\xi}_0 + \delta\boldsymbol{\xi}) = \boldsymbol{\xi}_0 + \delta\tilde{\boldsymbol{\xi}} = \mathbf{M}^N(\boldsymbol{\xi}_0) + \frac{\partial \mathbf{M}^N}{\partial \boldsymbol{\xi}} \delta\boldsymbol{\xi} + \cdots \quad (2.116)$$

we hereby get the *tangent map* $\delta\boldsymbol{\xi} \rightarrow \delta\tilde{\boldsymbol{\xi}}$, the (linear) map of infinitesimal deviations from the fixed point

$$\delta\tilde{\boldsymbol{\xi}} = M\delta\boldsymbol{\xi} \quad (2.117)$$

Here M is the two-by-two matrix $M_{ij} = \partial(\mathbf{M}^N)_i / \partial(\boldsymbol{\xi})_j$ and is called as the *monodromy matrix*. We implicitly assume M can be expressed in terms of matrix multiplication of N linearized bounce maps.

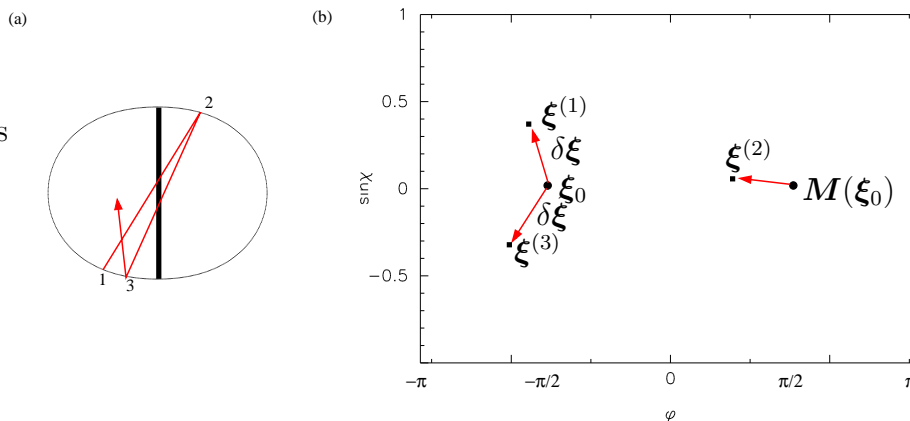


Figure 2.15: (a) The bouncing-ball (BB) periodic orbit (corresponding to fixed point $\boldsymbol{\xi}^{(0)} = (-\pi/2, 0)$) is the solid black line. The red trajectory drawn in red is a typical trajectory in the vicinity of the BB orbit. (b) The action of the exact section map \mathbf{M} and the monodromy operator M . A point $\boldsymbol{\xi}^{(1)} = \boldsymbol{\xi}_0 + \delta\tilde{\boldsymbol{\xi}}$ is mapped to $\boldsymbol{\xi}^{(2)} = \mathbf{M}(\boldsymbol{\xi}^{(1)})$, and $\boldsymbol{\xi}^{(3)} = \mathbf{M}^2(\boldsymbol{\xi}^{(1)})$. Here, $\boldsymbol{\xi}^{(3)}$ is back to the neighborhood of the original fixed point $\boldsymbol{\xi}^{(0)}$. The action of the monodromy matrix M for the two-bounce orbit is hence $\delta\tilde{\boldsymbol{\xi}} = M\delta\tilde{\boldsymbol{\xi}}$.

The motion generated in the vicinity of the fixed point (q_0, p_0) by the action of the monodromy matrix can be categorized by analyzing its eigen-solutions. We summarize here some of the salient features of the monodromy matrix.

Let $\mathbf{v}_{1,2}$ and $\lambda_{1,2}$ be the eigenvectors and eigenvalues of the monodromy matrix M

$$M\mathbf{v}_{1,2} = \lambda_{1,2}\mathbf{v}_{1,2} \quad (2.118)$$

Because the map is area-preserving and the monodromy matrix is nothing but the Jacobian matrix of the transformation from one point of the phase space to another,

$$\det M = 1 \quad (2.119)$$

This tells us that $\lambda_1\lambda_2 = 1$. Three possible scenarios are

- *Stable motion:* $\lambda_1 = \lambda_2^* = e^{i\varphi}$ The realness of the monodromy matrix then implies that $\mathbf{v}_1 = \mathbf{v}_2^* = \begin{pmatrix} a_1 \\ a_2 \end{pmatrix}$. The resulting motion can best be visualized by applying the monodromy matrix repeatedly to an arbitrary initial condition $\mathbf{V}_0 = \begin{pmatrix} \delta Q_0 \\ \delta P_0 \end{pmatrix} = c\mathbf{v} + c^*\mathbf{v}^*$ and calculating the position $\mathbf{V}_\nu = \begin{pmatrix} \delta Q_\nu \\ \delta P_\nu \end{pmatrix}$ after ν traversals of the periodic orbit

$$\mathbf{V}_\nu = M^\nu \mathbf{V} = ce^{i\nu\varphi}\mathbf{v} + c^*e^{-i\nu\varphi}\mathbf{v}^* \quad (2.120)$$

or expressed explicitly

$$\begin{pmatrix} \delta Q_\nu \\ \delta P_\nu \end{pmatrix} = \begin{pmatrix} \rho_1 \cos(\nu\varphi + \zeta_1) \\ \rho_2 \cos(\nu\varphi + \zeta_2) \end{pmatrix} \quad (2.121)$$

where $ca_{1,2} = \frac{1}{2}\rho_{1,2}e^{i\zeta_{1,2}}$. In the SOS, this represents a motion on invariant curves which are rotated ellipses around the fixed point (q_0, p_0) . Note that, when $\varphi/2\pi$ is irrational, the invariant ellipse is covered uniformly in the limit $\nu \rightarrow \infty$, but otherwise the set of points visited on the ellipse is a finite set. From our perspective, the most important property of a stable fixed point is that the resulting motion is *bounded* i.e. that an initial density of orbits started in the vicinity of the periodic orbit will return periodically to the same neighborhood. The simplest example of such a periodic orbit is the 2-bounce a.k.a. *bouncing ball* orbit on the short diameter $\phi = \pm\pi/2, \sin\chi = 0$. In Fig. 2.16, we plot the stable manifolds of the bouncing ball fixed point of an elliptic boundary⁹.

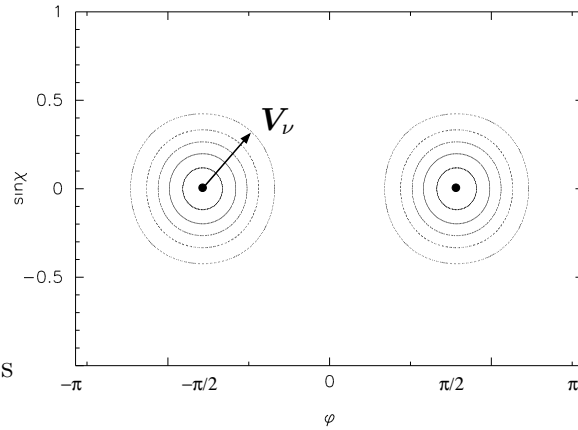


Figure 2.16: An actual segment of the SOS of an elliptic billiard of fractional deformation $\epsilon = 0.12$, around the stable bouncing ball orbit fixed points.

- *Unstable motion:* $\lambda_1 = 1/\lambda_2 = \pm e^\varphi > 1$ (Let's assume $|\lambda_1| > |\lambda_2|$ and hence that $\varphi > 0$). In this case

$$\begin{pmatrix} \delta Q_\nu \\ \delta P_\nu \end{pmatrix} = \begin{pmatrix} \rho_1 \cosh(\nu\varphi + \zeta_1) \\ \rho_2 \cosh(\nu\varphi + \zeta_2) \end{pmatrix} \quad (2.122)$$

which describes again invariant curves which are conic sections, but this time hyperbolae. Depending on the sign of λ_1 , the motion takes place either on one branch of the hyperbola ($\lambda > 0$) or is *reflection hyperbolic*, i.e. on each successive iteration of the periodic orbit, changes branch (see Fig. 2.17). The resulting motion is *exponentially unstable*, in the sense that any two initial conditions separated by an infinitesimal vector $\delta\xi$ in the vicinity of the fixed point

⁹This orbit exists in any convex billiard and lies along the longest and shortest cords which can be drawn into a given shape. The longer one is unstable and the shorter one is stable.

will be separated by an exponential distance $\propto e^{\nu\varphi}\delta\xi$ in the long time limit. Here φ is called the *Lyapunov exponent* and such a behavior is one of the ingredients of *chaotic dynamics*. One should however remember that our linearization holds only in the vicinity of the fixed point, and as such, our approximation degrades exponentially fast in time. It is clear that exponential behavior cannot be sustained forever because the system is bounded. The resulting complicated motion will be characterized further below.

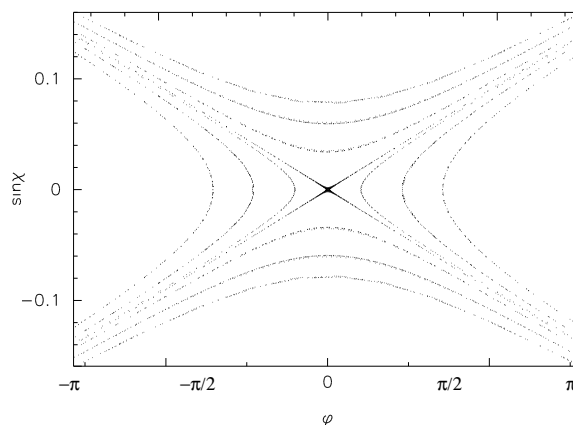


Figure 2.17: An actual segment of the SOS of an elliptic billiard of fractional deformation $\epsilon = 0.12$, around the unstable bouncing ball orbit fixed point at $\phi = 0, \sin \chi = 0$.

- *Marginally stable motion:* $\lambda_1 = \lambda_2 = \pm 1$. The corresponding invariant curves are straight lines in the SOS. Note again that this is a local description, and should break down unless there is a special symmetry of the system, rendering it global. The best example is the circular billiard, where we have found that the invariant curves in the SOS are the straight lines $p = \sin \chi = \text{const.}$, and that this behavior is global thanks to the linearity of the exact map Eq. (2.109). As in the case of the stable elliptic manifolds, as the motion is confined to a one-dimensional invariant curve which is retraced in an infinitely recurring motion, there can be intrinsically two types of such motion: periodic and quasi-periodic, that we already encountered before. In the periodic case, given an arbitrary initial point on the invariant curve, a finite number of points on it are visited. Owing to the rotational symmetry of the circle, there is an infinite family of such periodic orbits, and thus such a periodic orbit is *not isolated*. If we take a close look at the circle map Eq. (2.109), periodicity obviously depends on the kick-strength $p = \sin \chi$ and the condition is simply that the kick is a rational multiple of 2π

$$\delta\phi = 2 \cos^{-1}(\sin \chi) = 2\pi w \quad (2.123)$$

Here, w is nothing but the winding number Eq. (2.103), the ratio of radial to angular frequency, and is a rational number for a periodic orbit. On the other hand, when w is irrational, then the angular and radial rotation frequencies are incommensurate, so that the invariant curve is visited uniformly in the long

time limit. Of course, such quasi-periodic orbits are infinitely dense as are the irrational numbers on the real line, and thus occur infinitely more often than periodic orbits. That's why it's appropriate to say that the periodic orbits are of *measure zero* in the phase space.

The latter type of motion, embodied by the circle map, lives on the narrow borderland between the stable and unstable cases. And this is where we will begin our description of the mixed phase space, by slowly deforming the circle.

2.9 KAM Transition – from integrability to Chaos

What we will provide in this section is a largely qualitative picture of transition to chaos, by looking at a particular instance of Hamiltonian system, a billiard. The general theory is based on the formalism that has been suggested originally by Kolmogorov [106], and put into a rigorous framework by Arnold [107] and Moser [108].

What becomes of the invariant curves of the circle map Eq. (2.109), which are straight lines, when the boundary is deformed as prescribed by Eq. (2.113)? Let us assume that it deforms continuously into a curve γ , parametrized by ξ

$$p(\xi) = p_0 + v(\xi; \epsilon) \quad (2.124)$$

$$q(\xi) = \xi + u(\xi; \epsilon) \quad (2.125)$$

where $v(\xi; \epsilon)$ and $u(\xi; \epsilon)$ have to be periodic in ξ , and vanish in the limit $\epsilon \rightarrow 0$ so that the invariant curves are reduced to those of the circle. Now, consider an iteration of the circle-map Eq. (2.109), using our notation here, $q \rightarrow q + 2\pi w$. Eq. (2.124) would give us the next momentum step as

$$p(q + 2\pi w) = p(q) + v(q) \quad (2.126)$$

Because p and v have to be periodic in q , we should be able to expand them in a discrete Fourier series

$$p(q) = \sum a_k e^{ikq}, \quad v(q) = \sum b_k e^{ikq} \quad (2.127)$$

In order to find the curve γ we need to find the coefficients a_k from the SOS map Eq. (2.126)

$$a_k = -\frac{b_k}{1 - e^{ik2\pi w}} \quad (2.128)$$

The coefficients a_k do not approach zero as fast as b_k and for w rational become undefined. The orbits with rational winding numbers w are the periodic orbits of the circle. Hence on the entire winding number interval of the circle $-1 < w < 1$, there are so called “resonance” regions on and close to the rational numbers, where the perturbation theory would break down. This argument is just scratching the surface of the underlying problem, which in canonical perturbation theory is called

the *problem of small denominators*. It was pointed out originally by Poincaré, who developed the canonical perturbation theory to get an insight into the three-body problem [109]. KAM theorem asserts that sufficiently far away from such resonances and for low enough deformations, certain tori with irrational winding numbers do indeed persist. This can be seen in the SOS of the lowest deformation: the majority of the invariant curves are intact but distorted from their $\epsilon = 0$ shapes.

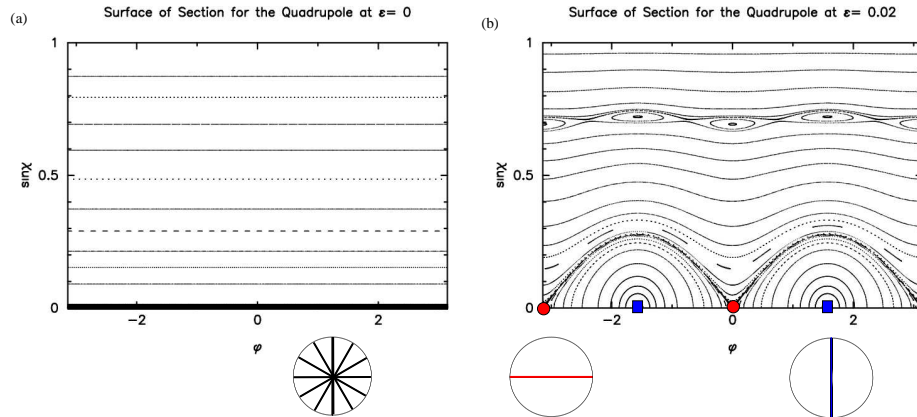


Figure 2.18: The bifurcation of the two-bounce orbit of the circle. (a) The original two-bounce orbit comes in an infinite family, some of which are shown in the trajectory plot below the section plot. The associated invariant curve is the thick black line in the SOS. (b) At a deformation of $\epsilon = 0.02$, one sees the two isolated two-bounce orbits. Drawn in blue is the stable fixed points and in red, the unstable partner.

As the KAM perturbation theory breaks down for rational tori, a legitimate question to ask is what the fate of the corresponding invariant curves is. This question is answered by the Poincaré-Birkhoff theorem. It states that, when the circle map Eq. (2.109) is perturbed to

$$p_{n+1} = p_n + \epsilon f(q_n, p_n) \quad (2.129)$$

$$q_{n+1} = q_n + 2 \cos^{-1} p + \epsilon f(q_n, p_n) \quad (2.130)$$

by the deformation, then for each unperturbed fixed point with winding number $w = \frac{r}{s} = \frac{1}{\pi} \cos^{-1} p$ which is a fixed point of s iterations of the map, $2s$ fixed points remain after the perturbation. The proof is relatively simple and can be found in Ref. [31], among others. The theorem is best illustrated by following the *bifurcation* of the infinite family of two-bounce orbits of the circle. According to the Poincaré-Birkhoff theorem, they should be replaced by four fixed points. Already at the lowest deformation, the infinite family of degenerate two-bounce orbits are replaced by two sets of two-bounce orbits¹⁰. One set is along the semi-minor axis of the

¹⁰One can show that for a convex billiard there is either two or an infinite number (only for the case of circle) of two-bounce orbits

quadrupole, with fixed points at $(\pm\frac{\pi}{2}, 0)$ on the SOS. To understand the type of motion involved, one can linearize the map around this fixed point as we outlined in the previous section. It turns out that the associated motion is stable and thus should have elliptic invariant manifolds surrounding it. These *resonance islands* are seen clearly in Fig. 2.18. It's now clear why straightforward perturbation theory would break down: one cannot even define a winding number in the usual sense for the newly generated periodic orbits on the elliptic invariant curves. The divergence of the perturbation series has thus a physical content, and should be interpreted as a signal that there is a fundamental change in topology of the orbits.

The other set of fixed points are located at $(0, 0)$ and $(\pi, 0)$, and these are unstable. The approximate curve joining these two latter points separates librational motion on the elliptic invariant curves corresponding to the stable two-bounce orbit from the rotational motion in the upper SOS, and therefore is called a *separatrix*, quite like its counterpart in the pendulum. However, the separatrix of a near-integrable system is very different in character from that of an integrable system. Because the circle does not possess such a structure, we turn to another integrable system, the elliptic billiard, to highlight the difference.

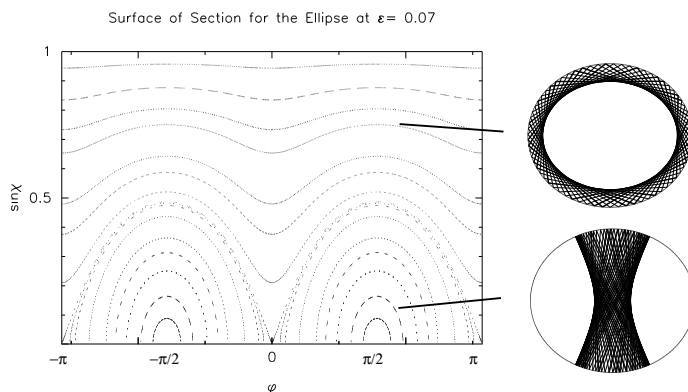


Figure 2.19: The SOS of ellipse at $\epsilon = 0.07$ deformation. Two representative orbits belonging to a rotational, whispering-gallery-like motion, and of librational, bouncing-ball-like motion.

The SOS of the ellipse is shown in Fig. 2.19. The ellipse displays rotational whispering-gallery like motion in the upper SOS, and stable librational motion around the fixed points $(\pm\frac{\pi}{2}, 0)$, enclosed by a sequence of elliptic invariant curves. As one goes out from these stable fixed points, one encounters the secondary fixed points¹¹. The frequency of motion on these secondary fixed points, number of bounces taken before the orbit closes on itself, is a multiple of the frequency of the primary orbit, two. As we reach the outskirts of the librational motion, the frequency of the secondary fixed points tends to infinity. Exactly *on the separatrix*, it is infinite. Points $Q_1 : (0, 0)$ and $Q_2 : (\pi, 0)$ on the separatrix can be singled out: they are fixed points of the exact two-iterate ellipse map M^2 .

¹¹These come in an infinite family owing to the integrability of the ellipse.

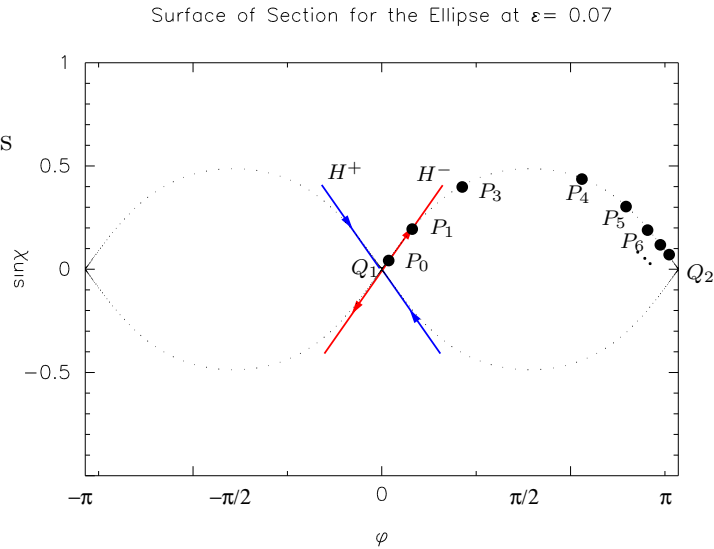


Figure 2.20: The separatrices of the ellipse at a deformation of $\epsilon = 0.07$. The blue axes represent the *linearized* stable manifolds H_- and the unstable manifolds H_+ , which is placed on the actual, non-linear manifolds of the fixed points Q_1 . The points P_n are obtained from the iterations of the two-bounce map M^2 on an initial point P_0 on the unstable manifold.

Consider now the four arms of the separatrix close to Q_1 , designated by H^+ and H^- , as shown in Fig. 2.20. If we pick up a point P_0^- on H^- and iterate it with the two-bounce forward map M^2 , such that $P_{i+1}^- = M^2(P_i^-)$, the successive iterates P_i^- move away from Q_1 towards Q_2 . At first P_i^- move exponentially fast away from Q_1 , as expected from linearized map, but as $i \rightarrow \infty$, the distance between successive iterations becomes smaller (exponentially), and P_i^- approaches Q_2 only *asymptotically* (i.e. never actually reaches it). This is the behavior which gives rise to the infinite period. The manifold H^- is called the *unstable manifold* of the fixed point at Q_1 . Any point P_0^+ started on H^+ , the *stable manifold*, on the other hand approaches Q_1 with the distance between successive iterates diminishing exponentially. From these definitions, it's clear that the unstable manifold H_- is the stable manifold of Q_2 and vice versa.

Now let's go back to a near-integrable deformation of the quadruple at $\epsilon = 0.03$. A closer look at the separatrix region entails a much more complicated behavior than that of the ellipse separatrix. In Fig. 2.21 is shown a magnified view of the vicinity of the separatrix, and one can notice the thin layer of chaotic region (see Fig. 2.21) embedded between two invariant curves. This region is generated by the intersection of a single separatrix trajectory (and its time-reversed partner) with the SOS.

Let's proceed as in the ellipse and construct the invariant manifolds passing through the fixed point Q_1 . Again, the linearized map close to Q_1 gives the linear stable and unstable manifolds H^\pm , which are locally like straight lines crossing each other at the fixed point Q_1 . However, as we iterate a point P_0^- on the unsta-

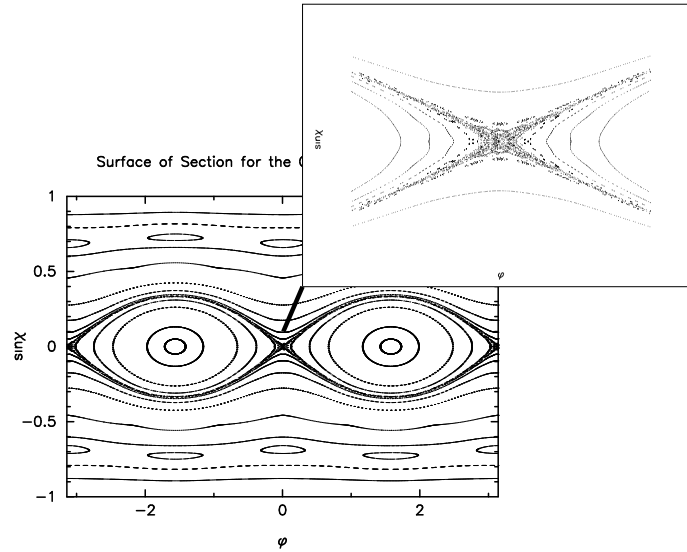


Figure 2.21: A zoom in to the separatrix region of the quadrupole 2-bounce orbit at a deformation $\epsilon = 0.03$. Note that the chaotic layer is delimited by KAM curves on both sides.

ble manifold H^- , the non-linearity of the exact map begins to show its presence. Instead of moving on discrete positions of a well-defined curve, the iterates begin to get scattered as the other fixed point is approached. To get an idea of the complicated structure of the underlying invariant manifold H^- , one has to iterate not one point but a continuous distribution of points, which initially lie on the linear section of H^- . This simulation is shown in Fig. 2.22. The invariant curve H^- starts out very similar to that of the separatrix curve of the ellipse, but instead of joining smoothly into the stable manifold H^+ of Q_2 , it begins to oscillate wildly around it, stretching and folding, intersecting it at what are the *homoclinic points*. Let's call this intersection points X_i , starting with the primary intersection at X_0 . Notice that the points X_i do move on a more regular curve, simply because they belong both to H^- of Q_1 and H^+ of Q_2 . As $i \rightarrow \infty$, X_i become more and more closely spaced. As a consequence, the loops between X_i stretch more and more. This is simply because the areas enclosed by successive intersection of the invariant curves (hatched regions in the figure) are mapped into each other, and the mapping is area preserving. This complicated tangle is the origin of the scatter generated by the iteration of a single point P_0 in Fig. 2.22 (a). The proof that this stretching and folding leads to chaotic motion near an unstable fixed point was given by Smale [110] using a simplified map reflecting the local non-linear behavior, the so called "horseshoe map". This chaotic behavior, defined above as an exponential instability, is understood easily. Take two points separated by a small distance within the tangle. Depending on what loop and which of the eigencurves (H^\pm) these points fall, they are mapped into widely different areas of the tangle. However, because the area of covered by the chaotic layer is small, the deviations are bounded from above, and the exponential behavior

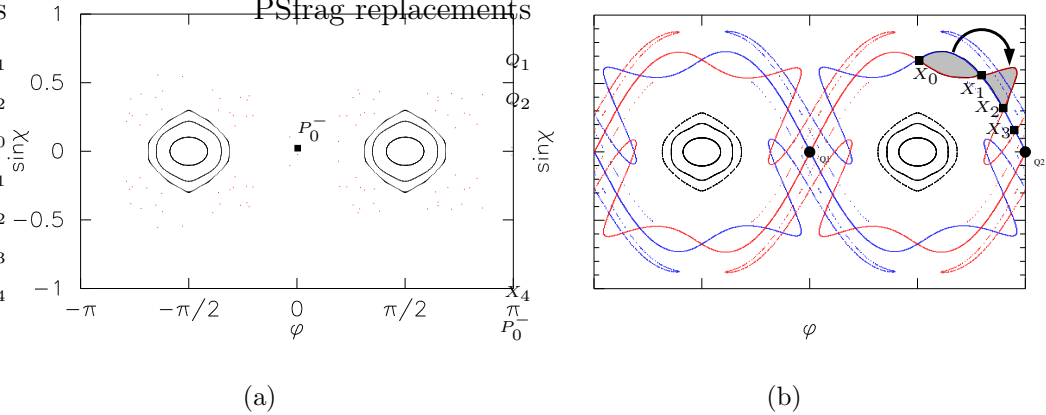


Figure 2.22: (a) A 50-bounce simulation of an initial condition P_0^- close to the fixed point $Q_1 : (0, 0)$. The subsequent intersections of motion with the SOS fail to fall on a continuous curve, which is a signature of chaotic motion (b) An initial ensemble of starting conditions (6000 points, gaussian distributed around $(0, 0)$) are propagated forward and backward to generate the homoclinic tangle. The red curve forms the unstable manifold of the fixed point $Q_1 : (0, 0)$ (and the stable manifold of $Q_2 : (\pi, 0)$), and the blue curve forms the stable manifold (unstable manifold of Q_2). Note that the area within the loops are conserved (hatched region) because of the property of Hamiltonian flow; thus when the intersections lie closer together the loops undergo wider excursions.

can only last upto a saturation distance.

The actual complication of a near-integrable or a mixed phase space system is that the behavior described above for a specific fixed point takes place on all scales. Since fixed points correspond to rational tori, there are as many fixed points of the circle-map as there are rational numbers in the winding number interval $-1 < w < 1$, which are infinitely many. Each of these fixed points disintegrates into a stable fixed point and its unstable partner after the deformation. An island chain is formed separated from each other and the intact KAM curves by a narrow chaotic separatrix layer emanating from the unstable fixed points. Furthermore, around each of these primary fixed points there are secondary fixed points with their unstable counterparts, and each of these displays the same behavior, and supports higher order fixed points around itself. We have to realize that this self-similar behavior can only be consistent if the resonance island sizes become smaller and smaller for winding numbers $w = p/q$ with larger denominators q , and for higher order fixed points as the rotation number increases. That's why an infinity of such resonance islands corresponding to high rotation numbers are not resolved at the scale we are plotting our SOS.

The transition to global chaos takes place as resonance islands and the separatrix layers grow in size and destroy the remaining KAM tori corresponding to irrational winding numbers enveloping them. In that sense, KAM tori are the last remnants of integrability which limits the unbounded phase space flow on the energy shell. The

earliest procedure to determine the transition to global chaos quantitatively, has been advanced by Chirikov for the standard map¹², and is known as the *overlap criterion* [31]. It postulates that, the last KAM curve between two primary resonances are destroyed, when the sum of the half widths of two island separatrices formed by the resonances, equals the distance between the resonances. The practicality of this approach stems from the assumption that the two resonances are independent of each other. Intuitively, the last KAM curve to be destroyed is expected to have the most irrational number as its winding number, i.e. the irrational number in the interval $[0, 1]$ which is hardest to approach through rational estimates. This turns out to be the inverse golden mean

$$|w_g| = \frac{\sqrt{5} - 1}{2} \approx 0.61803398874989 \dots \quad (2.131)$$

which corresponds to $|\sin \chi| \approx 0.362$. The golden mean has been found to be, within numerical error, the winding number associated with the last KAM curve to be destroyed for the standard map [111]. This however, is a good criterion for only certain simpler maps, for which local approximation reduce to the standard map with approximately uniform non-linearity parameter.

For billiard systems, the matters are more complicated, the basic reason being that certain assumptions of the KAM theorem are violated close to $\sin \chi \approx 1$, in the extreme whispering gallery limit. As a consequence, our discussion above describes well what is happening in a significant portion of the SOS, except a small neighborhood of $\sin \chi = 1$. Lazutkin's work [30] extends and complements the KAM scenario to convex billiard systems. He proved, using asymptotic techniques, that if ∂D is strictly convex (curvature never vanishes) with sufficiently smooth boundary, there exists a positive measure set of the phase space that is foliated by invariant tori and that this set accumulates near the boundary ∂D (i.e. $\sin \chi \approx 1$). Just as an illustration of the complications of the calculation involved, Lazutkin's proof required 553 continuous derivatives of $r(\phi)$ for his proof; later it was shown that six are enough [112]. Inspecting the deformations as high as $\epsilon = 0.11$, in Fig. 2.23(c), one finds in fact that there are invariant curves which are unbroken in the extreme whispering gallery limit, although the most irrational curves around $\sin \chi \approx 0.36$ are long dissolved.

Putting the complicated mathematics aside, the remarkable resilience of the extreme whispering gallery orbits can intuitively be understood. For high $\sin \chi$, the rays undergo a grazing motion, skipping along the boundary, and as $\sin \chi \rightarrow 1$, the boundary itself can be thought of as a periodic orbit of the map. It turns out that this periodic orbit is "effectively" stable in the momentum direction. Our usual tools of linearization cannot be applied here, because the effective map of a deformed billiard has a branch-point singularity at $\sin \chi = 1$. The expression of this map, which

¹²Standard map describes physically the SOS map of a "kicked rotator", a rigid rotor which is imparted delta function impulses periodically in time

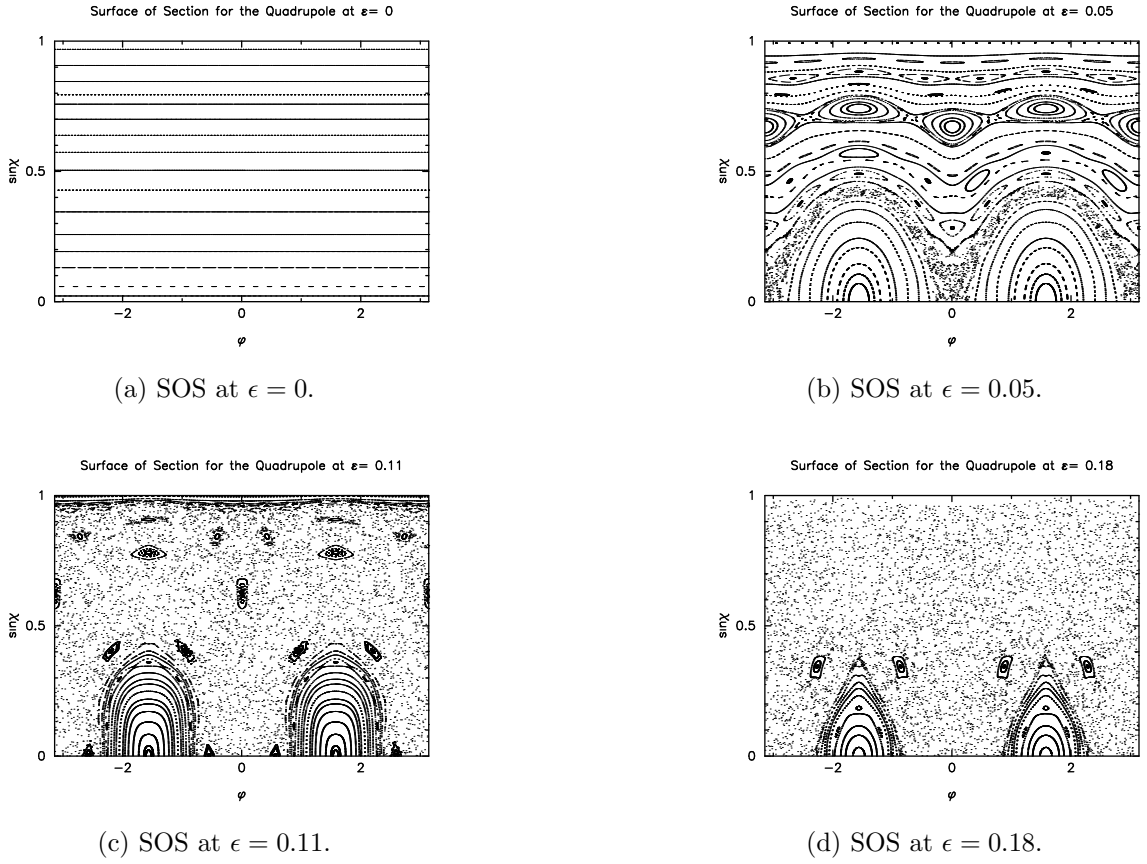


Figure 2.23: The SOS of a quadrupole at fractional deformations $\epsilon = 0, 0.05, 0.11, 0.18$. The closed curves and curves crossing the SOS represent types of regular motion, the regions of scattered points represent chaotic portions of phase space. A single trajectory in this “chaotic component” will explore the entire chaotic region. With increasing deformation the chaotic component of the SOS (scattered points) grows with respect to regular components. Note in (b) the separatrix region where the transition to chaotic motion sets in first

is valid for $\sin \chi \approx 1$ is given in [45].

$$p_{n+1} = p_n - \frac{2}{3\varrho'}(1 - p_n^2)^{3/2} \quad (2.132)$$

$$s_{n+1} = s_n + 2 \cos^{-1} p_n - 2(1 - \varrho)p_n(1 - p_n^2)^{1/2} \quad (2.133)$$

Here $p = \sin \chi$ and s is the arclength along the boundary measured from $\phi = 0$ and is considered to vary in the interval $(-\infty, \infty)$; $\varrho = \varrho(s)$ is the radius of curvature of the boundary at point s and is a periodic function thereof. The crucial observation is that the non-linearity in the kick strength vanishes as $(1 - p_n^2)^{3/2}$. This explains why Lazutkin tori persist longer than regular KAM tori: the effective non-linearity felt in the lower portions of the SOS is higher, and consequently the KAM transition

unfolds faster there.

As we move on to higher deformations, beyond $\epsilon \approx 0.18$, the golden mean curve breaks too, and the SOS is composed of two primary resonance islands, one corresponding to the bouncing ball orbit, and the other to the bowtie orbit. The complement is a simply-connected domain of chaos. Any initial condition in this region of SOS will come arbitrarily close to any other point of this region, given enough time. Beyond $\epsilon = 0.2$ the boundary loses its convexity, but still we don't end up with a uniform chaos as in a stadium.

2.10 Semiclassics in a mixed phase space

The EBK quantization method introduced in Section 2.4 relies heavily on the foliation of the entire phase space by invariant tori. The KAM scenario described above however shows that even an infinitesimal deviation from integrability, exemplified by a quadrupolar family of ϵ -deformations from a circular billiard, disrupts this continuous foliation at all scales. Existence of unbroken KAM tori for certain subregions of the constant energy hypersurface leads to the question whether we can construct an associated set of eigenstates for the quantum billiard. In this section, we would like to give a flavor of techniques falling under the first category within the classification scheme of Section 2.5.

This general question has been addressed by Lazutkin in Ref. [30], where it's shown that asymptotic eigenfunctions can be constructed which satisfy the Helmholtz equation Eq. (2.49) for the quantum billiard with an error of $O(k^{-\alpha})$, $0 < \alpha < 1$. Such asymptotic states (ψ, k) for which

$$(\nabla^2 + k^2)\psi(q) = O(k^{-\alpha}) \quad (2.134)$$

were discussed by introduced by Arnol'd [113]. The modes associated with the unbroken Lazutkin tori, the extreme whispering gallery modes, can be calculated using various asymptotic approaches. Each of them relies on a local analysis of the problem (in the configuration space), which yields "replacement tori" to quantize on. We will briefly sketch some of these methods, which already found their way into textbooks and monographs [66], to demonstrate their power and shortcomings:

1. Ray method "in the small": Here one replaces the ray dynamics in the billiard close to the boundary by a first approximation to get a closed congruence of rays i.e. a new torus. The mapping Eq. (2.132) can be rewritten in terms of the small grazing angle $\epsilon = \cos \chi$, and the ray motion can be shown to be bounded from below¹³ for a sufficiently small ϵ . As a result, it's possible to construct a

¹³We mentioned before that the prescribed motion is "effectively stable", the quotes stemming from the fact that the map cannot be linearized around a fixed point to talk about stability in the conventional sense. It however possible to show the boundedness of motion in an asymptotic sense [66]

caustic, which is given by

$$n(s) = \frac{1}{2}\varrho^{1/3}(s)\kappa^2 + O(\kappa^4) \quad (2.135)$$

where $n(s)$ is the normal distance of the caustic from the boundary at position s , $\varrho(s)$ is the curvature of the boundary, and κ is an appropriately chosen small parameter. From the considerations very similar to circle quantization, this allows us to construct approximate tori and proceed with the quantization. Analogous results have been found independently by Robnik and Berry [42] and Nöckel and Stone [3], who derived the corresponding invariant curves in the SOS, given by

$$\sin \chi(\phi) = \sqrt{1 - (1 - \sigma^2)\varrho^{-\frac{3}{2}}(\phi)} \quad (2.136)$$

Nöckel and Stone [3, 114] showed the validity of this invariant curve to hold in an adiabatic sense beyond the Lazutkin region $\sin \chi \approx 1$, and used it to derive a diffusion model. This idea was used to predict a universal behavior for resonance lifetimes and directionality for dielectric KAM billiards.

2. Parabolic Equation approximation: The idea here is to exploit the proximity of the caustic of the extreme whispering gallery orbits to the boundary. From Section 2.4, we know that the eigenfunctions are concentrated in a region between the boundary and the caustic, whose thickness can be inferred to be proportional to $k^{-2/3}$. In the semiclassical limit $k \rightarrow \infty$, this “boundary layer” is extremely narrow, beyond which the field drops to zero. Hence, it makes sense to rewrite the Helmholtz equation Eq. (2.49) in the “local coordinates” (s, n) , which becomes

$$\mathcal{L}\psi(s, n) = 0 \quad (2.137)$$

and the ansatz

$$\psi(s, n) = A(s, n)e^{iks} \quad (2.138)$$

is introduced, which exploits the fact that the Eikonal is approximately equal to the boundary length s , when the boundary layer is very thin. The fast variation of $\psi(s, n)$ along n can then be utilized by boundary layer technique to decouple the degrees of freedom. The advantage of this asymptotic expansion with respect to ray method in the small is that the modes are well-defined over the whole the domain, and the caustic singularity is avoided. A further advantage is that a systematic perturbation expansion can be carried out and higher order corrections calculated, if desired. However, the calculations become impractically cumbersome at higher orders.

3. Etalon method : Probably, a more intuitive name for this method would be “deformation method”. The aim is to choose a model problem which can be exactly solved, for instance by separation of variables, whose ray singularities have the same topology as that of the original problem. Then, the asymptotic structure of the already known uniform asymptotic expansion of

the model problem is utilized in such a way that the coefficients are replaced by functions of coordinates. The simplification is that those coefficients turn out to be polynomials, which can be determined by imposing the boundary conditions. For example, the singularities of a ray field is simply the caustic in the billiard problem. From KAM scenario we know that for the deformed quadrupole, the KAM invariant curves, and in particular the Lazutkin curves, preserve their topology with respect to the integrable circle. Thus for the low-deformation quadrupoles, circular billiard would serve as the model problem, and known (uniform) asymptotic expansions of Bessel functions can be used to get an etalon expansion. The results of this construction for the whispering gallery modes of arbitrarily deformed smooth, convex billiards can be found in Ref. [115].

As mentioned before, each of the methods above relies implicitly on the existence of a family of invariant curves. KAM scenario however includes a dense set of resonance gaps, which manifest themselves in the formation of resonance islands with its elliptic manifold around stable fixed points. The motion as we found is regular close to these fixed points. As a prototypical example, consider the stable bouncing ball motion along the short diameter of the deformed quadrupole. We can linearize the motion along the diameter and consider the dynamics of the deviations $(s, n(s))$, where s measures the distance travelled along the diameter and n denotes the transverse deviation (see Fig. 2.24).

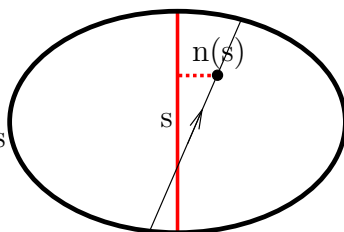


Figure 2.24: Local coordinate system for the bouncing-ball periodic orbit.

In the SOS, $n(s = md)\delta\phi_m$ and $dn/ds \propto \delta \sin \chi_m$ where $s \in (-\infty, \infty)$. Note that the motion is in straight lines between the bounces so that $n(s) = \alpha_m s + \beta_m$ when $md < s < (m+1)d$. It's thus ideally suited to write down the semi-classical ansatz in the coordinates (s, n) i.e. $\psi(s, n) = A(s, n) \exp(ikS(s, n))$. We are assured from the existence of invariant elliptic manifolds (which are invariant under the map M^2), that there will be a Lagrangian manifold providing us with the necessary quantization conditions. On the other hand, if we consider the problem in the extreme vicinity of the fixed point, where the section of the boundary is approximately parabolic, we realize that this is nothing but the Fabry-Perot resonator where Fox-Li theory [76] predicts that the eigenfunctions are approximately given by

$$\psi_{lm}(s, n) = A_{lm}(s, n) \exp \left[ik_{lm} \left(s + \frac{1}{a_{lm} + ib_{lm}} n^2 \right) \right] \quad (2.139)$$

for a stable resonator. Here a_{lm}, b_{lm} are real constants. This implies that the action, given by

$$S(s, n) = s + \frac{1}{a_{lm} + ib_{lm}} n^2 \quad (2.140)$$

is in general complex valued and that the rays live in a complex phase space. This is an instance of a general phenomenon; obviously any configuration leading to an (exponential) localization of waves would lead to complex rays. This seemingly contradictory result can be put to good use, and in fact an extended semiclassical theory including complex rays has been developed over the past two decades [85]. But tracing of rays in a complex phase space is complicated by the existence of multiple possible paths due to stokes surfaces, and the associated techniques have been more effective in initial value problems (beam propagation). It's therefore desirable to remain in the real phase space when treating boundary value problems. A technique based on parabolic equation approximation to do this effectively is described in Chapter 4.1.

2.11 Quantum Poincaré-SOS

All the techniques described so far replace the invariant curves (corresponding to Lazutkin curves and elliptic manifolds of stable fixed points) with a local approximation. A major shortcoming of these approaches is that this local replacement is assumed to be globally valid. For the stable fixed points for instance, the associated stable island is assumed to cover all the available phase space (which for the bouncing ball mode of the quadrupole for example, is geometrically not possible anyway). To what extent can we trust the so-constructed approximations then? It's clear the reliability argument have to be associated with the support of the modes *in the phase space*, not in the configuration space, because the limits to our manifold replacement is set by the size of the island, which lives in the SOS. Before we can do this, we have to learn how to cast the calculated modes onto the SOS. The present section outlines this procedure.

To begin with, “momentum content” of a mode $\psi(q)$ amounts to gauging the amount of $\mathbf{p} = \nabla S$, which can conveniently done by projecting the mode on states known to have a given momentum, like

$$\langle q|p\rangle = \frac{1}{\sqrt{2\pi}} e^{ik\mathbf{p}\cdot\mathbf{q}} \quad (2.141)$$

for which $(\nabla S)^2 = |p|^2 = 1$ and hence $\mathbf{p} = (\cos \alpha, \sin \alpha)$. Using Dirac's bra-ket notation,

$$\langle \mathbf{p}|\psi\rangle = \tilde{\psi}(\mathbf{p}) = \int d^2\mathbf{q} e^{-ik\mathbf{p}\cdot\mathbf{q}} \psi(\mathbf{q}) \quad (2.142)$$

which is nothing but the Fourier transform of $\psi(q)$. Hence the momentum content is given by

$$P(\mathbf{p}|\psi) = |\langle \mathbf{p}|\psi\rangle|^2 \quad (2.143)$$

where $P(\psi|p)$ is the momentum content of \mathbf{p} in the state ψ .

A two-dimensional Fourier transform would provide us with the momentum content of the mode, but we wouldn't be able to associate this momentum distribution with a particular neighborhood in the configuration space. This fundamental property of Fourier transform pairs is the Heisenberg's uncertainty principle of quantum mechanics in action. It states that for conjugate variables (q, p) of a Hamiltonian system ($\hbar = 1/k$)

$$\Delta q \cdot \Delta p \geq \frac{1}{2k} \quad (2.144)$$

where Δq and Δp are the "width"s of $\psi(q)$ and $\tilde{\psi}(p)$ in their respective coordinates. We instead want to associate a momentum content with each point in the configuration space. This can be accomplished by a "windowed" Fourier transform, and a convenient one simplifying calculations would be the choice of a Gaussian window. It's equivalent to projecting on states $|z\rangle = |\bar{\mathbf{p}}, \bar{\mathbf{q}}\rangle$ which are optimally localized in both momentum *and* configuration space. "Optimal" would mean in our case to saturate the inequality Eq. (2.144) at its lower bound

$$\Delta q = \frac{\sigma_0}{\sqrt{2k}} = \frac{\eta}{\sqrt{2}} \quad \Delta p = \frac{1}{\sqrt{2k}\sigma_0} \quad (2.145)$$

and equal resolution in both spaces is ensured through the choice of σ_0 , which is at our disposal and for best results it has to be carefully determined based on the domains of variation of the conjugate pair (\mathbf{p}, \mathbf{q}) . The desired states to project on are the coherent states given by

$$Z_{\bar{\mathbf{q}}\bar{\mathbf{p}}}(\mathbf{q}) = \left(\frac{1}{\pi\eta^2}\right)^{1/4} \exp(ik\bar{\mathbf{p}} \cdot \mathbf{q}) \exp\left(-\frac{1}{2\eta^2}|\mathbf{q} - \bar{\mathbf{q}}|^2\right) \quad (2.146)$$

where the prefactor ensures normalization. Note that the first exponential factor determines the selection of the momentum ($\bar{\mathbf{p}}$), and the second exponential factor restricts the probe to an isotropic window of size $\Delta q = \eta/\sqrt{2}$ around $\bar{\mathbf{q}}$ in the configuration space. The Fourier transform is again a localized gaussian, given by

$$\tilde{Z}_{\bar{\mathbf{q}}\bar{\mathbf{p}}}(\mathbf{p}) = \left(\frac{\eta^2}{\pi}\right)^{1/4} \exp(-ik(\mathbf{p} - \bar{\mathbf{p}}) \cdot \bar{\mathbf{q}}) \exp\left(-\frac{\eta^2}{2}|\mathbf{p} - \bar{\mathbf{p}}|^2\right) \quad (2.147)$$

Note that *both* scales Δq and Δp are sharpened as $k \rightarrow \infty$. We can now construct the windowed transforms by projecting on these states

$$\rho_\psi(\bar{\mathbf{q}}, \bar{\mathbf{p}}) = |\langle z|\psi\rangle|^2 = \left| \int d^2\mathbf{q} Z_{\bar{\mathbf{q}}\bar{\mathbf{p}}}^*(\mathbf{q})\psi(\mathbf{q}) \right|^2 \quad (2.148)$$

The resulting distribution $\rho_\psi(\bar{\mathbf{q}}, \bar{\mathbf{p}})$ is called the *Husimi distribution*, and is positive definite by definition in the phase space $(\bar{\mathbf{q}}, \bar{\mathbf{p}})$. This property is important to define a distribution per se. Another related phase space distribution is the Wigner

distribution, which was constructed by Wigner [116] in analogy with the classical phase space distribution. Although it is the bona fide phase space distribution from which all other phase space distributions are derived, its one serious disadvantage is that it may assume negative values in some regions of the phase space. Nevertheless, integration of over either the phase space or the configuration space variables yields correctly the complementary distribution. Husimi distribution can be obtained by Wigner distribution by smoothing with a Gaussian localized both in momenta and position.

Note that the Gaussian windowed Fourier transformation relies on the fact that the basis $\{|z\rangle\}$ is complete. One can in fact show that $\{|z\rangle\}$ resolves the unity

$$1 = \int dz d\bar{z} |z\rangle\langle z| \quad (2.149)$$

but because members of this set are not orthogonal $\langle z'|z\rangle \neq \delta(z, z')$, it's an *overcomplete* basis. The measure $dzd\bar{z}$ has to be carefully chosen depending on the coordinates chosen to label the states. Note that we have used a cartesian coordinates to define the Husimi distribution, but the integration can be performed in principle for any set of conjugate variables, and in that case the measure is determined by looking at the form of $dzd\bar{z}$.

In practice, defining a Husimi distribution for a specific system is a tricky matter, both in terms of definition and effective visual representation. The latter is because the phase space of the 2D billiard system we are interested in is four dimensional. One very straightforward way of visualization is as follows [117]: One divides the interior of ∂D into a rectangular grid. At each point of this grid one defines a set of coherent states with varying momentum direction $\bar{\mathbf{p}} = (\cos n\Delta\phi, \sin n\Delta\phi)$, $n = 0, 1, \dots, 2\pi/\delta\phi$ and calculates the overlap with the wavefunction $\psi(\mathbf{q})$. The result is plotted in terms of vectors, where the direction of vector is the direction $\bar{\mathbf{p}}$ and its length is proportional to the overlap. Because we are using the SOS for most of the classical calculations, we instead would like to see the dispositions of the states on the Poincaré SOS. This representation would also provide the best possible visualization.

For billiard systems, this idea was first carried out in Ref. [118], but a different section was used than we are using here. We instead follow an approach similar to the one described in Ref. [119]. Consider the projection of the mode onto the boundary $\Psi(\phi) = \psi(\phi, R(\phi))$. We could simply project this object onto the SOS described by the conjugate variables (ϕ, p_ϕ) . For deformed billiards, the conjugate momentum to ϕ is not $\sin\chi$, but the angular momentum which is a monotonic function of it, given by $\sin\chi/\cos\delta$, where δ is the angle between the radial direction and the normal vector at ϕ ; as $\epsilon \rightarrow 0$, $\delta \rightarrow 0$. This calculation cannot be carried out directly because the Dirichlet boundary conditions dictate that $\Psi(\phi) = 0$. However, a way around this can be found from semiclassical considerations. The argument outlined in Sect. 2.4 states that the Dirichlet boundary condition is in semiclassical limit equivalent to reflection. Thus, any mode can be approximately decomposed into two components ψ^+ and ψ^- , one incoming component (towards the boundary) and one outgoing, respectively. This decomposition can even be carried out for exact

modes, the calculation of which will be outlined in Chapter 3. The idea underlying our method here is the projection of either of the components onto the SOS

$$\rho_{\Psi}^{\pm}(\bar{\phi}, \bar{p}_{\phi}) = |\langle \bar{\phi}, \bar{p}_{\phi} | \psi^{\pm} \rangle|^2 \quad (2.150)$$

The transform used in the numerical production of all the Husimi distributions in this thesis can be written explicitly as

$$H_{\psi}(\bar{\phi}, \sin \bar{\chi}) = \langle \bar{\phi}, \bar{p}_{\phi}(\sin \bar{\chi}) | \psi^{\pm} \rangle = \int_{-\pi}^{\pi} d\phi \exp \left[-ik \left(\frac{\sin \bar{\chi}}{\cos \delta(\bar{\phi})} \right) \phi \right] \exp [-kR_0(\phi - \bar{\phi})^2] \Psi^+(\phi) \quad (2.151)$$

This distribution yields a resolution of order $(kR_0)^{-1/2}$ in the SOS.

2.12 Breakdown of local expansions

To develop a criterion as to what extent we can rely on the modes constructed from local approximations, we will again consider the bouncing-ball orbit. There is an infinite sequence of associated modes indexed by two quantum numbers (m, n) given by Eq. (4.47) (see Chapter 4.1). Using this expression we can easily construct the incoming component $\Psi^+(\phi)$ of the modes close to the fixed point $(\phi = \pi/2, \sin \chi = 0)$

$$\Psi^+(\delta\phi) \propto H_m \left(\frac{\delta\phi}{2w(\phi)} \right) \exp \left[ik \left(a + \frac{l^2}{4\mathcal{R}(\phi)} \right) \delta\phi^2 - \frac{\delta\phi^2}{w^2(\phi)} \right] \quad (2.152)$$

The expression is given on the boundary and $\delta\phi$ denotes the deviation from $\phi = \pi/2$. To construct this expression, we have used $x \approx l\delta\phi/2$ and $z \approx l - a\delta\phi^2$, $a = R_0(1 - 5\epsilon)/2$, and $l = 2R_0(1 - \epsilon)$ is the length of the semi-minor axis. We decomposed Ω into the radius of curvature of the wavefront $\mathcal{R}(\phi)$ and the width $w(\phi)$ of the beam. We next scale out the important physical parameters: $w(\phi) = \frac{1}{\sqrt{kt}} \tilde{w}(\phi)$, $\mathcal{R}(\phi) = l\tilde{\mathcal{R}}(\phi)$; the explicit forms of \tilde{w} and $\tilde{\mathcal{R}}$ are not important.

The ground state given by $m = 0$ is a pure Gaussian, and its Husimi projection $H_0(\phi, \sin \chi)$ viz. Eq. (2.151) has approximately an elliptic profile, which is aligned with the linear manifolds shown in Fig. 2.25(a), while the exact invariant manifolds of the quadrupole are shown in Fig. 2.25(b). The area covered by the projection is

$$\mathcal{A}_0 \sim \frac{1}{2k} \quad (2.153)$$

As the transverse mode number m increases the associated projection area on the section becomes a ring of area $\mathcal{A}_m \sim m\mathcal{A}_0$. Resultingly, when m becomes large enough, say when $m = M$, it reaches the boundaries of the island, or as in the case here, a large secondary island. Obviously, the original linearized dynamics description largely discords with the actual one, as seen in Fig. 2.25. Hence, modes will reliably describe the actual modes upto $M = O(k\mathcal{A})$, where \mathcal{A} is the area covered in the SOS by the island upto the appropriately defined boundaries. But what about

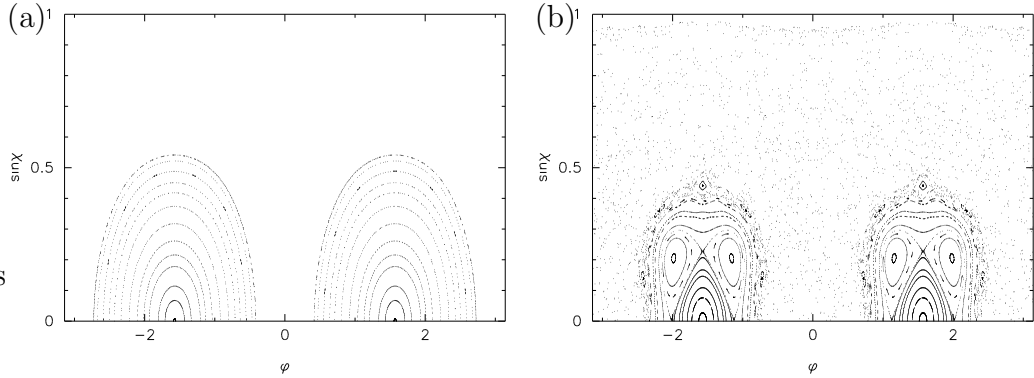


Figure 2.25: (a) Effective surface of section with linear elliptic manifolds, as calculated with Eq. (2.121) at a deformation of $\epsilon = 0.13$. Note that it's topologically not possible to cover the whole SOS with these approximate manifolds. (b) Exact SOS for the quadrupole at $\epsilon = 0.13$ deformation. Note the secondary island (which is associated with a bowtie-like orbit), and the finite extent of the primary island.

the smaller resonance islands which exist at smaller scales, scales which might not even be resolved in our plot of the SOS. It turns out that as long as the size of these structures are much less than $O(1/k)$, they give rise to negligible effects in the mode spectrum¹⁴. In the case they can be resolved, like the large secondary island in Fig. 2.25(b), it's possible to linearize the motion this time around the secondary fixed point and construct the successive modes. A similar discussion can be done for the modes corresponding to the Lazutkin tori. The picture which emerges from this discussion is that the total number of modes one can construct for a given k -interval around a $k_0 \rightarrow \infty$ is proportional to

$$N \sim k_0 \mathcal{A}_r \quad (2.154)$$

where \mathcal{A}_r is the total area of *regular* regions in the SOS. This approximate statement we have drawn from examples can be generalized to higher dimensions and rigorously proved for KAM systems. The precise statement and proof of this result is highly technical and can be found in Ref. [30].

2.13 PUSC and Quantum Scars

So far, we have carefully avoided the discussion of modes associated with the chaotic portions of the SOS. The simple reason is that as yet, there is no satisfactory procedure to construct individual modes based on structures in the corresponding regions of classical phase space. Fortunately, a lot is known about the *manifestations* of

¹⁴The same cannot be said for the mode eigenfunctions, unfortunately. See Ref.[113], which introduced the currently widely-accepted term “quasi-modes” in contrast to “modes”, exactly for this reason.

chaotic regions on the eigenfunctions and spectra of the quantum billiard problem, a central theme in the field of quantum chaos.

An appreciable amount of work in Quantum chaos is centered around the *principle of uniform semiclassical condensation* (PUSC) [120], which states that in the semiclassical limit $k \rightarrow \infty$, the phase space distribution of any eigenstate should be uniformly distributed on a classically invariant object (on the corresponding energy-hypersurface) in the phase space. This can be either invariant tori in the regular portions of the phase space or a whole chaotic component, whose projection on the SOS is the hyperbolic tangle. This final form of PUSC is based originally on suggestions/conjectures by Percival, Berry and rigorous theorems of SZCdV. Among other things, it predicts that the eigenfunctions of the quantum billiard can be separated into the two mutually exclusive sets of regular and irregular, depending on their phase space projections. This has far-reaching consequences, leading for example to strong statements about the statistics of eigenspectra. It's found that regular and chaotic states contribute independent sets of level sequences, which obey completely different statistical rules [121]. However, this approach lies outside the scope of this thesis.

According to PUSC, for a classically ergodic (strongly mixing) system, where the whole energy hypersurface is uniformly covered by a single classical trajectory, the eigenfunctions of the Helmholtz operator should be uniformly distributed over the whole phase space. This conjecture, first put forward by Berry [122], in the form that the Wigner distribution for all states in the limit $E \rightarrow \infty$ should approach the corresponding micro-canonical distribution

$$W(q, p) \rightarrow \rho_E(q, p) = \int dq dp \delta(H(q, p) - E) \quad (2.155)$$

For billiard systems we replace $\frac{E}{\hbar}$ with k , and write this as

$$W(q, p = \nabla S) \rightarrow \rho_k(q, p) = \int dq dp \delta(p^2 - 1) \quad (2.156)$$

This conjecture would lead to eigenfunctions which are random superposition of plane waves [99]. We noted before that there are notable exceptions to this conjecture, which originally showed up in a numerical study of the stadium billiard [104]. Certain states of the stadium were found to display a non-random enhancement along the short periodic orbits of the stadium, the most prominent being those associated with the bouncing ball orbit. The most surprising aspect of course is that all periodic orbits of the stadium are unstable, this being a necessary condition for hard chaos. That this is not an effect of the finiteness of k in the numerical calculations, and that the scars exist also in the asymptotic limit $k \rightarrow \infty$ was shown by a beautiful argument based on a time-domain analysis [123]. It has to be pointed out that this result can still be consistent with the theorems of SZCdV if the *fractional measure* of such states with respect to all states in the semiclassical limit vanishes.

The actual problem with our inability to construct modes associated with chaotic systems is, as we pointed out before, that the universal asymptotic expansion Eq. (2.50)

simply *doesn't exist* anymore. The reason is that this form of the expansion assumes that there is a finite number of Lagrangian manifolds, which can be patched together (at the caustics) to form a lower dimensional manifold. But the trajectories of a chaotic system, as explained in the previous paragraphs, typically explore the whole energy hypersurface. This can be imagined in two dimensions as trying to fill the whole plane of paper uniformly at a single unbroken pencil stroke. The size of the pencil tip is equivalent to asymptotic quantity k^{-1} . In the extreme limit, it becomes impossible to describe such a curve mathematically, even in principle. However, for intermediate values of k , when the pencil tip produces pixels of finite size, it's possible to find *effective* Lagrangian manifolds which will be localized close to periodic orbits to describe the scars inscribed *on a group of* asymptotic states. Then a more sensible approach is to describe the *statistical* behavior of group of eigenstates, in terms of averages over energies, coordinates, or other parameters. This topic, although under scrutiny for the past two decades, is still not satisfactorily resolved, and we will provide a more detailed analysis of a particular case based on existing lore in Chapter 5.

2.14 Refractive Billiards

Our original motivation was to study dielectric cavities using semiclassical methods. We have taken a long detour through the asymptotic description of quantum billiards, which is mathematically equivalent to the description of the (polarized) electro-magnetic modes of a *perfect metallic enclosure* ∂D in two dimensions. A dielectric cavity of shape ∂D is significantly different due to its openness, i.e. due the presence of loss from refraction or evanescent leakage as discussed in Chapter 1. Nonetheless we will show here that all of the asymptotic methods which yield analytic semiclassical approximations for the modes of closed cavities can also be generalized to calculate quasi-bound modes and emission patterns of dielectric cavities. We outline the general principles for integrable shapes (i.e. the dielectric generalization of EBK quantization) here and carry through the program in detail for the gaussian modes of isolated stable periodic orbits in Chapter 4. In addition, in contrast to the case of Dirichlet boundary condition, for which an exact correspondence between the Schrödinger equation and wave equation can be established, for the case of dielectric boundary conditions one finds a non-trivial difference between the asymptotic properties of these two equations which shows up in the phenomenon of Fresnel scattering which has no analog in quantum scattering as $\hbar \rightarrow 0$. This will be explained in detail below.

As shown in Chapter 3, the Maxwell equations for a dielectric cylinder of arbitrary cross-section ∂D can under certain conditions be reduced to the two-dimensional scalar Helmholtz equation

$$(\nabla^2 + N^2(\mathbf{q})k^2) \psi(\mathbf{q}) = 0 \quad (2.157)$$

with piecewise constant index of refraction $N(\mathbf{q})$ and continuity boundary conditions

$$\psi|_{\partial D^-} = \psi|_{\partial D^+}, \quad \frac{\partial \psi}{\partial \nu}|_{\partial D^-} = \frac{\partial \psi}{\partial \nu}|_{\partial D^+} \quad (2.158)$$

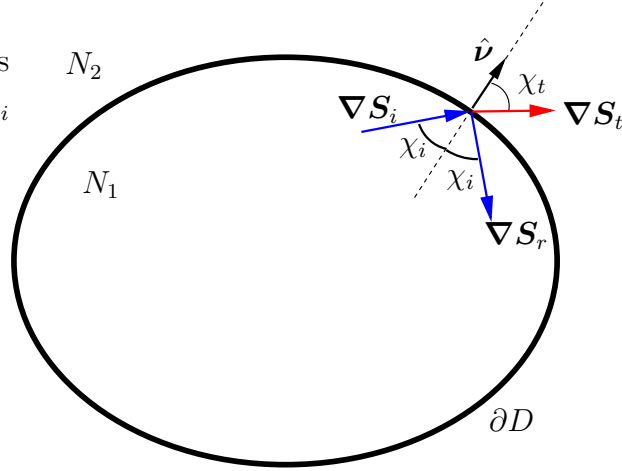


Figure 2.26: A schematics of the refractive billiard system and the variables used in the text.

We will continue to focus on the case of a uniform dielectric of index $N_1 = N$ surrounded by air ($N_2 = 1$); the generalization to arbitrary N_1, N_2 is immediate. Within the dielectric all arguments relating to the semiclassical ansatz Eq. (2.50) go through with the replacement $k \rightarrow Nk$ and with this replacement one gets the same form for the Eikonal equation Eq. (2.23) and transport equations. All the discussion of the initial value problem also is unchanged; thus we can express the solution in both regions by solving the ray motion, which proceeds on straight lines in each medium. A difference appears now on the boundary, where we must match interior and exterior solutions instead of imposing $\psi(q) = 0$. We will adopt the radiation boundary conditions for the exterior solutions, insisting that the exterior solution only involve outgoing waves at infinity. Thus we must solve the continuity conditions (2.158) with only outgoing waves in the exterior. As noted earlier, this will only be possible in general for complex values of k . The semiclassical ansatz reads

$$\psi_{1,2}(\mathbf{q}) = \sum_j A_{1,2}^j(\mathbf{q}) e^{iN_{1,2}kS_{1,2}^j} \quad (2.159)$$

where ψ_1 (ψ_2) is the solution inside (outside) the resonator and $N_1 = N, N_2 = 1$. Let's denote these components by the index i for incoming and r for reflected, inside, and the single outside component by t for transmitted. We will henceforth drop the region indices 1, 2. The nomenclature reflects the physical event of ray reflection/refraction at a dielectric interface, which is usually derived for plane waves scattering off a *plane* dielectric interface. Implementing the continuity conditions we find

$$NS_i(\mathbf{q}) = NS_r(\mathbf{q}) = S_t(\mathbf{q}), \quad \mathbf{q} \in \partial D \quad (2.160)$$

and

$$A_i(\mathbf{q}) + A_r(\mathbf{q}) = A_t(\mathbf{q}), \quad \mathbf{q} \in \partial D \quad (2.161)$$

Eq. (2.160) dictates that the tangential derivatives of S along the boundary are equal, too i.e. $N\hat{\mathbf{t}} \cdot \nabla S_i(\mathbf{q}) = N\hat{\mathbf{t}} \cdot \nabla S_r(\mathbf{q}) = \hat{\mathbf{t}} \cdot \nabla S_t(\mathbf{q})$. Combined with the Eikonal condition $(\nabla S)^2 = 1$, this implies that the normal derivatives are equal (up to a sign) as well. If we denote the angles $\nabla S_{i,r,t}$ make with the normal $\boldsymbol{\nu}$ by $\chi_{i,r,t}$ respectively, we obtain

$$N|\nabla S_i| \sin \chi_i = N|\nabla S_r| \sin \chi_r = |\nabla S_t| \sin \chi_t \quad (2.162)$$

The first equality is the same inequality we obtained for the quantum billiard, and with the proper choice of direction of ∇S with respect to the normal $\boldsymbol{\nu}$ pointing from region 1 to 2, yields the law of specular reflection $\sin \chi_i = \sin \chi_r$. We have made the following choice dictated by physical considerations

$$\boldsymbol{\nu} \cdot \nabla S_i = \cos \chi_i, \quad \boldsymbol{\nu} \cdot \nabla S_r = -\cos \chi_i, \quad \boldsymbol{\nu} \cdot \nabla S_t = \cos \chi_t \quad (2.163)$$

The last equality then yields

$$N \sin \chi_i = \sin \chi_t \quad (2.164)$$

the local equivalent of Snell's law of refraction. These constitute the "kinematic" part of the refraction boundary conditions. Eq. (2.158) with Eq. (2.160) and Eq. (2.163) yields

$$-N \cos \chi_i A_i(\mathbf{q}) + N \cos \chi_i A_r(\mathbf{q}) = -\cos \chi_t A_t(\mathbf{q}) \quad (2.165)$$

It's now possible to solve for amplitudes A_r and A_t in terms of A_i and χ_i using Eq. (2.161) and Eq. (2.165)

$$A_t = \frac{2N \cos \chi_i}{N \cos \chi_i + \cos \chi_t} A_i, \quad A_r = \frac{N \cos \chi_i - \cos \chi_t}{N \cos \chi_i + \cos \chi_t} A_i \quad (2.166)$$

These are the Fresnel formulas for reflection and refraction of EM waves at a dielectric interface [124] which determine for a given χ_i the amplitude of the reflected and refracted waves. Notice that in contrast to the plane wave results, these formulas are *local* in the sense that these conditions hold at each point of an arbitrary interface ∂D with an arbitrary composition of the inside solution $\psi_1(\mathbf{q})$.

We immediately see that much of the formalism we developed for Dirichlet boundary conditions (quantum billiards) will still hold with these new boundary conditions. This is because the law of specular reflection still holds at the boundary ∂D so that there is no difference in the internal ray dynamics. An integrable shape will still admit a solution of the form Eq. (2.50) with a finite number of terms and the Eikonals will be identical to the closed case. The amplitude transport equations inside and outside are also unchanged. The new feature is that there is a possible loss of amplitude or phase shift which occurs when an internal ray hits the boundary.

There are two cases to consider based on Eq. (2.166). If $\chi_i \geq \chi_c = \sin^{-1}(1/N)$ the ray/wave is totally internally reflected (TIR) and there is no current normal to the interface; in the Eikonal solution there will be no transmitted wave at infinity

from such a point on the boundary. Formally, in our solution $\chi_t = \frac{\pi}{2} + i\eta$ becomes a complex number, and so while the normal component $\boldsymbol{\nu} \cdot \nabla S_t = -i \sinh \eta$ is purely imaginary, the tangent component is purely real. Thus, locally the outside solution $\psi_t(\mathbf{q})$ decays away from the interface as it should, and the corresponding rays can be interpreted as propagating along the interface. Inspecting Eq. (2.166), we find $|A_r| = |A_i|$, i.e. that there is no loss in amplitude as we expect. However there is a non-trivial phase shift (as is well-known for TIR)

$$A_r = e^{i\zeta(\chi)} A_i. \quad (2.167)$$

The phase shift of the internally reflected wave component $\zeta(\chi_i)$ has the standard form and is a monotonically increasing function of $\chi_i - \chi_c$, approaching π as $\chi_i \rightarrow \pi/2$.

The condition $|A_r| = |A_i|$ implies that our internal problem is now identical to that of the quantum billiard except for the boundary phase shift which is now ζ instead of π . We can retrace all the steps we did in the EBK quantization e.g. of the circle and the quantization condition will be exactly the same as Eq. (2.66) with the replacement $\mu_b^i \pi \rightarrow \mu_b^i \zeta$. Note that μ_b^i only enters in the ‘‘radial’’ loop condition Eq. (2.69) and the semiclassical angular momentum quantization conditions is unchanged (except for the previously noted replacement $k \rightarrow Nk$ inside)

$$\sin \chi_i = \frac{m}{Nk}. \quad (2.168)$$

The explicit k -quantization condition for the dielectric circle in the case of total internal reflection is thus

$$2Nk[\sqrt{1 - \sin^2 \chi} - (\frac{\pi}{2} - \chi) \sin \chi] = 2\pi n + \frac{\pi}{2} + \zeta(\chi) \quad (2.169)$$

As before, these two transcendental equations can be solved to get the quantization conditions for k_{nm} , indexed by the two quantum numbers n and m . Clearly in this case k_{nm} will still be real. Thus our Eikonal approximation for the dielectric has found the energy shift of the resonances due to the penetration of the solution beyond the boundary but has failed to detect the evanescent leakage that such TIR whispering gallery states experience. This is not surprising since this effect is exponentially small in kR for WG modes. The reason for the exponential smallness in this case can be understood by the analogy to quantum scattering. As first pointed out by Johnson [17], the combination of the index step and the angular momentum barrier creates an effective well for the radial ‘‘motion’’; for TIR WG modes the solution must tunnel through the angular momentum barrier. The case of refractive WG states discussed below corresponds to above-barrier scattering in this radial potential. This argument is reproduced in Appendix B and an analytic form for the evanescent leakage is obtained.

The second case to consider for the dielectric circle is $\chi_i < \chi_c$ for which we have a non-zero refracted wave outside the dielectric. In this case the incident and reflected beam have no relative phase shift and we have

$$A_r = r(\chi) A_i \quad (2.170)$$

where $r(\chi)$ is real and is the fresnel reflection amplitude. Expressing this in the form $\exp(i \ln[r(\chi)])$ we can immediately write down the quantization condition for the case of these refractive states:

$$2Nk[\sqrt{1 - \sin^2 \chi} - (\frac{\pi}{2} - \chi) \sin \chi] = 2\pi n + \frac{\pi}{2} + i \ln[r(\chi)] \quad (2.171)$$

In this case it is clear that solutions only exist for complex k . As introduced in Chapter 1, the imaginary part of k will give the width of the quasi-bound state; this will be discussed in more detail for the general case in Chapter 3.

Can we still maintain in this case a correspondence between our Eikonal theory and a dynamics in phase space? In an important sense, yes. Given the maintenance of specular reflection the SOS dynamics for $(\phi_n, \sin \chi_n)$ inside is unchanged, however we must enlarge our description to keep track of the amplitude A_n as well. At each bounce for which $\chi_n < \chi_c$ amplitude is lost with a probability $T(\chi) = 1 - |r(\sin \chi)|^2$, where Eq. (2.166):

$$|r(\sin \chi)| = \left| \frac{N\sqrt{1 - \sin^2 \chi} - \sqrt{1 - N^2 \sin^2 \chi}}{N\sqrt{1 - \sin^2 \chi} + \sqrt{1 - N^2 \sin^2 \chi}} \right| \quad (2.172)$$

This effectively amounts to mapping a triplet $(A_n, \phi_n, \sin \chi_n) \rightarrow (A_{n+1}, \phi_{n+1}, \sin \chi_{n+1})$. The amplitude map which complements the billiard map is

$$A_{n+1} = |r(\sin \chi_n)| A_n \quad (2.173)$$

For each bounce below the line $\chi = \chi_c$ we generate outgoing refracted rays according to Snell's law with amplitude $T(\chi)$. If we neglect all phase shifts and just use this procedure with a specific choice for the initial ray distribution, we can generate for any shape a far-field "emission pattern" simply by keeping track of the rays as they pierce a circle of radius $r \gg R$. The resulting ray intensity patterns can be compared with the angular distribution of far-field emission patterns measured experimentally. This is precisely the "pseudo-classical" ray model introduced with less detailed justification by Nöckel and Stone [22, 114, 3, 16]. This model is used occasionally in the experimental analyses presented below. Our approach here indicates the possibility of keeping track of phase information in an extension of the model, but we do not attempt to work this out here. Note however that the effective map here is intrinsically stochastic, whereas the $\hbar \rightarrow 0$ limit of the Schrödinger equation would always yield a deterministic classical dynamics. The reason for this is that the effective "potential" in the wave equation of optics is k -dependent and in limit $k \rightarrow \infty$ the quantum uncertainty of transmission at an interface is not reduced to a vanishing energy window, but survives at all k . This is the difference between the wave equation and the Schrodinger equation alluded to in the beginning of this section; it does not show up within a single region of uniform index.

To summarize, it is possible to generalize Eikonal theory to calculate the quasi-bound states of complex k of dielectric cavities. This can be carried through analytically for the sets of states which can be found analytically in the case of closed

cavities of the same shape, i.e. all states for integrable shapes and certain subsets of the states associated with regular regions of the mixed phase space for generic shapes. A limitation of the Eikonal theory of dielectrics is that it doesn't include the effects of evanescent leakage so that totally-internally reflected states are predicted to have infinite lifetime (zero width) and there is no prediction as to their emission patterns at this level of approximation. Eikonal theory for individual quasi-bound states in the case of chaotic shapes or chaotic regions of phase space is not possible for the same reason it fails for the closed cavity. Even in this case a generalized billiard map can be used to generate information about the emission pattern if one has a good physical understanding of the appropriate initial conditions to use in the ray simulations.

A case in which one does have a physical understanding of the appropriate initial conditions is the dielectric ellipse billiard. Consider a dielectric cavity of elliptic cross-section, with a deformation $\epsilon = 0.12$ and an index of refraction $N = 1.49$. We have seen that the ellipse billiard is an integrable system. A natural initial condition to use to generate emission patterns from the dielectric ellipse is to start a bundle of rays uniformly on or near a single invariant curve of the ellipse. The upper part of the SOS consists of invariant curves which are very similar to that of the circular whispering gallery modes and possess caustics close to the boundary; these can be obtained approximately from Eq. (2.135), and the form of the invariant curves from Eq. (2.136). In fact, it can be shown that these formulas hold *exactly*, and the constant σ can be related to the product of angular momenta with respect to two foci and the kinetic energy of a point particle moving along the rays, both of which are conserved during the motion. In principle we could carry through the semiclassical quantization procedure for these quasi-bound states, generalizing the work of Keller [95] for the closed ellipse billiard. However for the emission pattern one need only choose an initial value for σ . We then start a uniform distribution of initial ray conditions on the selected invariant curve and let it propagate with the method outlined above, to get a weighted distribution in the farfield angle θ_{FF} . According to our current level of approximation, the modes associated with the invariant curves which don't cross the critical line are not emitting. The *highest lifetime* mode which emits belongs to the invariant curve which is tangent to the critical line. Notice that the points of tangency are the points of highest curvature, as is apparent from Eq. (2.136). Thus the associated modes emit at $\phi = 0$ and $\phi = \pi$, and the emission is tangent to the boundary, simply because the rays are totally internally reflected (see Fig. 2.27(a)). The farfield emission of such a mode obtained by the ray simulation method is shown in Fig. 2.27(b), green curve. A width can be assigned to the distribution by choosing a strip of initial conditions which have a width $\delta \sin \chi \sim (kR)^{-1}$, in accordance to our discussion in Sect. 2.11.

As we will argue in detail in Chapter 3, emission properties of a typical laser based on a dielectric resonator are to a good approximation given by the properties of the emitting mode (of the Helmholtz equation) having the longest lifetime. Thus, we should expect that a measurement on a laser based on an elliptic resonator with the above given parameters should result in the approximate farfield pattern in Fig. 2.27.

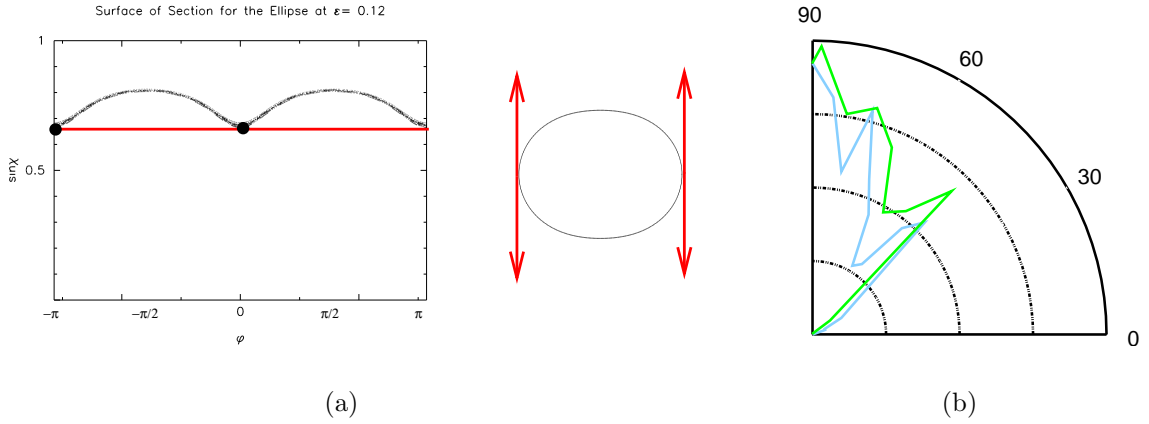


Figure 2.27: (a) Initial coordinates for ray simulation are chosen on the emitting invariant curve, which touches the critical line (red curve) $\sin \chi_c = 1/N$ at the points of highest curvature $\phi = 0, \pi$ leading to tangent emission, shown schematically on the right. (b) Observed farfield emission pattern is represented by the blue curve; the green curve is the result of simulation with initial conditions in (a).

Recent experiments on micro-lasers based in polymer samples with index of refraction $N = 1.49$ do indeed confirm this picture [43]. The measured farfield pattern is reproduced in Fig. 2.27(b), blue curve. The agreement is rather good.

Our examination of phase space dynamics suggests to us that the superficially similar dielectric shapes with different phase space structures may give qualitatively different emission patterns. Thus it may be interesting to compare the results just obtained for the ellipse with a quadrupole dielectric billiard with the same semi-major to semi-minor axis ratio (in the case considered here $\epsilon = 0.12$ corresponding to a ratio of ≈ 1.27). At this deformation the SOS (shown in Fig. 2.28(a)) for the quadrupole is primarily chaotic except for a few large stable islands corresponding to stable two and four-bounce orbits. Interestingly, exactly where we found the ray escape to occur in the ellipse, there are stable islands of the "diamond" four-bounce orbit. It is less obvious in this case how to choose the initial ray distribution to correspond to a given quasi-bound state of the resonator; Nöckel and Stone first studied the problem using the adiabatic invariant curves as initial conditions as discussed in the introduction. Further study has shown that the results are quite insensitive to this choice. Therefore we start an initial distribution of rays uniformly on the simply connected chaotic region above the critical line and propagate. The expected farfield emission pattern is shown in Fig. 2.28(b), green curve. It is indeed qualitatively different from that expected for the ellipse. This dramatic change in the emission pattern between the ellipse and the quadrupole was predicted [3] before it was recently observed [43]. The experimental results and its good agreement with theory is reproduced in Fig. 2.28(b). The effect measured here has been called "dynamical eclipsing"; the expected emission points $\phi = 0, \pi$ with the highest curvature

are eclipsed by the presence of the stable diamond orbit (see Fig. 2.28(a)). Such an emission pattern can be taken as a unique signature of the relevance of the KAM scenario and mixed phase space concepts to the emission properties of dielectric laser cavities. A detailed treatment of these experiments over a range of deformations and for several shapes is being prepared for publication [43]. This work finds that the dynamical eclipsing scenario provides only a partial explanation for the observed emission patterns.

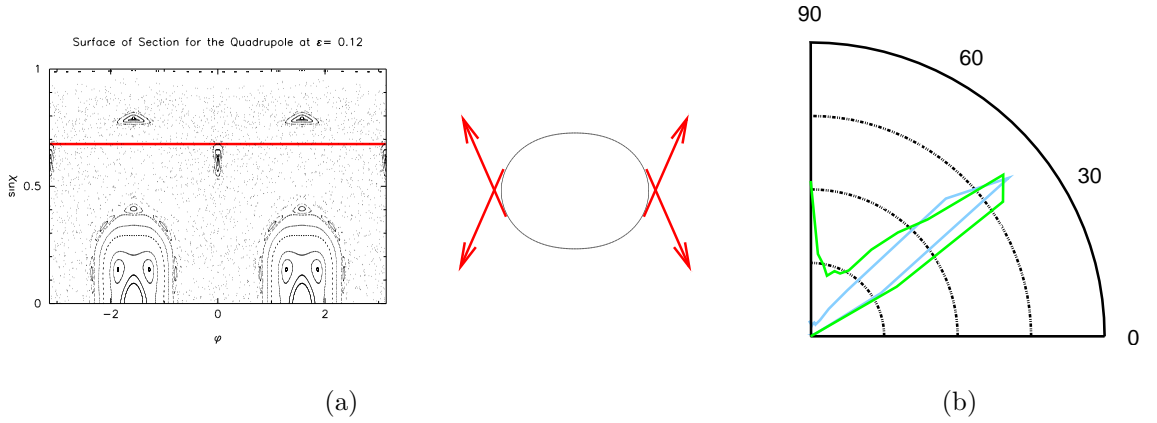


Figure 2.28: (a) Initial coordinates for ray simulation are chosen above the critical line (red curve) $\sin \chi_c = 1/N$. The stable diamond island leads to a large deviation from adiabatic motion close to the points of highest curvature $\phi = 0, \pi$, eclipsing the emission. As a result, rays escape through a flow around the island, leading to displaced emission points, shown schematically on the right. (b) Observed farfield emission pattern is represented by the blue curve; the green curve is the result of simulation with initial conditions in (a).

An interesting question is how precise does the shape of the boundary need to be to the intended shape (e.g. the ellipse) for the resonator modes to be well-described by the model shape. The qualitative answer is based on the phase space smearing of modes introduced in our discussion of the Husimi distributions above. The wave nature of the solutions will lead to a smearing of in the SOS of order $1/kR$; hence if two shapes have approximately the same SOS when coarse-grained on this scale they will have approximately the same mode structure and emission patterns.

Chapter 3

Scattering quantization method for optical billiards

3.1 Introduction

In this chapter, we will devise a numerical method to obtain the resonances of a dielectric rod of general cross-sectional area immersed in air. This type of a resonator (ARC) is the basic component of a new class of optical devices which has been of interest in the past decade. Specifically, we have in mind the application of these resonators as micro-lasers.

Our treatment will start with the Maxwell's equations for the electro-magnetic fields of the full three-dimensional structure, taking into account the vector degree of freedom of the fields, the polarization. We will show that under certain circumstances this problem can be reduced to the *two-dimensional* Helmholtz problem for a *scalar* field, obeying continuity boundary conditions at a dielectric interface. This is precisely the problem of the refractive billiard we have investigated in the previous chapter. The groundwork we have laid so far for the asymptotic states in the semi-classical limit will not only guide us through interpretation of the exact solutions, but also provide a framework to reduce the infinite-dimensional eigen-problem to a finite-dimensional one.

As noted earlier, a full description of a dielectric micro-laser has to take into account the non-linearities of the active medium which fills the resonator. In this chapter we limit ourselves to the standard description of laser resonators in terms of the resonances of the passive, linear cavity. A framework to go beyond this level of description will be presented in the last chapter of this thesis. Thus the solutions we obtain here are used as an *a posteriori* description of a typical experimental measurement, as we don't have at this point a theory to predict mode selection in experimental lasers and we find empirically that the observed lasing modes are not simply the highest Q modes of the resonator. Nevertheless, as experience shows, we can develop useful criteria for mode-selection based on the semiclassical description of the linear resonator, which is surprisingly well-matched by experimental measure-

ments.

Even at the level of linear description, there are important technical problems associated with an “open” system. The fields of a dielectric resonator pervades the whole two-dimensional space, unlike an ideal metallic cavity. As we have seen earlier, these conditions are not arbitrary, but are rather determined by the experimental setup used. In the typical setup for a micro-laser measurement, the resonator is excited by an electric or optical stimulus, and the radiated fields are measured in the farfield by a CCD camera. As already discussed, this situation is best described by Sommerfeld “outgoing wave” boundary conditions and leading to quasi-normal modes of the EM field at complex k . These Quasi-normal modes are not normalizable in the usual sense, because they grow indefinitely at infinity. As we will see, this singularity is harmless, and actually contains useful information about the lifetime of the resonance.

3.2 Reduction of Maxwell’s equations

Consider the problem of the excitation of electromagnetic waves in an infinite dielectric rod of arbitrary cross-section (see schematics in Fig. 3.1), which is extended along the z -axis. In practical situations, the structure is of finite extent and there are planar end-caps which makes it truly a resonator. In other cases, it’s a fiber-optic cable of practically infinite extent. In any case, we will for now assume translational symmetry along z -axis, and we will show later that this is a perfectly valid assumption for the modes of relevance to us.

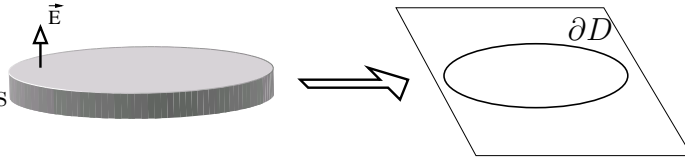


Figure 3.1: Illustration of the reduction of the Maxwell equation for an infinite dielectric cylinder to the 2D Helmholtz equation for the TM case (\mathbf{E} field parallel to axis) and $k_{\parallel} = 0$.

We will assume a harmonic variation in time for the electro-magnetic fields of the resonator:

$$\begin{Bmatrix} \mathbf{E} \\ \mathbf{B} \end{Bmatrix}(\mathbf{x}, t) = \begin{Bmatrix} \mathbf{E} \\ \mathbf{B} \end{Bmatrix}(\mathbf{x})e^{-i\omega t}, \quad (3.1)$$

where ω is the frequency of the field, and in general is a complex number. The spatial distribution of these fields are governed by the reduced Maxwell’s equations

$$\begin{aligned} \nabla \times \mathbf{E} &= ik\mathbf{B} & \nabla \cdot \mathbf{E} &= 0 \\ \nabla \times \mathbf{B} &= -in^2k\mathbf{E} & \nabla \cdot \mathbf{B} &= 0 \end{aligned} \quad (3.2)$$

where $k = 2\pi/\lambda = \omega/c$ is the wavevector in vacuum; $n = \sqrt{\mu\epsilon}$ is the index of refraction, μ is the permeability and ϵ is the dielectric constant of the medium,

which we assume to be *piecewise continuous* functions of position. It follows that both vector-fields satisfy the Helmholtz equation

$$(\nabla^2 + n(\mathbf{x})^2 k^2) \begin{Bmatrix} \mathbf{E} \\ \mathbf{B} \end{Bmatrix} = 0 \quad (3.3)$$

The translational symmetry along the z -axis allows us to express the z -variation of the fields as

$$\begin{Bmatrix} \mathbf{E} \\ \mathbf{B} \end{Bmatrix}(\mathbf{x}) = \begin{Bmatrix} \mathbf{E} \\ \mathbf{B} \end{Bmatrix}(x, y) e^{-ik_z z} \quad (3.4)$$

Following (author?) [124], we separate the fields and operators into components parallel and transverse to the z -axis:

$$\begin{Bmatrix} \mathbf{E} \\ \mathbf{B} \end{Bmatrix}(x, y) = \hat{\mathbf{z}} \begin{Bmatrix} E_z \\ B_z \end{Bmatrix}(x, y) + \begin{Bmatrix} \mathbf{E}_\perp \\ \mathbf{B}_\perp \end{Bmatrix}(x, y), \quad \nabla = \nabla_\perp + \hat{\mathbf{z}} \frac{\partial}{\partial z} \quad (3.5)$$

Writing out the transverse and longitudinal projections of Eqns. (3.2), we obtain after a few manipulations:

$$\mathbf{E}_\perp = -\frac{i}{\gamma^2} (k \hat{\mathbf{z}} \times \nabla_\perp B_z + k_z \nabla_\perp E_z) \quad (3.6)$$

$$\mathbf{B}_\perp = \frac{i}{\gamma^2} (n^2 k \hat{\mathbf{z}} \times \nabla_\perp E_z - k_z \nabla_\perp B_z) \quad (3.7)$$

where $\gamma^2 = n(\mathbf{x})^2 k^2 - k_z^2$. It's evident from these four (scalar) equations that E_z and B_z are the fundamental fields we should be after, and that once they are determined we can solve for \mathbf{E}_\perp and \mathbf{B}_\perp . Thus, the Maxwell's equations themselves completely decouple, which was already obvious from Eq. (3.3). The actual complication of solving the vector Helmholtz equation stems from the fact that the *boundary conditions* are coupled. The Maxwell boundary conditions are

$$\hat{\mathbf{n}} \times (\mathbf{E}_1 - \mathbf{E}_2) = 0, \quad \hat{\mathbf{n}} \cdot (n_1^2 \mathbf{E}_1 - n_2^2 \mathbf{E}_2) = 0 \quad (3.8)$$

$$\hat{\mathbf{n}} \times (\mathbf{B}_1 - \mathbf{B}_2) = 0, \quad \hat{\mathbf{n}} \cdot (\mathbf{B}_1 - \mathbf{B}_2) = 0 \quad (3.9)$$

in the absence of surface currents and charges and for a linear, isotropic medium. We will assume $n_1 = n > n_2 = 1$. Note that these are six conditions altogether. The subscripts denote the media on respective sides of the interface and $\hat{\mathbf{n}}$ is the unit normal on the interface, pointing out from the cylinder. We will also define the unit tangent vector at the interface, $\hat{\mathbf{t}} = \hat{\mathbf{z}} \times \hat{\mathbf{n}}$, yielding the triad $(\hat{\mathbf{z}}, \hat{\mathbf{t}}, \hat{\mathbf{n}})$ to express any given vector field at the interface. The boundary conditions (3.8)-(3.9) can be reexpressed in terms of the primary scalar fields E_z, B_z using

$$E_t = -\frac{i}{\gamma^2} (k \partial_n B_z + k_z \partial_t E_z) \quad (3.10)$$

$$E_n = \frac{i}{\gamma^2} (k \partial_t B_z - k_z \partial_n E_z) \quad (3.11)$$

$$B_t = \frac{i}{\gamma^2} (n^2 k \partial_n E_z - k_z \partial_t B_z) \quad (3.12)$$

$$B_n = -\frac{i}{\gamma^2} (n^2 k \partial_t E_z + k_z \partial_n B_z) \quad (3.13)$$

which are the projections of Eqns. (3.6)-(3.7) at the interface. It's possible to show that the resulting six scalar boundary conditions in terms of $E_{z1}, E_{z2}, B_{z1}, B_{z2}$ are not all linearly independent. One convenient choice of a linearly independent set of four boundary conditions comprises the continuity of the fields:

$$E_{z1} = E_{z2} \quad B_{z1} = B_{z2} \quad (3.14)$$

and the following condition on the tangent and normal derivatives of the fields:

$$\frac{k}{\gamma_1^2} \partial_n B_{z1} - \frac{k}{\gamma_2^2} \partial_n B_{z2} = - \left(\frac{k_z}{\gamma_1^2} - \frac{k_z}{\gamma_2^2} \right) \partial_t E_{z1} \quad (3.15)$$

$$\frac{n_1^2 k}{\gamma_1^2} \partial_n E_{z1} - \frac{n_2^2 k}{\gamma_2^2} \partial_n E_{z2} = + \left(\frac{k_z}{\gamma_1^2} - \frac{k_z}{\gamma_2^2} \right) \partial_t B_{z1} \quad (3.16)$$

Thus, a compact expression of the boundary value problem to be solved is given by the two-dimensional Helmholtz problem

$$[\nabla_{\perp}^2 + \gamma_i^2] \Psi_i(x, y) = 0 \quad (3.17)$$

supplemented with the boundary conditions

$$\Psi_1|_{\partial D} = \Psi_2|_{\partial D}, \quad A_1 \Psi_1|_{\partial D} = A_2 \Psi_2|_{\partial D} \quad (3.18)$$

where $\Psi = \begin{pmatrix} E_z \\ B_z \end{pmatrix}$, and A_1, A_2 are the matrices given by

$$A_1 = \begin{pmatrix} k k_z (n_2^2 - n_1^2) \partial_t & \gamma_2^2 \partial_n \\ n_1^2 \gamma_2^2 \partial_n & -k k_z (n_2^2 - n_1^2) \partial_t \end{pmatrix} \quad A_2 = \begin{pmatrix} 0 & \gamma_1^2 \partial_n \\ n_2^2 \gamma_1^2 \partial_n & 0 \end{pmatrix} \quad (3.19)$$

to be evaluated on ∂D . It's possible to solve this vector-partial differential equation with the method outlined in the following section. We are however interested only in the long-lived modes of the resonator. Modes with a finite k_z correspond in the semiclassical limit to rays which spiral up and down along the cylinder walls and escape through the end-caps by refracting out. Thus under most circumstances the longest lived modes have $k_z \approx 0$, and correspond to modes which are effectively two-dimensional, i.e. can be expressed by the dynamics of rays on the cross-sectional plane. In that case, the boundary conditions Eq. (3.18) also become diagonal and we have a complete decoupling. We will choose to work with $\psi_i(x, y) = E_{zi}(x, y)$ and $B_{zi}(x, y) = 0$, corresponding to TM polarized resonant modes, for which the problem reduces to the two-dimensional Helmholtz equation for the scalar field ψ with continuity conditions

$$(\nabla_{\perp}^2 + n_i^2 k^2) \psi_i(x, y) = 0 \quad (3.20)$$

$$\psi_1|_{\partial D} = \psi_2|_{\partial D}, \quad \partial_n \psi_1|_{\partial D} = \partial_n \psi_2|_{\partial D} \quad (3.21)$$

Note that this boundary value problem is equivalent to that of the stationary Schrödinger equation of quantum mechanics. Hereafter, we will drop all references to the original three-dimensional and vector character of the problem and work with Eqns. (3.20)-(3.21). This is exactly the system whose semiclassical limit $k \rightarrow \infty$ we analyzed in Chapter 2.

3.3 Scattering Quantization-Philosophy and Methodology

In this section we will describe a numerical method to solve Eq. (3.21), which is both efficient and physically appealing. Our approach is a generalization to open systems (specifically, dielectric resonators) of the *scattering quantization approach* to quantum billiards [69, 72]. This approach is based on the observation that every quantum billiard interior problem (Helmholtz equation for a bounded region with Dirichlet/Neumann boundary conditions) can be viewed upon as a scattering problem, and the spectrum can be uniquely deduced from the knowledge of the corresponding scattering operator. In the case of closed systems, the internal scattering problem can be mapped rigorously to an external scattering problem [73], and the resulting (exact) scattering matrix is unitary. For the dielectric resonator problem with Sommerfeld radiation boundary conditions, we will see that the corresponding scattering operator is inherently non-unitary, reflecting the physical fact that we are dealing with a leaky system. Thus we will define below a new “S-matrix” which is non-unitary and distinct from the true S-matrix describing external scattering from the system. We retain the terminology “S-matrix” nonetheless because of the conceptual similarity to the quantum billiard method of [69, 72]. The generalization of this approach to dielectric billiards was first made by Hackenbroich, Jacquod, Narimanov and Stone [125]. However the efficient algorithm presented below was developed in the current work in collaboration with Harald Schwefel.

We assume that the resonator is bounded by the interface ∂D of the form

$$r = R(\phi) \quad (3.22)$$

We decompose the internal and external fields into cylindrical harmonics with a constant k

$$\psi_1(r, \phi) = \sum_{m=-\infty}^{\infty} (\alpha_m H_m^+(nkr) + \beta_m H_m^-(nkr)) e^{im\phi} \quad r < R(\phi) \quad (3.23)$$

$$\psi_2(r, \phi) = \sum_{m=-\infty}^{\infty} (\gamma_m H_m^+(kr) + \delta_m H_m^-(kr)) e^{im\phi} \quad r > R(\phi) \quad (3.24)$$

Each of the terms

$$\psi_m^\pm(r, \phi) = H_m^\pm(nkr) e^{im\phi} \quad (3.25)$$

in the sum is a solution of the appropriate (interior or exterior) Helmholtz equation, but does not satisfy the matching conditions by itself. Note that owing to the completeness of the basis $\{\psi_m^\pm\}$, the expansion is exact for $r < R_{min}$ and $r > R_{max}$ as long as the sum runs over an *infinite* number of terms. The assumption that the expansions can be analytically continued to the region $R_{min} < r < R_{max}$ is

known as the Rayleigh hypothesis [126]. It has been shown [127] that for a family of deformations parametrized by ϵ , there is typically a critical deformation ϵ_c , beyond which the hypothesis breaks down because the expansion ceases to be analytic in the region $R_{min} < r < R_{max}$. For the deformations Eq. (3.22), this happens long after the shape becomes concave, a regime which we are not interested in. Although this issue seems thus to be resolved, we shall see that the potential for non-convergence is a precursor of coming numerical problems.

We will assume that we have only outgoing waves in the external region. By this, we mean that we will only keep the components in the expansion which will contribute outgoing plane waves at infinity. The large-argument asymptotic expansion of Hankel functions [96] becomes useful at this point

$$H_m^\pm(kr) \sim \sqrt{\frac{2}{\pi kr}} \exp \left[\pm i \left(kr - \frac{1}{2}m\pi - \frac{1}{4}\pi \right) \right] \quad (3.26)$$

Thus, we only keep H_m^+ in our expansion, which results in outgoing waves $\exp[i(kr - \omega t)]$.

Turning to the interior expansion, the regularity of the solution at the origin requires that we take $\alpha_m = \beta_m$, but we will not implement this condition at this stage. The continuity conditions Eq. (3.21) give us further relations among the remaining coefficients:

$$\psi_1(\phi, R(\phi)) = \psi_2(\phi, R(\phi)) \quad (3.27)$$

$$\frac{\partial \psi_1}{\partial r} \Big|_{\phi, R(\phi)} = \frac{\partial \psi_2}{\partial r} \Big|_{\phi, R(\phi)} \quad (3.28)$$

In Eq. (3.28), we have replaced the normal derivative condition by the radial derivative condition. This is possible because Eq. (3.27) dictates that the tangent derivatives are continuous, and combined with the normal derivative condition, yields the continuity of radial derivative (sufficiency can be demonstrated by a similar argument), given by

$$\frac{\partial}{\partial r} = \frac{1}{\sqrt{R^2(\phi) + (R'(\phi))^2}} \left(R(\phi) \frac{\partial}{\partial \nu} + R'(\phi) \frac{\partial}{\partial t} \right) \quad (3.29)$$

These conditions can be written out as

$$\sum_{m=-\infty}^{\infty} (\alpha_m H_m^+(nkR(\phi)) + \beta_m H_m^-(nkR(\phi))) e^{im\phi} = \sum_{m=-\infty}^{\infty} \gamma_m H_m^+(kR(\phi)) e^{im\phi} \quad (3.30)$$

$$n \sum_{m=-\infty}^{\infty} (\alpha_m H_m^{+'}(nkR(\phi)) + \beta_m H_m^{-'}(nkR(\phi))) e^{im\phi} = \sum_{m=-\infty}^{\infty} \gamma_m H_m^{+'}(kR(\phi)) e^{im\phi} \quad (3.31)$$

We multiply both sides by $w_n(\phi)e^{-in\phi}$ and integrate with respect to ϕ to get a matrix equation for the coefficient vectors $|\alpha\rangle, |\beta\rangle$ and $|\gamma\rangle$

$$H_1^+|\alpha\rangle + H_1^-|\beta\rangle = H_2^+|\gamma\rangle \quad (3.32)$$

$$DH_1^+|\alpha\rangle + DH_1^-|\beta\rangle = \frac{1}{n}DH_2^+|\gamma\rangle \quad (3.33)$$

Various physics motivated choices of the weight function $w(\phi)$ is possible [125], we choose $w(\phi) = 1$ here. Here, the matrices are defined by

$$[H_j^\pm]_{lm} = \int_0^{2\pi} d\phi H_m^\pm(n_j k R(\phi)) e^{i(m-l)\phi} \quad (3.34)$$

$$[DH_j^\pm]_{lm} = \int_0^{2\pi} d\phi H_m^{\pm'}(n_j k R(\phi)) e^{i(m-l)\phi} \quad (3.35)$$

Eliminating $|\gamma\rangle$ between Eq. (3.32) and Eq. (3.33), we obtain

$$\mathcal{S}(k)|\alpha\rangle = |\beta\rangle \quad (3.36)$$

where the matrix $\mathcal{S}(k)$ is given by

$$\mathcal{S}(k) = [n(DH_2^+)^{-1}DH_1^- - (H_2^+)^{-1}H_1^-]^{-1} [(H_2^+)^{-1}H_1^+ - n(DH_2^+)^{-1}DH_1^+] \quad (3.37)$$

As noted earlier, this S-matrix is different from the standard external scattering matrix introduced in Eq. (1.4). It is straightforward to check that for real k $\mathcal{S}(k)$ is non-unitary. Consider now the eigenvalue problem of $\mathcal{S}(k)$

$$\mathcal{S}(k)|\alpha\rangle = e^{i\varphi}|\alpha\rangle, \quad (3.38)$$

where for real k the phase φ is complex. Once we find a complex k_q where one (or several) of the φ is a multiple of 2π , we have $|\alpha\rangle = |\beta\rangle$, which is exactly the condition of regularity at the origin. This is the quantization condition which will provide us with the quantized eigenvalues and eigenvectors ($k_q, |\alpha^{(q)}\rangle$) of the interior problem we set out to find. One possible strategy is thus a scan through k in a given complex domain and the determination of the values of k for which we obtain an eigenvalue unity of $\mathcal{S}(k)$ within a given numerical precision. This condition is in general expressed in terms of the secular function $\zeta(k)$ [69] given by

$$\zeta(k) = \det[1 - \mathcal{S}(k)] \quad (3.39)$$

The spectrum is obtained as the zeros of the secular equation $\zeta(k) = 0$. As noted, the values k_q for which we obtain a unit eigenvalue and the secular function Eq. (3.39) has a root, is always complex and the eigenvalues of $\mathcal{S}(k)$ are not pure phases, $\varphi \in \mathbb{C}$. Additionally, the choice of outgoing waves only, restricts the eigenvalues *strictly* within the unit circle in the complex plane, i.e. $\text{Im}[\varphi] < 0$. The practical upshot of this is that this requires a two-dimensional root-search for the equation $\zeta(k) = 0$. However, there are several hurdles to be overcome before this method can be useful. The numerical algorithm proposed in the next section will equip us with an efficient root-finding method.

A physical interpretation of the internal scattering operator $\mathcal{S}(k)$ and its eigenvectors can be given even off-quantization ($\varphi(k) \neq 2\pi$) [128, 70]. We can visualize this approach in our case by dividing the interior of the resonator into two subdomains joined along the curve Γ , which we take to be circle of radius $R_\Gamma \lesssim R_{min}$, and

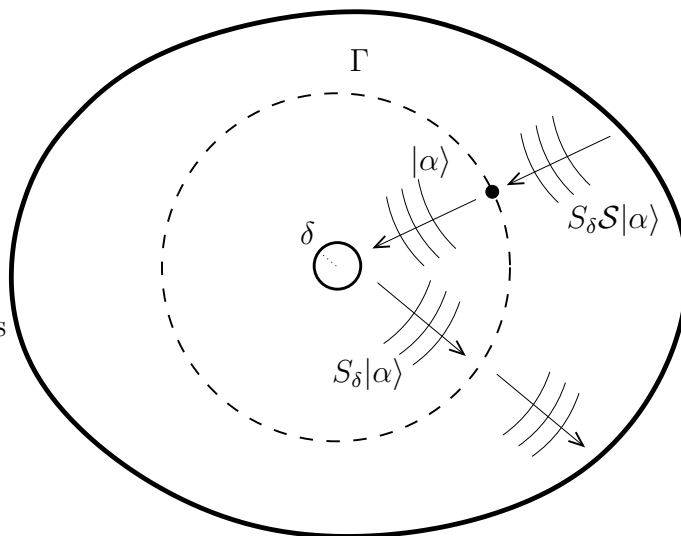


Figure 3.2: Schematics describing the quantum Poincaré mapping induced by the internal scattering operator.

considering it as a boundary at the junction of two back-to-back scattering systems. We furthermore introduce a tiny metallic inclusion of radius δ at the origin (this is introduced for the sake of the argument and can be omitted). This is our first scattering system, which scatters an incoming wave $|\beta\rangle$ into $|\alpha\rangle$ via the scattering operator S_δ

$$|\beta\rangle = S_\delta(k)|\alpha\rangle \quad (3.40)$$

$S_\delta(k)$ is exactly the exterior scattering operator for a metallic circle (immersed in a medium with index of refraction n):

$$[S_\delta(k)]_{mm'} = -\frac{H_m^-(nk\delta)}{H_m^+(nk\delta)}\delta_{mm'} \quad (3.41)$$

The second scattering system is the boundary itself, scattering an incoming wave (with respect to the boundary) $|\alpha\rangle$ into $|\beta\rangle$, and the scattering operator for this system is simply $\mathcal{S}(k)$ whose form is given in Eq. (3.37). Consider now a whole cycle, starting with the state $|\alpha\rangle$ on Γ , being first scattered off the tiny circle, then from the boundary returning to Γ again (see Fig. 3.2). The resulting scattered vector is $\mathcal{S} \cdot S_\delta|\alpha\rangle$. Now, as $\delta \rightarrow 0$, we have $S_\delta \rightarrow 1$, and the resulting scattered vector is $\mathcal{S}|\alpha\rangle$. This is the quantum analogue of the Poincaré SOS mapping on the section Γ , parametrized by $(\phi, \sin \chi)$. The individual normal modes ψ_m^\pm in our expansion correspond to modes which have a well-defined angular momentum $\sin \chi = \frac{m}{nkR_\Gamma}$, which is the momentum coordinate on this section. This link has been fruitfully used to obtain semi-classical forms of the scattering operator $\mathcal{S}(k)$, for various closed systems [128]. We will not pursue this approach here, but will make use of this visualization to develop a meaningful truncation scheme for a numerical implementation of our method.

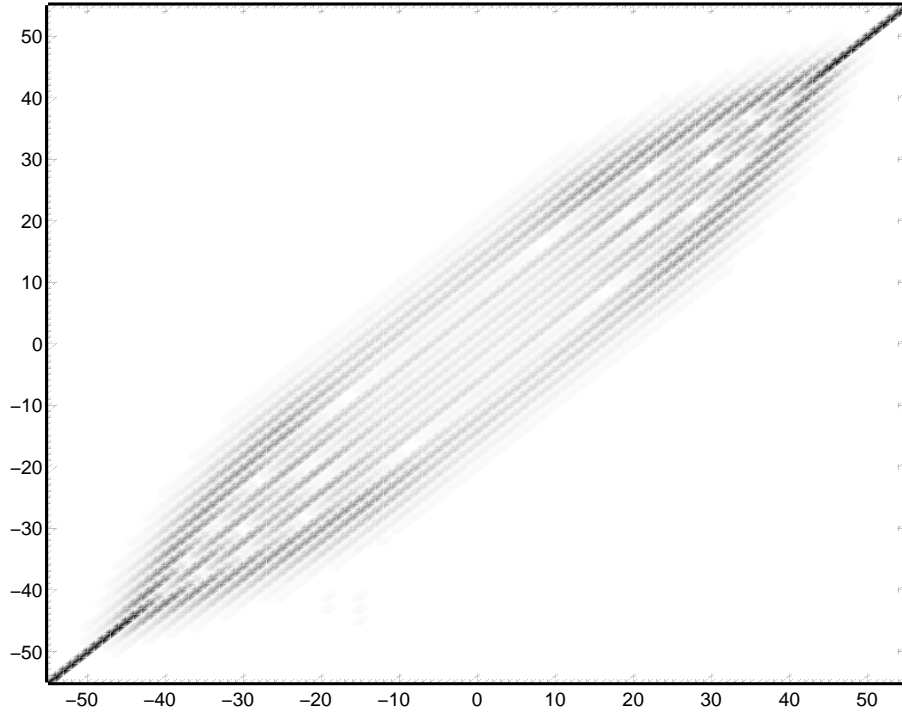


Figure 3.3: A gray-scale representation of the scattering matrix Eq. (3.37), calculated for a quadrupolar resonator at $\epsilon = 0.1$ deformation, $n = 2.5$ and $nkR = 40$. The number of evanescent channels used in the calculation is $\Lambda_{ev} = 15$. Note the strong diagonal form for $|m| > nkR$. The spread around the diagonal is proportional to the deformation. Here, the internal scattering couples approximately 20 angular momentum modes.

First of all, at a given k , an angular momentum eigenstate ψ_m^\pm , for which $m > nkR_{max}$ is a closed channel for our scattering system, because it corresponds to classical motion with a circular caustic of radius larger than R_{max} , as we saw in Section 2.4. Such channels are called *evanescent*, and are not expected to be scattered significantly. In fact, a plot of the matrix $\mathcal{S}(k)$ in Fig. 3.3 reveals that as m grows beyond a critical value $m_c \approx nkR_{max}$, the scattering matrix becomes strongly diagonal i.e. $[\mathcal{S}(k)]_{mm'} \approx \delta_{mm'}$ for $|m|, |m'| > m_c$. Furthermore, there is a transition region $nkR_{min} < |m|, |m'| < nkR_{max}$, where the matrix is heading towards diagonality, and this region corresponds to evanescent components which undergo an enhanced scattering because they overlap significantly with only certain regions of the resonator. Consequently, this region grows with the deformation of the resonator. On the other hand, the relative size of this region with respect to the whole range of m shrinks with increasing k . If we call the number of (positive) channels contributing to a given internal scattering matrix Λ , the size of the matrix is $N_{trunc} = 2\Lambda + 1$. The size-boundary corresponding to $\Lambda_{sc} = nkR_{min}$, is called the *semi-classical size*.

3.4 Numerical Implementation

We will now describe our numerical implementation of the solution of the eigenvalue problem

$$\mathcal{S}(k)|\alpha\rangle = e^{i\varphi(k)}|\alpha\rangle \quad (3.42)$$

based on the physical arguments of the previous section, and the subsequent hunt for quantization of k , defined by the existence of a $\varphi(k)$ among the eigenphases of $\mathcal{S}(k)$, which is a multiple of 2π .

The numerical problems already surface at the stage of computing the truncated scattering matrix $\mathcal{S}(k)$ itself. The expression given in Eq. (3.37) requires numerical inversion of 5 matrices. At a given k , as the number of channels Λ of the interior matrices designated by index 1 grows beyond Λ_{sc} , they become increasingly more singular. The problem can be diagnosed by looking at the variation of the *condition number* of the given matrices with their respective size Λ . The condition number λ of a matrix A is computed by its *singular value decomposition* (SVD) [129]:

$$A = U \cdot \text{diag}[w_j] \cdot V^T \quad (3.43)$$

where U and V are orthogonal matrices, and they have the same size as A as long as A is a square matrix, which is the case here. The diagonal matrix $\text{diag}[w_j]$ contains the *singular values* w_j . This decomposition is unique up to a permutation of columns/rows of the matrices involved, and its numerical implementation is standard [130]. The condition number is then defined by

$$\lambda = \frac{|w|_{max}}{|w|_{min}} \quad (3.44)$$

The matrix is singular if its condition number is infinite, and ill-conditioned if it's too large, and in that case the inversion given by

$$A^{-1} = V \cdot \text{diag}[1/w_j] \cdot U^T \quad (3.45)$$

is also ill-defined. In Fig. 3.4 we plot λ versus the size Λ of H_2^+ . Note that, there is a sharp boundary between regular and singular regimes of H_2^+ . Numerically, this is caused by the combination of two factors: approximate diagonal form of the matrices beyond the size Λ , and the large values of these diagonal entries:

$$[H_2^+]_{mm'} \sim H_m^+(nk\bar{R}) \sim \exp\left[m \cosh^{-1}\left(\frac{m}{nk\bar{R}}\right)\right] \delta_{mm'}, \quad |m| > nk\bar{R} \quad (3.46)$$

Here, \bar{R} is the average value of $R(\phi)$. As evident from our previous discussion, this ill-conditioning is caused by blindly including evanescent channels in the scattering problem. A quick solution is to truncate the matrices at the singularity boundary suggested by our semiclassical interpretation and include only $\Lambda_{sc} = nkR_{min}$ channels of $|m|$. But this turns out to produce some states which do not satisfy the boundary conditions well enough. As noted in [69] we have to keep some of the evanescent

channels Λ_{ev} , enough to be able to proceed with our numerical computation and provide the missing (evanescent) components of those states which require it. Thus, the properly truncated scattering matrix will have a size of $N_{trunc} = 2(\Lambda_{sc} + \Lambda_{ev}) + 1$.

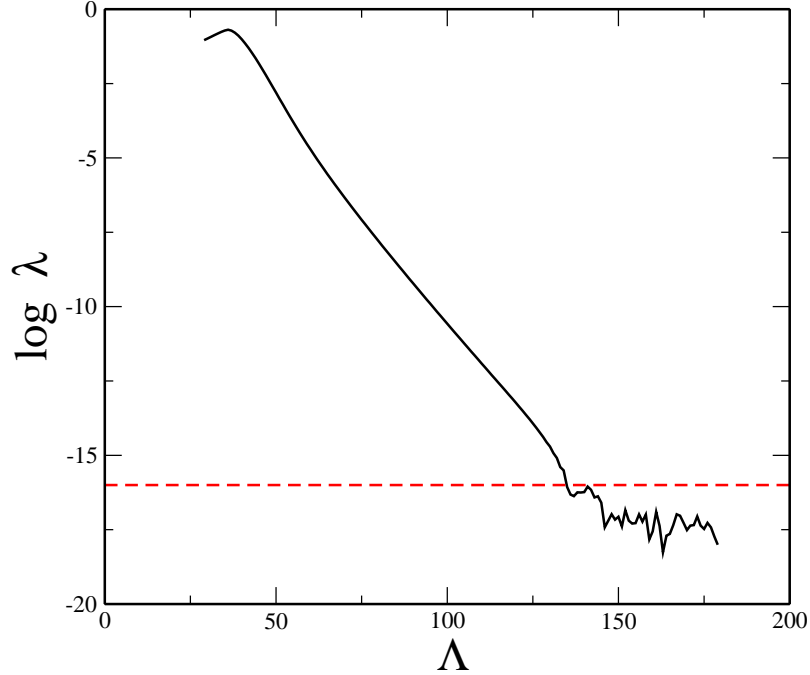


Figure 3.4: The logarithm of the condition number λ as a function of the size Λ of H_2^+ , calculated for quadrupolar resonator with deformation $\epsilon = 0.16$, $n = 3.2$ and $nkR = 128$. The dashed line represents the machine precision, where we cutoff the matrix in a typical calculation. In this example, this corresponds adding $\Gamma_{ev} \approx 8$ evanescent channels. This would be the singularity limit for a calculation with inversion. Owing to the diagonalization technique we are using, we can add many more channels without a numerical degradation.

It's worthwhile to interpret the meaning of the semi-classical size Λ_{sc} from the perspective of the scattering matrix as a quantum Poincaré map. We had defined the concept of the fundamental quantum cell in the SOS in Section 2.11, and found its area to be of the order of $\frac{1}{nkR}$. Hence, we find that the number of quantum cells covering the SOS bounded by $0 < \sin \chi < 1$, $-\pi < \phi < \pi$ is proportional to the semiclassical basis size Γ_{sc} . This can be interpreted as the limited resolution of a quantum Poincaré SOS mapping, induced by the internal scattering operator of a finite size resonator. In this respect, an analogous quantity within the realm of physical optics is the *Fresnel number*. The analogy becomes exact if we were to choose as a basis not the (angular) momentum representation Eq. (3.25), but a coherent state basis, which is optimally localized within the fundamental quantum cell in the SOS Γ .

From the above results we see that it is desirable to avoid the inversion leading

to \mathcal{S} . This can be done, but it comes at the cost of larger matrices. However, the advantage of added numerical stability makes it worthwhile to consider. This is accomplished by trading the eigenvalue problem Eq. (3.42) with a *generalized* eigenvalue problem. We rewrite Eqs. (3.32-3.33) in the form

$$A|\Upsilon\rangle = e^{i\varphi}B|\Upsilon\rangle \quad (3.47)$$

where the $2N_{trunc} \times 2N_{trunc}$ matrices are given by

$$A = \begin{pmatrix} H_1^+ & -H_2^+ \\ DH_1^+ & -\frac{1}{n}DH_2^+ \end{pmatrix}, \quad B = \begin{pmatrix} -H_1^- & 0 \\ -DH_1^- & 0 \end{pmatrix} \quad (3.48)$$

and

$$|\Upsilon\rangle = \begin{pmatrix} |\alpha\rangle \\ |\gamma\rangle \end{pmatrix} \quad (3.49)$$

As a result, we get both the inside and the outside vectors at one shot. This method turns out to be more stable than the one based on inversion, and is the one we use with N_{trunc} as above. The numerical problems associated with the regions of evanescent behavior ($R_{min} < r < R_{max}$) remain, but are tractable for $nkR \lesssim 200 - 300$ (this range is larger for modes without evanescent components).

3.5 Root-search strategy

A typical run at $nkR_0 = 80$ for $\epsilon = 0.1$ produces the eigenvalue distribution $\{e^{i\varphi_k}\}$ plotted in Fig. 3.5 in the complex $z = e^{i\varphi}$ plane. We will denote $\varphi = \theta + i\eta$, where θ and η are real numbers, so that $|z| = \exp(-\eta)$. Note that $\Lambda_{sc} = [nkR_0(1 - \epsilon)] = 93$ and we have included $\Lambda_{ev} = 55$ evanescent channels. Our first observation is that

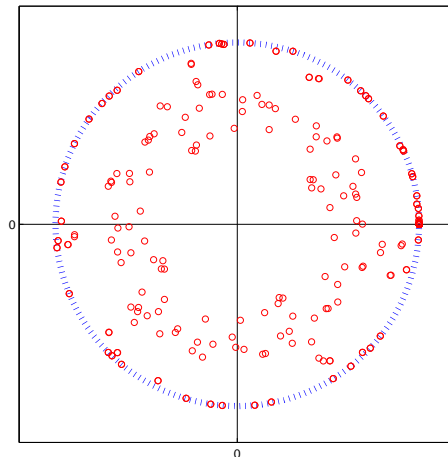


Figure 3.5: Distribution of scattering eigenphases (red circles) in the complex plane for $nkR = 106$, $\epsilon = 0.12$, $n = 2.65$. Blue dashed line is the unit circle $|z| = 1$.

all the eigenvalues are distributed within the unit circle $|z| = 1$ and that there is an

accumulation of eigenvalues on the boundary of the circle, particularly at $\theta = 2\pi^+$. As we have established, an eigenvalue for which $\varphi^{(l)}(k) = 2\pi$ within a given numerical precision yields a quantized mode of the resonator. However, we should resist the temptation to simply take all the scattering eigenstates whose eigenphases are $\varphi \approx 2\pi$ to be quantized. As was pointed out in Ref. [72] in the case of a closed system, there is an accumulation of scattering eigenphases at $\varphi \approx 2\pi^+$, which *do not* correspond to proper physical eigenmodes of the resonator. These are modes which are primarily composed of evanescent channels, and can easily be distinguished from regular modes, as we shall see below. It should be pointed out that this phenomenon is an artifact of the scattering quantization method.

A lot can be learned by way of a simple example. We will consider a case where we know the exact solutions, namely the dielectric circle. The exact eigenstates of the scattering matrix for the circle can be given a precise physical meaning in terms of classical processes in the semiclassical limit. They correspond to motion with a conserved angular momentum, or in terms of our notation in Section 2.14, a given impact angle $\sin \chi$ on the dielectric interface and the scattering matrix is diagonal in this representation. This signifies the fact that a “channel” with a given m upon encountering the boundary will be scattered to the same channel m i.e. specular reflection. The scattering matrix can be written as

$$[\mathcal{S}(k)]_{mm'} = -\delta_{mm'} \frac{H_m^+(nkR)}{H_m^-(nkR)} f_m(k) \quad (3.50)$$

where the function $f_m(k)$ is given by the following expression

$$f_m(k) = \frac{1 - n \frac{H_m^{+'}(nkR)}{H_m^+(nkR)} \frac{H_m^+(kR)}{H_m^{+'}(kR)}}{1 - n \frac{H_m^{-'}(nkR)}{H_m^-(nkR)} \frac{H_m^+(kR)}{H_m^{-'}(kR)}} \quad (3.51)$$

This form in terms of the particular ratios of Hankel functions will help us simplify the expressions considerably in the asymptotic limit $nkR \rightarrow \infty$. Notice that when $f_m(k) = 1$,

$$[S_c(k)]_{mm'} = -\frac{H_m^-(nkR)}{H_m^+(nkR)} \delta_{mm'} \quad (3.52)$$

is the *external* scattering matrix for the closed circular cavity, which is unitary. Then our quantization condition $[S_c(k)]_{mm'} = 1$ yields

$$J_m(nkR) = 0 \quad (3.53)$$

which is the exact quantization condition for wavevectors nk of a metallic cavity. Hence in the form Eq. (3.50), the corrections due to the openness of the system are lumped into the factor $f_m(k)$.

Let's first consider the diagonal elements of (3.50) for $m > nkR$. The appropriate expansion to use for the Hankel functions are given by the Debye asymptotic forms

[96]

$$H_m^\pm(z) = \frac{1}{\sqrt{2\pi m \tanh \alpha}} (p_-(\alpha)e^{-\Phi(\alpha)} \mp 2ip_+(\alpha)e^{\Phi(\alpha)}) \quad (3.54)$$

$$H_m^{\pm'}(z) = \sqrt{\frac{\sinh 2\alpha}{4\pi m}} (q_-(\alpha)e^{-\Phi(\alpha)} \pm 2iq_+(\alpha)e^{\Phi(\alpha)}) \quad (3.55)$$

Here,

$$\left\{ \begin{matrix} p_\pm(\alpha) \\ q_\pm(\alpha) \end{matrix} \right\} = 1 + \sum_{k=0} (\mp)^k \frac{\left\{ \begin{matrix} u_k(\coth \alpha) \\ v_k(\coth \alpha) \end{matrix} \right\}}{m^k} \quad (3.56)$$

In the above expression, $u_k(\coth \alpha)$ and $v_k(\coth \alpha)$ are polynomials in $\coth \alpha$, whose forms shall not concern us here. We have nevertheless included these prefactors to emphasize that the exponentially small first terms in the expansions Eq. (3.54) and Eq. (3.55) is lower order than *all* the terms $\left\{ \begin{matrix} p_\pm(\alpha) \\ q_\pm(\alpha) \end{matrix} \right\} e^{\Phi(\alpha)}$. Furthermore

$$\Phi = m(\alpha - \tanh \alpha) \quad (3.57)$$

where $\alpha = \cosh^{-1}(m/nkR)$. Similarly, we will use primed variables for $\alpha' = \cosh^{-1}(m/kR)$. Note that $\alpha' > \alpha \gg 1$.

With proper attention on exponentially small terms, we obtain

$$[\mathcal{S}(k)]_{mm} \sim 1 + i(1 + 2n)e^{-2m\alpha} \quad (3.58)$$

for $m \gg nkR$. These entries correspond to scattering of evanescent channels and result in eigenphases exponentially close to zero, $\varphi \sim (1 + 2n)e^{-2m\alpha}$. Thus, the accumulation of eigenphases on the unit circle close to the quantization point $\varphi = 2\pi$ in Fig. 3.5 can be linked to such extremely evanescent channels, which are not the physical modes of the cavity¹. Note that the number of such scattering eigenstates depends strongly on our choice of Λ_{ev} in our numerics and these states can be discarded after the calculation.

Next, we will look at the *internally reflected* channels. These are obtained for the entries $kR < m < nkR$. Because $m/kR > 1$, we can still use the expansions Eq. (3.54) and Eq. (3.55) for Hankel functions with arguments kR . For the Hankel functions $H_m^\pm(nkR)$, we will use the second set of Debye expansions [96]

$$H_m^\pm(nkR) \sim \sqrt{\frac{2}{\pi m \tan \beta}} \exp \left[\mp im(\beta - \tan \beta) \mp i\frac{\pi}{4} \right] \quad (3.59)$$

$$H_m^{\pm'}(nkR) \sim \left(\pm i \sin \beta - \frac{1}{2m \cos \beta \tan^2 \beta} \right) H_m^\pm(nkR) \quad (3.60)$$

where $\beta = \cos^{-1}(m/nkR)$. Inserting these expansions into Eq. (3.50) we obtain

$$[\mathcal{S}(k)]_m \sim e^{i\Theta} \left[1 - i \left(2n \sin \beta e^{-\alpha'} - i \frac{e^{-2m\alpha'}}{n \sin \beta} \right) \right] \quad (3.61)$$

¹These modes can be interpreted as *creeping waves*, which are evanescent modes which cling to the surface of the resonator [131].

where Θ , which is identical to the closed-circle eigenphase, is real and given by

$$\Theta(k) = -2m(\beta - \tan \beta) - \frac{\pi}{2} \quad (3.62)$$

These channels yield eigenphases which accumulate exponentially close to the unit circle $|z| = 1$, but unlike the evanescent modes Eq. (3.58), with arbitrary phases. Note that the exponentially small difference from $|z| = 1$ represents the evanescent leakage we were unable to detect semiclassically in Chapter 2. It's possible to assign a velocity to these eigenphases in k -space:

$$\frac{d\Theta}{d(nkR)} = 2 \sin \beta + O\left(\frac{1}{nkR}\right) > 0 \quad (3.63)$$

A useful observation at this point is that this velocity is twice the cosine of the conserved ray impact angle $\chi = \pi/2 - \beta$ in the circular billiard corresponding to the motion with angular momentum m . The picture this entails is the following: When we slowly increase k , the individual eigenphases move with an approximately constant but different speeds given by Eq. (3.63) counter-clockwise around the unit circle. Each time one of the eigenphases passes through $\varphi = 2\pi$, the quantization condition is fulfilled and the resulting eigenvector is a quantized mode of the resonator. Hence, the eigenvectors of $\mathcal{S}(k)$ can be assigned a physical meaning and identity even when k is not tuned to resonance $\varphi(k) = 2\pi$. In this case, they correspond to totally internal reflected whispering gallery modes.

Last, we investigate the classically open channels, which corresponds to rays which are *refracted* out. This regime is $m < kR$, and all the Hankel functions can be expanded using Eq. (3.59) and Eq. (3.60)

$$[\mathcal{S}(k)]_m \sim \frac{\sin \beta' - n \sin \beta}{\sin \beta' + n \sin \beta} e^{i\Theta} \quad (3.64)$$

Note that the algebraic prefactor is the Fresnel reflection factor for a ray coming in at an angle $\chi_i = \frac{\pi}{2} - \beta$. Thus, the proximity of the scattering eigenphase to the unit-circle is a measure of the lifetime. The smaller the radius of the eigenphase, the smaller is the associated lifetime. As we change k , the variation of the eigenphase of a given solution will be dominated by the phase-factor $e^{i\Theta}$. The path to quantization goes thus by first increasing $\text{Re}[k]$ until $\text{Re}[\Theta] = 2\pi$, and then adding a small imaginary part $i\Delta k$ so that

$$|e^{-i\Theta(k+i\Delta k)}| = \frac{\sin \beta' - n \sin \beta}{\sin \beta' + n \sin \beta} \quad (3.65)$$

driving the eigenphase right to the quantization point. From this condition, we can extract an approximate value for the imaginary part of the quasi-bound mode which will result:

$$\text{Im}[nkR] = -\frac{1}{2 \sin \beta} \left| \log \left[\frac{\sin \beta' - n \sin \beta}{\sin \beta' + n \sin \beta} \right] \right| \quad (3.66)$$

Thus we recover precisely the lifetime of refractive WG modes due to Fresnel scattering obtained semiclassically in Chapter 2.

The crucial point here is that these statements are only valid for an interval of the order of a mean-level spacing, so that β is approximately constant

$$\frac{d\beta}{d(nkR)} = O\left(\frac{1}{nkR}\right) \quad (3.67)$$

Furthermore, the assumption that $\text{Im}[nkR] \ll \text{Re}[nkR]$ is also implicit in these derivations. These procedures have to be taken with a grain of salt because of the Stokes phenomenon [86, 132] in the asymptotic expansion of the Hankel functions with complex argument. However, as long as the latter condition is satisfied, these estimates are valid.

In light of our findings for the undeformed case, it's possible to develop a powerful search strategy for the general, deformed case. The reason behind our ability to “track” the scattering eigenphases through quantization in the case of the circular resonator was the fact that the momentum channels didn't mix when we changed k , owing to the diagonality of the scattering matrix over all k i.e. there we had a good label m which was conserved. This will not be the case when we deform the resonator. For small deformations, the internal scattering matrix $\mathcal{S}(k)$ will remain approximately diagonal, with fluctuations due to inter-channel scattering. The resulting eigenstates will show a broadening in their angular momentum distributions. In that case, one can still define an average phase velocity given by

$$\frac{d\bar{\Theta}}{d(nk\bar{R})} = 2 \sin \bar{\beta} \quad (3.68)$$

defined by the average angular momentum disposition \bar{m}

$$\bar{m} = \frac{1}{2\Lambda + 1} \sum_{-\Lambda}^{\Lambda} m |\alpha_m|^2 \quad (3.69)$$

At first sight, there is no reason for such a solution to persist over a given interval Δk . Following Ref.[70], we suggest that the scattering eigenvectors have an identity beyond a given k -value, and more importantly, that the energy eigenvectors, the quantized modes, have an identity beyond the energy shell. We can quantify this statement by defining a simple scalar product between solutions at different k :

$$\langle \alpha(k) | \alpha(k + \Delta k) \rangle = \sum_m \alpha_m(k) \alpha_m^*(k + \Delta k) \quad (3.70)$$

Then our claim is tantamount to the adiabaticity of $\langle \alpha(k) | \alpha(k + \Delta k) \rangle$. The reason this is possible lies in the subtle correlations among the matrix elements induced by the underlying classical motion in the semiclassical limit. We have already emphasized the connection between the semiclassical scattering matrix and the classical

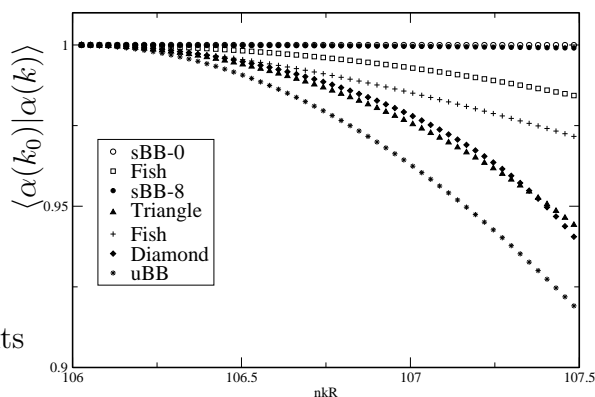


Figure 3.6: The tracing of the overlap calculated for a set of states in the interval $nkR = 106 - 107.5$, for $\epsilon = 0.12$ and $n = 2.65$. The associated classical structures are found by the Husimi projections of the respective states. The encoding is: sBB- n = n^{th} transverse excitation of the stable bouncing ball mode, uBB=unstable bouncing ball mode.

SOS map. As long as there are invariant curves in the SOS, which we have seen is guaranteed by the KAM scenario for near-integrable deformations in Section 2.9, there will be eigenstates of the scattering matrix which will display the aforementioned adiabatic behavior.

In Fig. 3.6 we trace the overlap Eq. (3.70) of a set of eigenvectors in an interval of the order of a mean-level spacing. First, a diagonalization of $\mathcal{S}(k)$ is performed at a k_0 , the eigenvectors determined, and then further diagonalizations are performed at $k_0 + n\Delta k$, where $\Delta nkR = 0.03$. At each step, there is in general a single state having markedly higher overlap with the respective *original state* at k_0 than the others and that value is plotted. The result shows that an adiabatic identity can be in fact defined for certain states. This procedure allows the tracking of majority of the states, as long as the deformation is not too large. In fact, it's possible to show that

$$\langle \alpha(k) | \alpha(k') \rangle = 1 + \Delta nkR \cdot O\left(\frac{1}{nkR}\right) \quad (3.71)$$

It turns out that one can extend this strategy to higher deformations, where the SOS displays large chaotic components, with proper attention on eigenstates which have an appreciable overlap with chaotic regions. A typical scenario which is encountered is the *avoided crossing* of two scattering eigenvectors. This is captured in Fig. 3.7, where two eigenvectors are traced over a mean-level spacing. Originally, the two states are well-distinguished; they have approximately zero overlap with each other. At the crossing they perturb each other strongly, and an approximate superposition state results. However, if we continue changing k , the states emerging from the avoided crossing will still have a pronounced overlap with the states before the crossing. Notice that the overlaps are calculated with reference to one of the original states $|\alpha_0\rangle$. This example represents a case where a numerical tracing algorithm has to be properly conditioned.

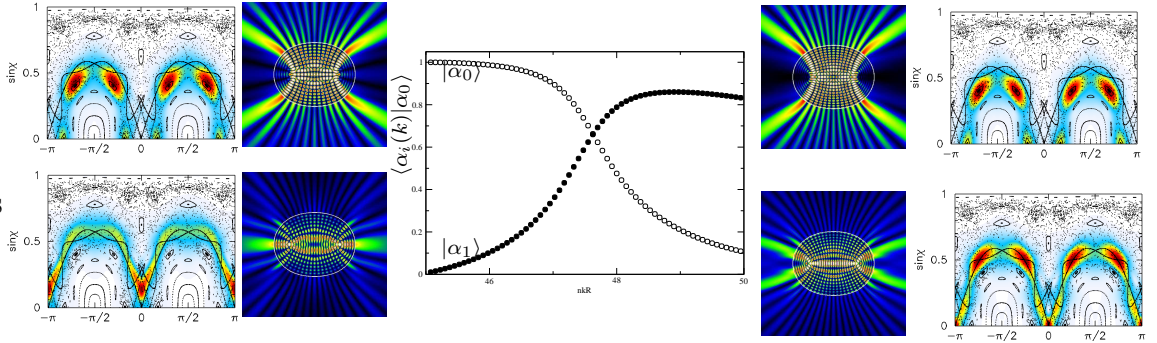


Figure 3.7: Two eigenvectors are traced by the criterion that the overlap is largest in two *consecutive* iterations. The figure shows the overlap of the two sets of states resulting with respect to one of the *initial* states, $|\alpha_0\rangle$.

After having established that we can assign an identity to the scattering eigenvectors and the possibility of tracing, we next investigate how the corresponding eigenphases move within the complex unit circle as we vary k , both through real and imaginary values. Fig. 3.8 shows such a tracing of several representative states. First, the initial eigenphases are followed by changing the k over real values, where each of the eigenphases follow approximately a circular trajectory, followed by a pure imaginary change in k resulting in the phases following almost perfect radial paths. This details of this behavior is nicely captured in Fig. 3.9 by plotting $|e^{i\varphi(k)}| = e^{\eta(k)}$ in the former trace and $e^{i\theta(k)}$ in the latter. This simple behavior of speeds can be understood from the fact that the classical channels (of angular momentum in our case) in the expansion preserve their identity over a mean level spacing, and the weight of these channels embodied in the expansion coefficients α_m change only $O\left(\frac{1}{nkR}\right)$. In conclusion, the radial and angular speeds of the eigenphases are approximately “decoupled”. Finally, the constancy of these speeds over the same interval is displayed in Fig. 3.10, which shows that $d\theta/d\text{Re}[k] \sim \text{const}$ and $d\eta/d\text{Im}[k] \sim \text{const}$.

We have developed an efficient numerical algorithm to determine the quasi-normal modes of an arbitrarily deformed dielectric resonator based on all of these observations:

1. A diagonalization of $\mathcal{S}(k)$ is performed at a given k , and N_{trunc} eigenphases and eigenvectors are determined, denoted by $|\alpha_0^{(i)}\rangle$, $i = 1, \dots, N_{trunc}$; $\langle m | \alpha_0^{(i)} \rangle = \alpha_m^{(i)}$.
2. A second diagonalization is performed at $k + \Delta k$, where Δk is a small complex number so that $|\Delta k| \ll k$.
3. Approximate radial and angular eigenphase speeds are determined.
4. Assuming the constancy of the individual speeds, an approximate quantization wavevector $k_q^{(i)}$ is determined for each of the initial eigenvectors.

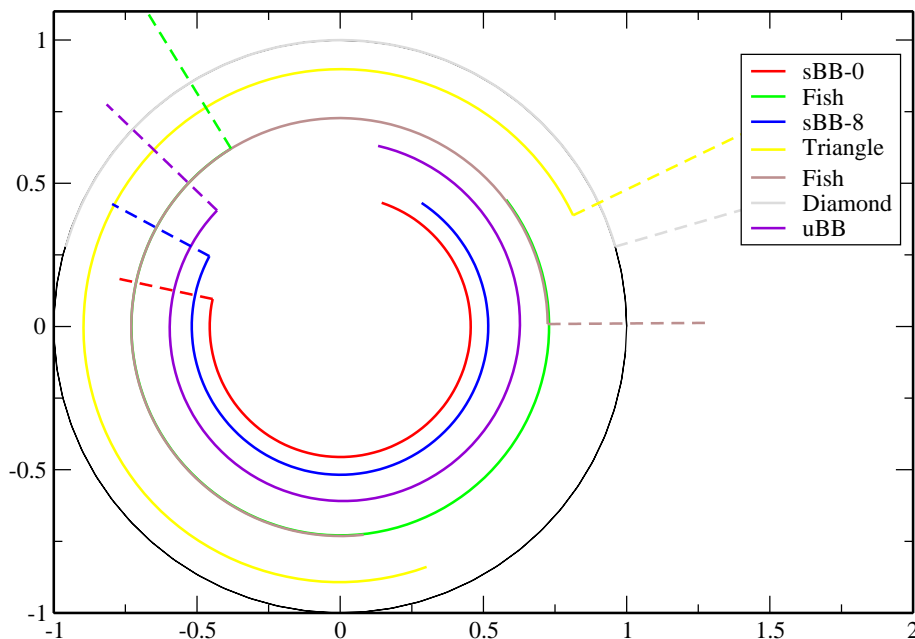


Figure 3.8: Several representative eigenphases traced in the complex plane through real and imaginary values of k . At first, real $\text{Re}[k]$ is varied, resulting in the circular arcs; subsequently $\text{Im}[k]$ is varied resulting in a radial motion. The simulations are performed at $\epsilon = 0.12$ quadrupolar deformation, $n = 2.65$.

5. Finally, the quasi-bound modes are constructed by

$$\psi_q^{(i)}(r, \phi) = \sum_{m=-\Lambda}^{\Lambda} \alpha_m^{(i)} J_m(nk_q^{(i)}r) e^{im\phi} \quad (3.72)$$

Due to the small change in $\{\alpha_m^{(i)}\}$ with k , we simply use their non-quantized values in the expansion with the extrapolated k -value $k_q^{(i)}$. We have checked that it's important to use $k_q^{(i)}$ instead of the original k .

In the ideal case, this means the determination of N_{trunc} quasi-bound modes in only two diagonalizations. In practice, this ideal limit is not attained. But, depending on the deformation and the value of nkR , a varying fraction of quasi-bound modes can be calculated approximately. Table Fig. 3.1 shows a typical run and the quality of the results compared to “exact” solutions.

The implementation of the algorithm can be adapted to the particular result of interest. In fact, when the quantization of a single state is desired, a more exact eigenphase quantization can be performed by multiple-scans with update of the speeds, quite like Newton's root-search method. However, the actual power of this approach, even if not applied as described above, lies in two aspects: Firstly, it gives a *discrete* set of states in one diagonalization, in contrast to methods based on external scattering approach. Second, the calculated scattering eigenstates have a conserved physical identity over a mean-level spacing and are in most cases related in

Table 3.1: A typical run at $kR_0 = 40$, $\epsilon = 0.12$ and $n = 2.65$. The first column represents the predicted value by constant speed requirement determined from two successive diagonalizations separated by $\Delta kR = 10^{-4} + i10^{-4}$. The second column is the error of this prediction, obtained by a full root search, measured by the distance in the complex plane between the eigenphase and the quantization point. The last two columns are the overlaps of the original eigenvectors (internal and external) with the actual quantized ones.

kR_q	$ e^{i\varphi} - 1 $	$\langle \alpha_q \alpha_0 \rangle$	$\langle \gamma_q \gamma_0 \rangle$
40.530139923096 - $i0.128341300297e - 03$	0.1049356E-01	0.935212779	0.815777069
40.354640960693 - $i0.346842617728e - 02$	0.2512625E-01	0.800668216	0.888131129
40.362663269043 - $i0.262046288699e - 01$	0.3483059E-01	0.875476530	0.959173141
40.597846984863 - $i0.617872737348e - 02$	0.4986330E-01	0.885584168	0.902043947
40.760002136230 - $i0.517168489750e - 03$	0.2216994E-02	0.900596963	0.598602624
39.372772216797 - $i0.782183464617e - 02$	0.3692186E-01	0.670832741	0.857146071
39.384689331055 - $i0.253524887376e - 02$	0.1560470E-01	0.644713713	0.768504668
39.524833679199 - $i0.416035996750e - 03$	0.6675268E-02	0.918124783	0.571120689
40.427906036377 - $i0.654014274478e - 01$	0.2790542E-02	0.989788008	0.989591927
40.367130279541 - $i0.640191137791e - 01$	0.2049567E-01	0.949528775	0.983221172
40.508068084717 - $i0.814560204744e - 01$	0.1035770E-02	0.979746925	0.983924594
40.537075042725 - $i0.717425644398e - 01$	0.6688557E-01	0.910022901	0.939244195
40.627620697021 - $i0.913884192705e - 01$	0.8095847E-02	0.858722180	0.846152346
39.421646118164 - $i0.850722268224e - 01$	0.5916540E-01	0.906494113	0.943557886
39.419769287109 - $i0.566106282349e - 04$	0.1063111E-01	0.939688864	0.531911062
39.733528137207 - $i0.175021495670e - 01$	0.3724663E-01	0.783724495	0.988899106
39.563480377197 - $i0.650179386139e - 01$	0.1242726E-02	0.990091490	0.989958495
39.685890197754 - $i0.770573019981e - 01$	0.1809454E-01	0.936621212	0.951369186
39.650619506836 - $i0.790241658688e - 01$	0.1439820E-01	0.934294618	0.935693384
39.369716644287 - $i0.169137448072e + 00$	0.3348814E-03	0.999949714	0.999923966
40.361137390137 - $i0.111876547337e + 00$	0.3443463E-02	0.998603169	0.996169638
40.389163970947 - $i0.635751348455e - 03$	0.3869480E-02	0.902893323	0.686779751
40.273880004883 - $i0.709924623370e - 01$	0.1889875E-02	0.987924322	0.995055099
40.207023620605 - $i0.329816946760e - 02$	0.5157299E-01	0.870880666	0.955577617
40.213146209717 - $i0.278946310282e - 01$	0.4355001E-01	0.850281901	0.996592453
39.904693603516 - $i0.224154405296e - 01$	0.2102797E-02	0.998176457	0.998674123
40.172363281250 - $i0.132210448384e + 00$	0.3454306E-03	0.999768065	0.999390566
40.137271881104 - $i0.873498693109e - 01$	0.6845250E-03	0.997220268	0.997824221
40.025264739990 - $i0.162262007594e + 00$	0.1378969E-03	0.999992333	0.999984896
40.064556121826 - $i0.597218498588e - 01$	0.1994631E-03	0.998558338	0.999194260
40.058116912842 - $i0.746092235204e - 03$	0.6044292E-02	0.948958619	0.983942653
39.997570037842 - $i0.659425705671e - 01$	0.1710776E-02	0.999267906	0.999318229
39.925022125244 - $i0.229551533266e - 04$	0.5157831E-04	0.999120149	0.934566350

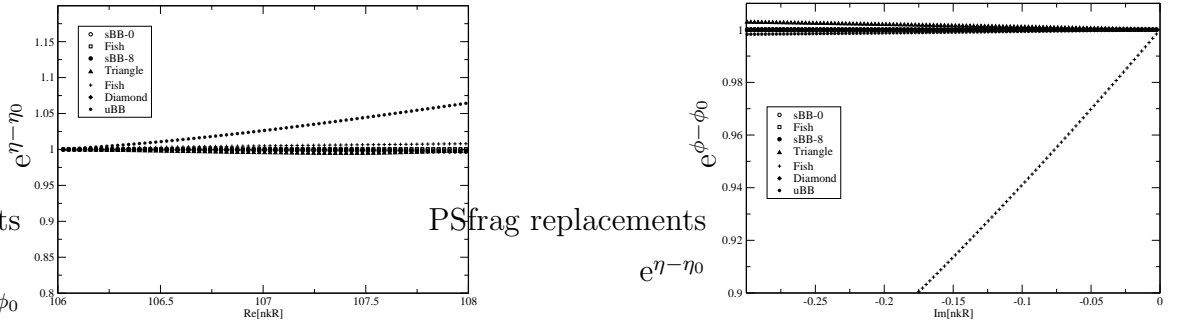


Figure 3.9: For the eigenstates of Fig. 3.8, variation of (a) $e^{\eta(k)}$ with change in $\text{Re}[k]$, (b) $e^{i\theta(k)}$ with change in $\text{Im}[k]$, normalized to initial values. Note that the variation is negligible. The larger variation of the second fish-eigenstate in (b) is due to an avoided crossing encountered during the imaginary k scan.

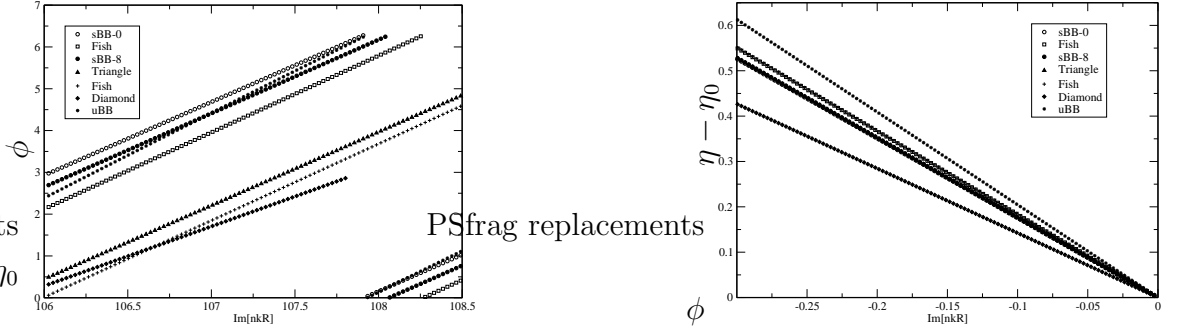


Figure 3.10: For the eigenstates of Fig. 3.8, variation of (a) $\theta(k)$ with a scan in $\text{Re}[k]$, (b) $\eta(k)$ with scan in $\text{Im}[k]$. Note that the variation in both cases display approximately constant slopes.

a simple way to the actual quasi-bound modes. For instance, the Husimi projections of the off-quantization eigenvectors are very close to the Husimi projections of the quantized counterparts. Another physical observable, which is unique to the open systems, is the farfield distribution. In typical micro-laser experiments, this is the quantity recorded and is one of the few clues a theorist has as to what is going on inside the resonator. Our algorithm is very efficient in providing a good idea of the possible farfields achievable with a given resonator shape and index of refraction. At a given k which is chosen close to the lasing frequency $\omega = ck$, we solve the scattering problem without reference to any quantization condition. The farfields are computed from the external wavefunction Eq. (3.24) by noting that the asymptotic form of the Hankel function for *large arguments* given by Eq. (3.26)

$$I(\phi) = \left| \sum_m \gamma_m e^{im(\phi - \frac{\pi}{2})} \right|^2, \quad (3.73)$$

where we have extracted all the quantities independent of m and ϕ . Experience shows that the farfield intensity distributions computed in this way are very well

behaved and insensitive to the k -value used, mainly because it does not include the at-times violent Hankel functions. The farfields computed in this way are virtually identical those obtained from the quantized modes within the linewidth of the laser.

On the other hand, it has to be pointed out that an attempt to plot a scattering eigenstate $|\alpha\rangle$, $e^{i\varphi}$ away from quantization is not meaningful because of the nature of the Hankel function basis. The internal field would be

$$\psi_1(r, \phi) = \sum_m \alpha_m (\mathbf{H}_m^+(nkr) + e^{i\varphi} \mathbf{H}_m^-(nkr)) e^{im\phi} \quad (3.74)$$

The existence of the factor $e^{i\varphi}$ exposes the z^{-m} singularity at the origin due to the Neumann components $N_m(z) = i(\mathbf{H}_m^-(z) - \mathbf{H}_m^+(z))$. That is one reason that we must use k_q in Eq.(3.72). This limitation is an artifact of the particular basis used, and does not arise for example for the case of an expansion in cartesian modes.

3.6 Scattering eigenstates and classical phase space structures

In this section, we would like to illustrate the relation between the scattering eigenvectors and classical phase space structures using the results generated by the numerical algorithm described in the previous section. Simultaneously, we will use this opportunity to back up some of the semiclassical ideas laid out in Chapter 2 with numerical results. We note at the beginning that the real-space plots and the Husimi distributions are constructed using the *unquantized* scattering eigenvectors, as we described in the previous section. For definiteness we will consider quadrupolar deformations

$$R(\phi) = 1 + \epsilon \cos 2\phi \quad (3.75)$$

parametrized by the deformation parameter ϵ . Consider first the near-integrable regime in the deformation. In Fig. 3.11(a), we plot a whispering gallery mode of the circle at $\epsilon = 0$ and in Fig. 3.11(b) is plotted a state which emits from the highest curvature points $\phi = 0, \pi$. The inspection of the respective Husimi distributions shows clearly that the first state is localized on an invariant curve $\sin \chi = \text{const.}$ and is totally internally reflected, because the localization is on $\sin \chi > \sin \chi_c$. Note that the second state is a deformed whispering gallery mode predicted by Lazutkin's theorem, localized on an invariant curve of the form Eq. (2.136).

Large stable islands in the SOS can support multiple modes. A typical sequence of such modes is shown in Fig. 3.12. These modes are Fabry-Perot-like modes associated with the stable bouncing ball motion. In Chapter 4 we will see that the higher order modes correspond to transverse excited modes, i.e. have multiple nodes transverse to the ray trajectory corresponding to the associated fixed point. In general, it's possible to find such series of modes corresponding to any stable island of sizable extent in the SOS.

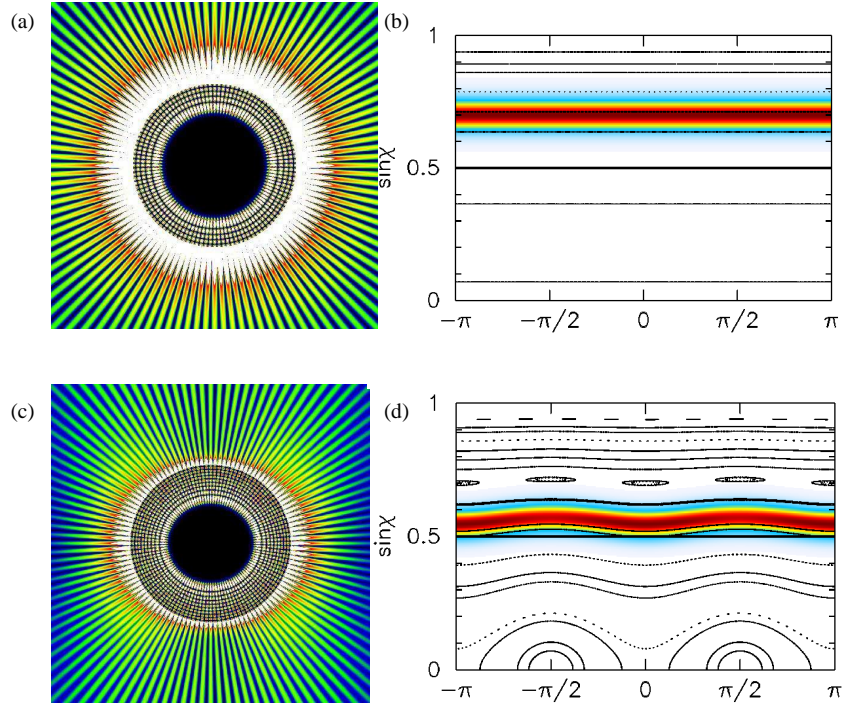


Figure 3.11: Real-space false color plot of a solution at (a) $\epsilon = 0$, and (c) $\epsilon = 0.03$. (b,d) Husimi projections of states (a,c). The solutions are obtained at $nkR = 82$ and $n = 2$.

The importance of periodic orbits is not limited to stable orbits. There is an infinite number unstable periodic orbits in the SOS. As will be argued in Chapter 5, short periodic orbits, especially those which are least unstable, can make their presence felt in the mode structure of the resonators. Such scarred modes, which display an enhanced intensity along an unstable periodic orbit, are widely studied [103, 80]. In numerical studies of Refs.[133, 70], evidence was found that modes can localize not only on the unstable fixed points but on their associated stable and unstable manifolds as well. In Fig. 3.13(a)-(f) we show a series of three states associated with the shortest unstable periodic orbit of the system, the unstable bouncing ball orbit. Note that the first mode represents the “fundamental” mode which localizes on the fixed point itself (see Fig. 3.13(b)). The real-space plots Fig. 3.13(c) and Fig. 3.13(e) don’t show any distinct structure. Their respective Husimi plots Fig. 3.13(d) and Fig. 3.13(f), however reveals that the modes localize on the heteroclinic intersections of the stable and unstable manifolds emanating from the unstable bouncing ball fixed points. A similar behavior was reported in Ref. [70] in the context of a quantum billiard.

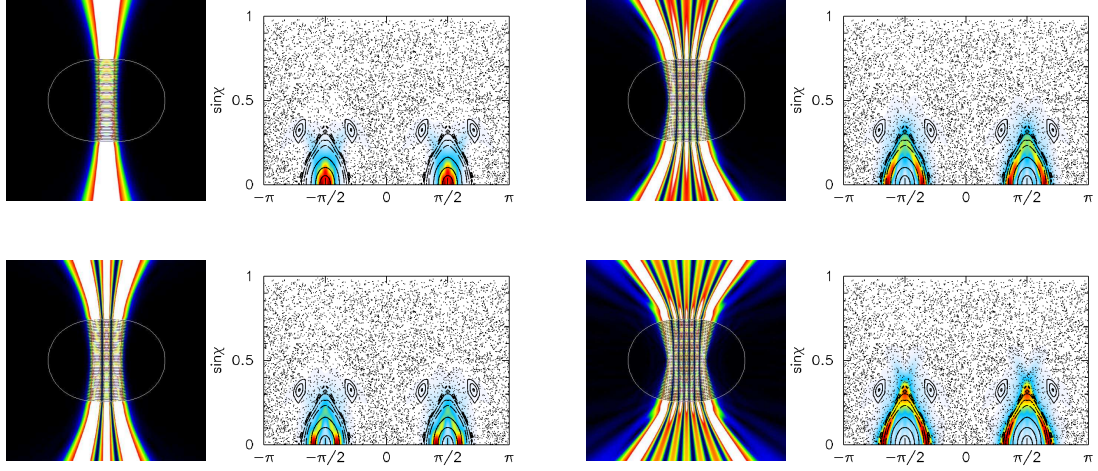


Figure 3.12: Real-space false color plots and Husimi projections of transverse excited bouncing ball modes. The solutions are obtained at $nkR = 106$ and $n = 2$.

3.7 Role of discrete symmetries

To be specific, we will again consider the example of a quadrupole. The symmetry rules we find are easily generalized by abstract group theoretic notation and arguments.

We will consider the problem of symmetries from two standpoints. First, we will use the geometric symmetry of the boundary conditions to reduce the size of our numerical system and classify the solutions. This is a rather straightforward application of group theory to the solutions of Helmholtz equation. Next, we will investigate the effects of the symmetries of the classical motion on the eigenphase distribution and the eigenvectors. Note that in the latter case the symmetries act in the phase space instead of the configuration space.

The symmetry group of the quadrupole is the point group $C_2 \otimes C_2 = (1, \sigma_x, \sigma_z, \sigma_{xz})$, the group of reflections with respect to semi-minor (z) and semi-major (x) axes of the quadrupole ($\epsilon > 0$), discussed in Section 4.10. Note that we define

$$\sigma_x : \phi \rightarrow -\phi \quad (3.76)$$

$$\sigma_z : \phi \rightarrow \pi - \phi \quad (3.77)$$

$$\sigma_{xz} : \phi \rightarrow \pi + \phi \quad (3.78)$$

The corresponding projection operators are given by

$$\mathcal{P}_{++} = \frac{1}{4}(1 + \sigma_z + \sigma_x + \sigma_{xz}) \quad (3.79)$$

$$\mathcal{P}_{+-} = \frac{1}{4}(1 + \sigma_z - \sigma_x - \sigma_{xz}) \quad (3.80)$$

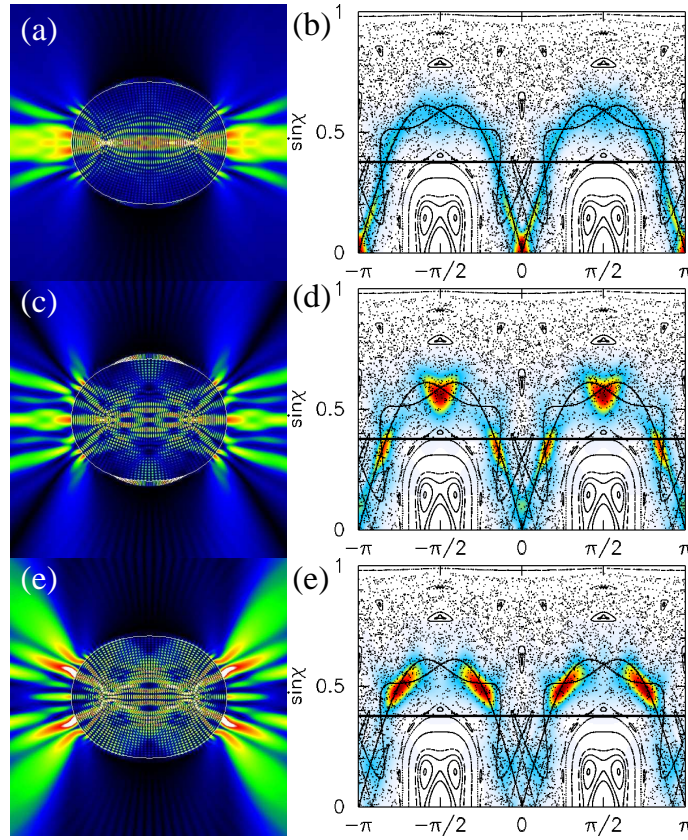


Figure 3.13: Real-space plots and Husimi distributions of scattering eigenvectors scarred by the unstable bouncing ball orbit. Superimposed on the SOS are the stable and unstable manifolds. (a),(b) fundamental mode; (c),(d) eigenvector scarred by (c),(d) the primary intersection and (e),(f) the secondary intersection. These solutions are found at $nkR = 106$, $\epsilon = 0.12$ and $n = 2.65$.

$$\mathcal{P}_{-+} = \frac{1}{4}(1 - \sigma_z + \sigma_x - \sigma_{xz}) \quad (3.81)$$

$$\mathcal{P}_{--} = \frac{1}{4}(1 - \sigma_z - \sigma_x + \sigma_{xz}) \quad (3.82)$$

Note that the label $(+, -)$ signifies that the corresponding symmetry projected solution has a node on x -axis and an anti-node on the z -axis. Let us now proceed to reduce the size of the eigensystem for the solution subspace with $(+, +)$ parity. For this we apply the corresponding projection operator on the Eqns. (3.30-3.31) to get, for example for (3.30)

$$\sum_{m=1}^{\Lambda} (\alpha_m + \tilde{\alpha}_m)(1 + e^{i\pi m})H_m^+(nkR(\phi)) \cos m\phi + \dots \quad (3.83)$$

where $\tilde{\alpha}_m = (-1)^m \alpha_{-m}$ etc. Thus every other element of the matrix vanishes. De-

noting $\xi_m = \alpha_{2m} + \tilde{\alpha}_{2m}$, we obtain the symmetry reduced equation

$$\mathcal{S}_{++}|\xi\rangle = e^{i\varphi_{++}}|\xi\rangle \quad (3.84)$$

where the individual blocks are quarter of their original sizes given by

$$\left[(D)\tilde{H}_j^\pm \right]_{lm} = \int_0^{\frac{\pi}{2}} d\phi \mathbf{H}_{2m}^{(l)}(n_j k R(\phi)) \cos 2m\phi \cos 2l\phi \quad (3.85)$$

in a rather condensed notation. Thus, the numerical diagonalization time can be reduced sixteen-fold if one wishes to determine symmetry-reduced eigenvectors of a specific type.

We have established that the classical phase space structure plays an important role in the structuring of the eigenvectors and quasi-normal modes. Hence, we would expect the symmetries of the classical SOS to manifest itself in determining the symmetry structure of the eigenvectors. In fact, the symmetry of the classical SOS can impose interesting limitations. A simple observation is for example that the fundamental mode of the bouncing-ball orbit can come only in two symmetry types: $(++)$ and $(+-)$, because it can't have a nodal line on the z -axis. Similarly, its transverse excitations can only display certain symmetry types and not others. We will return to this point in more detail in the next chapter.

An important observation is that in a single diagonalization, a given stable periodic orbit will have as many scattering eigenvectors associated with it (only the fundamental mode is counted) as the number of its bounces. These will be grouped together according to rules laid out in Sect. 4.11.

3.8 Conclusion and Outlook

There are two main limitations to the application of the numerical method reported in this chapter to higher values of k and higher deformations. The first limitation is related to the basis used to expand the scattering eigenvectors. Although the Hankel function basis has a nice semiclassical interpretation, representing the quantization of the canonical momentum of the SOS, the resulting Hankel function series is ill-conditioned. The breakdown of the numerical expansion can easily be observed on the real-space plots at the flattest part of the boundary, where $r = R_{min}$. The evanescent components ($m > kR_{min}$) take on very large values, and thus the solution becomes hyper-sensitive to the errors in their coefficients. On the other hand, a number of these channels have to be incorporated in order to get a sensible solution. It's often a good practice to diagonalize with many evanescent channels, but use only a fraction of the low-lying ones (in m) when plotting.

This problem may be overcome by using a shape-adapted basis. There are only a few possible choices, which are defined by separable coordinates. A good choice seems to be the modes of the elliptic coordinates. These are the Mathieu functions [89]. An important property of this set is that they are parametrized by the eccentricity

of the elliptic coordinates used. Thus it's highly promising to use the Mathieu basis set with the closest eccentricity to the shape under consideration.

The other limitation is the proliferation of avoided crossings at higher wavevectors k and deformations. This seems to be a fundamental difficulty inherent in the method.

Chapter 4

Gaussian Optics for Microcavities

4.1 Introduction

In Chapter 2, we found that a generic deformation such as the quadrupole will lead to a phase space for ray motion which has three types of possible motion (depending on the choice of initial conditions): oscillatory motion in the vicinity of a stable periodic ray orbit, chaotic motion in regions associated with unstable periodic ray orbits, and marginally stable motion associated with families of quasi-periodic orbits. The three types of motion described above are illustrated for the quadrupole billiard in Fig. 4.1 both in phase space and in real space.

We also found that the solutions of the wave equation for a generic shape such as the quadrupole can be classified by their association with these three different kinds of motion. The ray-mode (or wave-particle) correspondence becomes stronger as we approach the short-wavelength (semi-classical) limit, which in this work is defined by $kl \gg 1$ where k is the wavevector and l is a typical linear dimension of the resonator, e.g. the average radius. The modes associated with quasi-periodic families can be treated semiclassically by eikonal methods of the type introduced in Section 2.4 and 2.10, and referred to in its most general form as EBK (Einstein-Brillouin-Keller) quantization. The *individual* modes associated with unstable periodic orbits and chaotic motion cannot be treated by any current analytic methods (although spectrally and spatially averaged mode intensities and density of states can be found by analytic methods based on Gutzwiller's Trace Formula [134] and related methods; a discussion of these methods can be found in Chapter 5). Finally, the modes associated with stable periodic orbits can be treated by generalizations of gaussian optics and will be the focus of the current chapter. We remind the reader that such modes associated with stable bow-tie orbits were responsible for the dramatic lasing properties of quantum cascade lasers measured by Gmachl et al. [5]. It should be pointed out that the *spectra* of modes associated with stable periodic orbits can also be treated by the periodic orbit approach mentioned above and in the *stable* case explicit quantization rules can be found which are equivalent to our results for the closed cavity derived below [135].

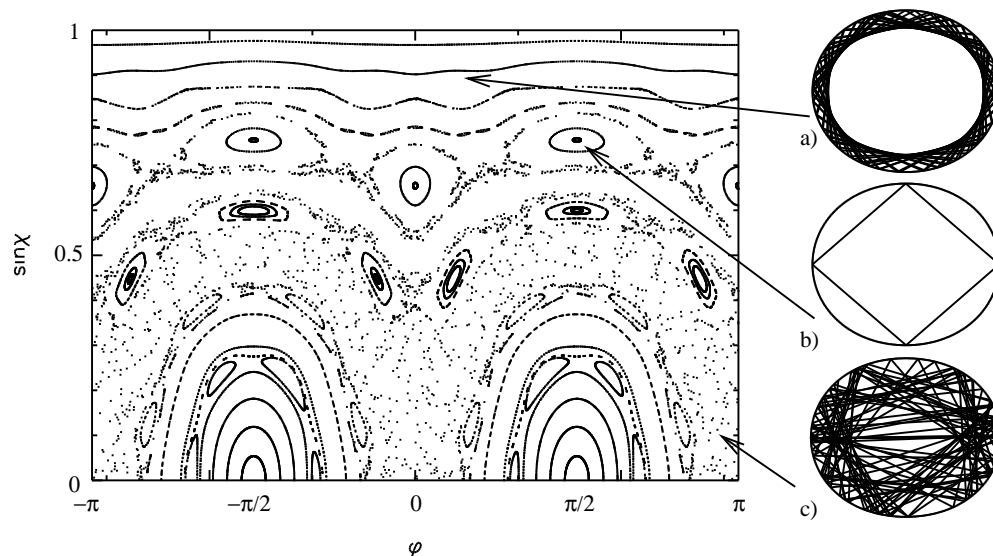


Figure 4.1: Surface of section illustrating the different regions of phase space for a closed quadrupole billiard with boundary given by $r(\phi) = R(1 + \epsilon \cos 2\phi)$ for $\epsilon = 0.072$. Real-space ray trajectories corresponding to each region are indicated at right: a) A quasi-periodic, marginally stable orbit. b) A stable four-bounce “diamond” periodic orbit (surrounded by stability “islands” in the SOS) c) A chaotic ray trajectory. Orbits of type (b) have associated with them regular gaussian solutions as we will show below.

Consider a mode is found by numerical solution, its interpretation in terms of the ray phase space can be determined with reasonable accuracy by means of the Husimi projection (cf. Section 2.11) onto the phase space (see Fig. 4.2), although as we pointed out before, for kl not much greater than unity the exact solutions tend to smear out in the phase space over regions of order $1/kl$ and do not correspond very closely to specific classical structures. For a closed generic ARC the full spectrum will look highly irregular (see Fig. 4.3(a)), but contained in the full spectrum will be regular sequences associated with tori and stable periodic orbits (Fig. 4.3(b)). The stable periodic orbit modes will give the simplest such sequences consisting of two different constant spacings, one associated with the longitudinal quantization of the orbit (free spectral range) and the other associated with transverse excitations. In the example of Fig. 4.3 the imbedded regular spectrum is due to the stable “bow-tie” orbit. The regular portion of the spectrum is extracted by weighting each level by the overlap of its Husimi function with the islands corresponding to the stable periodic orbit in the surface of section. Clearly, hidden within this complex spectrum are simple regular mode sequences of the type familiar from Gaussian optics. In the current chapter we show how to calculate the resonant energies and spatial intensity patterns of such modes associated with arbitrary stable periodic ray orbits for both the ideal closed resonator and a dielectric resonator of the same shape with arbitrary dielectric mismatch n . We shall refer to these as periodic orbit modes or PO modes.

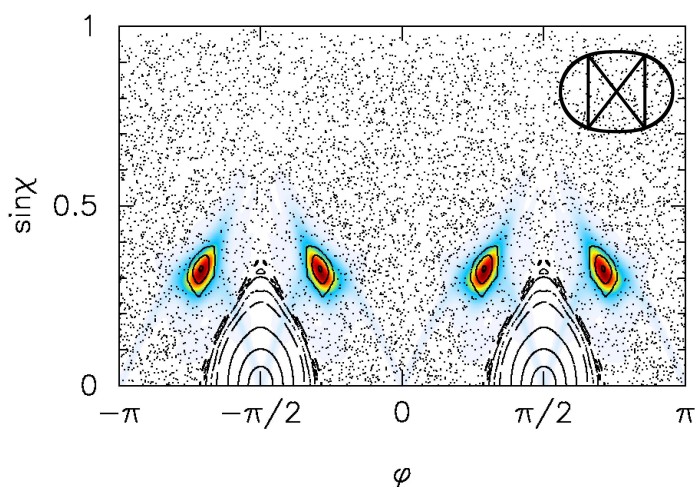


Figure 4.2: Black background gives the surface of section for the quadrupole at $\epsilon = 0.17$ for which the four small islands correspond to a stable bow-tie shaped orbit (inset). A numerical solution of the Helmholtz equation for this resonator can be projected onto this surface of section via the Husimi projection (cf. Section 2.11) and is found to have high intensity (in false color scale) precisely on these islands, indicating that this is a mode associated with the bow-tie orbit.

The treatment of this chapter is based on the *parabolic equation approximation* and related technical machinery, which was originally employed for the construction of the modes of multi-mirror resonators [66] among other problems. More recently, the application of these techniques to dielectric resonators was suggested by Nöckel in Ref. [136]. The current chapter is an extension of the work of the author and collaborators published in [137].

In the case of the open resonator, the modes have a width which can be expressed as a negative imaginary part of k , and some of the PO modes may be so broad (short-lived) that they would not appear as sharp spectral lines. Conversely there can be many long-lived modes associated with the chaotic regions, due to scarred states [52, 51, 53, 138] or dynamically localized states [139, 140] which are localized in the region of phase space above the critical angle for total internal reflection. Therefore it is not the case that all the high-Q modes are based on stable POs and describable by the theory below. Within the gaussian-optical theory we present below the width of the PO modes is entirely determined by Fresnel reflection at the interface and would be zero for a periodic orbit which has all bounces above the total internal reflection condition, but would be quite large for a periodic orbit, such as the two-bounce Fabry-Perot orbit, which has normal incidence on the boundary. An exact solution must find a non-zero width for *all* PO modes, due to evanescent leakage across a curved interface, even if all the bounces satisfy the total internal reflection condition. This same shortcoming was found for the EBK-quantized modes of integrable dielectric cavities discussed in Chapter Two.

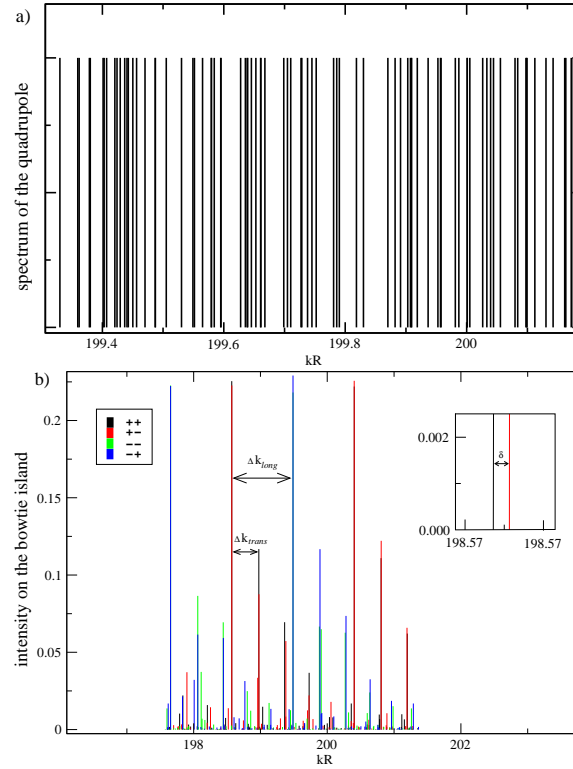


Figure 4.3: (a) Vertical lines indicate wavevectors of bound states of the closed quadrupole resonator for $\epsilon = 0.17$; no regular spacings are visible. (b) Spectrum weighted by overlap of the Husimi function of the solution with the bow-tie island as in Fig. 4.2. Note the emergence of regularly spaced levels with two main spacings Δk_{long} and Δk_{trans} . These spacings, indicated by the arrows, are calculated from the length of the bow-tie orbit and the associated Floquet phase (see Section 4.5 below). The color coding corresponds to the four possible symmetry types of the solutions (see Section 4.9 below). In the inset is a magnified view showing the splitting of quasi-degenerate doublets as discussed in 4.11. Note the pairing of the $(+, +)$ and $(+, -)$ symmetry types as predicted in Section 4.11. The different symmetry pairs alternate every free spectral range (Δk_{long}).

Another limitation of the gaussian theory of stable PO modes is that it predicts exactly degenerate modes when the associated orbit has discrete symmetries, even in cases for which a group-theoretic analysis shows that there can be no exact symmetries (this is the case, for example in the quadrupole). Instead the exact solutions will have some integer *quasi-degeneracy* in which the spectrum consists of nearly degenerate multiplets, whose multiplicity depends in detail on the particular PO mode. This point is illustrated by the inset to Fig. 4.3(b). We will show in Section (4.9) how to calculate the multiplicity of these quasi-degeneracies for a given PO.

4.2 Gaussian Optical approach to the Dirichlet cavity

Our aim is to project out the class of modes among the eigensolutions of the Helmholtz equation with Dirichlet boundary conditions

$$(\nabla^2 + k^2) \psi = 0, \quad \psi|_{\partial D} = 0 \quad (4.1)$$

which are localized on stable periodic ray orbits of the corresponding classical billiard. Because a local description is required, we will work in a local coordinate system on the periodic orbit, which is described in Fig. 4.4 and in more detail in Appendix C.

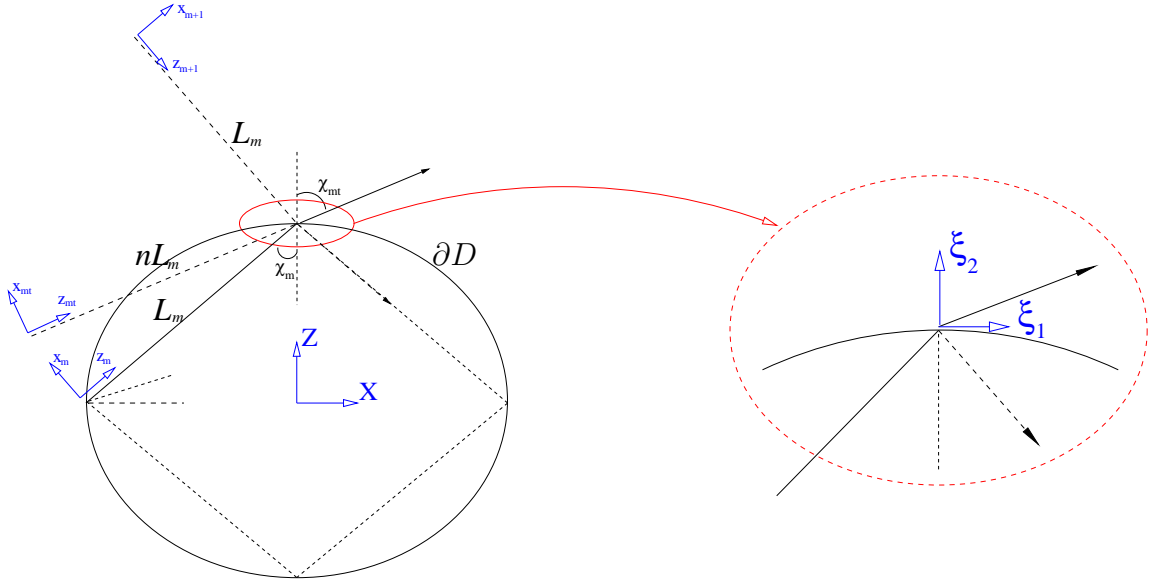


Figure 4.4: Coordinate systems used in the calculations. Only one of the bounces, the m^{th} bounce, is illustrated.

For a uniform medium, the rays orbits are straight lines. The “N-bounce PO”’s corresponding to a boundary ∂D are then the set of ray orbits which close upon themselves upon reflecting specularly N times. For a given period-N orbit (such as the period four “diamond” orbit shown in Fig. 4.4), let the length of m th segment (“arm”) be l_m , the accumulated distance from origin be $L_M = \sum_{m=1}^M l_m$, and $L = L_N$ be the length of the entire PO. We are looking for modal solutions which are localized around the PO and decay in the transverse direction, hence we express Eq. (4.1) in *Cartesian coordinates* (x_m, z_m) attached to the PO, where z_m -axis is aligned with m th arm and x_m is the transverse coordinate. We also use z to denote the cumulative length along the PO, which varies in the interval $(-\infty, +\infty)$.

We write the general solution as:

$$\psi(X, Z) = \sum_{m=1}^N \psi_m(x_m(X, Z), z_m(X, Z)) \quad (4.2)$$

where the “local set” (x_m, z_m) and the fixed set (X, Z) are related by shifts and rotations (see Appendix C). Next, in accordance with the parabolic equation approximation [66], we assume that the main variation of the phase in z -direction is linear (“slowly varying envelope approximation”)

$$S(z) = \int_{z_0}^z dz' \quad (4.3)$$

and factor it out:

$$\psi_m(x_m, z_m) = u_m(x_m, z_m) e^{ikz_m} \quad (4.4)$$

Here, we defined the origins of the local coordinates such that $z_m = z$ along the PO (see Fig. 4.4).

Next, we insert the solution Eq. (4.2) into Eq. (4.1) and using the invariance of the Laplacian, we obtain:

$$(\nabla_m^2 + k^2) \psi_m = 0 \quad (4.5)$$

and the boundary condition translates into

$$\psi_m + \psi_{m+1}|_{\partial D} = 0 \quad (4.6)$$

Here ∇_m is the Laplacian expressed in local coordinate system. This reduction is possible as long as the solutions are well-localized, and the bounce points of the PO are well-separated (with respect to k^{-1}), even if the PO were to self-intersect. These assumptions will be justified by the ensuing construction.

Dropping for the moment the arm index, we will focus on Eq. (4.5). Inserting Eq. (4.4), we obtain the partial differential equation

$$\frac{\partial^2 u}{\partial x^2} + \frac{\partial^2 u}{\partial z^2} + 2ik \frac{\partial u}{\partial z} = 0 \quad (4.7)$$

If we were to do a regular perturbation expansion in the small parameter $\epsilon = 1/k$, i.e. $u = \sum_n \epsilon^n u^{(n)}$, we would end up with the equation for the lowest order term

$$\frac{\partial u^{(0)}}{\partial z} = 0 \quad (4.8)$$

which has a solution $u^{(0)} = u^{(0)}(x)$. One can check that the application of boundary conditions at each z on the solution Eq. (4.2) constructed from $u^{(0)}$ of this form would lead to the trivial solution $\psi \equiv 0$ (considering for instance the simplest case of a bouncing ball orbit, for which $N = 2$ in Eq. (4.2)). The main culprit for the futility of a regular perturbation expansion is that $k \rightarrow \infty$ in Eq. (4.7) is a singular limit.

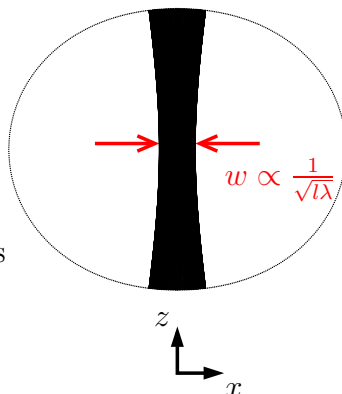


Figure 4.5: The bouncing ball mode transverse width is of the order of $1/\sqrt{k}$. The periodic orbit axis is also indicated.

A perturbation problem where the small parameter multiplies the highest derivative term(s) is a *singular perturbation* problem [86], and needs generically a careful treatment based on a priori knowledge about qualitative features of the expected solutions.

In our case, the failure of the regular perturbation expansion can be understood as follows. It's known from model problems [141] and numerical solutions that the modes localize on the periodic orbits in a narrow layer of the order of $\sqrt{l\lambda}$, where l is a typical linear dimension associated with the resonator (curvature of the boundary, size of resonator) (see Fig. 4.5). Hence, on the transverse section, the solutions will have a very fast variation, i.e. there will be a *boundary layer*, so that $u_{xx} \sim \frac{k}{l}u$. On the other hand, we assume that we have factored out the fast z -variation in Eq. (4.4), hence $u_z \sim u/l$, $u_{zz} \sim u/l^2$. We immediately see that it becomes illegitimate to drop the first term u_{xx} in Eq. (4.7), because it's of the same order as the last term.

It's standard in boundary layer theory [86, 142], on which the parabolic equation approximation is based, to stretch the “fast” variable (x) with the appropriate scale. Hence, we introduce the scaled variable $\tilde{x} = k^{1/2}x$, then apply a perturbation theory to the equation written the coordinates (\tilde{x}, z)

$$\frac{\partial^2 u}{\partial \tilde{x}^2} + \frac{1}{k} \frac{\partial^2 u}{\partial z^2} + 2i \frac{\partial u}{\partial z} = 0 \quad (4.9)$$

and arrive at the expansion of the original Helmholtz operator $\mathcal{L} = \nabla^2 + k^2$ in powers of k^{-1} :

$$\mathcal{L} = \mathcal{L}_0 + \frac{1}{k} \mathcal{L}_1 \quad (4.10)$$

where

$$\mathcal{L}_0 = \frac{\partial^2}{\partial \tilde{x}^2} + 2i \frac{\partial}{\partial z} \quad (4.11)$$

$$\mathcal{L}_1 = \frac{\partial^2}{\partial z^2} \quad (4.12)$$

The zeroth order problem

$$\mathcal{L}_0 u^{(0)} = 0 \quad (4.13)$$

is a partial differential equation of parabolic type, of the same form as the Schrödinger equation. Next, we make the ansatz

$$u^{(0)}(\tilde{x}, z) = c A(z) \exp \left[\frac{i}{2} \Omega(z) \tilde{x}^2 \right] \quad (4.14)$$

Inserting Eq. (4.14) into Eq. (4.13) and requiring it to be satisfied for all x , we obtain the relations

$$\Omega^2 + \Omega' = 0 \quad (4.15)$$

$$A\Omega + 2A' = 0 \quad (4.16)$$

Here and in the rest of the text we will use primes as a shorthand notation for a z -derivative. Next, making the substitution

$$\Omega = \frac{Q'(z)}{Q(z)} \quad (4.17)$$

we obtain

$$Q'' = 0 \quad (4.18)$$

$$\frac{Q'}{Q} + 2\frac{A'}{A} = 0 \quad (4.19)$$

Note that Eq. (4.18) is the Euler equation for ray propagation in a homogeneous medium with general solution $Q(z) = \alpha z + \beta$; we will be able to interpret $Q(z)$ below as describing a ray nearby the periodic orbit with relative angle and intercept determined by α, β .

4.3 Boundary Conditions

Having found the general solution of Eq. (4.13) along one segment of the periodic orbit we must impose the boundary condition Eq. (4.6) in order to connect solutions in successive segments. Writing out this condition:

$$\begin{aligned} & \frac{c_m}{\sqrt{Q_m(z_m)}} \exp \left(ikz_m + \frac{i}{2} \Omega(z_m) \tilde{x}_m^2 \right) \\ & + \frac{c_{m+1}}{\sqrt{Q_{m+1}(z_{m+1})}} \exp \left(ikz_{m+1} + \frac{i}{2} \Omega(z_{m+1}) \tilde{x}_{m+1}^2 \right) \Big|_{\partial D} = 0 \end{aligned}$$

This equation must be satisfied on an arc of the boundary of length $\sim \sqrt{\lambda l}$ around the reflection point. Since this length is much smaller than l we can express this

arc on the boundary ∂D as a quadratic curve, i.e. a parabola in this case, with ϱ being the curvature at the reflection point. We express the boundary condition in a (scaled) common local coordinate system for the incident and reflected fields $(\tilde{\xi}_1, \tilde{\xi}_2)$ pointing along the tangent and the normal at the bounce point (see Appendix C for an overview of the coordinate systems used), so that the equation for the boundary becomes

$$\tilde{\xi}_2 = -\frac{\tilde{\xi}_1^2}{2k\varrho_m} \quad (4.20)$$

Because the boundary condition must be satisfied on the entire arc it follows the phases of each term must be equal,

$$\begin{aligned} k \left(l_m + \frac{1}{\sqrt{k}} \tilde{\xi}_1 \sin \chi_m - \frac{1}{k} \frac{\tilde{\xi}_1^2}{2\varrho_m} \cos \chi_m \right) + \frac{1}{2} \frac{Q'_m}{Q_m} \left(\tilde{\xi}_1 \cos \chi_m + \frac{1}{\sqrt{k}} \frac{\tilde{\xi}_1^2}{2\varrho_m} \sin \chi_m \right)^2 = \\ k \left(l_m + \frac{1}{\sqrt{k}} \tilde{\xi}_1 \sin \chi_m + \frac{1}{k} \frac{\tilde{\xi}_1^2}{2\varrho_m} \cos \chi_m \right) + \frac{1}{2} \frac{Q'_{m+1}}{Q_{m+1}} \left(-\tilde{\xi}_1 \cos \chi_m + \frac{1}{\sqrt{k}} \frac{\tilde{\xi}_1^2}{2\varrho_m} \sin \chi_m \right)^2 \end{aligned}$$

and there is a amplitude condition as well,

$$\frac{c_m}{\sqrt{Q_m(L_m)}} + \frac{c_{m+1}}{\sqrt{Q_{m+1}(L_m)}} = 0$$

Here, the implicit assumption is that $\tilde{\xi}_1 = O(1)$, and we will carry out the solution of these equations to $O(1/\sqrt{k})$. Note that, it is sufficient to take $Q(z)|_{\partial D} \approx Q(l_m)$, at this level. In each segment we have three constants which determine our solution: c_m, α_m, β_m (where $Q_m(z) = \alpha_m z + \beta$); however due to its form our solution is uniquely determined by the two ratios $\beta_m/\alpha_m, c_m/\sqrt{\alpha_m}$. Therefore we have the freedom to fix one matching relation for the Q_m by convention, which then determines the other two uniquely. Deviating slightly from standard definitions we fix $Q_{m+1} = -Q_m$, then the amplitude and phase equality conditions give the relations:

$$\begin{pmatrix} Q_{m+1} \\ Q'_{m+1} \end{pmatrix} = \begin{pmatrix} -1 & 0 \\ \frac{2}{\varrho_m \cos \chi_m} & -1 \end{pmatrix} \begin{pmatrix} Q_m \\ Q'_m \end{pmatrix} \equiv \mathcal{R}_m \begin{pmatrix} Q_m \\ Q'_m \end{pmatrix} \quad (4.21)$$

and

$$C_{m+1} = e^{-i\pi/2} C_m \quad (4.22)$$

Here we always choose the principal branch of \sqrt{Q} . These conditions allow us to propagate any solution through a reflection point via the reflection matrix \mathcal{R}_m and Eq. (4.22). Note that with these conventions the reflection matrix differs from the standard ‘‘ABCD’’ matrix of ray optics for reflection at arbitrary incidence angle (in the tangent plane) from a curved mirror [76] merely by a minus sign. That this transformation in fact describes the coordinate transformation of a ray before and after a reflection within the coordinate system used, is shown in Appendix D. The extra minus sign arises because of the adoption of a coordinate system which

conserves handedness. From the calculation given in the appendix, it follows that Q_m and Q_{m+1} can be interpreted as the transverse coordinates of the incident and reflected rays with respect to the PO, and that then Eq. (4.21) describes specular ray reflection at the boundary, if the non-linear dynamics is linearized around the reflection point.

4.4 Ray dynamics in phase space

To formalize the relation to ray propagation in the paraxial limit we define the ray position coordinate to be Q and the conjugate momentum $P = Q'$, with z playing the role of the time. Let's introduce the column-vector $\begin{pmatrix} Q \\ P \end{pmatrix}$. The ‘‘fundamental matrix’’ Π is the matrix obtained by two such linearly independent vectors

$$\Pi = \begin{pmatrix} Q_1 & Q_2 \\ P_1 & P_2 \end{pmatrix} \quad (4.23)$$

where the linear independence, as expressed by the Wronskian condition $W(Q', Q) \neq 0$ reduces to $\det \Pi \neq 0$. Then, for example, the Euler equation Eq. (4.18) in each arm can be expressed as

$$\frac{d\Pi}{dz} = \mathcal{J}\mathcal{H}\Pi \quad (4.24)$$

where $\mathcal{H} = \begin{pmatrix} 0 & 1 \\ 0 & 0 \end{pmatrix}$ and $\mathcal{J} = \begin{pmatrix} 1 & 0 \\ 0 & -1 \end{pmatrix}$. It's straightforward to show that

$$\det \Pi(z) = \text{constant} \quad (4.25)$$

To take into account the discreteness of the dynamics in a natural manner, we will introduce ‘‘coordinates’’ for the ray, represented by a z -independent column vector h . Any ray of the m th arm in the solution space of Eq. (4.24) can then be expressed by a z -independent column vector h_m

$$\begin{pmatrix} Q(z) \\ P(z) \end{pmatrix} = \Pi(z)h_m \quad (4.26)$$

We will choose $\Pi(z) = \begin{pmatrix} 1 & z \\ 0 & 1 \end{pmatrix}$, so that $\Pi^{-1}(z) = \Pi(-z)$. Then if $Q_m(z) = \alpha_m z + \beta_m$, we have $h_m = \begin{pmatrix} \beta_m \\ \alpha_m \end{pmatrix}$. In this notation, propagation within each arm (i.e. $z + l < L_m$ where $L_{m-1} < z < L_m$) is induced by the ‘propagator’ Π

$$\begin{pmatrix} Q_m(z+l) \\ P_m(z+l) \end{pmatrix} = \Pi(l) \begin{pmatrix} Q_m(z) \\ P_m(z) \end{pmatrix}. \quad (4.27)$$

Note that Π is the ‘‘ABCD’’ matrix for free propagation[76]. Thus, for example $z \rightarrow z'$ propagation for $L_{m-1} < z < L_m < z' < L_{m+1}$ is

$$\begin{pmatrix} Q_{m+1}(z') \\ P_{m+1}(z') \end{pmatrix} = \Pi(z' - L_m)\mathcal{R}_m\Pi(L_m - z) \begin{pmatrix} Q_m(z) \\ P_m(z) \end{pmatrix} \quad (4.28)$$

Of special importance is the monodromy matrix, $\mathcal{M}(z)$, which propagates rays a full round-trip, i.e. by the length L of the corresponding PO and is given by

$$\mathcal{M}(z) = \Pi(z - L_{m-1})\mathcal{R}_{m-1}\Pi(l_{m-1}) \cdots \Pi(l_{m+1})\mathcal{R}_m\Pi(L_m - z) \quad (4.29)$$

for $L_{m-1} < z < L_m$. Note that $l_{m+N} = l_m$ and $\mathcal{R}_{m+N} = \mathcal{R}_m$. Although the specific form of $\mathcal{M}(z)$ depends on the choice of origin, z , it is easily shown that all other choices would give a similar matrix and hence the eigenvalues of the monodromy matrix are independent of this choice. We will suppress the argument z below.

4.5 Single-valuedness and quantization

Having determined how to propagate an initial solution (Q, P) an arbitrary distance around the periodic orbit we can generate a solution of the parabolic equation which satisfies the boundary conditions by an arbitrary initial choice $Q(0), P(0)$. However, as we argued before, an arbitrary solution of this type will not reproduce itself after propagation by L (one loop around the PO). Recalling that our solution is translated back into the two-dimensional space (X, Z) by Eq. (4.2), and that the function $\psi(X, Z)$ must be single-valued, we must require periodicity for our solutions

$$\psi(x, z + L) = \psi(x, z). \quad (4.30)$$

We will suppress again the reference to arm index and use the notation $\psi(x, z) = \psi_m(x_m, z_m)$ and $u(x, z) = u_m(x_m, z_m)$ whenever $L_{m-1} < z < L_m$. Since the phase factor in ψ advances by $\exp[ikL]$ with each loop around the periodic orbit, single-valuedness implies that

$$u(x, z + L)e^{ikL} = u(x, z). \quad (4.31)$$

This periodicity condition will only be solvable for discrete values of k and will lead to our quantization rule for the PO modes.

From the form of u in Eq. (4.14) we see that the phase $\Omega(z) = Q'/Q$ will be unchanged if we choose (Q, P) to be an eigenvector (q_i, p_i) ($i = 1, 2$) of the monodromy matrix

$$\mathcal{M}\begin{pmatrix} q_i \\ p_i \end{pmatrix} = \lambda_i \begin{pmatrix} q_i \\ p_i \end{pmatrix} \quad (4.32)$$

as in this case $Q'(z + L) = \lambda_{1,2}Q'(z)$ and $Q(z + L) = \lambda_{1,2}Q(z)$, so that the ratio $\Omega(z) = \Omega(z + L)$. The properties of the monodromy matrix for Hamiltonian flows is summarized in Section 2.8. What we need to know for our purpose here is that it is unimodular (symplectic) and that its eigenvalues come in inverse pairs, which are either purely imaginary (characterizing stable motion in the vicinity of the PO) or purely real (unstable and marginally stable motion). If the PO is unstable and the eigenvalues are real, then the eigenvectors and hence $\Omega(z)$ are real. But a purely real $\Omega(z)$ means that the gaussian factor in $u(x, z)$ is purely imaginary and the solution does not decay in the direction transverse to the PO, contradicting the initial assumption of the parabolic approximation to the Helmholtz equation. *Hence*

for unstable POs our construction is inconsistent and we cannot find a solution of this form localized near the PO.

On the other hand, for a stable motion around the PO, the eigenvalues come in complex conjugate pairs, $\lambda_{1,2} = e^{\pm i\varphi}$, and the reality of the monodromy matrix then implies that the *eigenvectors* cannot be purely real and are related by complex conjugation, $q_2 = q_1^*$ and $p_2 = p_1^*$. Eq. (4.25) then implies $pq^* - qp^* = \text{const}$. This constant is arbitrary, and we choose it to be

$$pq^* - qp^* = i. \quad (4.33)$$

which yields finally

$$|\psi|^2 = \frac{1}{q} \exp \left[-\frac{x^2}{2k|q|^2} \right] \quad (4.34)$$

fulfilling our initial premise that the resulting solution decays away from the PO, and that the range of the decay is $\sim \sqrt{\lambda l}$.

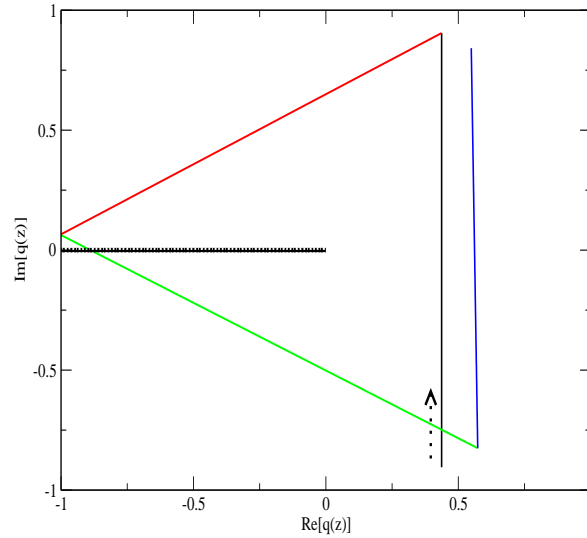


Figure 4.6: The path of $e^{i\pi m} q(z)$, ($z_{m-1} < z < z_m$, $m = 0 \dots N$) in the complex plane as z varies within a complete period for the solution in Fig. 4.7. The chosen branch-cut is shown with the rippled line extending from the origin to the negative real axis. The arrow indicates the motion of $q(z)$ as z starts out from $z = 0$ and completes a period.

Having made this uniquely determined choice (up to a scale factor) and using

$$\begin{pmatrix} q(z+L) \\ p(z+L) \end{pmatrix} = e^{i\varphi} \begin{pmatrix} q(z) \\ p(z) \end{pmatrix} \quad (4.35)$$

and $c_{m+N} = e^{-i\pi N/2} c_m$ we obtain

$$u(\tilde{x}, z + L) = e^{-\frac{i}{2}[\varphi + \pi(N + 2N_\mu)]} u(\tilde{x}, z) \quad (4.36)$$

From Eq. (4.30) and Eq. (4.4), we finally obtain the quantization rule for the wavevectors of the bound states of the closed cavity:

$$kL = \frac{1}{2}\varphi + 2\pi m + \text{mod}_{2\pi} \left[\left(\frac{1}{2}N + N_\mu \right) \pi \right] \quad (4.37)$$

where m is an integer, N is the number of bounces in the PO, φ is the Floquet phase obtained from the eigenvalues of the monodromy matrix and N_μ is an integer known as the Maslov index in the non-linear dynamics literature[65]. We have already encountered this index in Chapter Two, where it was related to the number of caustic crossings in EBK-quantized modes. Here, although it has a similar origin, it arises formally in the following manner. As already noted, the eigenvalues of the monodromy matrix for stable POs are complex conjugate numbers of modulus unity whose phase is the Floquet phase. We can define $\varphi = \text{Arg}[\sqrt{q(L)/q(0)}]$, where $\text{Arg}[\cdot]$ denotes the principal argument; hence the Floquet phase depends only on \mathcal{M} . However our solution, Eq. (4.14), involves the *square root* of $q(z)$ and will be sensitive to the number of times the phase of $q(z)$ wraps around the origin as z goes from zero to L . One instance of this behaviour is shown for the bowtie orbit in a quadrupole, in Fig. 4.6. As seen in the figure, there is no way of placing the branch-cut so that the period is completed without crossing it. The number of times the branch-cut is crossed is equal to the winding number. If this winding number (or Maslov index) is called N_μ then the actual phase advance along the PO is $\varphi + 2\pi N_\mu$; if N_μ is odd this leads to an observable π phase shift in the solution not included by simply diagonalizing \mathcal{M} to find the Floquet phase.

N_μ may be directly calculated by propagating $q(z)$:

$$N_\mu = \left[\frac{1}{2\pi i} \int_0^L d(\ln q(z)) \right] \quad (4.38)$$

where $[\cdot]$ denotes the integer part. There is no simple rule for reading off the Maslov index from the geometry of the PO; however the Maslov index doesn't affect the free spectral range or the transverse mode spacing.

Except for the Maslov index, the quantization rule Eq. (4.37) is familiar from Fabry-Perot resonators. The longitudinal mode index m gives rise to a free spectral range $\Delta k_{long} = 2\pi/L$ for gaussian modes of a stable PO of length L . The Floquet phase $\varphi/2L$ is the zero-point energy associated with the transverse quantization of the mode and we will shortly derive excited transverse modes with spacing φ/L . In Fig. 4.7, we plot for comparison the analytic solutions for the bow-tie resonance just derived in comparison to a numerical solution of the same problem; both the intensity patterns and the quantized value of k agree extremely well.

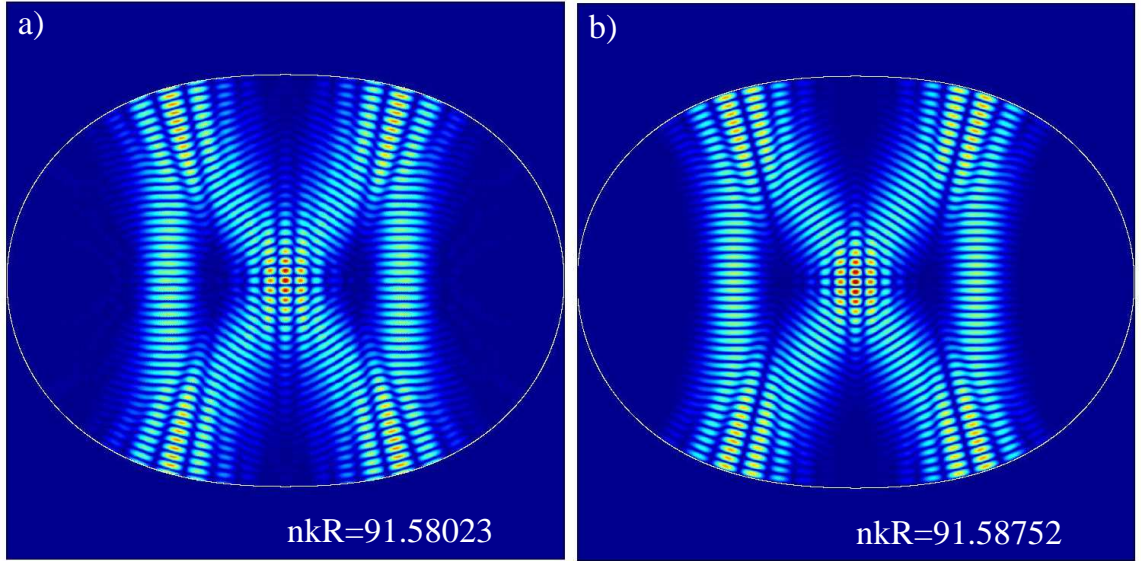


Figure 4.7: Intensity of the TM solution for a bow-tie mode plotted in a false color scale, (a) calculated numerically and (b) from the gaussian optical theory with parameters $m = 100$, $\varphi = 2.11391$, $N_\mu = 1$ and $N = 4$. Note the excellent agreement of the quantized values for kR (R is the average radius of the quadrupole).

4.6 Transverse excited modes

As is well known, the solution Eq. (4.14) is only one of the possible family of solutions of the parabolic equation Eq. (4.13) satisfying the boundary conditions Eq. (4.6) and the periodicity condition Eq. (4.30), the one corresponding to the ground state for transverse oscillations. Further solutions can be generated with algebraic techniques which were originally developed in the context of quantum oscillators [143]. If we refer to Eq. (4.13) we see that we are looking for solutions of $\mathcal{L}u = 0$, i.e. eigenfunctions of the differential operator with eigenvalue zero. It is natural following the analogy to quantum oscillators to seek additional solutions by defining lowering and raising operators

$$\Lambda(z) = iq(z)\frac{\partial}{\partial \tilde{x}} + p(z)\tilde{x} \quad (4.39)$$

$$\Lambda^\dagger(z) = iq^*(z)\frac{\partial}{\partial \tilde{x}} + p^*(z)\tilde{x}. \quad (4.40)$$

We can easily show that the operators $(\Lambda, \Lambda^\dagger, \mathcal{L})$ form an algebra. Namely, that $[\Lambda^\dagger, \mathcal{L}] = [\Lambda, \mathcal{L}] = 0$ and furthermore that $[\Lambda, \Lambda^\dagger] = i(p^*q - q^*p) = 1$. Defining the “ground-state” solution we have found as $u^{(0)}$, the commutation condition implies that $(\Lambda^\dagger u^{(0)})(x, z)$ is also a solution of $\mathcal{L}(u) = 0$. Further it can be checked that while $(\Lambda u^{(0)}) = 0$, $(\Lambda^\dagger u^{(0)})$ is a non-trivial solution. Repeated application of Λ^\dagger will generate an infinite family of solutions

$$u^{(\ell)}(\tilde{x}, z) = (\Lambda^\dagger)^\ell u^{(0)} \quad (4.41)$$

In order to find out how the generated solutions can be represented in terms of known functions, we will first establish their orthogonality properties. First, it's easy to show that the operation generates polynomials in \tilde{x} (with $q(z)$ dependent coefficients) in front of the original exponential i.e.

$$u^{(\ell)}(\tilde{x}, z) = P_\ell(\tilde{x}) \exp \left[\frac{i}{2} \Omega(z) \tilde{x}^2 \right] \quad (4.42)$$

Let's define a scalar product

$$\langle m|n \rangle = \int_{-\infty}^{\infty} dx u^{(n)}(\tilde{x}, z) (u^{(m)}(\tilde{x}, z))^* \quad (4.43)$$

One can show (for $m > n$) by repeated integration by parts and thereafter using the commutation relation, that

$$\langle n|m \rangle = \int_{-\infty}^{\infty} dx [\Lambda^m (\Lambda^\dagger)^n u^{(0)}] (u^{(0)})^* = n! \int_{-\infty}^{\infty} dx [\Lambda^{m-n} u^{(0)}] (u^{(0)})^* = 0 \quad (4.44)$$

Furthermore, using the above result for $m = n$

$$\langle n|n \rangle = n! \int_{-\infty}^{\infty} dx (u^{(0)})^* u^{(0)} = \sqrt{2\pi n!} \quad (4.45)$$

and it follows that

$$\int_{-\infty}^{\infty} dx P_n(x) P_m^*(x) \exp \left[-\frac{x^2}{2|q|^2} \right] = \delta_{n,m} \sqrt{2\pi n!} \quad (4.46)$$

From the theory of orthogonal polynomials, a set of polynomials defined in the domain $x = (-\infty, \infty)$, and orthogonal with a weight $w(x) = \exp \left[-\frac{x^2}{2|q|^2} \right]$, is uniquely defined[96]: they are the Hermite polynomials. After some rescaling and using the relation Eq. (4.33) we obtain the explicit expression

$$u^{(\ell)}(\tilde{x}, z) = \left(i \sqrt{\frac{q^*(z)}{2q(z)}} \right)^\ell H_\ell \left(\sqrt{Im \left[\frac{p(z)}{q(z)} \right]} \tilde{x} \right) u^{(0)}(\tilde{x}, z) \quad (4.47)$$

But do the solutions so generated still satisfy the boundary conditions? This can be shown either by resorting to an analysis like the one above, and showing that on the boundary, because of the conditions Eq. (4.21), the polynomials right before and after reflection are orthogonal with the same weight, and hence that they have to have the same value. A much easier way to see this is that $\Lambda^\dagger(z_i)|_{\partial D} = q_i^*(l)[i\Omega(l)\tilde{x}_i] + p_i(l)^*\tilde{x}_i|_{\partial D}$ is *to lowest order* identical to $\Lambda^\dagger(z_r)|_{\partial D}$, again because of Eq. (4.21).

We can find the wavevector quantization condition for this solution by calculating the additional phase acquired by $(\Lambda^\dagger u^{(0)})(x, z)$ upon performing one loop around the orbit $(\Lambda^\dagger u^{(0)})(x, z + L)$. Using Eq. (4.35), we find that

$$\Lambda^\dagger(z + L) = e^{-i\varphi} \Lambda^\dagger(z) \quad (4.48)$$

Thus this solution will acquire an additional phase $-\varphi$ with respect to $u^{(0)}$. This means that the l^{th} family of solutions

$$u^{(l)}(\tilde{x}, z) = (\Lambda^\dagger)^l u^{(0)} \quad (4.49)$$

will satisfy the wavevector quantization rule:

$$kL = (l + \frac{1}{2})\varphi + 2\pi m + \text{mod}_{2\pi} \left[\left(\frac{1}{2}N + N_\mu \right) \pi \right] \quad (4.50)$$

This result has the well-known interpretation of adding l transverse quanta $\Delta k_{\text{trans}} = \varphi/L$ to the energy of the ground state gaussian solution. Thus (in two dimensions) the general gaussian modes have two mode indices (l, m) corresponding to the number of transverse and longitudinal quanta respectively and two different uniform spacings in the spectra (see Fig. 4.3(b)).

As noted in the introduction, the solutions we have found by the parabolic equation method do not reflect correctly the discrete symmetries of the cavity which may be present. The theory of the symmetrized solutions and the breaking of degeneracy is essentially the same for both the closed and open cavity and will be presented in section 4.9 after treating the open case section 4.8.

4.7 Perturbation Theory

The quantization rule for wavevectors of a bounded two-dimensional system, Eq. (4.37), can be obtained by various methods [135, 144]. The real power and value of the boundary layer approach lies in its ability to provide higher order corrections. We will find that these corrections are not only functions of simple geometrical features of the boundary and the periodic orbit $(\varrho_k, \{l_k\}, \sin \chi_k)$, like the lowest order term, but increasingly depend on finer details of the boundary, the higher we go in order.

In this section and Appendix E, I will find the lowest order correction term to the eigenmodes of a Dirichlet cavity. The general methodology of the associated singular perturbation theory is laid out in Ref. [66]. The details of the calculation for a particular case however, is laden with complications like those related to the choice of the particular perturbation expansion to use, the implementation of the boundary conditions and the periodicity requirements, and even solvability. There is also the additional challenge of performing the calculation in a systematic and transparent fashion, possibly making use of an algebraic machinery.

To dispense with undue complications and bring forth the main features of the calculation, I will demonstrate the calculation for the simplest possible periodic orbit, the ‘‘bouncing ball’’ orbit. The main complication for higher period POs is that the symmetry axis of the original solution $u_0^{(\ell)}(\tilde{x} = 0)$ would not be compatible with the symmetry axis of the boundary. To lowest order, this doesn’t create a problem, but it turns out that at higher orders one has to work with an ‘‘astigmatic’’ basis (similar problem arises in the realm of physical optics, when axes of optical elements through which one wants to propagate a gaussian beam are not parallel to each other).

Let us look for the correction in a formal expansion of the form

$$k = k_0 + \frac{\delta_1}{\sqrt{k_0}} + \frac{\delta_2}{k_0} + \dots \quad (4.51)$$

where k_0 is given by Eq. (4.37). The ℓ th order eigenmode Eq. (4.47) will be expanded perturbatively as

$$\psi^{(\ell)} = e^{ik_0 z} \sum_{n=0}^{\infty} \frac{u_n^{(\ell)}(\tilde{x}, z)}{(\sqrt{k_0})^n} \quad (4.52)$$

Inserting these expansions into Eq. (4.5), we get

$$\mathcal{L} \sum_{n=0}^{\infty} \frac{u_n^{(\ell)}(\tilde{x}, z)}{(\sqrt{k_0})^n} = 0 \quad (4.53)$$

where

$$\mathcal{L} = \mathcal{L}_0 + \frac{2}{\sqrt{k_0}}\delta_1 + \frac{1}{k_0}(\mathcal{L}_1 + 2\delta_2) + \dots \quad (4.54)$$

\mathcal{L}_0 and \mathcal{L}_1 are as defined before, with $\tilde{x} = \sqrt{k_0}x$. We obtain the following recurrence

$$\mathcal{L}_0 u_0 = 0 \quad (4.55)$$

$$\mathcal{L}_0 u_1 + 2\delta_1 u_0 = 0 \quad (4.56)$$

$$\mathcal{L}_0 u_2 + 2\delta_1 u_1 + (\mathcal{L}_1 + 2\delta_2)u_0 = 0 \quad (4.57)$$

$$\vdots \quad (4.58)$$

Suppose now we are looking for a correction to $u_0^{(\ell)}$. For the solution $\psi^{(\ell)}$ (Eq. (4.52)) to be L -periodic, $u_n^{(\ell)}$ has to satisfy the Floquet condition

$$u_n^{(\ell)}(\tilde{x}, z + L) = e^{i\kappa_\ell} u_n^{(\ell)}(\tilde{x}, z) \quad (4.59)$$

We expand $u_n^{(\ell)}(\tilde{x}, z)$ using the basis Eq. (4.47):

$$u_n^{(\ell)}(\tilde{x}, z) = \sum_m \beta_{nm}^\ell(z) u_0^{(m)}(\tilde{x}, z) \quad (4.60)$$

Note that such an expansion is possible, because the basis set Eq. (4.47) forms a complete set to expand any function of \tilde{x} at a given z . As the calculations will show, under certain conditions it is possible to satisfy the important periodicity requirement Eq. (4.59). The solvability condition gives then the coefficients δ_i and $\beta_{nm}^\ell(z)$. The calculations are involved, mainly because the Dirichlet boundary conditions have to be implemented carefully, and are carried out in Appendix E. We find that the new wavevector in Eq. (4.51) is given by

$$k = k_0 + \frac{\delta_2}{k_0} + O(k_0^2) \quad (4.61)$$

where δ_2 , for lowest order bouncing ball mode is given by

$$\delta_2 = \frac{1}{8}|p|^4 + \frac{1}{\rho l}|q|^2|p|^2 + \frac{1}{2\rho l}(q^*)^2 p^2(1 + e^{i\varphi}) + \frac{6}{l}\eta_4|q|^4 \quad (4.62)$$

Here, $q = q(0)$ and $p = p(0)$ are the Floquet eigenvectors in Eq. (4.32) for the bouncing ball mode, calculated at the boundary $z = 0$, φ is the corresponding Floquet phase, l is the length of one segment of the periodic orbit, and ρ and η_4 are the geometric properties of the local section of the boundary, which is expressed in the local coordinates (ξ_1, ξ_2) as

$$\xi_2 = -\frac{\xi_1^2}{2\rho} + \eta_3\xi_1^3 + \eta_4\xi_1^4 \quad (4.63)$$

On the pragmatic side, it's hard to say that calculating this extra bit of information is worth the lengthy calculation after all, but our main motivation was to see the power of this formalism, to have a closer look at its mathematical structure, as well as to see its limitations. Thus some notes are of order here: First of all, the condition of solvability (see Appendix E), that φ/π be irrational, can be interpreted in terms of the usual (*regular*) perturbation theory, familiar to us from quantum mechanics. When φ/π is rational, we will have degeneracies in our original set of eigenvalues. It's well-known that perturbation in the presence of degeneracies is more complicated, and so is it here (see Ref. [145]). At this point, it's also worth noting that the zeroth order problem is equivalent to finding the Schrödinger-evolution of a wavepacket with time-dependent and periodic boundary conditions. Such problems have been extensively treated in literature, within different contexts [143, 146, 147]. Another important feature of the perturbation theory is that $\delta_m = 0$, for odd terms, so that the lowest order correction is of the order of $1/k_0$.

4.8 Opening the cavity - The dielectric resonator

We now consider the wave equation for a uniform dielectric rod of arbitrary cross-section surrounded by vacuum. As noted in Section 3.2, Maxwell's equations separate into TM and TE polarized waves satisfying

$$(\nabla^2 + n(\mathbf{r})^2 k^2) \psi = 0 \quad (4.64)$$

Maxwell boundary conditions translate into continuity of ψ and its normal derivative across the boundary ∂D , defined by the discontinuity in n . Here $\psi = E(\psi = B)$ for *TM(TE)* modes. We will only consider the case of a uniform dielectric in vacuum for which the index of refraction $n(\mathbf{r} \in D) = n$ and $n(\mathbf{r} \notin D) = 1$. Thus we have the Helmholtz equation with wave vector nk inside the dielectric and k outside. We furthermore impose the boundary condition that there exist only outgoing waves external to the cavity, i.e. we confine our attention to quasi-bound modes. This boundary condition combined with the continuity conditions cannot be satisfied for

real wavevectors k and instead leads to discrete solutions at complex values of k , with the imaginary part of k giving the width of the resonance. We now show how such quasi-bound modes can be incorporated into the gaussian optical resonance theory just described.

As before we look for solutions which, within the cavity, are localized around periodic orbits based on specular reflection within the cavity. In order to satisfy the boundary conditions the solutions outside the cavity will be localized around rays extending out to infinity in the directions determined by Snell's law at the bounce point of the PO. The quasi-bound state condition is imposed by insisting that the solutions along those rays to infinity are only outgoing. This can only be achieved by making k complex (assuming real index n). It is worth noting that there are well-known corrections to specular reflection and refraction at a dielectric interface, for example the Goos-Hänchen shift[148]. It is interesting to attempt to incorporate such effects into our approach at higher order, however we do not do so here and confine ourselves to obtaining a consistent solution to lowest order in kl .

As before we will define the solution as the sum of solutions $\psi_m(x_m, z_m)$ attached to each segment of the PO and define local coordinates (x_m, z_m) attached to the PO. Now in addition we need an outside solution at each reflection point ψ_{mt} with its own coordinate system (x_{mt}, z_{mt}) rotated by an angle given by Snell's law applied to the direction of the incident ray (see Fig. 4.4). The ansatz of Eq. (4.4) thus applies, where now the sum will run over $2N$ components, which will include the transmitted fields. Introducing the slowly varying envelope approximation Eq. (4.2) and the scalings $\tilde{x}_{mt} = \sqrt{k}x$, $\tilde{x}_m = \sqrt{nk}x$, we get the parabolic equation Eq. (4.13) for each component, at lowest order in k . The boundary conditions close to the m^{th} bounce point will take the form

$$\psi_i + \psi_r|_{\partial D^-} = \psi_t|_{\partial D^+} \quad (4.65)$$

and

$$\frac{\partial}{\partial n}\psi_i + \frac{\partial}{\partial n}\psi_r|_{\partial D^-} = \frac{\partial}{\partial n}\psi_t|_{\partial D^+} \quad (4.66)$$

Here $\partial/\partial n$ is the normal derivative at the boundary. The alternative indices i, r, t stand for $m, m+1$ and mt , respectively. Since the parabolic equation Eq. (4.13) is satisfied in appropriately scaled coordinates within each segment, we write all solutions in the general form $\psi_M = A_M \exp(i\Phi_M)$ where $\Phi_M = n_M kz + \frac{i}{2}Q'_M Q_M^{-1} \tilde{x}_M^2$ and $A_M = c_M/\sqrt{Q_M}$. Here M stands for m or mt and $n_m = n$, $n_{mt} = 1$. As for the closed case, we need to determine Q_M, Q'_M and c_M , so that the boundary conditions are satisfied, and then impose single-valuedness to quantize k .

Similarly to the closed case, the first continuity condition Eq. (4.65) must be satisfied on an arc of size $\sim \sqrt{\lambda l}$ on the boundary around each bounce point and that implies that the phases of the incident, transmitted and reflected waves must be equal. This equality will be implemented in the coordinate system $(\tilde{\xi}_1, \tilde{\xi}_2)$ along the tangent and normal to the boundary at the reflection point, as before. We can again expand the boundary as the arc of a circle of radius ϱ , the curvature at the

bounce point. Since the equations are of the same form for each reflection point it is convenient at this point to suppress the index m and use the indices i, r, t to denote the quantities associated with the incident, reflected and transmitted wave at the m^{th} bounce point.

The analysis of the phase equality on the boundary for the incident and reflected waves is exactly the same as in the closed case and again leads to Eq. (4.21) describing specular reflection. Equating the phases of the incident and transmitted wave leads to:

$$\begin{aligned}\Phi_i &= nk \left(l_k + \frac{1}{\sqrt{nk}} \tilde{\xi}_1 \sin \chi - \frac{1}{nk} \frac{\tilde{\xi}_1^2}{2\varrho} \cos \chi \right) + \frac{1}{2} \frac{Q'_i}{Q_i} \left(\tilde{\xi}_1 \cos \chi + \frac{1}{\sqrt{nk}} \frac{\tilde{\xi}_1^2}{2\varrho} \sin \chi \right)^2 \\ \Phi_t &= k \left(nl_k + \frac{1}{\sqrt{nk}} \tilde{\xi}_1 \sin \chi_t - \frac{1}{nk} \frac{\tilde{\xi}_1^2}{2\varrho} \cos \chi_t \right) + \frac{1}{2} \frac{Q'_t}{Q_t} \left(\tilde{\xi}_1 \cos \chi_t + \frac{1}{\sqrt{nk}} \frac{\tilde{\xi}_1^2}{2\varrho} \sin \chi_t \right)^2\end{aligned}\quad (4.67)$$

where we have defined $\chi = \chi_m, \varrho = \varrho_m$ and all quantities are evaluated at $z = l_k$. Recalling that $n \sin \chi_i = \sin \chi_t$ we get up to $O(1/\sqrt{k})$

$$\begin{pmatrix} Q_t \\ Q'_t \end{pmatrix} = \begin{pmatrix} 1/\mu & 0 \\ -\frac{2(1-\mu)}{\varrho \cos \chi} & n\mu \end{pmatrix} \begin{pmatrix} Q_i \\ Q'_i \end{pmatrix} \quad (4.68)$$

where $\mu = \cos \chi_i / \cos \chi_t$ and the relation $Q_i = \mu Q_t$ is a convention similar to $Q_r = -Q_i$. Again, the matrix in Eq. (4.68) is just the ABCD matrix for transmission of rays through a curved dielectric interface at arbitrary angle of incidence in the tangential plane [76].

Using the phase equality on the boundary the continuity of the field gives the general transport equation:

$$\frac{c_i}{\sqrt{Q_i}} + \frac{c_r}{\sqrt{Q_r}} = \frac{c_t}{\sqrt{Q_t}} \quad (4.69)$$

which becomes (using the conventions $Q_r = -Q_i, Q_t = Q_i/\mu$)

$$c_i + c_r = \sqrt{\mu} c_t \quad (4.70)$$

In order to find the quantization condition we need a direct relation between c_i and c_r as we had in the closed case. This is provided by the normal derivative boundary condition Eq. (4.66). This boundary condition requires a little more algebra. Notice first that, in

$$\partial_n \left[\frac{c}{\sqrt{Q}} e^{i\Phi} \right] = \left[-\frac{Q'}{2Q} \partial_n z + i \partial_n \Phi \right] \frac{c}{\sqrt{Q}} e^{i\Phi} \quad (4.71)$$

we can neglect the first term on the RHS, because it's $O(1/\sqrt{k})$. Hence, it's clear that once Eq. (4.65) is satisfied, this condition reduces to a statement about normal derivatives of phases:

$$c_i \frac{\partial}{\partial n} \Phi_i + c_r \frac{\partial}{\partial n} \Phi_r = \sqrt{\mu} c_t \frac{\partial}{\partial n} \Phi_t. \quad (4.72)$$

At the level of approximation needed, one finds the simple results $\partial_n \Phi_i = nk \cos \chi$, $\partial_n \Phi_r = -nk \cos \chi$, $\partial_n \Phi_t = k \cos \chi_t$, leading to

$$n\sqrt{\mu}(c_i - c_r) = c_t \quad (4.73)$$

and

$$c_r = \frac{n\mu - 1}{n\mu + 1} c_i. \quad (4.74)$$

Note the key result that

$$|c_r|^2 = \frac{|n \cos \chi_i - \cos \chi_t|^2}{|n \cos \chi_i + \cos \chi_t|^2} |c_i|^2 \quad (4.75)$$

which is precisely the Fresnel reflection law at a (flat) dielectric interface.

Now we impose the single-valuedness or periodicity condition to obtain the quantization rule for k .

$$\psi(x, z + L) = \psi(x, z) \quad (4.76)$$

Note however that we have a qualitatively different situation than for the closed cavity; some amplitude can be lost at each reflection and it will in general be impossible to make a loop around the PO and return to the same field amplitude unless k is complex. We have the condition

$$u(x, z + L)e^{inkL} = u(x, z) \quad (4.77)$$

which can be satisfied by choosing $Q(z), P(z)$ to be the appropriate eigenvector of the monodromy matrix (note that \mathcal{M} is unchanged from the closed case as it only pertains to the propagation of the phase) and with this choice the quantization condition becomes

$$nkL = \frac{1}{2}\varphi + 2\pi m + \text{mod}_{2\pi} \left[\left(\frac{1}{2}N + N_\mu \right) \pi \right] - i \sum_{b=1}^N \left| \log \left[\frac{n\mu_b - 1}{n\mu_b + 1} \right] \right|. \quad (4.78)$$

Recall that the Fresnel reflection law has the property that it gives a pure phase for rays incident above total internal reflection. Thus the new term in the quantization law due to Fresnel reflection can be either purely real (all bounces of PO totally internally reflected), purely positive imaginary (all bounces below TIR) or complex (some TIR bounces, some refracted bounces). If we define: $\varphi_f = \text{Re}[-i \sum_b^N \log \left[\frac{n\mu_b - 1}{n\mu_b + 1} \right]]$ and $\gamma_f = \text{Im}[-i \sum_b^N \log \left[\frac{n\mu_b - 1}{n\mu_b + 1} \right]]$ then the quantization rule gives

$$\text{Re}[nkL] = 2\pi m + \text{mod}_{2\pi} \left[\left(\frac{1}{2}N + N_\mu \right) \pi \right] + \varphi/2 + \varphi_f \quad (4.79)$$

$$\text{Im}[nkL] = -\gamma_f. \quad (4.80)$$

As noted above, this result is only in the leading order approximation. The question of what happens at and beyond the critical angle is complicated. One can

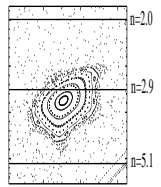
index of refraction	numerical calculation	gaussian quantization rule	surface of section
$n = 2.0$	$nkR = 100.53788 + 0.49758i$	$nkR = 100.53858 + 0.49635i$	
$n = 2.9$	$nkR = 100.59376 + 0.16185i$	$nkR = 100.53858 + 0.14178i$	
$n = 5.1$	$nkR = 100.84716 + 0.00245i$	$nkR = 100.85111 + 0.00000i$	

Table 4.1: Table comparing the gaussian optical prediction for the complex k values of bow-tie resonances of the quadrupole ($\epsilon = 0.17$) to numerically obtained values for three different indices of refraction corresponding to incidence below, at and above the critical angle for total internal reflection. The schematic at right depicts the bow-tie island in comparison to the critical line for total internal reflection for the three cases (horizontal lines).

try to make a more careful analysis by going to higher orders, but the futility of this is proven only when one is confronted with inconsistencies. It turns out that this regime is dominated by diffraction effects which are out of reach with the current expansion. This is also signaled by the appearance of the factor μ in Eq. (4.68).

In conclusion, within the current scheme, we cannot account for both the effects of evanescent leakage at a curved interface and the momentum width of the gaussian “beam” which leads to violations of ray optics. These effects will give a non-zero imaginary part (width) to all resonances, even those with all bounce points above TIR.

In Table 4.1 we present a comparison between the numerically obtained quantized wavevectors for a bow-tie resonance and the values for the real and imaginary part of k predicted by Eq. (4.78) for three different indices of refraction. Note that the best agreement is for the case far from total internal reflection, and the worst agreement is the case near TIR.

4.9 Symmetry Analysis and Quasi-Degeneracy

As noted above, the gaussian theory we have just presented predicts exact degeneracies if there exist several symmetry-related stable orbits (note that in this context the same path traversed in the opposite sense is considered a distinct symmetry-related orbit). However it is well-known that wave equations with discrete symmetries cannot in general have a degeneracy which is larger than the largest dimension of the irreducible representations of the symmetry group of the equation. Here we are concerned with the point group (rotations and reflections) of the dielectric resonator in two dimensions. Let G be a group which leaves the cavity invariant. Then, if $\psi(\mathbf{x})$ is a solution to the Helmholtz equation, so is $\psi(g\mathbf{x})$, where $g \in G$ and $\mathbf{x} = (X, Z)$. The

symmetrized solutions, i.e. solutions which transform according to the irreducible representations of G under the action of G , can be obtained by the projection operators of the group:

$$\mathcal{P}_m \psi(\mathbf{x}) = \frac{d_m}{|G|} \sum_{g \in G} \chi_m(g) \psi(g\mathbf{x}) \quad (4.81)$$

Here d_m is the dimensionality and $\chi_m(g)$ is the character of the m^{th} irreducible representation and the solution so obtained, denoted by $\psi_m(\mathbf{x})$ is the resulting symmetry-projected solution. For a given irreducible representation there are as many symmetrized solutions as the dimension of that irreducible representation of G . We will focus here on the case of the closed resonator, but the general principles apply to the open case as well.

4.10 Symmetrized modes for the quadrupole

Let's consider our canonical example, the quadrupole (see Fig. 4.4). The symmetry group of the quadrupole is $G = C_2 \otimes C_2 = \{1, \sigma_X, \sigma_Z, \sigma_X \sigma_Z\}$, the group of reflections about the X and Z axes. This group has four one-dimensional representations only, and thus cannot have *any* exactly degenerate solutions (barring accidental degeneracy). The existence of four irreducible representations means that given the one solution $\psi(X, Z)$ we have constructed to the Helmholtz equation, we can generate four linearly independent solutions by projection according to Eq. (4.81) above. We will label the representations by $m = (r, s)$, where $r, s = \pm$ denotes the action of inversion of X and Z respectively. The symmetrized solutions are then

$$\begin{aligned} \psi_{(++)} &= \frac{1}{4}(\psi_1 + \psi_2 + \psi_3 + \psi_4), & \psi_{(+-)} &= \frac{1}{4}(\psi_1 + \psi_2 - \psi_3 - \psi_4) \\ \psi_{(-+)} &= \frac{1}{4}(\psi_1 - \psi_2 + \psi_3 - \psi_4), & \psi_{(--)} &= \frac{1}{4}(\psi_1 - \psi_2 - \psi_3 + \psi_4) \end{aligned} \quad (4.82)$$

where

$$\psi_1 = \psi(X, Z), \quad \psi_2 = \psi(-X, Z), \quad \psi_3 = \psi(X, -Z), \quad \psi_4 = \psi(-X, -Z). \quad (4.83)$$

In this case the symmetrized solutions are just the solutions with definite parity with respect to the symmetry axes of the quadrupole.

The key point here is that within the parabolic equation approximation these four solutions are exactly degenerate, whereas our group-theoretic analysis for the exact Helmholtz equation tells us that they cannot be so, although they will be nearly degenerate. Moreover our original solution $\psi(X, Z)$ cannot be an exact solution, as it does not transform as *any* irreducible representation of the symmetry group. A further important point is that while we can always construct a number of symmetrized solutions equal to the sum of the dimensions of the irreducible representations, there is no guarantee that such a projection will yield a non-trivial solution. In fact in the case of the quadrupole we will show below that for each quantized value of k only two of the projected solutions are non-trivial, leading to quasi-degenerate doublets in

the spectrum. We will present below a simple rule which allows one to calculate the quasi-degeneracy given the periodic orbit and the symmetry group of the resonator.

Before discussing the general rule, we illustrate the basic procedure for the case of a bow-tie PO. Let l_1 and l_2 be the lengths of the vertical and diagonal legs of the bow-tie, so that $L = 2(l_1 + l_2)$ is the total length. Then,

- $g = 1$

$$\psi_1 = \psi(g\mathbf{x}) = \frac{1}{\sqrt{q(z)}} \exp \left[ikz + \frac{i}{2} \Omega(z)x^2 \right] \quad (4.84)$$

- $g = \sigma_X : (z \rightarrow L/2 + z, x \rightarrow -x)$

$$\psi_2 = \psi(g\mathbf{x}) = e^{\frac{1}{2}i\pi} \frac{1}{\sqrt{e^{i\varphi/2}q(z)}} \exp \left[ik(z + \frac{L}{2}) + \frac{i}{2} \Omega(z)x^2 \right] \equiv e^{i\zeta} \psi_1 \quad (4.85)$$

- $g = \sigma_Z : (z \rightarrow l_1 - z, x \rightarrow x)$

$$\psi_3 = \psi(g\mathbf{x}) = \frac{1}{\sqrt{q(l_1 - z)}} \exp \left[ik(l_1 - z) + \frac{i}{2} \Omega(l_1 - z)x^2 \right] \quad (4.86)$$

- $g = \sigma_X \sigma_Z : (z \rightarrow L/2 + l_1 - z, x \rightarrow -x)$

$$\psi_4 = \psi(g\mathbf{x}) = e^{\frac{1}{2}i\pi} \frac{1}{\sqrt{e^{i\varphi/2}q(l_1 - z)}} \exp \left[ik(\frac{L}{2} + l_1 - z) + \frac{i}{2} \Omega(l_1 - z)x^2 \right] \equiv e^{i\zeta} \psi_3 \quad (4.87)$$

where the phase factor $\zeta = 1/2(\pi - \varphi/2 + kL)$. Here we use the fact that $\mathcal{M}_L = \mathcal{M}_{L/2} \mathcal{M}_{L/2}$ for the bow-tie orbit, where \mathcal{M}_L is the monodromy matrix for the whole length L . It follows that $q(z + L/2) = e^{i\varphi/2}q(z)$. Note also the appearance of the factors $e^{\frac{1}{2}i\pi}$, which is due to the specific choice of branch-cut for $\sqrt{q(z)}$. Putting these together, we obtain

$$\begin{aligned} \psi_{(++)} &= \frac{1}{2}(\psi_1 + \psi_3)e^{i\frac{\zeta}{2}} \cos \frac{\zeta}{2} \\ \psi_{(+-)} &= \frac{1}{2}(\psi_1 - \psi_3)e^{i\frac{\zeta}{2}} \cos \frac{\zeta}{2} \\ \psi_{(-+)} &= \frac{1}{2i}(\psi_1 + \psi_3)e^{i\frac{\zeta}{2}} \sin \frac{\zeta}{2} \\ \psi_{(--)} &= \frac{1}{2i}(\psi_1 - \psi_3)e^{i\frac{\zeta}{2}} \sin \frac{\zeta}{2} \end{aligned} \quad (4.88)$$

The solutions are k -dependent and must be evaluated for the quantized values of k . Referring to the quantization condition Eq. (4.37) we find that the phase $\zeta = m\pi$ where m is the longitudinal mode index of the state. Hence

$$\begin{aligned} \psi_{(++)}, \psi_{(+-)} &\propto \cos \frac{\zeta}{2} = 0 & m = 1, 3, 5, \dots \\ \psi_{(-+)}, \psi_{(--)} &\propto \sin \frac{\zeta}{2} = 0 & m = 0, 2, 4, \dots \end{aligned} \quad (4.89)$$

Thus the quasi-degeneracy of the solutions is two for the bow-tie, the solutions with identical parity under σ_Z form the doublets (see inset Fig. 4.3(b) *Intro Fig3b*), and

these two parity types alternate in the spectrum every free spectral range. Note that while we have illustrated the analysis for the ground state ($\ell = 0$) one finds exactly the same result for the ℓ^{th} transverse mode, with doublets paired according to the index m , independent of ℓ .

This illustrates a general procedure, valid for any stable PO. First, one finds by the parabolic equation method a non-symmetrized approximate solution $\psi(X, Z)$ localized on the PO. Second, one generates the symmetrized solutions from knowledge of the irreducible representations of the symmetry group. Third, one evaluates these solutions for the quantized values of k ; the non-zero solutions give one the quasi-degeneracy and the symmetry groupings (e.g. $(++)$ with $(+-)$ in the above case). The same principles apply to mirror resonators with the same symmetry group. Note that in the case of a high symmetry resonator (or mirror arrangement) e.g. a square or a hexagon, for which there exist two dimensional irreducible representations, exact degeneracy is possible and can be found by these methods.

4.11 Simple Rule for Quasi-Degeneracy

Although the construction just presented allows one to find the quasi-degeneracy and symmetry pairing, it is convenient when possible to have a simple rule to get the quasi-degeneracy and symmetry-pairing from the geometry of the orbit. The quasi-degeneracy is easily determined by the following rule:

The quasi-degeneracy D is equal to the number of distinct classical periodic orbits which are related by the spatial symmetry group and time-reversal symmetry.

In this rule “distinct” orbits are defined as orbits which cannot be mapped into one another by time translation. Therefore a self-retracing orbit such as the Fabry-Perot, two-bounce orbit, only counts as one orbit and is non-degenerate (see Table 4.2). In contrast for a circulating orbit like the diamond no translation in time will take the orbit into its time-reversed partner. This rule can be obtained from semiclassical methods similar to the Gutzwiller Trace formula [149]. The density of states can be expressed by a summation over periodic orbits and their repetitions; for stable periodic orbits the summation over repetitions yields a delta function at the semiclassical energies [135] (corresponding to the same wavevectors as we find from our quantization rule). This approach would give an alternative derivation of our results which is less familiar in optics than the parabolic equation method we have chosen. However the semiclassical method makes it clear that there will be a mode for every distinct symmetry-related PO using the definition we have just given (of course in this method, as in the parabolic equation method, one would predict an exact degeneracy instead of the quasi-degeneracy we have discussed).

Let us illustrate the application of this rule. The bow-tie orbit goes into itself under all the reflection symmetries and so spatial symmetry generates no new orbits; however time-reversal changes the sense of traversal of each leg of the orbit and does give a distinct orbit. Thus the predicted quasi-degeneracy is two, which we found to be correct by our explicit construction above. In contrast, the triangle orbit (see

orbit	symmetry-related	time-reversal	quasi-degeneracy	symmetry-reduced orbit	symmetry-pairing
 bowtie	1	2	2		$[(++) , (+-)]$ $[(--) , (-+)]$
 diamond	1	2	2		$[(++) , (---)]$ $[(+-) , (-+)]$
 triangle	2	2	4		$[(++) , (+-)]$ $(-+), (---)]$
 fish	2	1	2		$[(++) , (-+)]$ $[(+-) , (---)]$
 fabry perot	1	1	1		$[(++)]$ $[(+-)]$

Table 4.2: Table illustrating the application of the two symmetry rules to five short POs. The second column is the total number of orbits of this shape related by spatial symmetry; the third column is the total number of orbits of this shape generated by time-reversal symmetry. By Rule 1 the quasi-degeneracy is the product of these two numbers. Column 4 gives the symmetry-reduced orbit which leads via Rule 2 to the symmetry pairing indicated in column 5.

Table 4.2) has a symmetry related distinct orbit and a definite sense of circulation which is reversed by time-reversal, hence it should have a quasi-degeneracy $2 \times 2 = 4$ leading to quartets instead of doublets. A few different cases of this rule are illustrated in Table 4.2.

The rule we have just given tells one the quasi-degeneracy, D , but not the symmetry-pairing. For the case of reflection symmetries one can state a second rule which determines these pairings. First fold the PO of interest back into the symmetry-reduced resonator [149] (see Table 4.2) using reflection until it completes *one period in the reduced resonator*. The symmetry-reduced resonator has boundaries which correspond to lines of reflection symmetry in the original problem. Anti-symmetric solutions with respect to each of these lines of symmetry correspond to Dirichlet boundary conditions; symmetric solutions must have zero derivative corresponding to Neumann boundary conditions. The boundary conditions at the true boundary of the resonator don't affect the symmetry pairing. For each symmetry choice one can evaluate the phase accumulated in the reduced resonator at each bounce, assigning a phase shift π to each bounce off a "Dirichlet" internal boundary, and zero phase shift for each bounce off a "Neumann" internal boundary. If two symmetry types lead to the same final phase shift (modulo 2π) then those two symmetry types will be paired and quasi-degenerate, otherwise not. A subtle issue is the question of how to count bounces at the corner between two boundaries. The answer is that the semiclassical method really sums over orbits nearby the PO which will then hit both boundaries and experience the sum of the two phase shifts.

We will illustrate this rule for the case of the bow-tie in the quadrupole. The symmetry reduced PO is shown in the last column of Table 4.2. It has one corner bounce, one bounce on the X axis and two boundary bounces. The boundary bounces don't matter as they will give the same phase shift for all symmetry types. The X axis bounce will give phase shift 0 for the $+$ symmetry of σ_Z and π for the $-$ symmetry. The corner bounce sums the two shifts and gives: $(+, +) \rightarrow 0, (+, -) \rightarrow \pi, (-, +) \rightarrow \pi, (-, -) \rightarrow 2\pi$. Adding these two shifts modulo 2π gives $[(+, +), (+, -)] \rightarrow 0, [(-, -), (-, +)] \rightarrow \pi$ corresponding to the symmetry pairing we found above. In Table 4.2, these two rules are applied to a number of relevant orbits in the quadrupole. It should be emphasized however that the group-theoretic projection method combined with the quantization rule which we illustrated in this section will work for any symmetry group and the rules that we have stated are just useful shortcuts.

The symmetry analysis above can only determine the existence of quasi-degenerate multiplets with small splittings, it cannot estimate the size of these splittings. In the phase space picture the splittings we are discussing come from tunneling between distinct periodic orbits, referred to as "dynamical tunneling" in the quantum chaos literature [150]. In Ref. [78], we have evaluated the average magnitude of these splittings. We will here limit ourselves to a qualitative discussion of the problem.

Tunneling in multi-dimensional systems, when compared to that occurring in 1D systems displays an important difference. Because the classical motion corresponding to a given mode proceeds on Lagrangian manifolds, which are of lower dimension

than the energy-hypersurface, the tunneling process occurs between these manifolds. Hence, the effective tunneling barrier is not formed by classical energy conservation, but by conservation of dynamical variables (more precisely, the tunneling occurs in the action space I , of the action-angle variables (I, θ) defined in Section 2.6). Because of this reason, this kind of phase-space tunneling in multi-dimensional systems is called *dynamical tunneling*. Dynamical tunneling in integrable multi-dimensional systems is essentially similar to the textbook example of tunneling in one dimension (note that conservative dynamics in 1D is always integrable), and the splittings in such a case come from first order perturbation theory in the tunneling matrix element through an effective barrier, just as they do for the one-dimensional double well potential. The associated splittings are found to be *exponential small* in energy. Systems of the type we are considering, with mixed dynamics however show a very striking difference. It has been found by both numerical simulations and analytic arguments that the dynamical tunneling splittings in mixed systems are typically many order of magnitude larger than found for similar but integrable systems [151, 152] (e.g in quadrupole vs. elliptical billiards). This difference can be traced to the mechanism of *chaos-assisted tunneling* (CAT). As opposed to the “direct” processes when the particle (ray) “tunnels” directly from one orbit to the other, the CAT corresponds to the following three-step process: (i) tunneling from the periodic orbit to the nearest point of the chaotic “sea”, (ii) *classical* propagation in the chaotic portion of the phase space until the neighborhood of the other periodic orbit is reached, (iii) tunneling from the chaotic sea to the other periodic orbit (see Fig. 4.8 for an illustration). Note that the chaos-assisted processes are formally of higher order in the perturbation theory. However the corresponding matrix elements are much larger than those of the direct process. This can be understood intuitively as the tunneling from the periodic orbit to the chaotic sea typically involves a much smaller “violation” of classical mechanics and therefore has an *exponentially larger* amplitude.

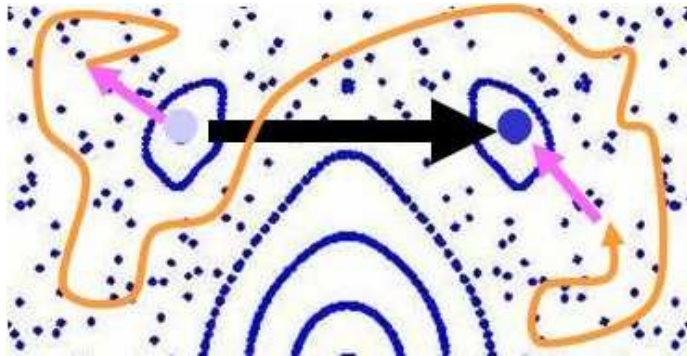


Figure 4.8: Schematic indicating a direct tunneling process (black arrow) and a chaos-assisted tunneling process (yellow arrow) which would contribute to splitting of bow-tie doublets.

The contribution of chaos-assisted tunneling can be evaluated both qualitatively

and quantitatively using the so called “three-level model” [151, 153], where the chaotic energy levels (the eigenstates localized in the chaotic portion of the phase space) are represented by a single state E_C with known statistical properties. The straightforward diagonalization of the resulting matrix yields [153]

$$\Delta E_{\text{CAT}} \simeq \frac{|V_{RC}|^2}{E_R - E_C} \quad (4.90)$$

where E_R is the semiclassical energy of the “regular” states (localized at the periodic orbits) which does not include the tunneling contribution, and V_{RC} is the corresponding coupling matrix element with the chaotic state. The resonant denominator in Eq. (4.90) leads to strong fluctuations of the CAT-related doublets, as is found in numerical simulations [153]. The average behavior of the splittings however is determined by the matrix element V_{RC} . By virtue of the Wigner transformation [134] it can be shown [154] that $|V_{RC}|^2$ is proportional to the overlap of the Wigner transforms of the “regular” and “chaotic” states:

$$|V_{RC}|^2 \propto \int d\phi \int d\sin\chi W_C(\phi, \sin\chi) W_R(\phi, \sin\chi) \quad (4.91)$$

Assuming that, as required by Berry’s conjecture [155], *on the average* the Wigner function of a chaotic state is equally distributed across the chaotic portion of the phase space, and using the analytical expressions for the regular eigenstates calculated earlier, we find [78]

$$\langle \Delta E_{\text{CAT}} \rangle \propto \exp(-\mathcal{A}kR_0) \quad (4.92)$$

where \mathcal{A} is the area in the Poincare Surface of Section (in $(\phi, \sin\chi)$ coordinates) occupied by the stable island supporting the regular eigenstate. Note that Eq. (4.92) holds only on average, since chaos-assisted tunneling always leads to strong fluctuations of the splittings which are *of the same order* as the average [78, 151]. Because of this reason, knowledge of the average splitting size does not accurately predict the splitting of a *specific doublet*, but rather can be incorporated into a statistical description. Note also that small violations of symmetry in the fabrication of the resonator may lead to much larger splittings than these tunnel splittings; such an effect was recently observed for triangle-based modes of GaAs ARC micro-lasers [51].

4.12 Conclusions and Relation to Experiment

We have generalized gaussian optical resonator theory to describe the resonances associated with stable periodic orbits of arbitrary shaped two-dimensional dielectric resonators using the parabolic equation method. The correspondence to ray optics emerges naturally when imposing the boundary conditions at the dielectric interface which leads to the appropriate ABCD matrices for reflection, transmission and propagation. For a perfectly-reflecting cavity one gets quantized solutions at real

values of k localized around the PO with mode spacings given by $\Delta k_{long} = 2\pi/L$, $\Delta k_{trans} = \varphi/L$ where L is the length of the PO and φ is the Floquet phase associated with the eigenvalues of the monodromy matrix (round-trip ABCD matrix). For a dielectric cavity one finds similarly localized quasi-bound solutions at quantized complex values of nk ; in this case the imaginary part of nk is determined by the Fresnel refractive loss at each bounce of the PO. Within this approximation the mode spacings are unchanged from the closed case (except for the trivial factor of n). These regular modes coexist in a generic resonator with more complicated modes associated with the chaotic regions of phase space.

We noted that for a cavity with discrete symmetries one will typically be able to construct several symmetry-related, nominally degenerate solutions of the Helmholtz equation for each PO. However group-theoretic arguments indicate that these solutions cannot be exactly degenerate and lead us to construct symmetrized solutions which form quasi-degenerate multiplets. We presented a construction and then two simple rules for calculating the quasi-degeneracy of these multiplets and their symmetry quantum numbers. We also point out that the splittings of these multiplets are much larger than expected, due to the phenomenon of “chaos-assisted” tunneling, and give estimate the average splitting in terms of classical quantities.

Generalization of our results to the three-dimensional case appears straightforward for the scalar case and one expects only to have three-dimensional versions of the ABCD matrices enter the theory leading to some difference in details (for a closed cavity this is done in Ref. [66]). More interesting would be the inclusion of the polarization degree of freedom, which seems possible in principle, but which we haven’t explored as yet.

There are several limitations of this work which needs to be addressed in a future work. One obvious shortcoming is the prediction of zero width modes for the dielectric cavity if the underlying PO has all of its bounces above total internal reflection.

Internal reflection is not perfect for these systems at any angle of incidence for two reasons. First, as these solutions describe gaussian beams with some momentum spread, every solution should have some plane-wave amplitude at an angle of incidence for which it can be partially transmitted. This type of correction exists even for a gaussian beam incident on an infinite planar surface and leads to an outgoing beam direction which can be significantly different from that predicted from Snell’s law; this kind of beam deflection in the farfield is analyzed in Section 5.4. For the case of the bow-tie modes of the dielectric resonator the effect of the momentum spread in inducing a finite width was also evaluated using a semiclassical method in Ref. [125]. Second, due to the curvature of the interface in such resonators, there will always be some evanescent leakage, which we can think of as due to direct tunneling through the angular momentum barrier as is known to occur even for perfectly circular resonators. The difficulty of accounting for such effects within the current formalism can best be appreciated by looking at the numerically calculated modes corresponding to the transverse excitations of the bowtie periodic orbit shown in Fig. 4.9. Since at the given parameter values the bowtie periodic orbit is at critical incidence, we would expect a tangent emission, at least for the fundamental mode. Note that the

deviation from this expectation is visible even to the naked eye. Furthermore, the higher order modes in Fig. 4.9(b) and Fig. 4.9(c) display strong deviations from a gaussian character, close to the interface.

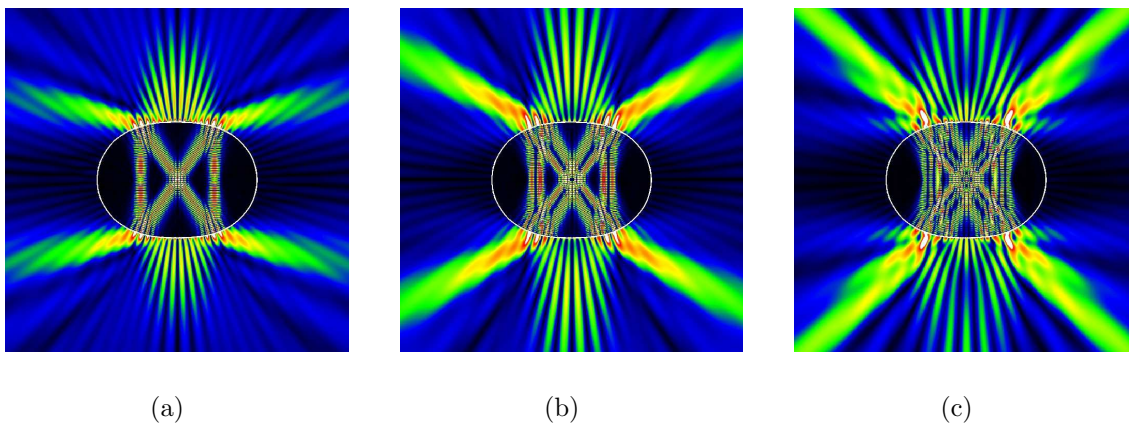


Figure 4.9: A numerically calculated transverse series of modes based on the bowtie periodic orbit. The calculations are performed at $nkR \approx 128$, $n = 3.3$, $\epsilon = 0.16$. With these parameters the bowtie periodic orbit hits the boundary exactly at the critical angle. (a) the fundamental mode, (b) the 1st excited mode (c) the second excited mode. Note the strong “near-field” fluctuations of especially the second order mode in (c).

Interestingly, the farfield emission pattern from the bow-tie modes of the quantum cascade laser measured in the experiment of ref. [5] is clearly best described by the second excited state of the bow-tie island (see Fig. 4.10). Thus its emission directionality is not trivially predictable from ray optics and the knowledge that a bow-tie mode is involved. The mode competition process which leads to selection of the second excited bow-tie mode as the dominant lasing mode is not yet understood and is the subject of current research.

Evaluation of corrections due to such diffractive effects cannot be carried out by simply calculating higher order corrections using the perturbation theory of Section 4.7. The difficulty can be however be understood within our formalism: When the incidence angle χ_i is close to the critical angle $\chi_c = \sin^{-1}(1/n)$, $1/\mu$ becomes a small parameter. Looking at the transmitted beam phase in Eq. (4.67), we find that when $\cos \chi_t \rightarrow 0$, certain terms might become comparable to lower order terms in \sqrt{nk} . This destroys the asymptotic hierarchy and, actually, creates a new one. I will shortly describe what is happening, but will not carry out the calculation.

The scattering of a gaussian or in fact any finite beam at a dielectric interface has been studied in Section 5.4. There, we found that one observes certain shifts in the farfield emission directionality, with respect to expectations based on ray-optics. We also noted that in the vicinity of the interface, the field is dominated by diffraction effects (for beams close to critical incidence). Such *non-specular* effects in

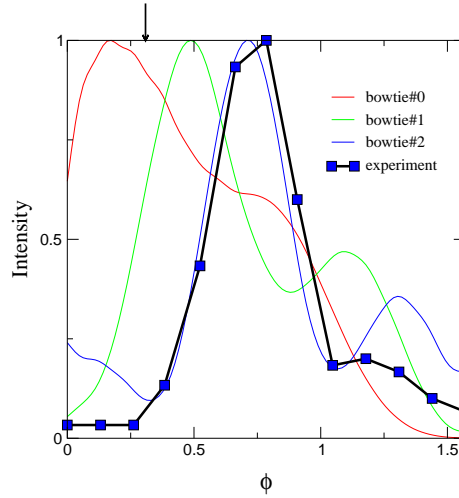


Figure 4.10: The farfield emission patterns of the transverse excitations of the bowtie modes of Fig. 4.9 compared to the experimentally measured farfield pattern. The arrow denotes the direction of tangent emission.

the “near-field” have been studied using certain integral representations (for example the angular spectrum decomposition). It has been established that the reflected [156] beam undergoes a combination of four distinct non-specular effects, namely, lateral, focal and angular shifts and a modification of the beam waist. These can be parametrized by two *complex* shifting lengths, δl and δf . The reflected beam within its own coordinate axes (x_r, z_r) can be expressed as

$$\psi_r \propto \exp [ikz_r + ik\Omega(z_r - \delta f)(x_r - \delta l)^2] \quad (4.93)$$

Note that we have used unscaled coordinates. Now, such shifts could have been accommodated within our current formalism, were it not for the fact that these shifts are intermediate in scale between the cavity length scale (l) and the scale set by our asymptotic parameter \sqrt{k} : one finds that $\delta l \sim k^{-1/4}$ [156]. This would mean that the beam axis is shifted in the transverse section by $\delta \tilde{x} \sim k^{1/4}$, an asymptotically large scale! Such situations, where multiple asymptotic length scales plague the system, can be handled by the technique of *multiple scales analysis* [142] and I hope to address this problem in future work.

A related problem is the treatment of modes when the stable periodic orbit in question is very close (on a wavelength scale) to another one. Such a situation is depicted in Fig. 2.25(b). There, the bowtie orbit has just bifurcated by a period-doubling bifurcation from the stable bouncing ball orbit. Again the problem is similar to the situation of a one-dimensional double-well potential. A possible treatment is a coupled-mode theory, based on Gaussian modes calculated from local treatment of each fixed point, which can yield the values of splittings. A more desirable approach would be to devise a new, uniform ansatz for the solution close to bifurcation, which is similar to the normal forms employed in diffraction catastrophes [99], and were used to calculate spectra of periodic orbits close to bifurcation [157].

Chapter 5

Non-classical phenomena in Dielectric Resonators

5.1 Introduction

In the previous chapters, we have seen the rise to power of semiclassical asymptotics in constructing certain solutions of the Helmholtz equation and their interpretation. In Chapter 2 we have seen how to construct the asymptotic $k \rightarrow \infty$ eigensolutions of *integrable* shapes, via EBK quantization. For this we have used dynamical information of the motion of rays which obey not only much simpler differential equations but are effectively visualized due to their “classical” character; we have noted that this construction *required* the existence of *smooth* surfaces in the phase space which have a lower dimensionality. Subsequently, we have considered non-integrable shapes where the phase space is more complicated and lower dimensional manifolds are not guaranteed to exist. For reasonable deformations and the near-integrable regime where KAM scenario works, we were able to construct semi-classical solutions which worked well *locally* in phase space. In the previous chapter, in that spirit, we have described a method enabling us to construct a sequence of eigenmodes from ray motion on stable islands of classical resonance, both for closed and open cavities.

Troubles with semiclassical asymptotics have surfaced at various stages. In the case of EBK quantization of the circle billiard, the asymptotic expressions we obtained were singular on a well-defined curve, called the caustic. We had to go beyond the notion of rays to get a well-defined expression. In the case of the dielectric circle, the lifetimes of totally internally reflected states were found to be infinite within the framework of rays, although from the exact solutions of the Helmholtz equations we knew perfectly well that there were no infinite-lifetime i.e. bounded modes of the dielectric circle. In a very similar context, in Chapter 4 we found that the ray transformations for the case of a periodic orbit with critical incidence for at least one of its bounce points were singular. A much more dramatic problem was our inability to express the solutions of deformed shapes which were based on chaotic components of the corresponding SOS. Lack of well-behaved invariant curves in certain regions of

the SOS was the main culprit. There are many other phenomena in the realm of optics and quantum mechanics, where the straightforward application of semi-classical asymptotics based on classical motion fails locally or globally (in the configuration space). The problem of caustics is an example where this failure is local, and the case of chaotic wavefunctions represents a global breakdown. We will call such phenomena “non-classical”, because information obtained from classical motion will in general not be sufficient to circumvent the aforementioned problems.

We will proceed to investigate two of such non-classical problems, namely the case of scarred states and non-specular effects, in depth. The stage will be naturally set by an experiment on GaN microcavities that we recently analyzed. As we will see, things don’t look as catastrophic as they sound.

5.2 Blue Lasers: Experimental Setup and Results

In this section, we will go through a hands-on analysis of an actual experimental realization of systems and concepts that we have been investigating theoretically, namely a GaN micro-laser based on a dielectric resonator of quadrupolar deformation [52]. Since this is one of the few places in this thesis where we will discuss a typical experiment in depth, I will seize the opportunity to discuss shortly history and the structure of such a device. Further details can be found in Ref. [79].

The interest in GaN (and related compounds such as InGaN, AlGaIn) stems from its unique optical properties, which allow light-emission in a wide range of optical frequencies ranging from green to ultraviolet (UV) combined with a low power consumption. The former property stems from GaN being a wide-bandgap semiconductor with a bandgap energy of about 3.45eV which corresponds to an emission wavelength of about 360nm . Alloying with Al and In allows a range of emission frequencies. The latter property stems from its high internal quantum efficiency for conversion from electrical to optical. Two main obstacles in the development of optical devices based on GaN has been the lack of a suitable substrate to grow on (because of unfeasibility of growing bulk GaN), and the difficulty of producing reasonably p-doped GaN layers, necessary for the formation of the bandgap. These problems have been partially overcome, using a variety of ingenious techniques. However, the former problem is still a formidable challenge for miniaturized laser resonators, which operate in the conventional Fabry-Perot configuration. The Fabry-Perot setup, where radiation is confined between two highly reflective mirrors, has worked well for majority of lasers. However, with the advent of solid state lasers of microscopic scales, and especially with GaN-based lasers, it has been increasingly difficult to produce the key component of such a resonator: highly reflective microscopically sized mirrors which are realized by distributed Bragg reflectors (DBRs) at these scales. Growing of DBRs in GaN devices, where each part of the reflector has a different lattice constant, results in cracking and hence catastrophic device failures because of lattice mismatch. Hence, the principle of total internal reflection for mode-confinement incarnated in a planar dielectric micro-resonator has been viewed

as one way of alleviating such problems.

In the present experiments, details of which can be found in [79], the micro-laser device is produced by growing GaN on a sapphire substrate, and etching the resulting wafer using a mask and standard photolithography into a $2\mu\text{m}$ high pillar with a quadrupolar deformation of the cross-section, $r(\phi) = R_0(1 + \epsilon \cos 2\phi)$ where $R_0 = 100\mu\text{m}$. The resulting structure, which has an index of refraction $n = 2.65$, is optically pumped at 355nm normal to the plane of the pillar and emits at 375nm . Light emitted from the side-walls is collected through an aperture subtending a 5° angle and passed through a lens and collected on a CCD camera in the farfield. Farfield is defined as a regime where the CCD-cavity distance is much larger than the emission wavelength (in our case this ratio is $\approx 10^3$).

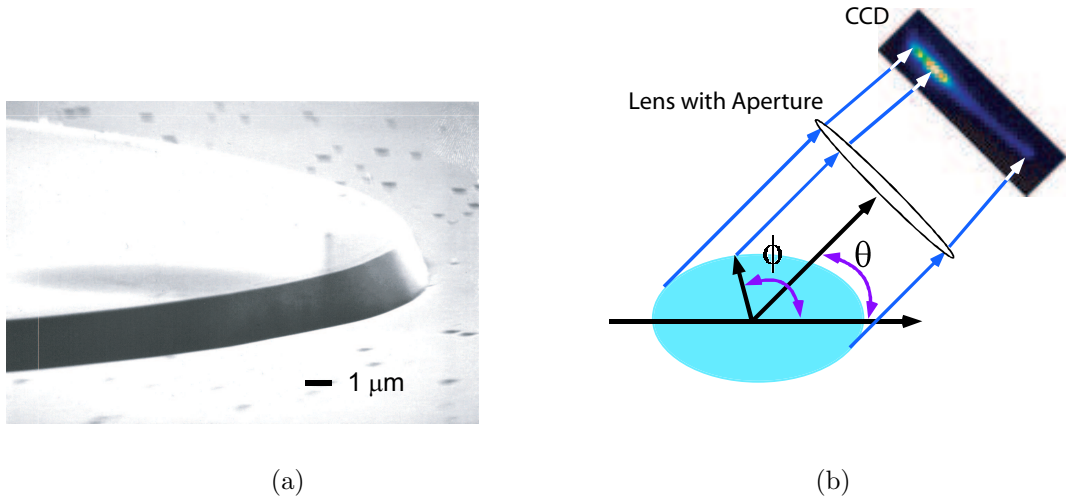


Figure 5.1: (a) A scanning electron micrograph of the GaN resonators used in the experiments. The device in the figure has a diameter of $200\mu\text{m}$. (b) Experimental setup for measuring simultaneously far-field intensity patterns and images of the sidewall emission.

There are two data-acquisition modes. In the *farfield* acquisition mode, the CCD camera is used without the lens and the aperture as a simple photo-diode, and at each farfield angle θ , the farfield emission intensity $I_{FF}(\theta)$ is recorded. In the second mode, the *imaging* mode, the CCD camera records a magnified image of the intensity profile on the sidewall viewed from angle θ in the farfield. The pixels then can be mapped to sidewall angle ϕ via the solution of a simple transcendental equation. This yields a two-dimensional plot, called the *image-field*, where a given data point $I(\phi, \theta)$ denotes the intensity emitted from sidewall position ϕ towards the farfield angle θ . The latter can easily be converted to an incidence angle $\sin \chi$, using Snell's law and basic trigonometry. Hence, what we are recording is actually a phase space plot of the emitted radiation. This correspondence is put into a rigorous basis in Appendix F. A few comments are in order here. The aperture has an important role of defining a window in the direction space ($\Delta \sin \chi$), so that a given pixel

on the camera can be identified upto a diffraction limited resolution with a pair $(\phi, \sin \chi)$. Mathematically, the effect of the lens-aperture combination is equivalent to a windowed Fourier transform of the incident field on the lens [158]. Note that infinite aperture limit is simply a Fourier transform of the incident field and we lose all the information about direction $\sin \chi$, consistent with our intuition with conjugate variables. It has to be emphasized that we are only probing the farfield, and hence the image-data does not contain the “near-field” details we would see in a typical numerical solution, nor does it contain information about the internally reflected components of internal the cavity field (see Appendix F for further details). On the other hand, it endows us with valuable information as to the $\sin \chi$ - ϕ correlations in the emitted field, allowing us to put forward a ray interpretation of the emission and hence the internal resonance.

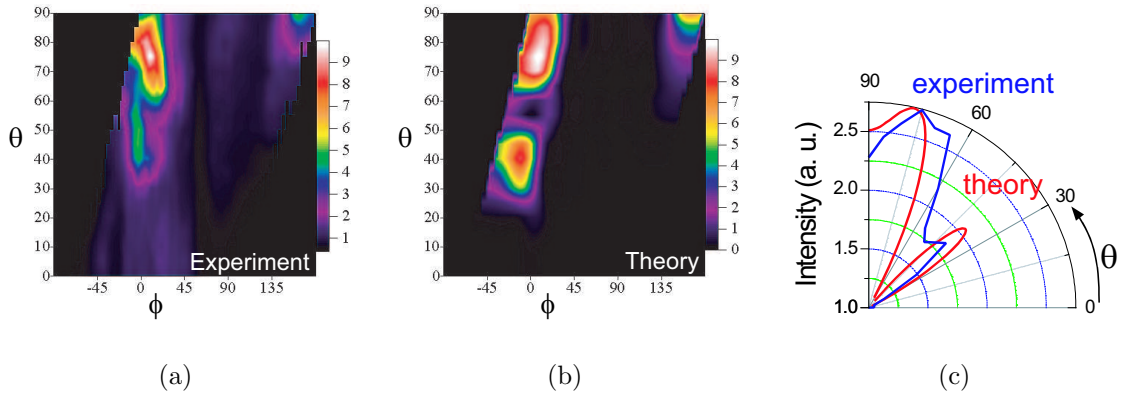


Figure 5.2: (a) Experimental data showing in color scale the CCD images (converted to sidewall angle ϕ) as a function of camera angle θ . Three bright spots are observed on the boundary for camera angles in the 1st quadrant, at $\phi \approx 17^\circ, 162^\circ, -5^\circ$. (b) Calculated image field corresponding to the scarred mode shown in Fig. 5.5. (c) Calculated and experimental far-field patterns obtained by integrating over ϕ for each θ .

We will now focus on the data collected for $\epsilon = 0.12$ quadrupoles. The image-field is displayed in Fig. 5.2(a) and the farfield is shown in Fig. 5.2(c). The data show that the maximum intensity in the 1st quadrant is observed at angle $\theta \approx 74^\circ$ and is emitted from the region of the sidewall around $\phi \approx 17^\circ$. The data also show a secondary bright spot at slightly negative $\phi \approx -5^\circ$ and another one at $\phi \approx 162^\circ$. The observation of a small number of well-localized bright spots on the sidewall suggests a lasing mode based on a short periodic ray trajectory. In Fig. 5.3, we have indicated the approximate positions of the 4 bright spots on the boundary (the imagefield can be unfolded to the range $\theta = 0 \dots 2\pi$ using the symmetry of the quadrupole). In the same figure is shown a view of the SOS at this deformation.

The only stable structures which would result in localized modes in the framework of the previous chapter, are the bouncing ball and the bowtie islands. For comparison,

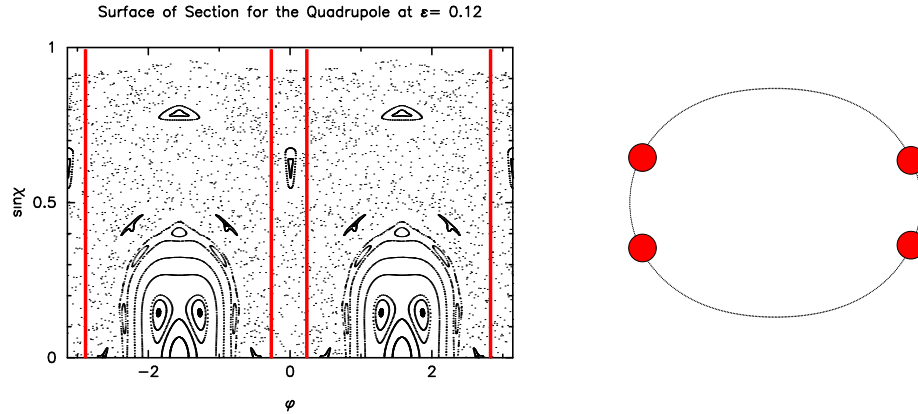


Figure 5.3: The SOS of the quadrupolar billiard at a deformation of $\epsilon = 0.12$. The red vertical lines indicate the values of ϕ at which the bright spots in the imagefield are observed. On the right is a schematic of the bright spots in the real space.

the stable bouncing ball mode would emit from $\phi = 90^\circ$ in the direction $\theta = 90^\circ$. The stable four-bounce bow-tie mode, dominant in the devices of Ref. [5], is also ruled out by our data. It is very low-Q at this deformation due to its small angle of incidence and would give bright spots at $\phi = 90^\circ \pm 17^\circ$, far away from the brightest spot at $\phi = 17^\circ$ (see Fig. 5.3). There is however a pair of symmetry-related isosceles triangular periodic orbits with bounce points very close to the observed bright spots (see inset to Fig. 5.3). The two equivalent bounce points of each triangle at $\phi = \pm 17^\circ$ and $180^\circ \pm 17^\circ$ have $\sin \chi \approx 0.42$, very near to the critical value, $\sin \chi_c = 1/n = 0.38$, whereas the bounce points at $\phi = \pm 90^\circ$ have $\sin \chi = 0.64$ and should emit negligibly (Fig. 5.3). This accounts for the three bright spots observed experimentally in Fig. 5.2(a) (the fourth spot at $\phi \approx 197^\circ$ does not emit into the first quadrant. Note furthermore the proximity of the four of the bounce points to critical incidence; a simple-minded ray tracing would suggest that a mode localized on this periodic orbit would emit approximately tangentially, which would result in farfield maxima which is more or less consistent with the farfield distribution Fig. 5.2(c).

All this would be explained with our view of modes of the previous chapter, were it not for the fact that the triangular periodic orbit is unstable at this deformation. In Fig. 5.4, we plot the trace of the monodromy matrix as a function of deformation, which shows that at deformation $\epsilon = 0.12$, $Tr(M) = -5.27$. The triangular periodic orbit is unstable with a Lyapunov exponent of $\lambda \approx 1.62$ (see Fig. 5.4). We have remarked in Section 4.5 that our method of constructing a localized mode on a periodic orbit fails, if the orbit is unstable. Failure of the method however doesn't mean that a localized mode does not exist. In fact, numerical solution of the quasi-bound states at this deformation, using the method of Chapter 3, finds modes localized on the triangular orbit, as seen in the configuration space plot in Fig. 5.5(a). A much clearer picture free of interference fringes is provided by the Husimi plot of this mode in Fig. 5.5 projected onto the SOS. The brightest spots clearly coincide with the triangular fixed points, and the whole density is localized in midst of the chaotic sea

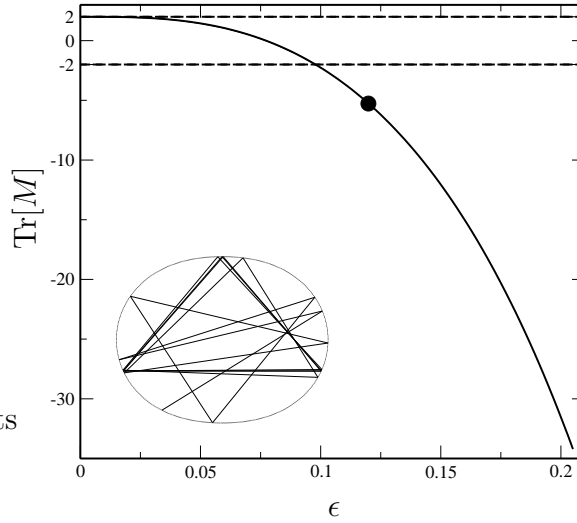


Figure 5.4: The variation of trace of the monodromy matrix with respect to the quadrupolar deformation ϵ . The black circle indicates the experimental value $\epsilon = 0.12$, at which $\text{Tr}(M) = -5.27$. The two dashed lines delimit the regime $-2 < \text{Tr}(M) < 2$ at which the triangular orbit is stable. In the inset is shown real space simulation of a ray orbit started with initial conditions which are away from the triangle fixed point at least by $\delta\phi = 10^{-3}$, $\delta \sin \chi = 10^{-4}$, followed for 20 bounces.

for no apparent reason of classical origin. This mode is an instance of a *scarred state* that we briefly discussed in Section 2.13 and is one of the most surprising and exotic objects uncovered by quantum chaos theory.

Note however that the numerical calculations are performed at $nkR \approx 129$, whereas the experimental lasing frequency corresponds to $nkR \approx 4400$. Despite this difference of more than one order of magnitude, the agreement of the results (farfield, image-field) are surprisingly good. To resolve this paradox we need to discuss some aspects of scarred modes.

“Scarring” refers strictly to the imprint left by short, *unstable* periodic orbits in a group of states [103]. There is still a lot of discussion about the quantification of this imprint [80], but for our modest purposes here, the simplest and most intuitive of such measures is the enhancement of eigenstate intensity along (a tube surrounding) a given unstable periodic orbit and its invariant manifolds (the latter is best measured in the SOS). Understanding the phenomenon of scarring requires a major departure from the philosophy we have been fostering. Namely, the extended EBK quantization, and by this we refer collectively to modes which can be constructed from invariant manifolds (see Chapters 2 and 4), matches a unique invariant classical structure to a unique wavefunction. Scarring on the other hand refers to a statistical phenomenon. It’s a statistically significant correction to Berry’s conjecture [99] that for ergodic systems individual eigenstates will cover all the available energy hypersurface, up to uncorrelated Gaussian fluctuations. Take a short periodic orbit, which is still a classical invariant of measure zero in ergodic systems. The effects of this orbit

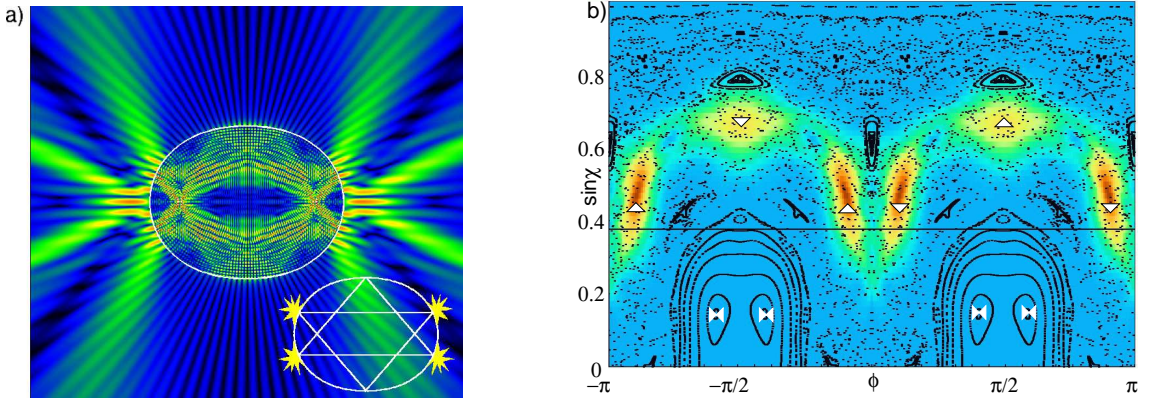


Figure 5.5: (a) Real-space false color plot of the modulus of the electric field for a calculated quasi-bound state of $nkr_o \approx 129$ (n is the index of refraction, k is the real part of the resonant wavevector) and $\epsilon = 0.12$ which is scarred by the triangular periodic orbits shown in the inset (M. V. Berry has termed this the “Scar of David”). The four points of low incidence angle which should emit strongly are indicated. (b) Husimi (phase-space distribution) for the same mode projected onto the surface of section of the resonator. The x-axis is ϕ_W and the y-axis is $\sin \chi$, the angle of incidence at the boundary. The surface of section for the corresponding ray dynamics is shown in black, indicating that there are no stable islands (orbits) near the high intensity points for this mode. Instead the high intensity points coincide well with the bounce points of the unstable triangular orbits (triangles). The black line denotes $\sin \chi_c = 1/n$ for GaN; the triangle orbits are just above this line and would be strongly confined whereas the stable bow-tie orbits (bow-tie symbols) are well below and would not be favored under uniform pumping conditions.

and its associated hyperbolic manifolds will be seen in a group of eigenstates at a certain energy range Δk , which repeats more or less periodically. On the other hand, a single eigenmode requires information about a large number of periodic orbits for its semiclassical construction. The ensuing dichotomy is actually two sides of the same coin. The former view is in general taken by time-domain approaches, which is also the framework the original explanation of this phenomenon [103] was based on. It was shown that the short-time dynamics of the wavepacket could be constructed from the linearized hyperbolic motion (see Section 2.8) in the semiclassical limit. This information can be used to recover a low energy-resolution local spectrum by a simple Fourier transform. Thus, information contained in a given short periodic orbit and its vicinity was found to be encoded in a group of eigenstates. The alternative description adopts the energy-domain view, and was advanced by Bogomolny [81] in a configuration space description and by Berry [159] in a phase space description. Despite the advantages of time-domain wavepacket propagation methods (in that it avoids singularities which shows up at focal points in the energy-domain wavefunctions), we will follow Bogomolny’s configuration space description because it is the closest to the spirit of this thesis.

5.3 Configuration Space theory of Scars

We have to make our peace with the fact that we cannot calculate single eigenmodes, or in other words, a semiclassical ansatz for the eigenmodes of the Helmholtz operator does not exist which uses finite amount of classical information in its construction. The non-existence is of course a vague statement, which shall be clarified. This point of view is central to Bogomolny's derivation, which follows a rather odd route to derive an expression for the *average eigenmode intensities*. The original derivation has been carried out by Bogomolny [81] for a completely ergodic system, the stadium billiard. Thus, from our perspective, we will have to be reckoning with two approximations. First, the quadrupole at $\epsilon = 0.12$ is not ergodic, but the inspection of the SOS shows that there is a large chaotic component, which comprises the triangle fixed points and its vicinity, which includes a large number of isolated unstable periodic orbits. Furthermore, the Husimi projection of the numerical solution we found shows that the localization is not effected by regular invariant curves, but is a pure wave phenomenon. Hence, *locally* we can assume that we satisfy the requirements of an ergodic system. Secondly, the experimental system is a dielectric resonator instead of a quantum billiard; fortunately all the fixed points undergo critical reflection, so that up to certain phase shifts in the semiclassical limit, we have ray motion undergoing specular reflection. After the derivation we will discuss possible extension of the formalism to an open system.

Consider the 2D quantum billiard problem

$$(\nabla^2 + \lambda_n) \psi_n(q) = 0, \quad \psi_n|_{\partial D} = 0 \quad (5.1)$$

where $\lambda_n = k_n^2$. We would like to determine the doubly averaged quantity

$$\langle\langle |\psi(q)|^2 \rangle\rangle = \frac{1}{N} \sum_n f_{\Delta\lambda}(\lambda_n - \lambda) \int d^2q' f_{\Delta q}(q' - q) |\psi_n(q)|^2 \quad (5.2)$$

where N is a normalization factor ensuring $\int d^2q \langle\langle |\psi(q)|^2 \rangle\rangle = 1$, $f_{\Delta\lambda}(\lambda)$ and $f_{\Delta q}(q)$ are arbitrary smoothing functions in energy and coordinate, whose form we take to be

$$f_{\Delta x}(x) = \frac{1}{\sqrt{2\pi\Delta x^2}} \exp\left[-\frac{x^2}{2\Delta x^2}\right] \quad (5.3)$$

An access to super-energy-shell quantities is in general provided by the Green's function of the system

$$(\nabla_q^2 + \lambda) G(q, q'; \lambda) = \delta^2(q - q') \quad (5.4)$$

with the same boundary conditions. Using the completeness of the basis functions $\{\psi_n\}$, the elementary expression for $G(q, q'; \lambda)$ follows

$$G^\pm(q, q'; \lambda) = \sum_n \frac{\psi_n(q)\psi_n^*(q')}{\lambda - \lambda_n \pm i\epsilon} \quad (5.5)$$

and making use of Dirac identity

$$\text{Im} [G^\pm(q, q'; \lambda)] = \mp \pi \sum_n \psi_n(q) \psi_n^*(q') \delta(\lambda - \lambda_n) \quad (5.6)$$

Thus, we can obtain the desired quantity (5.2) by integrating this expression with the weight functions

$$\langle\langle |\psi(q)|^2 \rangle\rangle = \frac{\langle\langle \text{Im} [G(q, q; \lambda)] \rangle\rangle}{\int d^2q \langle\langle \text{Im} [G(q, q; \lambda)] \rangle\rangle} \quad (5.7)$$

where we choose $G = G^+$. In this form, this expression has not more than a symbolic value. To make further progress, we will use Gutzwiller's expression [134] for the Green's function in the semiclassical limit $\lambda \rightarrow \infty$

$$G_{sc}(q, q'; \lambda) = \frac{1}{i\sqrt{2\pi ik}} \sum_{\gamma_j} \sqrt{|D_j|} \exp \left[ikS_j(q, q') - i\mu_j \frac{\pi}{2} \right] \quad (5.8)$$

The summation is over all classical paths γ_j connecting q and q' , which includes the direct path and all the specularly reflected ones; the action $S_j(q, q')$ is the path length and μ_j is an integer index which counts the number of conjugate points [134] and twice the number of reflections along path γ_j . Finally, $D_j(q, q')$ is the Jacobian of the transformation induced by $S_j(q, q')$, which is simply the 2×2 determinant

$$D(q, q') = - \begin{vmatrix} \frac{\partial^2 S}{\partial x \partial x'} & \frac{\partial^2 S}{\partial x \partial y'} \\ \frac{\partial^2 S}{\partial y \partial x'} & \frac{\partial^2 S}{\partial y \partial y'} \end{vmatrix} \quad (5.9)$$

where $q \equiv (x, y)$. However, calculation of the diagonal Green's function $G(q, q; \lambda)$ in Eq. (5.7) has to take into account the singularity at $q = q'$ of the exact Green's function [160] in Eq. (5.4)

$$\lim_{q' \rightarrow q} G(q, q'; \lambda) \sim G_0(q, q'; \lambda) = -\frac{i}{4} \text{H}_0^+(\sqrt{\lambda}|q - q'|) \quad (5.10)$$

Note that

$$\begin{aligned} G_0 &\sim -\frac{i}{4} \sqrt{\frac{2}{\pi k|q - q'|}} \exp \left[ik|q - q'| - i\frac{\pi}{4} \right] && \text{for } k|q - q'| \gg 1 \\ &\sim \frac{1}{2\pi} \ln [k|q - q'|] && \text{for } k|q - q'| \ll 1 \end{aligned} \quad (5.11)$$

When q and q' are substantially separated from each other (much larger than $1/k$) then Eq. (5.11) contributes to the direct path in Eq. (5.8), but when we are interested in the diagonal Green's function Eq. (5.11) has an important contribution. Thus, formally we can write the asymptotic expansion

$$\lim_{q' \rightarrow q} G(q, q'; \lambda) = (\ln k)g_0 + (k^0)g_1 + \left(\frac{1}{\sqrt{k}}\right)g_2 + O\left(\frac{1}{k}\right) \quad (5.12)$$

where the first two terms on the right are obtained from Eq. (5.11), and the last term is essentially $g_2(q, q; \lambda) = \sqrt{k} \cdot G_{sc}(q, q; \lambda)$. Returning to the calculation of Eq. (5.7), we obtain

$$\text{Im} [G(q, q; \lambda)] = -\frac{1}{4}J_0(0) + \frac{1}{\sqrt{k}}\text{Im} [g_2(q, q; \lambda)] \quad (5.13)$$

We finally obtain

$$\langle\langle |\psi(q)|^2 \rangle\rangle = \frac{1}{\Omega} \left[1 - \frac{2}{\sqrt{k}} \left(\langle\langle \text{Im} [g_2(q, q; k)] \rangle\rangle - \frac{1}{\Omega} \int d^2q \langle\langle \text{Im} [g_2(q, q; k)] \rangle\rangle \right) \right] \quad (5.14)$$

where Ω is the area enclosed by the cavity. We can now concentrate on the semiclassical evaluation of $\langle\langle g_2(q, q; \lambda) \rangle\rangle$. Let us first discuss the implications of smoothing. The terms in the sum (5.8) are essentially a sum of the form

$$F_k(L_j) = \sqrt{D_j} e^{ikL_j} \quad (5.15)$$

where $L_j(q) = S_j(q, q)$ is the geometric length of trajectory γ_j . The energy smoothing operation in a window Δk performed by a window function $f_{\Delta k}(k - k')$ can formally be written as

$$\int dk' f_{\Delta k}(k - k') F_k(L_j) \approx F_k(L_j) f_{\Delta L}(L_j) \quad (5.16)$$

where we have simply used the Fourier transform invariance of Gaussians, so that $\Delta L = 1/\Delta k$. Thus, by smoothing over an energy interval Δk , we restrict the sum over paths γ_j which are not longer than $1/\Delta k$. This comes as a tremendous relief, because it's a task bordering at impossibility to encode all the possible closed ray orbits. It's known that for an ergodic system there is an exponential proliferation of the number of orbits with the length (this was shown for a special system, the Sinai billiard, and *periodic* orbits by Berry [161]). What is worse, the weight factors $\sqrt{D_j}$ are known not to counterbalance this proliferation, so that even if we were -in principle- to find all the orbits, the full series without smoothing would be a divergent series in this "raw" form. These results have been rigorously demonstrated in slightly different contexts [162] and remedies were formulated by "conditioning" the divergent series [163, 164].

Similarly, the configuration space smoothing teaches us another lesson. Going through the same arguments, we can expand the action L_j around $q' = q$:

$$L_j(q') = L_j(q) + \nabla L_j|_q \cdot \Delta \mathbf{q} \quad (5.17)$$

so that

$$\int d^2q' f_{\Delta q}(q - q') \sqrt{D_j(q')} e^{ikL_j(q')} \sim \sqrt{D_j(q)} e^{ikL_j(q)} f_{1/\Delta q}(|\delta p|) \quad (5.18)$$

where

$$|\delta \mathbf{p}| = |\nabla L_j(q)| \quad (5.19)$$

where the notation gives away the physics, because the quantity on the right is the momentum (ray direction) mismatch at the point q for a closed ray trajectory

$$|\nabla L_j(q)| = |\nabla_{q'} S(q', q'') + \nabla_{q''} S(q', q'')|_{q'=q''=q} \quad (5.20)$$

and from Section 2.2, we know

$$\mathbf{p}' = \nabla_{q'} S(q', q'') \quad \mathbf{p}'' = -\nabla_{q''} S(q', q'') \quad (5.21)$$

Thus, the biggest contribution to the smoothed wavefunction at q will come from closed trajectories which have a small momentum mismatch (less than $1/\Delta q$) at that point. Particularly, periodic orbits which close upon themselves smoothly, will provide the largest contribution. In conclusion, to calculate $\langle\langle |\psi(q)|^2 \rangle\rangle$, we have to perform the sum over shortest periodic orbits passing through q and closed orbits with momentum mismatch $\delta p < 1/\Delta q$.

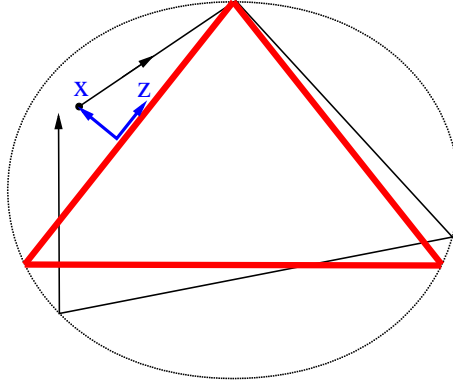


Figure 5.6: The periodic orbit coordinates used in the text, for the particular case of a triangular periodic orbit. The trajectory in black is a closed trajectory in the vicinity.

Let's calculate the contribution of a particular short periodic orbit γ_j . Following Gutzwiller [134], we introduce a special coordinate system, which is quite similar to the one in Chapter 4, to make optimum use of the dynamical information pertaining to the vicinity of the particular periodic orbit. Let z be a coordinate axis placed along the periodic orbit, and x be the transverse coordinate (see Fig. 5.6; note that Bogomonly's derivation denotes these coordinates by x and y respectively). We expand the action $S_j(q, q)$ around $(x = 0, z)$ for small deviations in x , transverse to the PO :

$$S_j(q, q) = L_j + Q_j(z)x + \frac{1}{2}W_j(z)x^2 \quad (5.22)$$

where L is the length of the periodic orbit which is independent of z , $Q_j(z) = \hat{\mathbf{x}} \cdot (\nabla_q S_j + \nabla'_q S_j)|_{x=0, z} = 0$ because of the zero momentum mismatch on the periodic orbit, and $W_j(z)$ contains the second derivatives:

$$W_j(z) = \left(\frac{\partial^2 S_j}{\partial x'^2} + 2 \frac{\partial^2 S_j}{\partial x' \partial x''} + \frac{\partial^2 S_j}{\partial x''^2} \right)_{\substack{x' = x'' = 0 \\ z' = z'' = z}} \quad (5.23)$$

We will in the following calculation drop the orbit index j . In (x, z) coordinates, the determinant \sqrt{D} can be simplified, too. This is because one of the coordinates, z , coincides with the direction of ∇S in the vicinity of $x = 0$ (see Fig. 5.6). Thus, because $(\nabla S)^2 = 1$ (this is the “energy shell” statement in our case; i.e. satisfaction of Eikonal equation), we have

$$\left(\frac{\partial S}{\partial z'}\right)^2 = \left(\frac{\partial S}{\partial z''}\right)^2 = 1 \quad (5.24)$$

differentiating first expression with respect to x'' and the second with respect to x' , we get

$$\frac{\partial^2 S}{\partial x'' \partial z'} \frac{\partial S}{\partial z'} = \frac{\partial^2 S}{\partial x' \partial z''} \frac{\partial S}{\partial z''} = 0 \quad (5.25)$$

As long as q is not a focal point of the periodic orbit, $\frac{\partial S}{\partial z} \neq 0$. Hence, Eq. (5.9) reduces to

$$D(z) = -\frac{\partial^2 S}{\partial x' \partial x''} \Big|_{\substack{x'=x''=0 \\ z'=z''=z}} \quad (5.26)$$

Note that, calculation of $W(z)$ and $D(z)$ requires calculation of quantities like

$$\frac{\partial^2 S}{\partial x' \partial x''} = \frac{\partial p'}{\partial x''} \quad (5.27)$$

where p' is the transverse momentum, and these can be extracted from the linearized tangent map $(\delta x', \delta p') \rightarrow (\delta x'', \delta p'')$ for one traversal of the periodic orbit

$$\begin{pmatrix} \delta p' \\ \delta p'' \end{pmatrix} = \begin{pmatrix} \frac{\partial p'}{\partial x'} & \frac{\partial p'}{\partial x''} \\ \frac{\partial p''}{\partial x'} & \frac{\partial p''}{\partial x''} \end{pmatrix} \begin{pmatrix} \delta x' \\ \delta x'' \end{pmatrix} \quad (5.28)$$

comparing this with the definition of the monodromy matrix Eq. (4.29) with elements $[\mathcal{M}]_{ij} = m_{ij}$ we can write

$$D(z) = \frac{1}{m_{12}(z)}, \quad W(z) = \frac{\text{tr} \mathcal{M} - 2}{m_{12}(z)} \quad (5.29)$$

We can finally express the contribution of a single periodic orbit γ_j to $\langle\langle g_2(q, q; \lambda) \rangle\rangle$

$$\langle\langle g_2 \rangle\rangle_j = \frac{1}{i\sqrt{2\pi i}} \left\langle \left\langle \sum_n \sqrt{|D_n(z)|} \exp \left[ik \left(nL + \frac{1}{2} W_n(z) x^2 \right) - in\nu(z) \frac{\pi}{2} \right] \right\rangle \right\rangle \quad (5.30)$$

The sum n runs over the repetitions of the primitive periodic orbit we are considering. Note that we have replaced μ by $\nu(z)$, which is now a (longitudinal) coordinate-dependent index. We will come back to this later. We can make further progress by finding the forms of n -pass functions $W_n(z)$ and $D_n(z)$.

Consider the expression of the primitive orbit monodromy matrix \mathcal{M} in terms of its eigenvalues $\lambda_{1,2}$. Since $\det \mathcal{M} = 1$, an $O(2)$ transformation induced by

$$R(\theta) = \begin{pmatrix} \cos \theta & -\sin \theta \\ \sin \theta & \cos \theta \end{pmatrix} \quad (5.31)$$

will diagonalize \mathcal{M} . Thus, the elements of \mathcal{M} are parametrized uniquely by $(\theta, \lambda_1, \lambda_2)$

$$M = R(\theta)\text{diag}[\lambda_1, \lambda_2]R(-\theta) \quad (5.32)$$

We are in particular interested in $m_{12} = (\lambda_1 - \lambda_2) \sin \theta \cos \theta$. Because the same $R(\theta)$ will diagonalize the n-pass monodromy matrix \mathcal{M}^n , with the eigenvalues $\lambda_{1,2}^n$, we have $m_{12} = (\lambda_1^n - \lambda_2^n) \sin \theta \cos \theta$ and $\text{tr}[\mathcal{M}^n] = \lambda_1^n + \lambda_2^n$. Substituting these values in Eq. (5.29), we obtain

$$D_n = D \frac{\lambda_1 - \lambda_2}{\lambda_1^n - \lambda_2^n}, \quad W_n = D_n (\lambda_1^n + \lambda_2^n - 2) \quad (5.33)$$

Because the periodic orbits involved are unstable periodic orbits by assumption, the eigenvalues are either ordinary or reflection hyperbolic (see Section 2.8), given by $\lambda_{1,2} = \exp \pm u$ or $\lambda_{1,2} = -\exp \pm u$ with $u \in \mathbb{R}^+$, respectively. It's possible to carry out the sum Eq. (5.30) exactly, in what Bogomolny calls the ‘‘resonance approximation’’ $|\lambda_1| \gg 1 \gg |\lambda_2| = \lambda_1^{-1}$, which physically corresponds to the periodic orbit being highly unstable, so that $D_n = D\lambda_1^{1-n}$, $W_n = W$

$$\langle\langle g_2 \rangle\rangle_j = \frac{2}{i\sqrt{2\pi i}} \left\langle \left\langle \sqrt{|D_j(z)|} \exp \left[\frac{i}{2} k W_j(z) x^2 \right] F_j(k) \right\rangle \right\rangle \quad (5.34)$$

The function $F_j(k)$ is a periodic function of k :

$$F_j(k) = \frac{u_j e^{i\Phi_j(k)}}{2 \sinh \frac{u_j}{2}} \sum_{m=-\infty}^{\infty} \frac{1}{|\Phi_j(k) - 2\pi m|^2} \quad (5.35)$$

where $\Phi_j(k) = kL_j - \nu_j\pi/2 + iu_j/2$. The index ν_j has actually a z -dependence which can be written as

$$\begin{aligned} \nu_j(z) &= \bar{\nu}_j - 1 & \text{sign}[W(z)] < 0 \\ &= \bar{\nu}_j & \text{sign}[W(z)] > 0 \end{aligned} \quad (5.36)$$

Where ν_j is the invariant Maslov index of the particular periodic orbit. This quantity can be determined by successively plotting the (linear) unstable manifolds on the section planes formed by (x, p_x) at successive points z along the PO, and counting the total number of times N_μ the manifolds wind around the SOS origin in one period of the orbit [165]. Then $\nu_j = 2(N_\mu + N_r)$ where N_r is the number of bounces to take into account Dirichlet boundary conditions. We should note here that N_μ is identical to the one we introduced in the stable orbit quantization, namely Eq. (4.37). There, in a very similar manner, it represents the number of windings of the *stable* manifolds.

Let us choose the orbit $j = 3$ to be the unstable triangle orbit of interest to us and define

$$\Delta_3(x, z, k) = \text{Im} [\langle\langle g_2 \rangle\rangle] \quad (5.37)$$

which is the oscillatory contribution to the average wave function density (Eq. (5.14)) in the vicinity of the triangle periodic orbit as a function of k . The k -dependence of this quantity is determined by the denominator of the sum in Eq. (5.35) which

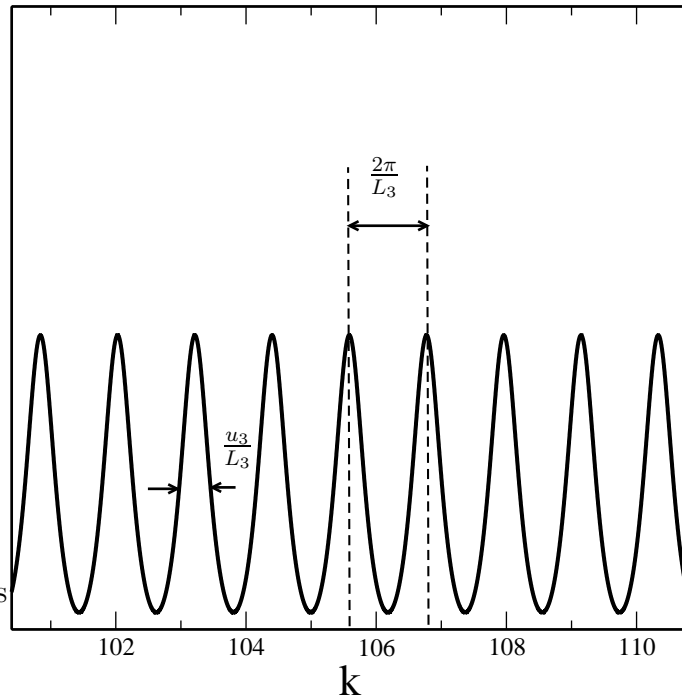


Figure 5.7: The function $F_j(k)$ calculated for the parameters of the unstable triangle at $\epsilon = 0.12$. The length of the orbit is $L = 5.3$ and $u = 1.62$. Note that the spectral peaks are well-resolved.

leads to series of peaks of uniform height spaced by precisely $2\pi/L_3$ (where L_3 is the length of the triangle orbit) and of width u_3/L_3 (see Fig. 5.7). This is the key result of the calculation. There is an enhanced *average* wavefunction intensity due to the presence of the unstable periodic triangle orbit in the vicinity of that orbit with an amplitude that depends both on the orbit's stability and on k . The k -dependence obeys the longitudinal version of the EBK quantization rules, i.e. the peak enhancement varies periodically with a “free spectral range” $\delta k = 2\pi/L_3$ just as we would find for the ground state gaussian mode if the orbit were stable! However instead of delta function peaks, as we would have for EBK or gaussian states, the spectral weight of the enhancement is broadened by the stability exponent u_3 of the orbit. At the same time there are no well-defined transverse excitations as there are in the Gaussian case (the last two observations turn out to be related).

This result sheds light on what the approximations leading to this final expression amount to: we have only taken into account the linear behavior close to the unstable periodic orbit in question; the instability exponent u_3 describes “escape” from the vicinity of the periodic orbit and this is embodied by a complex “quantization” energy $k = k_r + ik_i$, whose imaginary part is simply proportional to the Lyapunov exponent. This is the simple physical reason behind the broadening of the density peaks. Exactly the same picture is found by the time-dependent wavepacket propagation methods [117], where the spectrum is resolved up to a width given by

the Lyapunov exponent. Of course unlike the imaginary part of k that we find for resonator modes, which describes true escape to infinity, here the escape is just into the chaotic component of phase space (recall we have treated here an ideal billiard without escape) and the imaginary part of k is an artifact of our approximations. “Chaotic” modes with infinite lifetime exist, but we cannot find them by analytic methods.

Having discussed the k -dependence of $\Delta_3(x, z, k)$, let us now discuss its spatial structure. We find from Eq. (5.34) that the triangle periodic orbit gives a contribution which displays characteristic gaussian fringes transverse to it. These fast transverse oscillations have a spatial period and amplitude proportional to $1/\sqrt{k}$ ¹. Note that the spatial smoothing has to be done on a scale such that these fringes are resolved. This constrains the smoothing window to a size between $1/k$ and $1/\sqrt{k}$ in an actual calculation. Another notable feature is the divergence of the amplitude at points along the periodic orbit where $m_{12}(z) = 0$. These are the focal points of the periodic orbit and the divergence is not physical. As we discussed in Section 2.4, it’s an artifact of the semiclassical approximation; but nevertheless it hints to the right behavior of enhanced wavefunction amplitude at these points (see the exact solution corresponding to the unstable two-bounce orbit in Fig. 3.13(a) for example, where the focal points can be clearly identified).

Let’s finally come back to the solutions we found numerically for the unstable triangle. Both the configuration space and the Husimi representation show a well-defined enhancement in intensity along the two symmetry related triangular periodic orbits. The fact that scarring is so well-defined in a single eigenmode is not inconsistent with the Bogomolny formulation. The triangular periodic orbit has a Lyapunov exponent of $u \approx 1.62$, thus the resonance peaks in $F_j(k)$ are well-resolved. Furthermore the mean-level spacing at $nkR \approx 120$ is large enough to yield such a clean scar. At energies where the actual experiment is performed, which corresponds to $nkR \approx 4400$, a numerical solution is not only out of question but also loses its meaning. For at such high energies there will be several eigenmodes which contribute to lasing, which will lie in a narrow interval given by the laser linewidth. The measurements spatial and energetic resolution will not resolve the individual states. The measured quantity is then essentially the quantity $\langle\langle |\psi(q)|^2 \rangle\rangle$ that we have calculated by the above method, and is well described by our numerical solution at nkR values far from the experimental value.

Before closing this section, we should emphasize that for a system like the quadrupole which has a discrete symmetry group, the average wavefunction should be calculated separately for each irreducible group, along similar lines as the calculation performed in Section 4.9. This can be done by calculating symmetry projected Green’s functions. Since we will not perform an actual calculation here, we invite the reader to the original reference [81] (and [166]).

¹Note that the scales are restored by W and D , such that the period is $\propto \sqrt{l/k}$ and amplitude $\propto 1/\sqrt{kl}$, where l is a characteristic length of the system.

5.4 Non-specular effects in emission in refractive billiards

Closer inspection of the imagefield in Fig. 5.2(a), however presents an intriguing puzzle from the point of view of ray optics. A mode localized on these triangular orbits would be expected to emit from the four bounce points approximately in the tangent direction according to Snell’s law; this means that the bright spot at $\phi = 17^\circ$ should emit into the direction $\theta \approx 115^\circ$ (Fig. 5.4), whereas the data clearly indicate that the 17° bright spot emits in the direction $\theta = 72^\circ$. Thus the emission pattern violates the intuitive expectations of ray optics by 43° , a huge discrepancy (see Fig. 5.4). Moreover, $\lambda/nR = 2.8 \times 10^{-3}$, so we are far into the regime in which the wavelength is small compared to the geometric features of the resonator and ray optics would be expected to be a good approximation. To ensure that this is not an effect we are unable to capture because of the discrepancy in the energies between the numerical solution and the actual experimental value, we have to determine what imagefield would result if the same experiment was performed on the numerically found solution in Fig. 5.5(a). The way to do this is described in Appendix F. The imagefield corresponding to the numerical resonance calculated using the expression Eq. (F.11) is reproduced in Fig. 5.2(b). The good agreement with the experimental data in Fig. 5.2(a) suggests that we have to look for the culprit somewhere else.

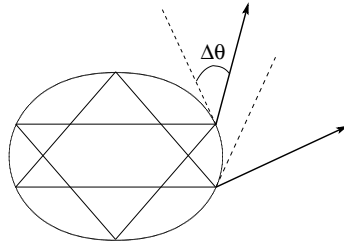


Figure 5.8: Schematics showing the three emitted “beams” detected in the experiment (solid lines) and illustrates their strong deviation from Snell’s law (dashed tangent lines).

The resolution of this apparent paradox is suggested by the numerical data of Fig. 5.5(b). It is clear that the scarred mode, while localized around the triangle orbit, has a significant spread in angle of incidence, $\Delta \sin \chi \approx 0.2$. This means that we must regard the scarred mode as a bounded beam with a large angular spread, with some components almost totally reflected and other components transmitted according to the Fresnel transmission law. Below, we will show that such a beam incident on a dielectric interface is strongly deflected in the farfield away from the tangent direction expected from a naive application of Snell’s law. We call this effect Fresnel Filtering (FF).

The effect occurs for a bounded beam of arbitrary cross-section incident from a semi-infinite medium of index n into vacuum, although it will be quantitatively altered in a resonator due to the curvature and (or) the finite length of the boundary.

We thus begin with the planar example, which we solve analytically, before presenting numerical results for quadrupolar asymmetric resonant cavities (ARCs) [3]. There is a large body of literature on reflection of a beam from a dielectric interface near or above the critical angle, as the reflected beam exhibits the Goos-Hänchen lateral shift as well as other non-specular phenomena [167]. However only a few of these works address the transmission [168, 169] of the beam and none appear to have identified the FF effect.

For simplicity, we consider a two-dimensional planar interface which separates two semi-infinite regions with a relative index of refraction n . Consider a beam E_i that is incident from the denser region, with a central incidence angle θ_i . The basic effect is independent of the nature of the input beam as long as it is focused and has significant angular spread. Thus, we will take the beam to be Gaussian with a minimum beam waist w (which we use to scale all lengths) at a distance z_o from the interface

$$E_i(x_i, z_i) = \frac{E_0 w}{w_i} \exp \left[- \left(\frac{x_i}{w_i(z_i)} \right)^2 + inkz_i \right] \quad (5.38)$$

where the beam waist variation is given by

$$w_i^2(z_i) = w^2 + i \frac{2z_i}{nk} \quad (5.39)$$

This expressions are written in the native coordinates of the beam, $\mathcal{S}_i : (x_i, z_i)$, where z_i is situated along the beam axis, so that $z_i = 0$ line coincides with the minimum beam-waist (see Fig. 5.9). Since we know the solution of the plane-waves scattering problem at a dielectric interface [124] exactly, we ideally would like to represent the incident beam as a superposition of plane-waves. This can be accomplished by the Weyl representation, or what is better known in the optics community, by the *angular spectrum representation* [170]

$$E_i(x_i, z_i) = \frac{E_0 n k w}{2\sqrt{\pi}} \int_{-\infty}^{\infty} ds \exp \left[- \left(\frac{n k w s}{2} \right)^2 + ink (s x_i + c z_i) \right] \quad (5.40)$$

where $c = \sqrt{1 - s^2}$ and the the sign of the square root has to be carefully chosen so as to satisfy the boundary conditions at infinity. At first look, the maning of this expression is clear: we simply synthesize the gaussian beam from plane-waves of fixed wavevector magnitude nk with directionalities $s = \sin \Delta\theta_i = \sin(\theta - \theta_i)$ with respect to beam axis, weighted with a gaussian profile in direction space. However, the exact representation requires that we include *evanescent components* with $|s| > 1$, i.e. plane-waves which have a complex direction $\Delta\theta_i$. These simply amount to waves which are damped in the z direction with a decay constant $k\sqrt{s^2 - 1}$ ($|s| > 1$) [171]. These components are necessary for the correct description of wave phenomena in systems with discontinuous boundaries.

We furthermore introduce the refracted beam coordinates $\mathcal{S}_e : (x_e, z_e)$ with its z_e axes tilted by θ_e with respect to the surface normal, where θ_e is obtained by simply

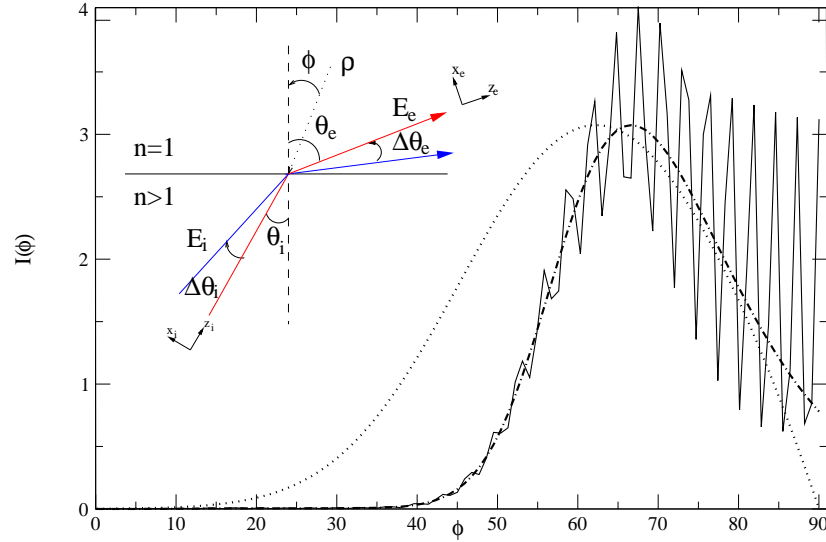


Figure 5.9: Angular farfield intensity distributions $I(\phi) = |E_e(\phi)|^2$ for: (dotted line): critical incidence on a planar interface with $n = 1.56$, $\Delta = 8.82$, $z_0 = 5$ using the gaussian model (Eq. (5.52)). (solid line): Exact quasi-normal mode with diamond geometry at $nk_o r_o \approx 90$, for a quadrupolar ARC with $\varepsilon = 0.1$, $n = 1.56$. (dot-dashed line): Chiral version of diamond resonance (see text) which eliminates interference effects. Inset: Coordinates and variables for the GM calculation.

applying Snell's Law: $\sin \theta_e = n \sin \theta_i$ (see Fig. 5.9). The refracted beam can now be simply constructed by utilizing the expansion Eq. (5.40). Because the boundary conditions are linear, if each plane-wave in the spectrum satisfies the boundary conditions, the superposition is guaranteed to satisfy it, too. Thus, the emitted beam is given by

$$E_e(x_e, z_e) = \frac{\Delta}{2\sqrt{\pi}} \int_{-\infty}^{\infty} ds t(s) \exp \left[- \left(\frac{\Delta}{2} \right)^2 + i\Delta\sqrt{1-s^2}z_0 \right] \times \exp \left[i\frac{\Delta}{n} (\sin \Delta\theta_e(s)x_e + \cos \Delta\theta_e(s)z_e) \right] \quad (5.41)$$

where now each incoming plane wave component at deviation $\Delta\theta_i = \sin^{-1} s$ is refracted into a plane-wave at direction $\sin \Delta\theta_e$ with respect to z_e axis such that

$$\sin(\theta_i + \Delta\theta_i) = n \sin(\theta_e + \Delta\theta_e) \quad (5.42)$$

with amplitude given by the Fresnel refraction coefficient

$$t(s) = \frac{2 \cos(\theta_i + \Delta\theta_i)}{\cos(\theta_i + \Delta\theta_i) + \sqrt{\sin^2 \theta_e - \sin^2(\theta_i + \Delta\theta_i)}} \quad (5.43)$$

The term $\exp[i\Delta\sqrt{1-s^2}z_0]$ is due to the accumulation of the phase from the origin $z = 0$ to the interface at $z_i = z_0$. Furthermore, we have introduced the important dimensionless quantity $\Delta = nk_w$.

This expression can now be used to determine the field on the $z > 0$ side of the interface. Since we are not interested in the “nearfield” phenomena but the farfield, it proves convenient to introduce the polar coordinates (ρ, ϕ) attached to the interface. Then the integral Eq. (5.40) can be rewritten as

$$E_e(\rho, \phi) = \frac{E_0 \Delta}{2\sqrt{\pi}} \int_{-\infty}^{\infty} ds t(s) \mathcal{G}(s) e^{\lambda f(s)} \quad (5.44)$$

where the “profile” $\mathcal{G}(s)$ is given by:

$$\mathcal{G}(s) = \exp \left[- \left(\frac{\Delta}{2} \right)^2 s^2 + i \Delta \sqrt{1 - s^2} z_o \right] \quad (5.45)$$

and

$$f(s) = i \cos(\phi - \theta_e - \Delta \theta_e(s)) \quad (5.46)$$

The integral in Eq. (5.44) is to be evaluated in the asymptotic limit $\lambda = \Delta \rho / n \rightarrow \infty$. This can be conveniently done using a saddle point integration. Before we deform the contour of integration, it's worth establishing the analytic structure of the integrand. Note that we can rewrite the function $f(s)$ as

$$f(s) = i \sqrt{1 - n^2 \sin^2 \theta_i - n^2 \cos 2\theta_i s^2 + s \sqrt{1 - s^2} \sin 2\theta_i} \quad (5.47)$$

This expression reveals the critical points $s = \pm 1$ and $s = \pm \sin(\theta_i - \theta_c)$, which are first order branch-points. The final critical point is the saddle point determined by

$$\frac{df}{ds} = i \sin(\phi - \theta_e - \Delta \theta_e(s)) \frac{d\Delta \theta_e}{ds} = 0 \quad (5.48)$$

which results in the real saddle

$$s_0(\phi) = \frac{1}{n} \left(\sin \phi \cos \theta_i - \sin \theta_i \sqrt{n^2 - \sin^2 \phi} \right) \quad (5.49)$$

provided $d\Delta \theta_e/ds = 0$ or ∞ .

Equation Eq. (5.49) can be rewritten as $n \sin(\theta_i + \Delta \theta_i) = \sin \phi$ and selects the incident directions which refracts to the observation point ϕ .

Noting that

$$\left. \frac{d^2 f}{ds^2} \right|_{s=s_0} = -i \left(\left. \frac{d\Delta \theta_e}{ds} \right|_{s=s_0} \right)^2 \quad (5.50)$$

and

$$\left. \frac{d\Delta \theta_e}{ds} \right|_{s=s_0} = \frac{\sqrt{n^2 - \sin^2 \phi}}{\sqrt{1 - s_0^2} \cos \phi} \quad (5.51)$$

so that we get the lowest order asymptotic term

$$E_e(\rho, \phi) = \frac{E_0 \Delta}{\sqrt{2i \frac{\Delta}{n} \rho}} J(s_0) t(s_0) \mathcal{G}(s_0) \exp \left(i \frac{\Delta}{n} \rho \right) + O \left(\frac{1}{\Delta \rho} \right) \quad (5.52)$$

where the transmission function, evaluated at the relevant saddle point $s_0(\phi)$ is given by

$$t[s_0(\phi)] = \frac{2\sqrt{n^2 - \sin^2 \phi}}{\sqrt{n^2 - \sin^2 \phi} + n\sqrt{1 - \sin^2 \phi}} \quad (5.53)$$

and the “divergence” factor $J(s_0)$ is

$$J[s_0(\phi)] = \frac{\sqrt{1 - s_0^2} \cos \phi}{\sqrt{n^2 - \sin^2 \phi}} \quad (5.54)$$

The saddle point equation Eq. (5.49) can be rewritten as $n \sin(\theta_i + \Delta\theta_i) = \sin \phi$; this saddle point value selects the angular component which refracts into the observation direction, ϕ , by Snell’s law. However, the amplitude factor obtained by Gaussian integration around the saddle point shifts the maximum of the outgoing beam away from the Snell direction. As noted, the effect occurs for narrow beams with an arbitrary (non-Gaussian) wavevector distribution $\mathcal{B}(s)$; in such a case the factor $\mathcal{G}(s_0)$ in Eq. (5.52) is replaced by $\mathcal{B}(s_0)$.

Two technical points are in order here: First, there may be branch-cut contributions (case $d\Delta\theta_e/ds = \infty$) to integration along the steepest descent path, as found in analysis of the reflected beam (see for example [168]). Such contributions are subdominant with respect to the first order asymptotic term derived in Eq. (5.52). Second, there is another saddle point (case $d\Delta\theta_e/ds = 0$), $\tilde{s}_0 = \cos(\theta_i)$, which corresponds to angular components with grazing incidence to the interface. Because the Fresnel transmission factor vanishes for such components, \tilde{s}_0 contributes to the integral only at order $\mathcal{O}(\rho^{-3/2})$ and is important only very near $\phi = \pi/2$. We neglect this contribution here.

Eq. (5.52) gives the angular beam profile in the far-field, which is non-zero for any incident angle θ_i , even $\theta_i > \theta_c = \sin^{-1}(1/n)$. *The key point is that the angular maximum of this outgoing beam, ϕ_{max} , is in general not at the angle θ_e predicted by applying Snell’s law to the central incident beam direction, θ_i .* Instead, because of the fast variation of the refraction angle with respect to the incoming angle, the beam direction is shifted by an angle $\Delta\theta_{FF}$ that corresponds to less refraction than expected from Snell’s law. This angular deflection can be quite large for incidence near θ_c in typical microcavity resonators; in Fig. 5.9 the dotted curve is the result of Eq. (5.52) for critical incidence, for which the Snell angle is $\phi = 90^\circ$, but $\phi_{max} = 62^\circ$ giving $\Delta\theta_{FF}^c = 28^\circ$. The far-field peak-shift, $\Delta\theta_{FF}$, depends on the beam width Δ and on n ; analysis of the stationary phase solution gives the result that, at $\theta_i = \theta_c$

$$\Delta\theta_{FF}^c \approx (2/\tan \theta_c)^{1/2} \Delta^{-1/2} \quad (5.55)$$

which predicts that $\Delta\theta_{FF}^c \approx 30^\circ$ for the parameters of Fig. 5.9.

Clearly the same FF effect will occur in emission from dielectric resonators, and its magnitude will be similar to the planar case when the typical radius of curvature is much larger than w . Before we investigate the emission of triangular scarred states, we would like to discuss this effect for modes of the resonator, which are known to

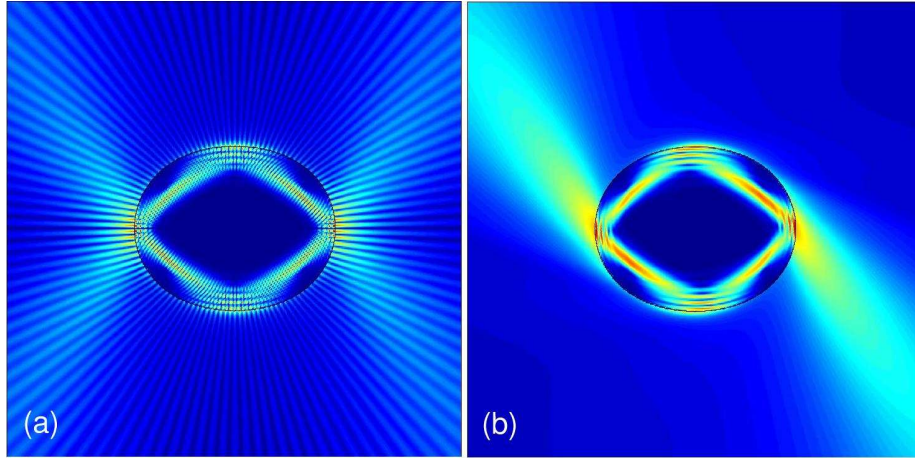


Figure 5.10: (a) Field intensity plot (gray-scale) for a diamond resonance of the quadrupole at critical incidence for the points at $\phi_w = 0, \pi$, calculated numerically at $nk_o r_o \approx 90$, $n = 1.56$, $\epsilon = 0.1$. Note that there is negligible emission from the upper and lower bounce points at $\phi_w = \pm 90^\circ$ because they are above the critical angle (b) Chiral counterpart of this exact resonance, simulating a gaussian beam (see text).

have a simple gaussian profile; these are the stable island states we investigated in Chapter 4. An ideal case to study are the resonances based on the stable four-bounce (diamond) PO at $\epsilon = 0.1$ and varying index of refraction n . In Fig. 5.10 (a) we plot one representative quasi-bound mode at $n = 1.56$ (the index is chosen so that $\theta_i = \theta_c$ for this mode); the corresponding far-field angular intensity is plotted in Fig. 5.9. One can see the rapid oscillations due to interference, but in Fig. 5.9 it is clear that the maximum of the intensity is displaced from $\phi = 90^\circ$ as expected because of FF. To compare the size of the effect with that of GM, it is convenient to eliminate the interference by calculating the “chiral” resonance, shown in Fig. 5.10 (b). This is the original resonance with the negative angular momentum components projected out, hence generating a uni-directional beam (this is simply done by “desymmetrizing” with the recipe given in Section 4.10 and rules of 4.11). Plotting this chiral resonance in Fig. 5.9 (dotted-dashed line) gives the diamond resonance a smooth envelope without the oscillations. Regarding this chiral resonance as a beam that is incident at $\phi_w = 0$ on the boundary, with an angle of incidence $\theta_i \approx 39^\circ$, we can compare the FF shift with that of GM. From Fig. 5.9 one can see that the resonance emission peaks at $\phi_{max} \approx 66^\circ$, whereas GM gives a similar envelope that is slightly shifted, with $\phi_{max} \approx 62^\circ$.

To evaluate systematically the FF effect, we have calculated the far-field peaks of the set of diamond resonances while varying the index of refraction, so that θ_c is scanned through the PO incidence angle $\theta_i \approx 39^\circ$. To remain as close as possible to our GM with fixed Δ , we have chosen the resonances so that nkR is approximately constant. In Fig. 5.11, the numerical resonance peak is compared to the calculated

value ϕ_{max} from Eq. (5.52) and to that predicted by Snell's law. One can see that maximum deviation takes place at θ_c .

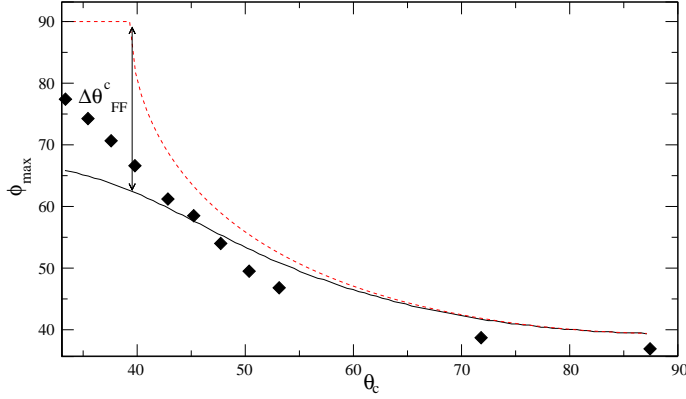


Figure 5.11: Comparison of peak angular farfield values ϕ_{max} for varying critical angle $\theta_c = \sin^{-1}(1/n)$. (Diamonds): exact resonances at $nk_o r_o \approx 90$. (Solid line): GM calculation with $\Delta \approx 8.82$. (Dashed line): Snell's law prediction: $\sin \phi_{max} = n \sin \theta_i$ where $\theta_i \approx 39^\circ$. $\Delta \theta_{FF}^c$ designates the deviation from Snell's law at $\theta_c = \theta_i$.

Returning now to the emission of the scarred state in Fig. 5.5(a), we plot in Fig. 5.12 the central beam emission angle χ_e^0 versus central incidence angle χ_i^0 . To model the experiment we assume that the probability distribution for the incidence angle $\mathcal{B}(s)$ is approximately the same as the cross-section of the Husimi distribution of Fig. 5.5(b) evaluated at the triangle bounce point $\phi_W = 17^\circ$. We find a very large angular shift $\Delta \theta_{FF}$, in approximate agreement with the numerically found farfield (we don't expect precise quantitative agreement since the curvature of the resonator also has some effect on the far-field pattern, giving a different value of θ_{FF} than for the planar interface).

It's clear this effect will be crucial for analysis of the emission patterns of dielectric micro-lasers, because the dominant lasing mode will be often based on long-lived and localized quasi-normal modes which always involve ray components close to critical incidence. Furthermore, even if the experiments are performed deep in the semiclassical limit $nkR \rightarrow \infty$, localization (in SOS, per coordinate) will be of order $1/\sqrt{nkR_0}$ (as is for stable island modes for example) leading to a spectral width $\Delta \propto \sqrt{nkR_0}$, so from Eq. (5.55), the deviation angle at critical incidence $\theta_{FF}^c \propto (nkR)^{-1/4}$ and hence may be large for $nkR \sim 10^2 - 10^3$, as in recent experiments on semiconductor ARC lasers [5, 48, 52].

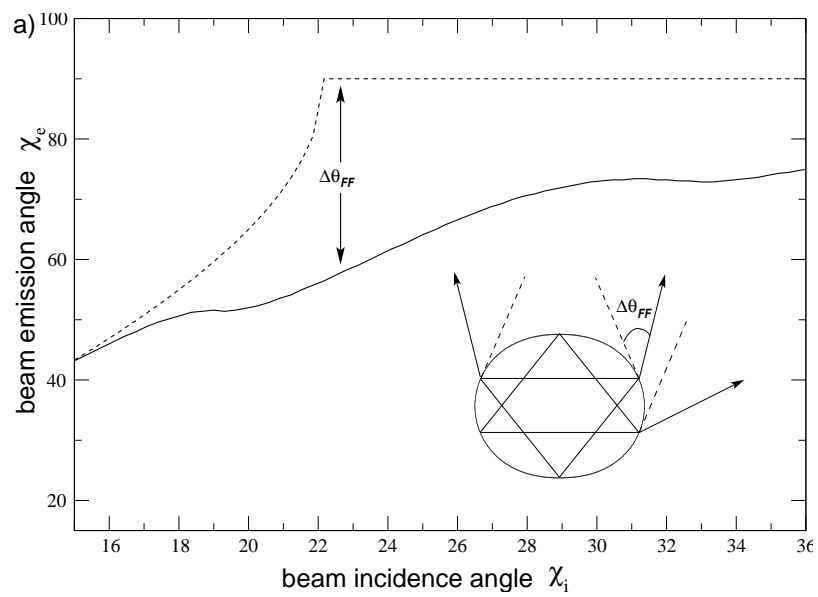


Figure 5.12: Solid line: Central beam emission angle χ_e^o vs. central incidence angle χ_i^o for a beam of angular spread equivalent to the scarred mode of Fig. 5.5 incident on a plane interface. Dashed line is Snell's law, the discrepancy is the Fresnel Filtering angle $\Delta\theta_{FF}$. Inset schematic shows the three emitted "beams" detected in the experiment and illustrates their strong deviation from Snell's law (dashed tangent lines).

Chapter 6

Towards a Non-Linear Theory of Dielectric Resonators

6.1 Introduction

The theory of lasers, including the full non-linearity of the laser equations has been developed and solved (in various limits) over a period of almost 45 years [76, 172, 173]. Real lasers are based on three, four or multiple level atomic, molecular or solid-state media and the matter-light interaction can be quite complex. However almost all of the laser literature has focused on the simplest possible resonator modes, e.g. linear Fabry-Perot modes, often treated in single-mode approximations or neglecting spatial variation in the field intensity. Our interest in this thesis has been dielectric resonators with a high degree of spatial complexity to their mode structure. Hence in this chapter our primary interest is to begin formulating a laser theory in which the spatial complexity of dielectric cavity modes can be taken into account. Therefore we will treat the properties of the active medium in the most elementary way, describing it by a two-level model.

Such a minimalistic model of a laser is the *semi-classical laser theory* of Haken [173]. The terminology reflects the treatment of the radiation field as a classical field obeying Maxwell's equations. Note that this is distinct from the use of "semi-classical" as the short-wavelength limit, that we have used in the past chapters.

Following the standard semi-classical laser theory [173, 174], we start with the Maxwell-Bloch equations in the form

$$\nabla^2 E - \frac{1}{c^2} \ddot{E} = \frac{4\pi}{c^2} \left[\ddot{\tilde{P}}^+ + (\ddot{\tilde{P}}^+)^* \right] \quad (6.1)$$

$$\dot{\tilde{P}}^+ = -(i\omega_a + \gamma_\perp) \tilde{P}^+ + \frac{g^2}{i\hbar} ED \quad (6.2)$$

$$\dot{D} = \gamma_\parallel (D_0 - D) - \frac{2}{i\hbar} E \left[(\tilde{P}^+)^* - \tilde{P}^+ \right] \quad (6.3)$$

These set of equations describe the interaction of a single polarization state of the classical electromagnetic field of magnitude $E(q, t)$ with an ensemble of two-level

atoms. Let the individual two-level atoms in the medium have energy levels and eigenstates given by $(\epsilon_i, |i\rangle)$, $i = 1, 2$, where $\epsilon_2 - \epsilon_1 = \hbar\omega_a$. Typically $\omega_a \sim 10^{15} \text{s}^{-1}$. When an electric field is applied, the time-dependent evolution of the individual atomic wave-functions is given by

$$|\psi(t)\rangle = c_1(t)|1\rangle + c_2(t)|2\rangle \quad (6.4)$$

if we denote the density matrix elements of this system by $\rho_{ij}(t) = c_i^*(t)c_j(t)$, then Eq. (6.2)-(6.3) are just the rewriting of the density matrix evolution equations, with an emphasis on observable attributes of the ensemble. The magnitude of the average polarization induced $\tilde{\mathbf{P}} = n_a \langle \psi | e\mathbf{r} | \psi \rangle$ can be written as $\tilde{P} = n_a(g\rho_{12} + g^*\rho_{12}^*) = \tilde{P}^+ + \tilde{P}^-$, where $\tilde{P}^+ = (\tilde{P}^-)^* = n_a g \rho_{12}$. Here $g = \langle 1 | e\mathbf{r} | 2 \rangle$ is the *field-matter coupling constant*, and n_a is the average density of atoms. We assume that the polarization is in the direction of the singly polarized electric field $E(q, t)$, and discard all references to vector character of the variables from now on. $D(q, t)$ is the average inversion of the atomic medium, written in terms of the diagonal entries of the atomic density matrix as $D = n_a(\rho_{22} - \rho_{11})$. Thus, $D > 0$ represents the situation when there is in average more electrons in the upper level than the lower level, i.e. an inverted population. Note that in the real physical system, there are a host of other degrees of freedom which interact with the field. The cumulative effect of the neglected degrees of freedom enter the Maxwell-Bloch equations as phenomenological damping constants γ_\perp and γ_\parallel , giving rise to *homogeneous broadening*. In general $\gamma_\perp \gg \gamma_\parallel$. Because of the relaxation terms, and to initiate the lasing process, energy must be supplied to the medium to keep it active. This constant energy supply is simulated by adding a constant pumping rate $\gamma_\parallel D_0$ to the inversion equation Eq. (6.3). Finally, we recognize the first equation Eq. (6.1) to be the inhomogeneous version of the wave-equation Eq. (2.2) containing an additional polarization term $\tilde{P}(q, t)$. Eqs. (6.1)-(6.3) then is a coupled non-linear set of equations for $(E, \tilde{P}, D)(q, t)$.

First, let's factor out the fast time-dependence of the fields $F \equiv E, \tilde{P}$, which we assume is close to the resonant atomic transition frequency ω_a :

$$F(q, t) = F^+(q, t)e^{-i\omega_a t} + F^-(q, t)e^{i\omega_a t} \quad (6.5)$$

where $F^- = (F^+)^*$. The simplification of the above equations can be achieved by two standard approximations: the *slowly varying amplitude approximation* (SVA) and *rotating wave approximation* (RWA).

Within SVA, we assume that the time dependence left in $F^\pm(q, t)$ is much slower than ω_a , i.e. $|\dot{F}^\pm| \ll \omega_a |F^\pm|$. And RWA assumes that $+$ fields are only coupled to $+$, and vice versa. Hence, the following replacements can be justified

$$\ddot{E} \rightarrow -\omega_a^2 E^+ - 2i\omega_a \dot{E}^+, \quad \ddot{P}^+ \rightarrow -\omega_a^2 P^+ \quad (6.6)$$

Rewriting Eqs. (6.1)-(6.3)

$$\dot{E}^+ = \frac{i}{2\omega_a} (\omega_a^2 + c^2 \nabla^2) E^+ + 2i\pi\omega_a P^+ \quad (6.7)$$

$$\dot{P}^+ = -\gamma_{\perp}P^+ + \frac{g^2}{i\hbar}E^+D \quad (6.8)$$

$$\dot{D}^+ = \gamma_{\parallel}(D_0 - D) - \frac{2}{i\hbar} [E^+(P^+)^* - (E^+)^*P^+] \quad (6.9)$$

Note that in the last equation, because of RWA, E^+ couples only to P^- . The solution of these equations is still a formidable problem, because these equations actually represent an infinite set of non-linear (ordinary) differential equations in time, one for each point in space. The next step is the expansion of the electric field and the polarization in terms of the modes of the empty cavity:

$$F^+(q, t) = \sum f_m(t)\psi_m(q, t) \quad (6.10)$$

where $f_m \equiv (e_m, p_m)$. This expansion is exact if $\{\psi_m(q, t)\}$ forms a complete set. In standard treatments, $\{\psi_m(q, t)\}$ is chosen to be the modes of an equivalent closed (Dirichlet) cavity, for which this requirement is satisfied. A realistic cavity however, and in particular dielectric resonators, have leakage and hence a coupling to the external world. This leakage is in practice taken into account by introducing a phenomenological modal decay constant κ_m while keeping the complete set of closed cavity modes. For dielectric cavities, it would be desirable to use instead the set of quasi-bound modes which we have discussed in previous chapters, because they contain the key to the determination of the emission pattern; closed cavity modes are only defined within the resonator. Their completeness and orthogonality however poses problems, mainly because of the singularity they possess at spatial infinity. The investigation of this possibility is one direction of research we would like to pursue in future. Here, we will stick to the convention to make our points.

We assume that $\{\psi_m\}$ is a complete, orthogonal and normalized set of modes defined within the cavity. It's straightforward to see that if we keep all the infinity of modes in the expansion, we don't gain anything. The non-linear equations will couple then an infinity of terms, and the only achievement will be the reduction of infinite set of equations into a countable set of infinite. The major step forward at this point is the truncation of the expansion Eq. (6.10) to a small set of modes, which can resonate with the atomic medium. These are the modes whose natural oscillations are close to ω_a .

6.2 Single-mode Lasing

To gain an understanding of the lasing process, we now assume the simplest scenario to hold: the expansion contains only one term. This approximation is called the *single-mode approximation*. We will keep the index m of the mode in question. Inserting $F(q, t) = f_m(t)\psi_m(q)$, using $\nabla^2\psi_m = -(\omega_m^2/c^2)\psi_m$ and integrating both sides of equations with $\psi_m(q)$ we get the following set of three equations:

$$\dot{e}_m = (i\Delta_m - \kappa_m)e_m + 2i\pi\omega_a p_m \quad (6.11)$$

$$\dot{p}_m = \gamma_{\perp} p_m + \frac{g^2}{i\hbar} e_m D_{mm} \quad (6.12)$$

$$\dot{D}_{mm} = \gamma_{\parallel} (D_0 - D_{mm}) - \frac{2A_0}{i\hbar} (e_m p_m^* - e_m^* p_m) \quad (6.13)$$

In the above equations, $\Delta_m = \omega_a - \omega_m$ is the *detuning*, and

$$D_{mm}(t) = \int_D d^2q |\psi_m(q)|^2 D(q, t) \quad (6.14)$$

is the “diagonal” inversion and $A_0 = \int_D d^2q |\psi_m(q)|^4$. We have managed to turn the system into a discrete dynamical system. I will discuss this aspect after analyzing the *stationary solutions* of the single mode problem.

Note that $D_{mm} - D_0 = e_m = p_m = 0$ is always a solution, which in this context is called the “non-lasing” solution. Physically, this solution corresponds to the situation where the pump strength D_0 is so small that we cannot fulfill the lasing condition and the device operates like a regular lamp. The fact that the electric field is zero although there is a non-zero input energy can be attributed to the fact that the energy fed is lost into the heat bath through damping. In essence, e_m represents the *coherent* part of the radiation [173].

For a pump power $D_0 > D_c$, another solution becomes possible. This solution can be determined by the ansatz

$$f_m(t) = \tilde{f}_m e^{-i\Delta\Omega_m t} \quad (6.15)$$

where \tilde{f}_m are constant in time. Inserting into Eqs. (6.12)-(6.13), we find

$$D_{mm} = \frac{D_0}{1 + \frac{4g^2 A_0}{\hbar^2} \frac{\gamma_{\perp}}{\gamma_{\parallel}} \frac{|\tilde{e}_m|^2}{\gamma_{\perp}^2 + (\Delta\Omega_m)^2}} \quad (6.16)$$

The above equation shows that the inversion is reduced from its value when $e_m = 0$; this is the simplest manifestation of *saturation of inversion* when lasing transition occurs. Power is coherently fed into the radiation field, so that the effective inversion can only keep up with this with a reduced value. Note that the reduction is proportional to $n_m = |\tilde{e}_m|^2$, which is proportional to the photon number in mode m .

Inserting Eq. (6.16) into Eq. (6.12), and the resulting expression into Eq. (6.11), and separating the real and imaginary parts, we can determine the frequency $\Delta\Omega_m$:

$$\Delta\Omega_m = \frac{\Delta_m}{1 + \frac{\kappa_m}{\gamma_{\perp}}} \quad (6.17)$$

This formula tells us that the lasing frequency $\Omega_m = \omega_a + \Delta\Omega_m$, given by

$$\Omega_m = \frac{\kappa_m \omega_a + \gamma_{\perp} \omega_m}{\gamma_{\perp} + \kappa_m} \quad (6.18)$$

is in general different from the empty cavity frequency ω_m , and that $\omega_a < \Omega_m < \omega_m$. Thus the lasing frequency is “pulled” towards the oscillation frequency of the

subsystem with the longer lifetime. In particular, when $\kappa_m \ll \gamma_\perp$, i.e. when the atomic lifetime is short compared to the cavity lifetime, then $\Omega_m \rightarrow \omega_m$ and the system lases at the empty cavity resonance frequency. It should be pointed out that the single-mode case is unique among other lasing solutions in that the resulting lasing frequency is independent of the photon number n_m . Finally, it is worth writing the self-consistent solutions explicitly, because this will enable us to extract the physical scales of the problem

$$D_s \equiv D_{mm} = \frac{\hbar\kappa_m(\Delta\Omega_m^2 + \gamma_\perp^2)}{2\pi\omega_a g^2 \gamma_\perp} \quad (6.19)$$

The inversion D_{mm} is found to get clamped to the saturated value D_s after the lasing transition occurs, i.e. pumping harder ($D_0 \uparrow$) will not continue to invert the population (at this level of approximation). The electric field amplitude is given by

$$|\tilde{e}_m| = e_s \sqrt{\frac{D_0}{D_s} - 1} \quad (6.20)$$

where

$$e_s = \sqrt{\frac{\gamma_\parallel \gamma_\perp^2 + \Delta\Omega_m^2}{\gamma_\perp (4g^2 A_0)/\hbar^2}} \quad (6.21)$$

Notice that the phase of the electric field remains undetermined in this formalism. And finally, the polarization is

$$p_m = \frac{g^2}{i\hbar - i\Delta\Omega_m + \gamma_\perp} D_s e_s \sqrt{\frac{D_0}{D_s} - 1} \quad (6.22)$$

Here, the real and imaginary parts of p_m has different scales. Eqs. (6.11)-(6.13) can be reduced to a standard form by scaling the variables with the following scales, which can be directly read off from the above formulas for the solutions

$$e_c = \frac{\hbar\sqrt{\gamma_\parallel\gamma_\perp}}{2g\sqrt{A_0}}, \quad D_c = \frac{\hbar\gamma_\perp\kappa_m}{2\pi g^2\omega_a}, \quad p_c = \frac{\hbar\kappa_m\sqrt{\gamma_\parallel\gamma_\perp}}{4\pi ig\omega_a\sqrt{A_0}} \quad (6.23)$$

Using these scales, we obtain the dimensionless single-mode laser equations:

$$\dot{e} = (-\kappa + i\Delta)e + \kappa p \quad (6.24)$$

$$\dot{p} = \gamma_\perp(-p + ed) \quad (6.25)$$

$$\dot{d} = \gamma_\parallel [(d_0 - d) - (e^*p + ep^*)] \quad \left(d_0 \equiv \frac{D_0}{D_c} \right) \quad (6.26)$$

With the variable change $n = d - d_0$, these equations are the a complex generalization of the *Lorentz equations*. The Lorentz equations are coupled non-linear ODEs which have become a paradigm system for exhibiting dynamical chaos. Note here that because we have started with a non-linear wave-equation, our electric field solutions can exhibit chaotic dynamics in the classical sense. It is found [175] that this system displays a wide range of dynamical behavior:

- The origin $e = p = n = 0$ is a fixed point and is the only fixed point
- There exist two critical values of d_0 , d_c^1 and d_c^2 . The origin is a stable fixed point for $0 < d_0 < d_c^1$ (in our case $d_c = 1$ due to the scaling we have chosen).
- For $d_0 > d_c^1$, a Hopf bifurcation to a limit cycle (periodic solution) occurs, which is stable for $\kappa < \gamma_{\parallel} + 1$ (this is the lasing solution).
- For $\kappa > \gamma_{\parallel}$, this limit cycle is only stable for $d_c^1 < d_0 < d_c^2$. When $d_0 > d_c^2$, a transition to finite amplitude oscillation about the limit cycle occurs. It's not clear to what physical solution this corresponds to for a laser.

One should note that, although the similarity of the laser equations to Lorentz equations indicate the possible existence and appearance of chaotic instabilities, time-scale considerations (magnitude relations between $\Delta, \kappa, \gamma_{\parallel}, \gamma_{\perp}$) typically rule out the full dynamics of the Lorentz equations [176]. However in recent years lasers designed to be in the chaotic regime have been extensively studied.

Going beyond single-mode theory is highly complicated, and various approximation schemes have been developed suitable to the particular case of the material system used, based on *adiabatic elimination*. This has lead to the following very broad classification of lasers [177]:

- **Class A** : (e.g. He-Ne, Ar, Kr, dye) $\gamma_{\perp} \sim \gamma_{\parallel} \gg \kappa$

The equations for d and p can be solved by adiabatic elimination and one single non-linear equation describes the laser

- **Class B** : (e.g. ruby, Nd, CO, semiconductors) $\gamma_{\perp} \gg \kappa \sim \gamma_{\parallel}$

Only polarization p can be adiabatically eliminated and the dynamics is ruled by the coupled rate equations for field e and population inversion d . Fixed points and periodic oscillations are then possible.

- **Class C** : (far infrared lasers) $\gamma_{\perp} \sim \gamma_{\parallel} \sim \kappa$

No adiabatic elimination is possible and the solutions show the full complexity of the Lorentz system.

6.3 Adiabatic Elimination

Before embarking into the multi-mode equations, I would like to demonstrate what is meant by *adiabatic elimination*. The rate constants can be divided into two groups, such that all the constants within each set have the same order of magnitude. By arbitrary selection of one rate constant from each group, the ratio between the smaller and the larger of the two rates is the smallness parameter ϵ of the adiabatic elimination procedure. Consider the case of Class A and assume $\Delta = 0$. In this case all

the dynamical variables are real. We get

$$\dot{e} = -\kappa(e - p) \quad (6.27)$$

$$\dot{p} = -\gamma_{\perp}(p - ed) \quad (6.28)$$

$$\dot{d} = -\gamma_{\parallel}(d - d_0 + 2ep) \quad (6.29)$$

Here, the two groups are $\{\kappa\}$ and $\{\gamma_{\perp}, \gamma_{\parallel}\}$. Let $\kappa/\gamma_{\perp}, \kappa/\gamma_{\parallel} = O(\epsilon)$, and $\gamma_{\parallel}/\gamma_{\perp} = O(1)$. By rescaling time to $\tau = \kappa t$, we get for the last two equations

$$O(\epsilon)\dot{p} = -p + ed \quad (6.30)$$

$$O(\epsilon)\dot{d} = -(d - d_0 + 2ep) \quad (6.31)$$

From here, we obtain the stationary values of p, d :

$$d = \frac{d_0}{1 + 2e^2} \quad p = \frac{ed_0}{1 + 2e^2} \quad (6.32)$$

Eq. (6.27) becomes

$$\dot{e} = -e + \frac{ed_0}{1 + 2e^2} \quad (6.33)$$

Physically, this means that the atomic variables respond so fast that they all are “enslaved” [178] by the field.

At this point, we should discuss the rate constants of the systems we are interested in, which are in general semiconductor systems. For example, GaN, which was used in the experiments of Chapter 5, has the following values: $\gamma_{\perp} \sim 10^{13} s^{-1}$, $\gamma_{\parallel} \sim 10^{10} s^{-1}$ and $\kappa \sim 10^{11} s^{-1}$. The cavity decay time varies of course from mode to mode, but the experimental values correspond to $\kappa < 10^{11} s^{-1}$. Thus, we have $\kappa \lesssim \gamma_{\parallel}$ and we are really dealing with Class B in our case.

6.4 Multi-mode Lasing

Under these circumstances, a suitable model for our case is given by the following form of the scaled Maxwell-Bloch equations Eq. (6.7)-(6.9):

$$\dot{e} = -\left(\kappa - \frac{i}{2\omega_a}[\omega_a^2 + c^2\nabla^2]\right)e + \kappa p \quad (6.34)$$

$$\dot{p} = -\gamma_{\perp}(p - ed) \quad (6.35)$$

$$\dot{d} = \gamma_{\parallel}[d_0 - d - (e^*p + p^*e)] \quad (6.36)$$

Note that d_0 is the scaled pump parameter, so that the first instability occurs at $d_0 \sim 1$. Also, recall that the variables here have both spatial and temporal dependence. Now, let's eliminate the polarization following a Class B treatment

$$p = ed \quad (6.37)$$

we obtain the coupled set of Class B equations

$$\dot{e} = -\kappa(1-d)e + \frac{i}{2\omega_a}[\omega_a^2 + c^2\nabla^2]e \quad (6.38)$$

$$\dot{d} = -\gamma_{\parallel}[-d_0 + (1+|e|^2)d] \quad (6.39)$$

These equations are well-justified for the systems of our interest, as γ_{\perp} is at least three orders of magnitude larger than the other time scales. Hence it can serve as the point of departure for all future considerations. We can now introduce the modal expansion $e(q, t) = \sum_m e_m(t)\psi_m(q)$ and the following ansatz [179] for the inversion:

$$d = d_0 \left(1 - \sum_{m,n} d_{mn}(t)\psi_m(q)\psi_n^*(q) \right) \quad (6.40)$$

to end up with the following set of equations

$$\dot{e}_m = -\kappa(1-d_0)e_m + i\Delta_m e_m - \kappa d_0 \sum_{jln} e_j d_{ln} \Gamma_{jlnm} \quad (6.41)$$

$$\dot{d}_{mn} = -\gamma_{\parallel}(d_{mn} - e_m e_n^*) \quad (6.42)$$

$$(6.43)$$

In these equations,

$$\Gamma_{jlnm} = \int d^2q \psi_j(q)\psi_l^*(q)\psi_n(q)\psi_m^*(q) \quad (6.44)$$

We should note that one implicit assumption in this expansion technique is that the pump is not significantly above the first laser threshold, so that $|e_m|^2$ is a small parameter. Assuming now a time-dependence

$$e_m(t) = e_m^{(0)} e^{i\Omega_m t} \quad (6.45)$$

one finds (note that we are deviating from our standard notation of denoting these frequencies by $\Delta\Omega_m$)

$$d_{mm} = |e_m^{(0)}|^2 \quad (6.46)$$

$$d_{mn} = \gamma_{\parallel} e_m^{(0)*} e_n^{(0)} \frac{\exp[i(\Omega_m - \Omega_n)t]}{\gamma_{\parallel} + i(\Omega_m - \Omega_n)} \quad (6.47)$$

i.e.

$$d(q, t) = d_0 \left(1 - \sum_m |e_m^{(0)}|^2 |\psi_m(q)|^2 - \sum_{m \neq n} \frac{e_m^{(0)*} e_n^{(0)}}{1 + i \left[\frac{\Omega_m - \Omega_n}{\gamma_{\parallel}} \right]} \psi_m^*(q)\psi_n(q) e^{i(\Omega_m - \Omega_n)t} \right) \quad (6.48)$$

We see in this expression that the holes “burnt” into the inversion are spatially modulated by occupation of modes with different spatial distributions. Our analysis can proceed in two directions at this point, based on physical considerations.

6.4.1 Diagonal Inversion: Non-degenerate lasing

Under the assumption $\frac{\Omega_m - \Omega_n}{\gamma_{\parallel}} \gg 1$

$$d(q, t) \approx d(q) = d_0 \left(1 - \sum_m |e_m^{(0)}|^2 |\psi_m(q)|^2 \right) \quad (6.49)$$

The inversion is approximately stationary in time. Under this condition it is possible to attain a multi-mode operation. This is because, looking at the field evolution equation (6.38), if $d(q, t) = d(q)$, we can strictly expand $e(q, t)$ in a finite number of frequencies Ω_m in its Fourier expansion. Note that then

$$d_{mn} \approx d_{mm} \delta_{mn} \quad (6.50)$$

Under these conditions one can assume that [173]

$$\overline{e_m(t) e_n^*(t)} = \overline{e_m^{(0)} e_n^{(0)*} e^{i(\Omega_m - \Omega_n)t}} \approx \delta_{mn} |e_m^{(0)}|^2 \quad (6.51)$$

i.e. that if we take a time-average over a time-interval longer than $1/(\Omega_m - \Omega_n) \ll 1/\gamma_{\parallel}$, then the off-diagonal fluctuations self-average to zero. Here the implicit assumption is that there is no phase-locking involved. Then, we can multiply both sides of the equation Eq. (6.41) by e_n^* and average over the necessary self-averaging period. If we take the real part of the resulting expression we obtain

$$\dot{n}_m = \frac{\partial}{\partial t} (e_m e_m^*) = 0 = -2\kappa(1 - d_0)n_m - 2\kappa d_0 \sum_l n_m n_l \Gamma_{mlm} \quad (6.52)$$

Consider a set of modes $m \in \mathcal{L}$ which are close to the threshold, so that $n_m \neq 0$. The rest of the modes contain only a few photons and can be omitted from the above set of equations. We get

$$d_0 \sum_{l \in \mathcal{L}} A_{ml} n_l = d_0 - 1 \quad (6.53)$$

Here, $A_{ml} = \Gamma_{mlm} = \int d^2q |\psi_m(q)|^2 |\psi_n(q)|^2$. Note that for this equation to have a solution at all, $d_0 > 1$. This is a deceptively simple linear problem for photon numbers n_m which are lasing simultaneously, which contains as parameters spatial overlaps of the modes which are lasing. This is the simplest possible framework to analyze the effect of spatial complexity of empty-cavity modes on lasing.

There are two non-physical attributes of this model however. The first is that the lifetimes of individual modes are absent. This is an important shortcoming, since as we pointed out before, dielectric modes, in contrast to the conventional Fabry-Perot modes, exhibit a rather broad distribution of lifetimes. Thus, lifetimes, in addition to spatial distribution of modes will be an important factor in the mode selection process. Second, the limited linewidth of the laser has apparently disappeared from the equations. Thus, as far as frequency of resonator modes are concerned, the active medium doesn't distinguish one mode from the other. This is not a very serious

problem, since we can limit the contributing set of modes \mathcal{L} manually. However, we can refine our model if we go back and polish certain approximations we made.

The modal lifetimes can be heuristically introduced by rewriting Eq. (6.41) as

$$\dot{e}_m = -\kappa\left(\frac{\kappa_m}{\kappa} - d_0\right)e_m + i\Delta_m e_m - \kappa d_0 \sum_{jln} e_j d_{ln} \Gamma_{jlnm} \quad (6.54)$$

The ratio κ_m/κ appears because our scales Eq. (6.23) includes a reference lifetime κ . The linewidth can be also included by replacing Eq. (6.37). We introduce

$$p(q, t) = \sum_m p_m^{(0)} e^{i\Omega_m t} \psi_m(q) \quad (6.55)$$

and insert this expression along with Eq. (6.49) and Eq. (6.45) into Eq. (6.35). Integrating both sides of the resulting expression with ψ_n^*

$$p_m = \frac{\gamma_\perp}{i\Omega_m + \gamma_\perp} \sum_l \langle m|d|l \rangle e_l \quad (6.56)$$

here we used the shorthand $\langle m|d|l \rangle = \int d^2q \psi_m(q) d(q) \psi_l^*(q)$. Physically, we introduced just the retarded response of the polarization to lowest order (instead of the instantaneous adiabatic following) which would effectively contribute a frequency dependent linear index of refraction to the system. We can incorporate this into our previous result by the replacement $\langle m|d|l \rangle \rightarrow \langle m|d|l \rangle \gamma_\perp / (\gamma_\perp + i\Omega_m)$. The improved expression for stationary photon numbers is then given by

$$1 - \frac{\kappa_m}{\kappa d_0 g(\Omega_m)} = \sum_{l \in \mathcal{L}} A_{ml} n_l \quad (6.57)$$

This is precisely the expression one would obtain from laser rate equations [173, 172] with the assumption of stationarity of the photon numbers.

One difficulty with solving Eq. (6.57) is that, although the equation is linear, the modes \mathcal{L} to be kept in the equation is not known a priori. Thus, an arbitrary set will in general not have a solution. However, it is possible to obtain physical results by simple models for the spatial and spectral structure of the empty-cavity mode. Calculations for a simple model of a Fabry-Perot cavity were carried out in Ref. [174], and for an ergodic system where the matrix elements A_{ml} can be obtained from random matrix theory (but with a constant modal decay constant κ), in Ref. [180].

One possible direction of research is hence the investigation of the solution of equations of type Eq. (6.57), where the numerical calculations of quasi-bound modes can serve as a suitable input. Ultimately, a semi-classical calculation of the matrix A_{ml} can be attempted, too, where the matrix can be divided into compartments depending on the type of modes entering the expressions (chaotic, stable island and torus modes).

6.4.2 Non-Diagonal Inversion: Degenerate lasing

Consider the opposite case when in Eq. (6.48), there is a certain set of modes for which $\frac{\Omega_m - \Omega_n}{\gamma_{\parallel}} \ll 1$. This would generically happen for example in case of an existing degeneracy because of a symmetry of the resonator, or more relevant to our case, when the system is chaotic and we are looking at the high-mode density limit of semi-classical frequencies.

In that case it's possible to attain a multi-mode operation because a stationary inversion can result

$$d(q, t) \sim d(q) = d_0 \left(1 - \sum_m |e_m^{(0)}|^2 |\psi_m(q)|^2 - \sum_{m \neq n} e_m^{(0)*} e_n^{(0)} \psi_m^*(q) \psi_n(q) \right) \quad (6.58)$$

From the point of view of spatial hole burning, the resulting hole burnt will be highly sensitive to the amplitudes $e_m^{(0)}$ of the degenerate modes, and this in turn effects the dynamics, and the form of the stationary solutions. Note the form of the resulting solution of the radiation field:

$$e(q, t) = \sum_{\mu} \Psi_{\mu}(q) e^{i\Omega_{\mu} t} \quad (6.59)$$

where

$$\Psi_{\mu}(q) = \sum_{m \in M_{\mu}} e_m^{(0)} \psi_m(q) \quad (6.60)$$

where M_{μ} is the set of almost degenerate modes which lase at about the same frequency Ω_{μ} .

There are a few references to such a scenario in literature. This phenomenon is similar to the so-called *cooperative frequency locking*, for which experimental indications exist, but theoretical results do not abound.

It has to be pointed out that in the generic case most of the modes will be in the intermediate regime $\frac{\Omega_m - \Omega_n}{\gamma_{\parallel}} \sim 1$. It has been shown [181] that for the simple case of a two-mode (specifically, two quasi-degenerate transverse Fabry-Perot modes) competition that the proximity of the empty-cavity frequencies lead to strong non-linear phase couplings, resulting in *mode pulling/pushing*. A multi-mode solution (with a stationary inversion) may or may not exist depending on the parameters of the system. Of crucial importance is the demonstration that modes lock into each other and oscillate at a single lasing frequency when their original frequency difference is appreciably smaller than γ_{\parallel} .

Note that we are talking here not about a accidental degeneracy where the modes in question may have widely different spatial patterns and lifetimes. A good example is the set of modes related to an unstable periodic orbit of a dielectric resonator, i.e. modes scarred by the same unstable periodic orbit. Because, from our discussion of the Bogomolny theory in Chapter 5, in the deep semi-classical regime, we expect that the averaged mode intensity in a given wave-vector interval is strongly affected by the underlying periodic orbit.

Thus, a possible scenario is that within the (cold-cavity) spectrum under the gain curve (of width γ_{\perp}), degenerate modes that lie within a distance γ_{\parallel} , will pull each other to result in a new non-linear mode with a single frequency Ω .

Based on this conjecture, it is possible to obtain the equation governing the spatial structure of the resulting non-linear modes. We will use Eq. (6.59) but leave the functions $\Psi_{\mu}(q)$ undetermined. Because the polarization follows the field adiabatically for the systems of our interest, we can also write

$$p(q, t) = \sum_{\mu} p_{\mu}(q) e^{i\Omega_{\mu} t} \quad (6.61)$$

In these expansions, $\Psi_{\mu}(q)$ and $p_{\mu}(q)$ are no longer chosen to be cold-cavity eigenfunctions, but their spatial form will be allowed to be defined by the non-linear dynamics. Inserting these ansätze into the Maxwell-Bloch equations, we obtain the equation

$$\left[(1 + 2\tilde{\Omega}_{\mu}) + \tilde{\nabla}^2 - F(\{|\Psi_{\nu}|^2\}) \right] \Psi_{\mu}(q) = 0 \quad (6.62)$$

which is a coupled set of non-linear Schrödinger equations. The non-linear term is given by

$$F(\{|\Psi_{\nu}|^2\}) = 2i\tilde{\kappa} \frac{\tilde{\gamma}_{\perp}}{-i\Omega_{\mu} + \tilde{\gamma}_{\parallel}} \frac{d_0}{1 + 2\sum_n g(\Omega_n) |\Psi_{\nu}|^2} \quad (6.63)$$

where

$$\tilde{\Omega}_{\mu} = \frac{\Omega_{\mu}}{\omega_a}, \quad \tilde{\kappa} = \frac{\kappa}{\omega_a}, \quad \tilde{\nabla}^2 = \frac{c^2}{\omega_a^2} \nabla^2 \quad (6.64)$$

with additional matching conditions on the resonator boundary. A single-mode version of this equation without the above justification was given in Ref. [182]. This reference contains numerical solution of Eq. (6.64) for single-mode solutions of a dielectric cylinder, i.e. the non-linear whispering gallery modes. We hope to investigate this kind of coupled non-linear system in future work.

Chapter 7

Conclusion and Open Questions

In the past chapters, our main motivation has been to account for the properties of dielectric resonators based on the dynamics of the underlying ray motion, which the problem reduces to in the short-wavelength limit. The present work has benefitted substantially from the past research on asymmetric resonant cavities carried out in the same group; the main shift in emphasis with respect to earlier work which centered on ray models has been the development of local asymptotic models and wave correction to ray models in physically relevant situations.

We have shown that among the irregularly spaced (spectrum-wise) “chaotic” modes of a generic deformed resonator, one can project out a set of regularly spaced modes, which are based on regular phase space structures. These states live on local tori (topologically) and possess two approximate quantum numbers. Access to these states is made possible by the use of the boundary layer theory (parabolic equation approximation), a powerful tool in asymptotic analysis of partial differential equations. The literature contains the treatment of metallic cavities. We have extended it to open resonators, analyzed the (quasi-)degeneracy structure due to point group symmetries of the boundary shape and predicted the scaling of average tunnel splittings. There are certain features of this theory which needs improvement, and I believe the underlying technique is flexible enough to accommodate these. The most important shortcoming is the prediction of zero-width for totally internally reflected modes. Obviously there is an exponentially small tunneling contribution which is missed by the original ansatz. It was pointed out that this contribution can be captured through the application of a multiple-scales analysis.

An efficient numerical algorithm was developed to calculate the quasi-bound modes of dielectric cavities. The solutions obtained by this technique have been instrumental in analyzing certain experiments as well as the reliability of asymptotic expansions. One improvement this algorithm needs is the extension of its validity to higher wavenumbers, and deeper into semi-classical regime. It seems straightforward to generalize this algorithmic approach to deformed spherical dielectrics, where it may be even more efficient relative to existing approaches.

The analysis of an experiment on semiconductor microlasers has led us to consider wave corrections to ray theory predictions, which were found to lead to significant

deviations in observed emission patterns, even deep in semiclassical regime, when ray theory is expected to give reliable results. A scar theory of open systems leaves much to be desired. The existent scar theories were developed with closed systems in mind. There, the broadening of the spectral peaks are due to Lyapunov escape from the unstable orbit. It might well be that the finite leakage of open systems can enhance scars, by leading to escape from the cavity before the full complexity of the chaotic motion around the unstable fixed point can unfold. This of course leads to the interesting question whether trace formulas and Bogomolny's formulation can be extended to open systems.

The most interesting and promising extension of our work is the generalization of certain concepts and ideas we have entertained in the linear regime to include non-linearities. We have pointed out two directions of possible future research. An important desirable feature of a non-linear theory of dielectric cavities is the use of quasi-bound modes instead of closed cavity modes, since the emission patterns then can be obtained in the most direct way.

Last but not least, three dimensional generalization of semi-classical techniques seem to offer considerable promise. I have spent some time on generalizing the EBK quantization conditions to cylindrical cavities, taking into account the dynamics of the polarization degree of freedom and the motion of rays along the axial direction. It seems possible to formulate a generalized quantization condition involving rotation matrices. However, conclusive results are lacking at this point.

Appendix A

Uniform expressions valid on the caustic

To understand what happens *on* the caustic, where both expressions Eq. (2.75) and Eq. (2.78) become indefinite, there are various approaches. We will here employ a method based on local analysis of the Helmholtz equation itself, which is quite transparent and also is along the same spirits as Chapter 4. Let's analyze the nature of the singularity in the phase in the problematic area via the coordinate transformation

$$r = a + \rho \tag{A.1}$$

where $a = m/k$. Then, the phases can be written as

$$S_{\pm}(r, \phi) \sim a\phi \pm \frac{2\sqrt{2}}{3a^{1/2}}\rho^{3/2} \tag{A.2}$$

The validity of our asymptotic limit $kS_{\pm} \gg 1$ is jeopardized when $kS_{\pm} \sim O(1)$, and that happens as we can see when

$$\rho \sim k^{-3/2} \tag{A.3}$$

Now, let's zoom into this problematic area by "stretching" the coordinate ρ

$$r = a + \epsilon\tilde{r} \tag{A.4}$$

where ϵ is a small number yet undetermined and substituting $\psi = f(\tilde{r})e^{im\phi}$, with $m = ka$, into the Helmholtz equation

$$\left[\frac{1}{\epsilon^2} \frac{d^2}{d\tilde{r}^2} + \frac{1}{a} \left(1 - \epsilon \frac{\tilde{r}}{a}\right) \frac{d}{d\tilde{r}} + k^2(2\epsilon\tilde{r}) \right] f(\tilde{r}) = O(\epsilon^2) \tag{A.5}$$

According to the method of dominant balance [86] that we employed for the derivation of our ray asymptotics earlier, asymptotic expansion of differential equations obey a universal economy principle, and only few of the terms are expected to balance each other. A sensible balance takes place with the choice $\epsilon = k^{-2/3}$, which is

also reinforced with our previous observation that our original asymptotic expansion breaks down in an interval of size proportional to $k^{-2/3}$. Then, to lowest order, the equation for $f(\tilde{r})$ is reduced to

$$\frac{d^2 f}{d\tilde{r}^2} + \frac{2}{a}\tilde{r}f = 0 \quad (\text{A.6})$$

This is the Airy equation, and has the general solution

$$f = c_1 \text{Ai}(-(2/a)^{1/3}\tilde{r}) + c_2 \text{Bi}(-(2/a)^{1/3}\tilde{r}) \quad (\text{A.7})$$

The constants are determined by matching with the “outer region” solutions, Eq. (2.75) and Eq. (2.78). As $\tilde{r} \rightarrow -\infty$, $\text{Ai}(-(2/a)^{1/3}\tilde{r})$ is exponentially small, whereas $\text{Bi}(-(2/a)^{1/3}\tilde{r})$ is exponentially large, therefore $c_2 = 0$. As $\tilde{r} \rightarrow \infty$, on the other hand, we can use the asymptotic expansion of $\text{Ai}()$

$$\text{Ai}(-(2/a)^{1/3}\tilde{r}) \sim -\frac{a^{1/12}e^{-i\pi/4}}{2^{13/12}\sqrt{\pi}} \left(\frac{e^{-i\frac{2\sqrt{2}}{3a^{1/2}}\tilde{r}^{3/2}}}{\tilde{r}^{1/4}} - \frac{e^{i\pi/2}e^{i\frac{2\sqrt{2}}{3a^{1/2}}\tilde{r}^{3/2}}}{\tilde{r}^{1/4}} \right) \quad (\text{A.8})$$

The first term matches with the “incoming ray” solution S_2 (as given in Eq. (2.73) and Eq. (A.2)), if the constant c_1 is determined to be

$$c_1 = -2^{5/6}\sqrt{\pi}e^{i\pi/4} \quad (\text{A.9})$$

which also matches to the “outgoing ray” solution Eq. (2.72). The final expression for the asymptotic solution is

$$\psi(r, \phi) = -2^{5/6}\sqrt{\pi}e^{i\pi/4}\text{Ai}(-2^{1/3}a^{-1/3}k^{2/3}(r-a))e^{im\phi} \quad (\text{A.10})$$

The above asymptotic expansion Eq. (A.8) of the Airy function enables us to see clearly what’s happening at the caustic: An incoming (circular) wave is scattered into an outgoing circular wave with a scattering phase shift of $\pi/2$. This is exactly the caustic phase shift we have used in the previous section, that a ray picks up at each passage through a caustic. Note that physically, this is not different from the phase shift of π acquired at each reflection on ∂D . Using the language of Quantum mechanics, in the latter the wave is reflected from an infinitely high potential barrier and in the former, the wave is reflected off a smooth potential barrier. Because the wavefield leaks into the smooth barrier through tunneling, the acquired phase shift is less. The above procedure can be generalized to higher dimensions, and caustics can be classified by the nature of the singularities of differentiable mappings. The caustic behavior of the wave-fields can then be described by generalized Airy functions [84]. As a historical side-note, the original Airy function was invented actually just for this purpose by G. B. Airy, first appearing in his talk “On the intensity of light in the neighborhood of a caustic” delivered to the Cambridge Philosophical Society in 1838.

Appendix B

Tunneling in the dielectric cylindrical cavity

For the circular cavity, the exact solutions can be obtained without difficulty. This can serve as a good basis to check the semiclassical results we obtained so far. The solutions, obtained in Chapter 3 are given by

$$\psi_1(r, \phi) = \alpha_m J_m(Nk_{mn}r)e^{im\phi}, \quad r < R \quad (\text{B.1})$$

$$\psi_2(r, \phi) = \gamma_m H_m^+(k_{mn}r)e^{im\phi}, \quad r > R \quad (\text{B.2})$$

Note that keeping only $H_m^+(kr)$ in the outside solution tantamounts to outgoing wave boundary conditions, as can be justified by using the large argument asymptotics of the Bessel functions. The quantized eigenvalues are found from a transcendental equation obtained by the application of continuity conditions

$$NJ_{m+1}(Nk_{mn}R)H_m^+(k_{mn}R) - J_m(Nk_{mn}R)H_{m+1}^+(k_{mn}R) = 0 \quad (\text{B.3})$$

It's possible to show that the above equation is *strictly* satisfied for complex k_{mn} values. Thus there is no solution with a real k_{mn} , which we would expect for TIR modes with

$$\sin \chi > \frac{1}{n} \quad (\text{B.4})$$

We can use the semiclassical quantization conditions around and use it to calculate an effective Fresnel reflection coefficient $r(\chi)$ for the exact case. In principle, using Eq. (2.169), we can treat $r(\sin \chi)$ as an unknown function and solve for it in terms of m and $Nk_{mn}R$

$$r(\sin \chi) = \exp \left[2i \left(\sqrt{(Nk_{mn}R)^2 - m^2} - m \cos^{-1} \left(\frac{m}{Nk_{mn}R} \right) \right) + i \frac{\pi}{2} \right] \quad (\text{B.5})$$

Then we can use the exact quantization condition Eq. (B.3) to generate $(m, k_{mn}R)$ pairs (for $m \gg 1$ and $k_{mn}R \gg 1$), and determine $r(\sin \chi)$. Results of this numerical calculation is shown in Fig. B.1, where we plot $|r(\sin \chi)|^2$ as it is complex in general. The result is compared in the same plot to the Fresnel formula Eq. (2.166).

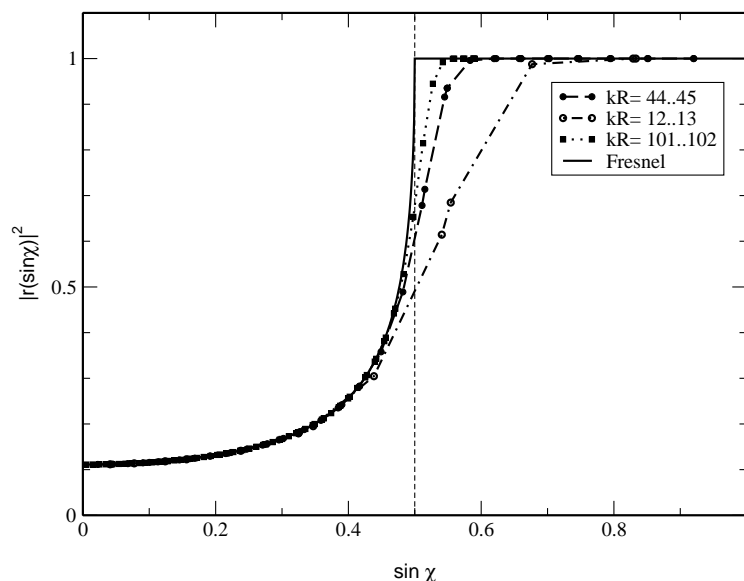


Figure B.1: The reflectivity calculated using Eq. (B.5) with exact quantized wavevectors calculated using Eq. (B.3) at different regimes of NkR . Note that as $k \rightarrow \infty$ the calculated reflectivities approach those obtained from Fresnel law Eq. (2.172). The dashed vertical line represents the critical value $\sin \chi_c = 1/N$. The calculations are performed for an index of refraction $N = 2$.

One observes that there is always a nonzero transmission probability for incidence above the critical angle $\sin \chi_c$. Using appropriate asymptotic expressions for Bessel functions to solve Eq. (B.3), it's possible to show [16] that for $m \sim NkR \gg 1$ ($\sin \chi \rightarrow 1$) the imaginary part of the quantized eigenvalue is given by

$$\text{Im}[NkR] \sim -e^{-2\gamma} \text{Re}[NkR] \sin \chi \quad (\text{B.6})$$

where

$$\gamma = \frac{1}{2} \log \left[\frac{1+q}{1-q} \right] - q \quad (\text{B.7})$$

and $q = \sqrt{1 - 1/N^2}$. The appropriate procedure to reach this result requires to keep $\sin \chi = \frac{m}{NkR} \sim 1$ constant while $m \rightarrow \infty$ and $NkR \rightarrow \infty$. From here, one can extract the behavior of how $|r|^2$ approaches 1 as $\sin \chi \rightarrow 1$

$$1 - |r|^2 \sim \cos \chi e^{-2\gamma} \text{Re}[NkR] \sin \chi \quad (\text{B.8})$$

This extra *exponentially small* “leakage” of the amplitude is attributed to the curvature of the boundary. This phenomenon is known as *frustrated total internal reflection*. Its remarkable similarity to the barrier penetration problem of quantum mechanics can be demonstrated by looking at the problem in radial dimension, as was first pointed out by Johnson [17]. This can be done without difficulty because

the system is separable and we set $\psi(r, \phi) = \frac{R(r)}{\sqrt{r}} \exp[im\phi]$ in Eq. (2.157), to get

$$\frac{d^2 R(r)}{dr^2} + V_{eff}(r)R(r) = k^2 R(r) \quad (\text{B.9})$$

where the effective potential is given by

$$V_{eff} = k^2(1 - n^2(r)) + \frac{m^2 - \frac{1}{4}}{r^2} \quad (\text{B.10})$$

This situation describes (in the semiclassical limit) a point particle with energy $E = k^2$ subject to a potential $V_{eff}(r)$. The profile of this potential is plotted in Eq. (B.2).

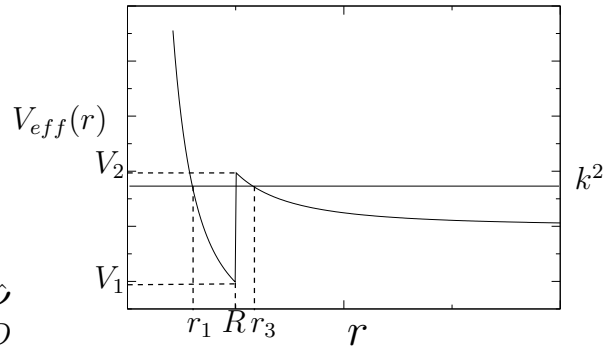


Figure B.2: The effective potential $V_{eff}(r)$ for $m = 70$, $kR = 100$, $n = 2$.

The second term, called the centrifugal potential, is a manifestation of angular momentum conservation. Note that we would have a simple attractive well of a finite depth if it were not for this term. The repulsive centrifugal barrier turns this into a barrier of a finite width. A classical particle of energy $E = k^2$ such that $V_1 < k^2 < V_2$ launched in the region $r < R$ will be trapped there forever. The particle will bounce back and forth between the two turning points r_1 and r_2 . The barrier forms two disjoint regions of motion, in the sense that a particle started outside the barrier with the same energy $V_1 < k^2 < V_2$ will remain outside the barrier, with a turning point at $r = r_3$. Semiclassical solutions, which is simple one-dimensional WKB in this case, will be oscillatory in the classically allowed regions, $r_1 < r < r_2$ and $r > r_3$ display exponential behavior otherwise. These are the long-lived resonances, and the quantized (complex) energies k can be found by matching the solutions consistently. Thus the finite lifetimes can be attributed to the exponentially decaying tail which connects to an external oscillatory solution; the particle is said to tunnel through the barrier. It's known since the Gamow theory of α -particle decay that the transmission probability is exponentially small in energy and given by

$$T \sim \exp \left[2 \int_{r_2}^{r_3} dr \sqrt{V(r) - E} \right] \quad (\text{B.11})$$

Note that we obtain such long-lived resonances for the condition $V_1 < k^2 < V_2$, where

$$V_1 = k^2(1 - N^2) + \frac{m^2}{R^2}, \quad V_2 = \frac{m^2}{R^2} \quad (\text{B.12})$$

We assumed $m \gg 1$ and dropped the $1/4$. The resulting condition for long-lived resonances is

$$\frac{m}{NR} < k < \frac{m}{R} \quad (\text{B.13})$$

which is just the condition of TIR, $1 > \sin \chi > 1/N$ using Eq. (2.168).

For $k^2 > V_2$ we obtain the above barrier resonances. Classically, this corresponds to particles moving unconfined but feeling the attraction of the potential. A particle launched inside towards the barrier would slow down and then gradually increase its speed and escape to infinity. The semiclassical solutions will reflect the behaviour by exhibiting a finite reflectivity. We would imagine that by increasing the energy indefinitely we should be able to attain zero reflection eventually. That this does not happen can be seen from the reflectivity we calculated previously in Eq. (2.172). Keeping m constant and increasing k , we obtain $\sin \chi \rightarrow 0$ and

$$|r| \rightarrow \frac{1 - N}{1 + N} \quad (\text{B.14})$$

the reflectivity saturates at a fixed value given by the index of refraction. This behaviour constitutes the main difference between a quantum mechanical potential and an ‘‘optical potential’’. The basic reason for this qualitative difference is that the depth of the optical potential Eq. (B.10) is $\Delta V = V_2 - V_1 = k^2(1 - N^2)$; it is proportional to the energy $E = k^2$. Thus as we increase the energy, the well becomes effectively more attractive and saturates the reflection.

Appendix C

Coordinate Systems on the PO

The coordinate systems we use are illustrated, in Fig. 4.4. There is a fixed coordinate system (X, Z) , which is attached to some appropriate point in the cavity, preferably to a high symmetry point. The ‘mobile’ coordinate systems (x_m, z_m) are fixed on segments of the periodic orbit, so that their z -axes are parallel to the segment and in such a way as to conserve handedness among the different systems. This means in particular that, for a BB orbit for example (where $\sin \chi_m = 0$), $x_{m+1} = -x_m$. This is to ensure that for a periodic orbit with an odd number of bounces, the coordinate system obtained after a loop has the same chirality as the one we began with. The origins are defined to conveniently take into account the zeroth order phase accumulation between successive bounce-points, i.e. the origin of the m^{th} coordinate system is set back from the bounce point by a distance $\sum_{n=1}^m l_n$. We will use the alternative indices i, r , and t to denote the incident, reflected and the transmitted components, when considering a single scattering (or alternatively, bounce) event, and drop the reference to the arm indices.

Here, ξ_i ($i = 1, 2$) are the local coordinates at each bounce, such that ξ_2 is along the normal at the bounce point, and $\hat{\xi}_1 \cdot \hat{x}_m > 0$. The bounce index will be suppressed, as long as it doesn’t create confusion. The form of the boundary is taken to be of quadratic form

$$\xi_2 = -\frac{\xi_1^2}{2\rho} \quad (\text{C.1})$$

where ρ is the local radius of curvature. Here we use an approximation to the actual boundary ∂D , which takes into account the curvature to lowest order in ξ_1 . We furthermore define the scaled versions of the coordinates, which we denote with tildes added on top of the unscaled ones: $\tilde{\xi}_i = \sqrt{k}\xi_i$ and $\tilde{x}_m = \sqrt{k}x_m$. Note that the coordinates are of dimension $[\sqrt{L}]$. Consider the bounce-point m . The coordinates are related by the following transformations

$$z_m = l_m + \xi_1 \sin \chi_m + \xi_2 \cos \chi_m \quad (\text{C.2})$$

$$z_{m+1} = l_m + \xi_1 \sin \chi_m - \xi_2 \cos \chi_m \quad (\text{C.3})$$

$$z_{mt} = nl_m + \xi_1 \sin \chi_m + \xi_2 \cos \chi_m \quad (\text{C.4})$$

and

$$x_m = \xi_1 \cos \chi_m - \xi_2 \sin \chi_m \quad (\text{C.5})$$

$$x_{m+1} = -\xi_1 \cos \chi_m - \xi_2 \sin \chi_m \quad (\text{C.6})$$

$$x_{mt} = \xi_1 \cos \chi_{mt} - \xi_2 \sin \chi_{mt} \quad (\text{C.7})$$

where χ_{mt} is related to χ_m by Snell's law of refraction : $\sin \chi_{mt} = n \sin \chi_m$. Normal derivatives then can be easily found through

$$\frac{\partial}{\partial n} = \frac{1}{\sqrt{1 + \xi_1^2/\rho^2}} \left(\frac{\partial}{\partial \xi_2} + \frac{\xi_1}{\rho} \frac{\partial}{\partial \xi_1} \right) \quad (\text{C.8})$$

Appendix D

Linear Ray Reflection & Refraction transformations

Consider first the reflection event. Denote the incoming ray by

$$Q_i(z_i) = \alpha_i z_i + \beta_i \quad (\text{D.1})$$

Here $Q_i(z_i)$ is the x -coordinate of the ray position in the incoming coordinate system (x_i, z_i) at z_i . The reflected ray Q_r and the transmitted ray Q_t are similarly characterized by (α_r, β_r) and (α_t, β_t) , respectively. The ray slopes are given by the angles (ψ, ψ', ψ_t) in the figure, such that $\alpha_i = \tan \psi$ and $\alpha_r = -\tan \psi'$. First, note that

$$\chi' - \delta\alpha - \chi = \psi' \quad (\text{D.2})$$

and also

$$\chi' = \chi + \psi - \delta\alpha \quad (\text{D.3})$$

From the last two we get

$$\psi - 2\delta\alpha = \psi' \quad (\text{D.4})$$

Then consider the parametrization of the surface in (x_i, z_i) and (x_r, z_r) . Using Eqs. (C.2,C.5), we solve for ξ_1 in $x_i(\xi_1) = \alpha_i z_i(\xi_1) + \beta_i$, and inserting this into $\tan \delta\alpha = \xi_1/\rho$ we get

$$\delta\alpha = \frac{Q_i(l)}{\rho \cos \chi} \quad (\text{D.5})$$

Here we assumed $Q_i(l)/\rho \ll 1$ and that $\chi < \pi/2$. Doing the same in the reflected coordinate system, one also obtains

$$Q_r(l) = -Q_i(l) \quad (\text{D.6})$$

Thus, the *linear* transformation law for reflection becomes

$$P_r + P_i = \frac{2Q_i}{\rho \cos \chi} \quad (\text{D.7})$$

$$Q_r + Q_i = 0 \quad (\text{D.8})$$

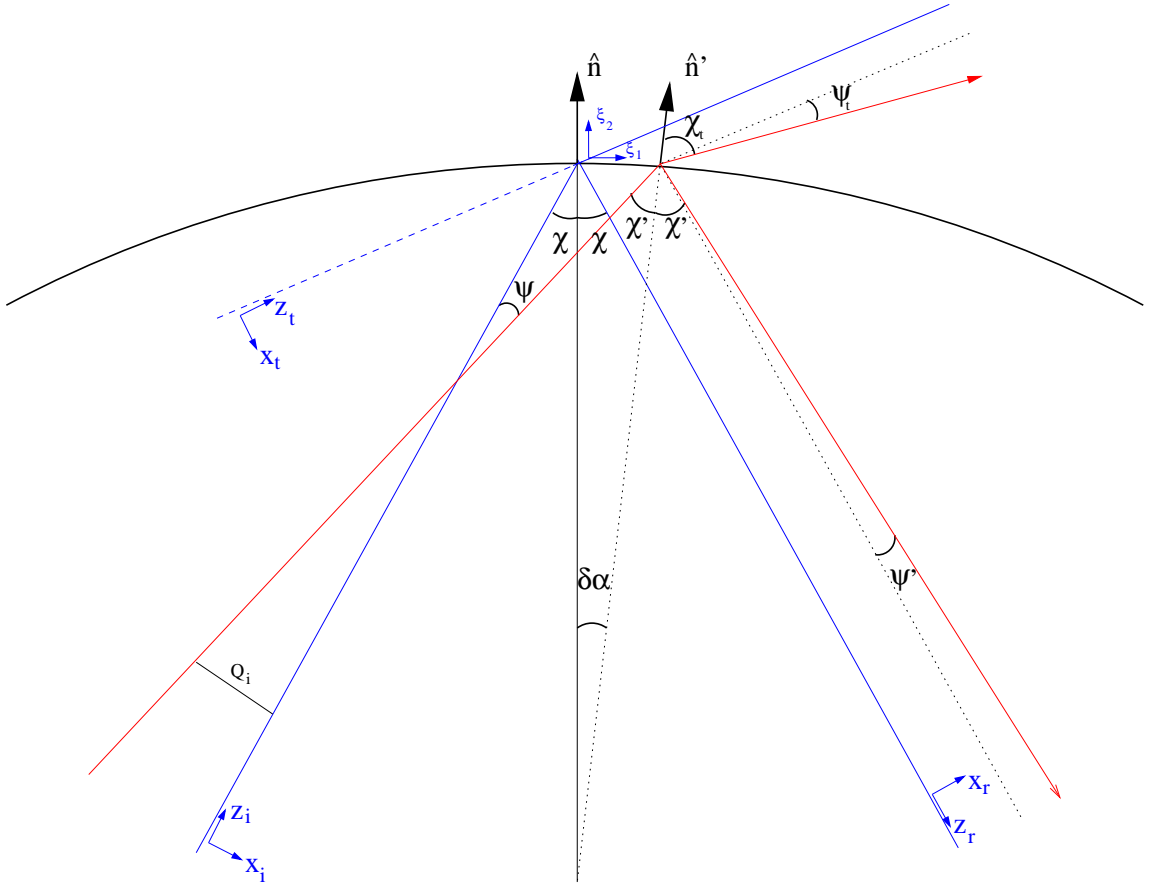


Figure D.1: Coordinates of a single ray bounce event for the derivation of the ray reflection and refraction transformations

All the quantities are calculated at $z_i = z_r = l$. Note also that this approximate transformation has a symplectic structure, a feature which is important for our construction.

To derive the linear ray transmission transformation, we write the Snell's law of refraction in terms of the infinitesimal deviation angles (ψ, ψ_t)

$$n \sin(\chi_i + \psi - \delta\alpha) = \sin(\chi_t + \psi_t - \delta\alpha) \quad (\text{D.9})$$

using Eq. (D.5), we get

$$\psi_t - \delta\alpha = n\mu(\psi - \delta\alpha) \quad (\text{D.10})$$

which leads to

$$P_t - n\mu P_i = \frac{2Q_i}{\rho \cos \chi} (1 - n\mu) \quad (\text{D.11})$$

Here, $\mu = \cos \chi_i / \cos \chi_t$. To find how Q_i and Q_t are related, we again calculate both of these quantities as a function of ξ_1 on the boundary, to find

$$\mu Q_t - Q_i = 0 \quad (\text{D.12})$$

Appendix E

Perturbation Theory for Gaussian Modes

We will start with Eq. (4.53). The following observation is very useful in the construction to follow. Each equation in this recurrence system can be written in the general form

$$\mathcal{L}_0 u_n^{(\ell)} = - \sum_{n=1} \mathcal{L}_{\frac{n}{2}} u_n^{(\ell)} + c_n(\{\delta_i\}) u_0^{(\ell)} \quad (\text{E.1})$$

where $\mathcal{L}_{m+\frac{1}{2}} \equiv 0$, and $c_n(\delta_i)$ is a function of the constants δ_i , $i = 1, \dots, n$. We have chosen this clumsy-looking convention because in inhomogeneous systems, $\mathcal{L}_{m+\frac{1}{2}} \neq 0$, and we want to keep some statements as general as possible. First, note that an operator $\mathcal{L}_{n/2}$ acting on a L -periodic function will produce another L -periodic function i.e. if $K_n^{(\ell)}(\tilde{x}, z) = \sum \mathcal{L}_{n/2} u_n^{(\ell)}(\tilde{x}, z)$, then

$$K_n^{(\ell)}(\tilde{x}, z + L) = e^{i\kappa_\ell} K_n^{(\ell)}(\tilde{x}, z) \quad (\text{E.2})$$

where $\kappa_\ell = -(\ell + \frac{1}{2})\varphi$. This particular Floquet index follows from induction, starting with Eq. (4.56). Then we can expand

$$K_n^{(\ell)}(\tilde{x}, z) = \sum \gamma_{nm}^\ell(z) u_0^{(m)}(\tilde{x}, z) \quad (\text{E.3})$$

Note that this and Eq. (E.2) require that

$$\gamma_{nm}^\ell(z + L) = e^{i(\kappa_m - \kappa_\ell)} \gamma_{nm}^\ell(z) \quad (\text{E.4})$$

Last but not least, we expand $u_n^{(\ell)}$ using the complete set of quasi-modes $u_0^{(\ell)}$ which satisfy the boundary conditions and are (Floquet-) periodic

$$u_n^{(\ell)} = \sum_m \beta_{nm}^\ell(z) u_0^{(m)}(\tilde{x}, z) \quad (\text{E.5})$$

To ensure periodicity, these z -dependent coefficients have to satisfy the Floquet condition as well

$$\beta_{nm}^\ell(z + L) = e^{i(\kappa_m - \kappa_\ell)} \beta_{nm}^\ell(z) \quad (\text{E.6})$$

After these preparatory steps to ensure the satisfaction of the periodicity condition, we have to make sure we satisfy the boundary conditions at higher orders, too. For this we need to incorporate higher order surface corrections. Thus, at each bounce we assume the surface ∂D has the shape

$$\xi_2 = -\frac{\xi_1^2}{2\rho} + \eta_3 \xi_1^3 + \eta_4 \xi_1^4 \quad (\text{E.7})$$

note that this type of expansion comes from the Taylor expansion of the actual surface $\xi_2 = D(\xi_1)$ for small ξ_1 (recall that $\xi_1 = O(1/\sqrt{k_0})$).

We will now proceed to find the lowest order correction terms using Eq. (E.7). On each segment of the PO, we will expand

$$e^{ik_0 z}|_{\partial D} = \exp \left[ik_0 \left(l_k - \frac{\tilde{\xi}_1^2}{2k_0 \rho_k} \right) \right] \left(1 + \frac{i}{\sqrt{k_0}} \eta_3 \tilde{\xi}_1^3 + \frac{i}{k_0} \eta_4 \tilde{\xi}_1^4 \right) \quad (\text{E.8})$$

We can now implement the boundary conditions Eq. (4.6)

$$\psi_i|_{\partial D} = e^{ik_0 z}|_{\partial D} \left[u_0^{(\ell)} + \frac{1}{\sqrt{k_0}} u_1^{(\ell)} + \frac{1}{k_0} u_2^{(\ell)} \right] \Big|_{\partial D} \quad (\text{E.9})$$

We will furthermore expand

$$u_0^{(\ell)} \Big|_{\partial D} = u_0^{(\ell)}(\tilde{x}, l_k) - \frac{\tilde{\xi}_1^2}{2k_0 \rho_k} \frac{\partial}{\partial z} u_0^{(\ell)}(\tilde{x}, l_k) \quad (\text{E.10})$$

this procedure is justified because $\{u_0^{(\ell)}\}$ were found to be complete on the domain $z = \text{const}$. Using Eq. (E.5) and Eq. (E.10) in Eq. (E.9), we obtain

$$\psi_i|_{\partial D} = e^{ik_0 z} \left[1 + \frac{1}{\sqrt{k_0}} \mathcal{L}_{\partial D}^{(1)} + \frac{1}{k_0} \mathcal{L}_{\partial D}^{(2)} + O\left(\frac{1}{k_0^{3/2}}\right) \right] \left(\delta_m^\ell + \sum_{nm} \frac{1}{(\sqrt{k_0})^n} \beta_{nm}^\ell(z) \right) u_0^{(m)} \Big|_{\partial D} \quad (\text{E.11})$$

where the expressions for the first few boundary operators are given by

$$\mathcal{L}_{\partial D}^{(1)} = i\eta_3 \tilde{\xi}_1^3 \quad (\text{E.12})$$

$$\mathcal{L}_{\partial D}^{(2)} = -\frac{\tilde{\xi}_1^2}{2\rho_k} \frac{\partial}{\partial z} + i\eta_4 \tilde{\xi}_1^4 \quad (\text{E.13})$$

their action to be evaluated at $z = l_k$. Eq. (4.6) can now be written order by order

$$u_0^{(\ell)}(l_k^-) + u_0^{(\ell)}(l_k^+) = 0 \quad (\text{E.14})$$

$$\mathcal{L}_{\partial D}^{(1)} u_0^{(\ell)} + \sum \beta_{1m}^\ell u_0^{(m)} \Big|_{l_k^-} + () \Big|_{l_k^+} = 0 \quad (\text{E.15})$$

$$\mathcal{L}_{\partial D}^{(2)} u_0^{(\ell)} + \mathcal{L}_{\partial D}^{(1)} \sum \beta_{1m}^\ell u_0^{(m)} + \sum \beta_{2m}^\ell u_0^{(m)} \Big|_{l_k^-} + () \Big|_{l_k^+} = 0 \quad (\text{E.16})$$

Here, we have suppressed the dependence on \tilde{x} for the sake of visibility. Inspecting this recurrence, one easily finds that the whole calculation boils down to determination of terms $\mathcal{L}_{\partial D}^{(n)} u_0^{(\ell)}$. Note that $\partial\beta/\partial z$ terms don't show up at these lowest orders. It's easy to see that the action of the operators $\mathcal{L}_{\partial D}^{(n)}$ will produce polynomials in \tilde{x} with z -dependent coefficients i.e. one can write

$$\mathcal{L}_{\partial D}^{(n)} u_0^{(\ell)} = P(\tilde{x}) u_0^{(0)} \quad (\text{E.17})$$

which have to be re-expressed in terms of an expansion in the complete set $\{u_0^{(\ell)}\}$. Let's therefore define coefficients $\Gamma_{nm}^\ell(z)$ by

$$\mathcal{L}_{\partial D}^{(n)} u_0^{(\ell)}|_{l^\pm} = \sum_m \Gamma_{nm}^\ell(l^\pm) u_0^{(m)}(l^\pm) \quad (\text{E.18})$$

These and $\gamma_{nm}^\ell(z)$ can be calculated straightforwardly by finding the polynomials P and K , respectively, and then expanding these polynomials in terms of $\{u_0^{(\ell)}\}$. However, they can also be found by a much more efficient algebraic technique, which we will adopt here.

Since we are operating in the Hilbert space of functions $\{u_0^{(\ell)}\}$ (essentially, we have a Hilbert space attached to each z), any operation involving a multiplication by \tilde{x} and a derivative with respect to \tilde{x} can be replaced by operators $(\Lambda, \Lambda^\dagger)$ using Eq. (4.39) and Eq. (4.40). Thus we can formally write

$$\mathcal{D} \left[\tilde{x}, \frac{\partial}{\partial \tilde{x}} \right] = \mathcal{D} [q\Lambda^\dagger - q^*\Lambda, i(p\Lambda^\dagger - p^*\Lambda)] \quad (\text{E.19})$$

Thus we can write

$$\mathcal{L}_{\partial D}^{(1)} = i\eta_3(q\Lambda^\dagger - q^*\Lambda)^3 \quad (\text{E.20})$$

In order to write \mathcal{L}_1 (in Eq. (4.57)) and $\mathcal{L}_{\partial D}^{(2)}$ (in Eq. (E.13)), we make use of Eq. (4.55)

$$\frac{\partial}{\partial z} = \frac{1}{2i} \frac{\partial^2}{\partial \tilde{x}^2} \quad (\text{E.21})$$

which allows us to write

$$\mathcal{L}_1 = -\frac{1}{4}(p\Lambda^\dagger - p^*\Lambda)^4 \quad (\text{E.22})$$

$$\mathcal{L}_{\partial D}^{(2)} = \frac{i}{4\rho_k}(q\Lambda^\dagger - q^*\Lambda)^2(p\Lambda^\dagger - p^*\Lambda)^2 + i\eta_4(q\Lambda^\dagger - q^*\Lambda)^4 \quad (\text{E.23})$$

Note that for the reflected wave, operators Eq. (E.20)-Eq. (E.23) have expressions differing only in sign

$$\mathcal{L}_{\partial D}^{(1,2)}|_{l_k^+} = -\mathcal{L}_{\partial D}^{(1,2)}|_{l_k^-} \quad (\text{E.24})$$

We will now implement this perturbation theory to find the lowest order corrections to the ground state $u_0^{(0)}$ of the bouncing ball mode. At $O(1/\sqrt{k_0})$, solving Eq. (4.56), we obtain

$$\frac{\partial\beta_{1m}^0}{\partial z} = i\delta_1\delta_m^0 \quad (\text{E.25})$$

The boundary conditions have to be satisfied at $z = l$ and $z = 2l$. Eq. (E.14) is satisfied by construction. Eq. (E.15), using Eq. (E.24) and Eq. (E.14) gives

$$\beta_{10}^0(l^-) - \beta_{10}^0(l^+) = 0 \quad (\text{E.26})$$

and a similar condition at $z = 2l$. In other words, $\sum_{\pm} \Gamma_{10}^0(l_k^{\pm}) = 0$. Now let's implement the periodicity condition. Eq. (E.6) is equivalent to the statement

$$\oint dz \frac{\partial \beta_{10}^0}{\partial z} = \sum_{l_k, \pm} \Gamma_{10}^0(l_k^{\pm}) + 2i\delta_1 l = 0 \quad (\text{E.27})$$

Finally, using Eq. (E.26) we reach the conclusion that the lowest order correction vanishes: $\delta_1 = 0$. We also set $\beta_{10}^0 = 0$. To find a non-trivial correction, we proceed to the next term at $O(1/k_0)$. Eq. (4.57) gives

$$2i \frac{\partial \beta_{2m}^0}{\partial z} = -\gamma_{2m}^0 - 2\delta_2 \delta_m^0 \quad (\text{E.28})$$

where γ_{2m}^0 can be calculated using Eq. (E.22)

$$\gamma_{24}^0 = -\frac{1}{4}p^4 \quad \gamma_{22}^0 = \frac{3}{4}p^2|p|^2 \quad \gamma_{20}^0 = -\frac{1}{4}|p|^4 \quad (\text{E.29})$$

and at this point, it's uplifting to see the satisfaction of the Floquet conditions Eq. (E.4). The boundary conditions Eq. (E.16) can be implemented by first determining $\Gamma_{2m}^{\ell}(l^{\pm})$, using Eq. (E.23)

$$\begin{aligned} \Gamma_{2m}^0(l^-) &= i \left(\left[\frac{1}{4\varrho} q^2 p^2 + \eta_4 q^4 \right] \delta_m^4 - \left[\frac{1}{4\varrho} (q^2 |p|^2 + 2p^2 |q|^2) + 3\eta_4 q^2 |q|^2 \right] \delta_m^2 \right. \\ &\quad \left. + \left[\frac{1}{2\varrho} (|q|^2 |p|^2 + (q^*)^2 p^2) 3\eta_4 |q|^4 \right] \delta_m^0 \right) \end{aligned} \quad (\text{E.30})$$

$$\quad (\text{E.31})$$

where (q, p) are evaluated $z = l^-$, with the incident ray parameters and $\Gamma_{2m}^0(l^+) = -\Gamma_{2m}^0(l^-)$. Note that, to calculate the latter one has to use the reflected ray parameters. Thus we can write

$$\beta_{2m}^0(l^+) - \beta_{2m}^0(l^-) = \Gamma_{2m}^0(q_1(l), p_1(l)) + \Gamma_{2m}^0(q_2(l), p_2(l)) \quad (\text{E.32})$$

$$\beta_{2m}^0(2l^+) - \beta_{2m}^0(2l^-) = \Gamma_{2m}^0(q_2(2l), p_2(2l)) + \Gamma_{2m}^0(q_1(2l), p_1(2l)) \quad (\text{E.33})$$

These equations look hopelessly untamable, but fortunately one can use some special properties of the BB motion to reach a simpler expression. First of all, note that if the total Floquet phase for a roundtrip is φ , then

$$\begin{pmatrix} q_2(l) \\ p_2(l) \end{pmatrix} = e^{i\varphi/2} \begin{pmatrix} q_1(0) \\ p_1(0) \end{pmatrix} \quad (\text{E.34})$$

and supplementing this by Eq. (4.21), we can express all the quantities on the right by merely the parameters $q(0)$, $p(0)$ and φ . The system Eq. (E.25) with boundary conditions Eq. (E.32) and Eq. (E.33), supplemented with the Floquet condition

Eq. (E.6), is an inhomogeneous Sturm-Liouville problem and might or might not have a solution. The condition for solvability is that the homogeneous problem shouldn't have any non-trivial solutions. The solution to the homogenous problem is simply ($m \neq 0$)

$$\beta_{2m}^0(z) = \text{const.} \quad (\text{E.35})$$

For this constant to be zero, the Floquet condition Eq. (E.6) requires that $e^{im\varphi} \neq 1$ for $\forall m$ and this is only possible when φ/π is irrational, except when $m = 0$. For $m = 0$, the necessary condition for solvability is obtained by integrating the inhomogeneous equation for $m = 0$ over one period and demanding consistency. We obtain

$$\oint dz \frac{\partial \beta_{20}^0}{\partial z} = \frac{1}{8i}(|p_1|^4 + |p_2|^4)l + 2i\delta_2 l = \sum_{l_k, \pm} \Gamma_{20}^0(l_k^\pm) \quad (\text{E.36})$$

which finally yields a condition on δ_2 , hence determining the correction to the quantization condition

$$\delta_2 = \frac{1}{8}|p|^4 + \frac{1}{\varrho l}|q|^2|p|^2 + \frac{1}{2\varrho l}(q^*)^2 p^2(1 + e^{i\varphi}) + \frac{6}{l}\eta_4|q|^4 \quad (\text{E.37})$$

Here $q = q(0)$ and $p = p(0)$. There remains one doubt which we have to absolve ourselves from. Because the original problem was self-adjoint, the perturbation theory has to yield real number corrections. The expression Eq. (E.37) for δ_2 however, at a first look, is not manifestly real. Our conscience can be cleared by making sure the third term is real. This can be done numerically (by constructing the eigensolutions of the monodromy matrix), and it turns out this term is in fact real. Finally, one can go ahead and check whether this lengthy calculation has brought us any closer to the exact value. For a quadrupolar cavity of deformation $\epsilon = 0.05$, the lowest order eigenvalue of the ground-state BB mode at principal quantum number $m = 122$ is

$$k_0 = \frac{\varphi}{4l} + \frac{\pi}{2l} + \frac{m\pi}{l} \quad (\text{E.38})$$

the value can be calculated with the parameters of the BB orbit, $\varrho = 1.203333$, $l = 1.9$, $\varphi = 1.9067414$ to be $k_0 = 202.29916865$, while the ‘‘exact’’ value calculated from the numerical solution of the Helmholtz equation is $k = 202.30066044$, with an estimated error of the order of 10^{-8} . Now, including the correction we have calculated (the extra parameter needed here is the surface correction, $\eta_3 = 0$, $\eta_4 = -0.11058$)

$$k = k_0 + \frac{\delta_2}{k_0} = 202.30152109 \quad (\text{E.39})$$

the error from the exact value being of order $10^{-4} = O(1/k_0^2)$.

Appendix F

The Lens Transform for a Cavity

In the experimental imaging system, radiation emanating from the resonator is collected through an aperture and after passing through a lens, an image is recorded for a discrete number of angles in the farfield. The resonator is placed at the focal plane of the lens, so that the image is effectively formed at infinity.

Just in front of the lens the field distribution is given by the resonance wavefunction $\Psi(x)$ which, at the observation (FF) angle θ , can be expressed as:

$$\Psi(x) \sim \sum_m \gamma_m H_m^+(k\sqrt{x^2 + z_1^2}) e^{im(\phi+\theta)} \quad (\text{F.1})$$

where $\phi = \tan^{-1} \frac{x}{z_1} \approx \frac{x}{z_1}$. The lens effectively adds a quadratic phase, so that the field immediately behind the lens is given by

$$\Psi'(x) = \Psi(x) P(x) \exp \left[-i \frac{k}{2f} x^2 \right] \quad (\text{F.2})$$

Here $P(x)$ is the *pupil function*, which takes care of the effect of the aperture, f is the focal length of the lens and x is the position on the lens. The field at the camera is given by propagating this field with the Fresnel propagator [158], which is well-justified as the lens-camera distance is much larger than the wavelength

$$\Psi''_\theta(u) = \frac{k}{iz_2} \int_{-\infty}^{\infty} dx \Psi'(x) \exp \left[i \frac{k}{2z_2} (u-x)^2 \right] \quad (\text{F.3})$$

Using the expression Eq. (F.1) for the wavefunction

$$\Psi''_\theta(u) = \frac{k}{iz_2} e^{i \frac{k}{2z_2} u^2} \sum_m \gamma_m \quad (\text{F.4})$$

$$\times \int_{-\infty}^{\infty} dx P(x) H_m^+(k\sqrt{z_1^2 + x^2}) e^{im(\theta + \frac{x}{z_1})} e^{i \frac{k}{2} (\frac{1}{z_2} - \frac{1}{f}) x^2} e^{-i \frac{k}{z_2} ux} \quad (\text{F.5})$$

Using the large argument asymptotic expansion of the Bessel functions:

$$H_m^+(k\sqrt{x^2 + z_1^2}) \sim \sqrt{\frac{2}{k(x^2 + z_1^2)^{1/2}}} \exp \left[ik\sqrt{x^2 + z_1^2} - im \frac{\pi}{2} - i \frac{\pi}{4} \right] \quad (\text{F.6})$$

Expanding the square root in the exponential to $O(\frac{x}{z_1})^4$, i.e. to the same order as the Fresnel approximation and rearranging the terms,

$$\Psi''_{\theta}(u) = \frac{k}{iz_2} e^{i\frac{k}{2z_2}u^2} \sum_m \gamma_m \frac{1}{kz_1} e^{ikz_1+im\theta-im\frac{\pi}{2}-i\frac{\pi}{4}} \quad (\text{F.7})$$

$$\times \int_{-\infty}^{\infty} dx P(x) e^{im\frac{x}{z_1}-\frac{k}{z_2}ux} e^{i\frac{k}{2}(\frac{1}{z_1}+\frac{1}{z_2}-\frac{1}{f})x^2} \quad (\text{F.8})$$

The second exponent in the integral is exactly the lens law, so it vanishes. Setting $\frac{m}{k} = R_0 \sin \chi_m$, the intensity recorded at the pixel u of the camera at the farfield angle θ can asymptotically be written as

$$|\Psi''_{\theta}(u)|^2 \sim \left| \sum_m \gamma_m H_m^+(kz_1) e^{im\theta} \int_{-\infty}^{\infty} dx P(x) \exp \left[i\frac{k}{z_2} (MR_0 \sin \chi_m - u)x \right] \right|^2 \quad (\text{F.9})$$

where $M = z_2/z_1$ is the magnification of the lens. For a simple aperture, $P(x)$ is given by

$$P(x) = \begin{cases} 1, & |x| < A/2 \\ 0, & |x| > A/2 \end{cases} \quad (\text{F.10})$$

so that the integral can be performed exactly to yield

$$|\Psi''_{\theta}(u)|^2 \sim \left| A \sum_m \gamma_m H_m^+(kz_1) e^{im\theta} \text{sinc} \left[\frac{1}{\Delta} (\sin \chi_m - \frac{u}{MR_0}) \right] \right|^2 \quad (\text{F.11})$$

where $\Delta = \frac{2z_1}{AkR_0}$ and $\text{sinc}(x) = \sin x/x$. Note that in the short-wavelength limit $\Delta \rightarrow 0$ and $\frac{1}{\pi} \text{sinc}(\frac{x}{\Delta}) \rightarrow \delta(x)$. This expression allows us to make predictions based on short-wavelength limit and geometric ray optics, which includes effects of diffraction as well. For instance, for a circular cylindrical resonator, the resonances are composed of a single angular momentum component m (and its degenerate partner $-m$). In that case, according to the expression Eq. (F.11),

$$|\Psi''_{\theta}(u)|^2 \propto \left| \delta(\sin \chi_m - \frac{u}{MR_0}) e^{im\theta} \pm \delta(\sin \chi_m + \frac{u}{MR_0}) e^{-im\theta} \right|^2 \quad (\text{F.12})$$

Note that the image-field contains only information captured from the farfield distribution. The actual details of the resonance in the ‘‘nearfield’’ can be quite different, due to evanescent contributions close to critical incidence. For instance, the points of brightest emission inferred from the image-field might be shifted due to an ‘‘optical mirage’’-like effect (see Fig. 4.9(c)). The mirage is formed not because of a continuously varying index of refraction but a discontinuous interface.

The image-field has an interesting connection to the (SOS projected) Husimi-Poincaré distribution. The Husimi distribution of the field projected onto the SOS at a distance $R \rightarrow \infty$ is given by

$$H_{\Psi}(\theta, p_{\theta}) = \left| \sum_m \gamma_m H_m^+(kR) e^{im\theta} e^{-\frac{1}{2}\eta^2(m-p_{\theta})^2} \right|^2 \quad (\text{F.13})$$

Comparing with Eq. (F.11), we see that the two functions contain almost the same information. In fact, by choosing an aperture which has a Gaussian transmittance $P(x)$, one would obtain exactly the same form as Eq. (F.11). Note that the freedom of smoothing to obtain various phase space distributions which represent the same physical system gains here a physical meaning, namely it translates to the choice of optical apparatus (lens, aperture etc.) to observe the resonator.

Bibliography

- [1] <http://www.sentech.com>.
- [2] A. Imamoglu. <http://www.ece.ucsb.edu/sqo>.
- [3] J. U. Nöckel and A. D. Stone. Ray and wave chaos in asymmetric resonant optical cavities. *Nature*, 385:45–47, 1997.
- [4] J. U. Nöckel. <http://darkwing.uoregon.edu/~noeckel>.
- [5] C. Gmachl, F. Capasso, E. E. Narimanov, J. U. Nöckel, A. D. Stone, J. Faist, D. L. Sivco, and A. Y. Cho. High-power directional emission from microlasers with chaotic resonators. *Science*, 280:1556–1564, 1998.
- [6] P. T. Leung, S. Y. Liu, and K. Young. Completeness and orthogonality of quasi-normal modes in leaky optical cavities. *Phys. Rev. A*, 49:3057–3067, 1994.
- [7] E. S. C. Ching, P. T. Leung, A. M. van den Brink, W. M. Suen, S. S. Tong, and K. Young. Quasinormal-mode expansion for waves in open systems. *Rev. Mod. Phys.*, 70:1545–1554, 1998.
- [8] Y. Yamamoto and R. E. Slusher. Optical processes in microcavities. *Phys. Today*, 46:66–73, 1993.
- [9] G. Chen, R. K. Chang, S. C. Hill, and P. W. Barber. Frequency splitting of degenerate spherical cavity modes - stimulated raman-scattering spectrum of deformed droplets. *Opt. Lett.*, 16:1269–1271, 1991.
- [10] G. Chen, M. M. Mazumder, Y. R. Chemla, A. Serpenguzel, R. K. Chang, and S. C. Hill. Wavelength variation of laser-emission along the entire rim of slightly deformed microdroplets. *Opt. Lett.*, 18:1993–1995, 1993.
- [11] S. L. McCall, A. F. J. Levi, R. E. Slusher, S. J. Pearton, and R. A. Logan. Whispering-gallery mode microdisk lasers. *Appl. Phys. Lett.*, 60:289–291, 1992.
- [12] R. E. Slusher, A. F. J. Levi, U. Mohideen, S. L. McCall, S. J. Pearton, and R. A. Logan. Threshold characteristics of semiconductor microdisk lasers. *Appl. Phys. Lett.*, 63:1310–1312, 1993.

- [13] A. F. J. Levi, R. E. Slusher, S. L. McCall, T. Tanbunek, D. L. Coblenz, and S. J. Pearton. Electrically pumped, room-temperature microdisk semiconductor lasers with submilliampere threshold currents. *IEEE Trans. Electron Devices*, 39:2651–2651, 1992.
- [14] Lord Rayleigh. On waves propagated along the plane surface of an elastic solid. *Proc. Lond. Math. Soc.*, 17:4–11, 1885.
- [15] Lord Rayleigh. *The problem of the whispering gallery*, pages 617–620. Cambridge, Cambridge, UK, 1912.
- [16] J. U. Noeckel. *Resonances in nonintegrable open systems*. PhD thesis, Yale University, 1997.
- [17] B. R. Johnson. Theory of morphology-dependent resonances - shape resonances and width formulas. *J. Opt. Soc. Am. A.*, 10:343–352, 1993.
- [18] L. Collot, V. Lefevreseguin, M. Brune, J. M. Raimond, and S. Haroche. Very high-q whispering-gallery mode resonances observed on fused-silica microspheres. *Europhys. Lett.*, 23:327–334, 1993.
- [19] S. M. Spillane, T. J. Kippenberg, and K. J. Vahala. Ultralow-threshold raman laser using a spherical dielectric microcavity. *Nature*, 415:621–623, 2002.
- [20] A. F. J. Levi, R. E. Slusher, S. L. McCall, J. L. Glass, S. J. Pearton, and R. A. Logan. Directional light coupling from microdisk lasers. *Appl. Phys. Lett.*, 62:561–563, 1993.
- [21] D. Y. Chu, M. K. Chin, W. G. Bi, H. Q. Hou, C. W. Tu, and S. T. Ho. Double-disk structure for output coupling in microdisk lasers. *Appl. Phys. Lett.*, 65:3167–3169, 1994.
- [22] J. U. Nöckel, A. D. Stone, and R. K. Chang. Q-spoiling and directionality in deformed ring cavities. *Opt. Lett.*, 19:1693–1695, 1994.
- [23] A. Mekis, J. U. Nöckel, G. Chen, A. D. Stone, and R. K. Chang. Ray chaos and q spoiling in lasing droplets. *Phys. Rev. Lett.*, 75:2682–2685, 1995.
- [24] J. U. Nöckel, A. D. Stone, G. Chen, H. L. Grossman, and R. K. Chang. Directional emission from asymmetric resonant cavities. *Opt. Lett.*, 21:1609–1611, 1996.
- [25] R. K. Chang and A. K. Campillo, editors. *Optical Processes in Microcavities*. World Scientific, Singapore, 1996.
- [26] H. M. Lai, P. T. Leung, K. Young, P. W. Barber, and S. C. Hill. Time-independent perturbation for leaking electromagnetic modes in open systems with application to resonances in microdroplets. *Phys. Rev. A*, 41:5187–5198, 1990.

- [27] K. M. Lee, P. T. Leung, and K. M. Pang. Iterative perturbation scheme for morphology-dependent resonances in dielectric spheres. *J. Opt. Soc. Am. A-Opt. Image Sci. Vis.*, 15:1383–1393, 1998.
- [28] M. V. Berry. Regularity and chaos in classical mechanics, illustrated by three deformations of a circular billiard. *Eur. J. Phys.*, 2:91–102, 1981.
- [29] V. I. Arnold. *Mathematical methods of classical mechanics*. Springer, New York, USA, 1989.
- [30] V. F. Lazutkin. *KAM theory and semiclassical approximations to eigenfunctions*. Springer, New York, USA, 1993.
- [31] A. J. Lichtenberg and M. A. Leiberman. *Regular and chaotic dynamics*. Springer, New York, USA, 1992.
- [32] L. E. Reichl. *The transition to chaos in conservative classical systems: quantum manifestations*. Springer, New York, USA, 1992.
- [33] A. Dodabalapur, E. A. Chandross, M. Berggren, and R. E. Slusher. Applied physics - organic solid-state lasers: Past and future. *Science*, 277:1787–1788, 1997.
- [34] Z. Bao, J. A. Rogers, A. Dodabalapur, A. J. Lovinger, H. E. Katz, V. R. Raju, Z. Peng, and M. E. Galvin. Polymer light emitting diodes: new materials and devices. *Opt. Mater.*, 12:177–182, 1999.
- [35] G. D. Chern, H. E. Tureci, A. Douglas Stone, M. Kneissl, N. M. Johnson, and R. K. Chang. Uni-directional lasing from ingan multiple quantum-well spiral-shaped micropillars. unpublished.
- [36] F. Treussart, N. Dubreuil, J. C. Knight, V. Sandoghdar, J. Hare, V. Lefevre-Seguin, J. M. Raimond, and S. Haroche. Microlasers based on silica microspheres. *Ann. Telecommun.-Ann Telecommun.*, 52:557–568, 1997.
- [37] S. X. Qian, J. B. Snow, H. M. Tzeng, and R. K. Chang. Lasing droplets - highlighting the liquid-air interface by laser-emission. *Science*, 231:486–488, 1986.
- [38] S. X. Qian and R. K. Chang. Multiorder stokes emission from micrometer-size droplets. *Phys. Rev. Lett.*, 56:926–929, 1986.
- [39] M. M. Mazumder, G. Chen, R. K. Chang, and J. B. Gillespie. Wavelength shifts of dye lasing in microdroplets - effect of absorption change. *Opt. Lett.*, 20:878–880, 1995.
- [40] J. Popp, M. H. Fields, and R. K. Chang. Injection seeding of lasing in microdroplets. *Opt. Lett.*, 22:139–141, 1997.

- [41] S. S. Chang, N. B. Rex, and R. K. Chang. Chemical lasing in pendant droplets: lasing-spectra, emission-pattern, and cavity-lifetime measurements. *J. Opt. Soc. Am. B-Opt. Phys.*, 16:1224–1235, 1999.
- [42] M. Robnik and M. V. Berry. Classical billiards in magnetic-fields. *J. Phys. A-Math. Gen.*, 18:1361–1378, 1985.
- [43] H. G. L. Schwefel, N. B. Rex, H. E. Tureci, R. K. Chang, and A. D. Stone. Dramatic shape sensitivity of emission patterns for similarly deformed cylindrical polymer lasers.
- [44] A. D. Stone. Wave-chaotic optical resonators and lasers. *Phys. Scr.*, T90:248–262, 2001.
- [45] J. U. Nöckel. Angular momentum localization in oval billiards. *Phys. Scr.*, T90:263–267, 2001.
- [46] F. Capasso, C. Gmachl, D. L. Sivco, and A. Y. Cho. Quantum cascade lasers. *Phys. Today*, 55:34–40, 2002.
- [47] A. F. J. Levi, S. L. McCall, S. J. Pearton, and R. A. Logan. Room-temperature operation of submicrometer radius disk laser. *Electron. Lett.*, 29:1666–1668, 1993.
- [48] E. Gornik. Geometrical shaping of microlaser emission patterns. *Science*, 280:1544–1545, 1998.
- [49] J. U. Nöckel. Optical feedback and the coupling problem in semiconductor microdisk lasers. *Phys. Status Solidi A-Appl. Res.*, 188:921–928, 2001.
- [50] S. Gianordoli, L. Hvozdar, G. Strasser, W. Schrenk, J. Faist, and E. Gornik. Long-wavelength $\lambda = 10\mu\text{m}$ quadrupolar-shaped gaas-algaas microlasers. *IEEE J. Quantum Electron.*, 36:458–464, 2000.
- [51] C. Gmachl, E. E. Narimanov, F. Capasso, J. N. Baillargeon, and A. Y. Cho. Kolmogorov-arnold-moser transition and laser action on scar modes in semiconductor diode lasers with deformed resonators. *Opt. Lett.*, 27:824–826, 2002.
- [52] N. B. Rex, H. E. Tureci, H. G. L. Schwefel, R. K. Chang, and A. D. Stone. Fresnel filtering in lasing emission from scarred modes of wave-chaotic optical resonators. *Phys. Rev. Lett.*, 88:art. no. 094102, 2002.
- [53] S. B. Lee, J. H. Lee, J. S. Chang, H. J. Moon, S. W. Kim, and K. An. Observation of scarred modes in asymmetrically deformed microcylinder lasers. *Phys. Rev. Lett.*, 8803:art. no. 033903, 2002.
- [54] S. Chang, R. K. Chang, A. D. Stone, and J. U. Nöckel. Observation of emission from chaotic lasing modes in deformed microspheres: displacement by the stable-orbit modes. *J. Opt. Soc. Am. B-Opt. Phys.*, 17:1828–1834, 2000.

- [55] A. W. Poon, F. Courvoisier, and R. K. Chang. Multimode resonances in square-shaped optical microcavities. *Opt. Lett.*, 26:632–634, 2001.
- [56] I. Braun, G. Ihlein, F. Laeri, J. U. Nöckel, G. Schulz-Ekloff, F. Schuth, U. Vietze, O. Weiss, and D. Wöhrle. Hexagonal microlasers based on organic dyes in nanoporous crystals. *Appl. Phys. B-Lasers Opt.*, 70:335–343, 2000.
- [57] M. V. Berry and K. E. Mount. Semiclassical approximations in wave mechanics. *Rep. Prog. Phys.*, 35:315–&, 1972.
- [58] M. V. A. Berry. *Semiclassical Mechanics of regular and irregular motion*, pages 171–271. North Holland, Amsterdam, 1983.
- [59] A. Einstein. Zum quantensatz von sommerfeld und epstein. *Verhandl. Deut. Physik. Ges.*, 19:82–92, 1917.
- [60] P. S. Epstein. Hamilton-jacobische funktion und quantentheorie. *Verhandl. Deut. Physik. Ges.*, 19:116–129, 1917.
- [61] L. Brillouin. Remarques sur la mcanique ondulatoire. *Le Journal de Physique et le Radium*, 12:353–368, 1926.
- [62] J. B. Keller. Corrected bohr-sommerfeld quantum conditions for nonseparable systems. *Ann. Phys.*, 4:180–188, 1958.
- [63] M. Born. *Mechanics of the atom*. Ungar, New York, USA, 1960.
- [64] P. S. Epstein. Zur quantentheorie. *Ann. d. Physik*, 51:168–188, 1916.
- [65] V. P. Maslov and M. V. Fedoriuk. *Semi-Classical Approximation in Quantum Mechanics*. Reidel, Boston, USA, 1981.
- [66] V. M. Babič and V. S. Buldyrev. *Asymptotic Methods in Shortwave Diffraction Problems*. Springer, New York, USA, 1991.
- [67] A. H. Barnett. *Dissipation in deforming chaotic billiards*. PhD thesis, Harvard University, 2000.
- [68] A. B. Manenkov. Radiation modes of a fiber .1. construction and properties. *IEE Proc.-Optoelectron.*, 141:287–295, 1994.
- [69] E. Doron and U. Smilansky. Semiclassical quantization of chaotic billiards - a scatteringtheory approach. *Nonlinearity*, 5:1055–1084, 1992.
- [70] S. D. Frischat and E. Doron. Quantum phase-space structures in classically mixed systems: A scattering approach. *J. Phys. A-Math. Gen.*, 30:3613–3634, 1997.

- [71] M. Hentschel and K. Richter. Quantum chaos in optical systems: The annular billiard. *Phys. Rev. E*, 66:art. no.–056207, 2002.
- [72] B. Dietz, J. P. Eckmann, C. A. Pillet, U. Smilansky, and I. Ussishkin. Inside-outside duality for planar billiards - a numerical study. *Phys. Rev. E*, 51:4222–4231, 1995.
- [73] J. P. Eckmann and C. A. Pillet. Spectral duality for planar billiards. *Commun. Math. Phys.*, 170:283–313, 1995.
- [74] A. E. Siegman. Laser beams and resonators: The 1960s. *IEEE J. Sel. Top. Quantum Electron.*, 6:1380–1388, 2000.
- [75] A. E. Siegman. Laser beams and resonators: Beyond the 1960s. *IEEE J. Sel. Top. Quantum Electron.*, 6:1389–1399, 2000.
- [76] A. E. Siegman. *Lasers*. University Science Books, Mill Valley, California, 1986.
- [77] V. A. Fock. *Electromagnetic diffraction and propagation problems*. Pergamon, Oxford, UK, 1965.
- [78] H. E. Tureci, H. G. L. Schwefel, A. D. Stone, and E. E. Narimanov. Gaussian-optical approach to stable periodic orbit resonances of partially chaotic dielectric micro-cavities. *Opt. Express*, 10:752–776, 2002.
- [79] N. B. Rex. *Regular and chaotic orbit Gallium Nitride microcavity lasers*. PhD thesis, Yale University, 2001.
- [80] L. Kaplan. Scars in quantum chaotic wavefunctions. *Nonlinearity*, 12:R1–R40, 1999.
- [81] E. B. Bogomolny. Smoothed wave-functions of chaotic quantum-systems. *Physica D*, 31:169–189, 1988.
- [82] H. E. Tureci and A. D. Stone. Deviation from snell’s law for beams transmitted near the critical angle: application to microcavity lasers. *Opt. Lett.*, 27:7–9, 2002.
- [83] J. B. Keller and R. M. Lewis. *Asymptotic methods for partial differential equations: The reduced wave equation and Maxwell’s equations*. Plenum Publishing, NY, 1995.
- [84] Yu. A. Kravtsov and Yu. I. Orlov. *Caustics, catastrophes and wave fields*. Springer, Berlin, Germany, 1999.
- [85] S. J. Chapman, J. M. H. Lawry, J. R. Ockendon, and R. H. Tew. On the theory of complex rays. *SIAM Rev.*, 41:417–509, 1999.

- [86] C. M. Bender and S. A. Orszag. *Advanced mathematical methods for scientists and engineers*. Springer, New York, USA, 1999.
- [87] M. Born and E. Wolf. *Principles of Optics*. Cambridge University Press, Cambridge, UK, 1980.
- [88] R. Courant and D. Hilbert. *Methods of mathematical physics*. John Wiley & sons, New York, USA, 1989.
- [89] P. M. Morse and H. Feshbach. *Methods of Theoretical Physics, Part I and II, Section 2.3, "Motion of Fluids"*. McGraw-Hill, New York, NY, USA, 1953.
- [90] M. V. Berry. Waves and thoms theorem. *Adv. Phys.*, 25:1–26, 1976.
- [91] R. Gilmore. *Catastrophe theory for scientists and engineers*. Dover Publications, Inc., New York, USA, 1993.
- [92] D. Ludwig. Uniform asymptotic expansions at a caustic. *Comm. Pure Appl. Math.*, 29:215–150, 1966.
- [93] M. V. Berry. Uniform approximation for potential scattering involving a rainbow. *Proc Phys Soc Lond*, 89:479–&, 1966.
- [94] J. Oprea. *Differential Geometry and Its Applications*. Prentice Hall, New York, USA, 1996.
- [95] J. B. Keller. Asymptotic solution of eigenvalue problems. *Ann. Phys.*, 9:24–75, 1960.
- [96] M. Abramovitz and I. A. Stegun. *Handbook of mathematical functions*. Dover, New York, USA, 1972.
- [97] H. A. Kramers. Wellenmechanik und halbzahlige quantisierung. *Zeitschrift fr Physik*, 39:828–840, 1926.
- [98] G. Birkhoff. Dynamical systems. *Acta Math*, 50, 1927.
- [99] M. V. Berry. Regular and irregular semiclassical wavefunctions. *J. Phys. A-Math. Gen.*, 10:2083–2091, 1977.
- [100] A. I. Schnirelman. *Usp. Mat. Nauk.*, 29:181, 1974.
- [101] S. Zelditch. *Duke Math. J.*, 55:919, 1987.
- [102] Y. C. de Verdiere. *Commun. Math. Phys.*, 102:497, 1985.
- [103] E. J. Heller. Bound-state eigenfunctions of classically chaotic hamiltoniansystems - scars of periodic-orbits. *Phys. Rev. Lett.*, 53:1515–1518, 1984.

- [104] S. W. McDonald. Quantum poincare sections for 2-dimensional billiards. *Phys. Rev. E*, 47:986–991, 1993.
- [105] H. Poritsky. The billiard ball problem on a table with convex boundary - an illustrative dynamical problem. *Annals of Mathematics*, 51:446 – 470, 1950.
- [106] A. N. Kolmogorov. *Dokl. Akad. Nauk. SSSR*, 98:527, 1954.
- [107] V. I. Arnold. Generation of quasi-periodic motion from a family of periodic motions. *Dokl Akad Nauk Sssr*, 138:13–&, 1961.
- [108] J. Moser. *Nachr. Akad. Wiss. Göttingen II, Math. Phys. Kl.*, 1, 1962.
- [109] H. Poincaré. *Les Methodes Nouvelles de la Mechanique Celeste*. Gauthier-Villars, Paris, France, 1892.
- [110] S. Smale. Differentiable dynamical systems. *Bull. Amer. Math. Soc.*, 73:747–817, 1967.
- [111] J. M. Greene. Two-dimensional measure-preserving mappings. *Journal of Mathematical Physics*, 9(5):760–768, 1968.
- [112] R. Douady. *Applications du theoreme des tores invariants*. PhD thesis, Université Paris VII, 1982.
- [113] V. I. Arnold. Modes and quasimodes. *Funktsional'nyi Analiz i Ego Prilozheniya*, 6:12–20, 1972.
- [114] J. U. Nöckel, A. D. Stone, G. Chen, H. L. Grossman, and R. K. Chang. Directional emission from asymmetric resonant cavities. *Opt. Lett.*, 21:1609–1611, 1996.
- [115] V. F. Lazutkin. Asymptotics of eigenfunctions of laplacian concentrated near the boundary of a region. *USSR Comp. Math. Phys.*, 7:37–52, 1967.
- [116] E. Wigner. On the quantum correction for thermodynamic equilibrium. *Phys. Rev.*, 40:749–759, 1932.
- [117] E. J. Heller. *Wavepacket dynamics and quantum chaology*, pages 547–663. North Holland, Amsterdam, 1989.
- [118] B. Crespi, G. Perez, and S. J. Chang. Quantum poincare sections for 2-dimensional billiards. *Phys. Rev. E*, 47:986–991, 1993.
- [119] G. Hackenbroich and J. U. Nöckel. Dynamical tunneling in optical cavities. *Europhys. Lett.*, 39:371–376, 1997.
- [120] M. Robnik. pages 251–274. Plenum, NY, 1988.

- [121] M. Robnik. Recent developments in the energy-level statistics in generic systems between integrability and chaos. *Chaos Solitons Fractals*, 5:1195–1218, 1995.
- [122] M. V. Berry. Semiclassical mechanics in phase space - study of wigners function. *Philos. Trans. R. Soc. Lond. Ser. A-Math. Phys. Eng. Sci.*, 287:237–271, 1977.
- [123] P. W. Oconnor and E. J. Heller. Quantum localization for a strongly classically chaotic system. *Phys. Rev. Lett.*, 61:2288–2291, 1988.
- [124] J. D. Jackson. *Classical electrodynamics*. John Wiley & Sons, Inc., New York, USA, 1998.
- [125] E. E. Narimanov, G. Hackenbroich, P. Jacquod, and A. D. Stone. Semiclassical theory of the emission properties of wave-chaotic resonant cavities. *Phys. Rev. Lett.*, 83:4991–4994, 1999.
- [126] Lord Rayleigh. On the dynamical theory of gratings. *Proc. Roy. Soc.*, A79:399–416, 1907.
- [127] P. M. van den Berg and J. T. Fokkema. The rayleigh hypothesis in the theory of diffraction by a perturbation in a plane surface. *Radio Sci.*, 15:723–732, 1980.
- [128] D. Klakow and U. Smilansky. Wavefunctions, expectation values and scars on poincare sections - a scattering approach. *J. Phys. A-Math. Gen.*, 29:3213–3231, 1996.
- [129] G. H. Golub and C. F. V. Loan. *Matrix Computations*. Johns Hopkins University Press, Baltimore, MD, USA, 1993.
- [130] W. H. Press, S. A. Teukolsky, Vetterling W. T. and Flannery B. P. *Numerical Recipes in C*. Cambridge University Press, Cambridge, UK, 1992.
- [131] H. M. Nussenzveig. *Diffraction effects in semiclassical scattering*. Cambridge University Press, Cambridge, UK, 1992.
- [132] Bleistein N. and Handelsman R. A. *Asymptotic expansion of integrals*. Dover Publications, Inc. New York, USA, 1986.
- [133] T. Prosen and M. Robnik. Survey of the eigenfunctions of a billiard system between integrability and chaos. *J. Phys. A-Math. Gen.*, 26:5365–5373, 1993.
- [134] M. C. Gutzwiller. *Chaos in classical and quantum mechanics*. Springer, New York, USA, 1990.
- [135] W. H. Miller. Semiclassical quantization of nonseparable systems: A new look at periodic orbit theory. *J. Chem. Phys.*, 63:996–999, 1975.

- [136] F. Laeri and J.U. Nöckel. *Nanoporous compound materials for optical applications - Microlasers and microresonators*. Academic Press, San Diego, 2001.
- [137] H. E. Tureci, H. G. L. Schwefel, A. D. Stone, and E. E. Narimanov. Gaussian-optical approach to stable periodic orbit resonances of partially chaotic dielectric micro-cavities. *Opt. Express*, 10:752–776, 2002.
- [138] E. J. Heller. Bound-state eigenfunctions of classically chaotic hamiltonian-systems - scars of periodic orbits. *Phys. Rev. Lett.*, 53:1515–1518, 1984.
- [139] O. A. Starykh, P. R. J. Jacquod, E. E. Narimanov, and A. D. Stone. Signature of dynamical localization in the resonance width distribution of wave-chaotic dielectric cavities. *Phys. Rev. E*, 62:2078–2084, 2000.
- [140] J. U. Nöckel. Angular momentum localization in oval billiards. *Phys. Scr.*, T90:263–267, 2001.
- [141] V. S. Buldyrev. *Asymptotic behavior of solutions of the wave equations that are concentrated near the axis of a two-dimensional waveguide in an inhomogeneous medium*, pages 1–23. Consultants Bureau, New York, 1969.
- [142] J. Kevorkian and J. D. Cole. *Multiple scales and singular perturbation methods*. Springer, New York, USA, 1996.
- [143] N. A. Chernikov. System whose hamiltonian is a time-dependent quadratic form in x and p . *Sov Phys-Jetp Engl Trans*, 26:603–608, 1968.
- [144] J. B. Keller and S. I. Rubinow. Asymptotic solution of eigenvalue problems. *Ann. Phys.*, 9:24–75, 1960.
- [145] V.F. Lazutkin. Spectral degeneracy and 'small denominators' in the asymptotics of eigenfunctions of 'bouncing ball' type. *Vestnik Leningrad Univ. Math.*, 2:103–116, 1975.
- [146] J. R. Ray. Exact-solutions to the time-dependent schrodinger-equation. *Phys. Rev. A*, 26:729–733, 1982.
- [147] R. Almeida and D. A. Morales. Exact solution to a general quantum mechanical problem with time-dependent boundary conditions. *Int. J. Quantum Chem.*, 63:827–833, 1997.
- [148] J. W. Ra, H. L. Bertoni, and L. B. Felsen. Reflection and transmission of beams at a dielectric interface. *SIAM J. Appl. Math.*, 24:396–413, 1973.
- [149] J. M. Robbins. Discrete symmetries in periodic-orbit theory. *Phys. Rev. A.*, 40:2128–2136, 1989.
- [150] M. J. Davis and E. J. Heller. Multidimensional wave functions from classical trajectories. *J. Chem. Phys.*, 75:246, 1981.

- [151] O. Bohigas, S. Tomsovic, and D. Ullmo. Manifestations of classical phase space structures in quantum mechanics. *Phys. Rep.*, 223:45, 1993.
- [152] S. D. Frischat and E. Doron. Semiclassical description of tunneling in mixed systems: case of the annular billiard. *Phys. Rev. Lett.*, 75:3661, 1995.
- [153] F. Leyvraz and D. Ullmo. The level splitting distribution in chaos-assisted tunneling. *J. Phys. A*, 29:2529, 1996.
- [154] E. E. Narimanov. unpublished.
- [155] M. V. Berry. Regular and irregular semiclassical wavefunctions. *J. Phys. A*, 10:2083, 1977.
- [156] W. Nasalski, T. Tamir, and L. Lin. Displacement of the intensity peak in narrow beams reflected at a dielectric interface. *J. Opt. Soc. Am. A*, 5:132–140, 1988.
- [157] H. Schomerus and M. Sieber. Bifurcations of periodic orbits and uniform approximations. *J. Phys. A-Math. Gen.*, 30:4537–4562, 1997.
- [158] J. W. Goodman. *Introduction to Fourier Optics*. Mc Graw-Hill, New York, USA, 1996.
- [159] M. V. Berry. Quantum scars of classical closed orbits in phase-space. *Proc. R. Soc. London Ser. A-Math. Phys. Eng. Sci.*, 423:219–231, 1989.
- [160] E. N. Economou. *Green's Functions in Quantum Physics*. Springer, New York, USA, 1979.
- [161] M. V. Berry. Quantizing a classically ergodic system - sinai billiard and the kkr method. *Ann. Phys.*, 131:163–216, 1981.
- [162] B. Eckhardt and E. Aurell. Convergence of the semi-classical periodic orbit expansion. *Europhys. Lett.*, 9:509–512, 1989.
- [163] A. Voros. Unstable periodic-orbits and semiclassical quantization. *J. Phys. A-Math. Gen.*, 21:685–692, 1988.
- [164] P. Cvitanovic. Invariant measurement of strange sets in terms of cycles. *Phys. Rev. Lett.*, 61:2729–2732, 1988.
- [165] S. C. Creagh, J. M. Robbins, and R. G. Littlejohn. Geometrical properties of maslov indexes in the semiclassical trace formula for the density of states. *Phys. Rev. A*, 42:1907–1922, 1990.
- [166] Gutzwiller M. C. The quantization of a classically ergodic system. *Physica D*, 5:183–2075, 1982.

- [167] T. Tamir. Nonspecular phenomena in beam fields reflected by multilayered media. *J. Opt. Soc. Am. A-Opt. Image Sci. Vis.*, 3:558–565, 1986.
- [168] J. W. Ra, H. L. Bertoni, and L. B. Felsen. Reflection and transmission of beams at a dielectric interface. *SIAM J. Appl. Math.*, 24:396–413, 1973.
- [169] Y. M. M. Antar. Transmitted field of a gaussian laser-beam at total internal-reflection. *Can. J. Phys.*, 55:2023–2035, 1977.
- [170] L. Mandel and E. Wolf. *Optical coherence and quantum optics*. Cambridge University Press, Cambridge, UK, 1995.
- [171] M. V. Berry. Evanescent and real waves in quantum billiards and gaussian beams. *J. Phys. A-Math. Gen.*, 27:L391–L398, 1994.
- [172] M. Sargent III, M.O. Scully, and W.E. Lamb Jr. *Laser Physics*. Addison-Wesley, Trabzon, Turkey, 1974.
- [173] H. Haken. *Light (Volume 2)*. North-Holland Physics Publishing, Amsterdam, Netherlands, 1985.
- [174] H. Haken and H. Sauermann. Nonlinear interactions of laser modes. *Z. Phys.*, 173:261, 1963.
- [175] A. C. Fowler, J. D. Gibbon, and M. J. McGuinness. The complex lorentz equations. *Physica D*, 4:139–163, 1982.
- [176] S. Residori, P. L. Ramazza, E. Pampaloni, and F. T. Arecchi. Pattern formation and competition in nonlinear optics. *J. Nonlinear Opt. Phys. Mater.*, 5:367–386, 1996.
- [177] F. T. Arecchi, G. L. Lippi, G. P. Puccioni, and J. R. Tredicce. Deterministic chaos in laser with injected signal. *Opt. Commun.*, 51:308–314, 1984.
- [178] H. Haken. *An Introduction to Synergetics*. Springer, Berlin, Germany, 1983.
- [179] K. Staliunas, M. F. H. Tarroja, and C. O. Weiss. Transverse mode locking, antilocking and self-induced dynamics of class-b lasers. *Opt. Commun.*, 103:69–75, 1993.
- [180] T. Sh. Misirpashaev and C. W. J. Beenakker. Lasing threshold and mode competition in chaotic cavities. *Phys. Rev. A.*, 57:2041–2045, 1998.
- [181] V. Zehnle. Theoretical analysis of a bimode laser. *Phys. Rev. A.*, 57:629–644, 1998.
- [182] T. Harayama, P. Davis, and K. S. Ikeda. Nonlinear whispering gallery modes. *Phys. Rev. Lett.*, 82:3803–3806, 1999.